

INFORMATION TO USERS

This manuscript has been reproduced from the microfilm master. UMI films the text directly from the original or copy submitted. Thus, some thesis and dissertation copies are in typewriter face, while others may be from any type of computer printer.

The quality of this reproduction is dependent upon the quality of the copy submitted. Broken or indistinct print, colored or poor quality illustrations and photographs, print bleedthrough, substandard margins, and improper alignment can adversely affect reproduction.

In the unlikely event that the author did not send UMI a complete manuscript and there are missing pages, these will be noted. Also, if unauthorized copyright material had to be removed, a note will indicate the deletion.

Oversize materials (e.g., maps, drawings, charts) are reproduced by sectioning the original, beginning at the upper left-hand corner and continuing from left to right in equal sections with small overlaps. Each original is also photographed in one exposure and is included in reduced form at the back of the book.

Photographs included in the original manuscript have been reproduced xerographically in this copy. Higher quality 6" x 9" black and white photographic prints are available for any photographs or illustrations appearing in this copy for an additional charge. Contact UMI directly to order.

UMI

A Bell & Howell Information Company
300 North Zeeb Road, Ann Arbor MI 48106-1346 USA
313/761-4700 800/521-0600

ADVANCES IN PULMONARY MONITORING AND THORACIC IMAGING

Thomas Florian Schuessler

Department of Biomedical Engineering,
McGill University, Montréal, Québec, Canada.

A Thesis submitted to the Faculty of Graduate Studies and Research
in December 1996 in partial fulfillment of the requirements of the degree of
Doctor of Philosophy.

© Thomas F. Schuessler 1996



National Library
of Canada

Acquisitions and
Bibliographic Services

395 Wellington Street
Ottawa ON K1A 0N4
Canada

Bibliothèque nationale
du Canada

Acquisitions et
services bibliographiques

395, rue Wellington
Ottawa ON K1A 0N4
Canada

Your file *Votre référence*

Our file *Notre référence*

The author has granted a non-exclusive licence allowing the National Library of Canada to reproduce, loan, distribute or sell copies of this thesis in microform, paper or electronic formats.

The author retains ownership of the copyright in this thesis. Neither the thesis nor substantial extracts from it may be printed or otherwise reproduced without the author's permission.

L'auteur a accordé une licence non exclusive permettant à la Bibliothèque nationale du Canada de reproduire, prêter, distribuer ou vendre des copies de cette thèse sous la forme de microfiche/film, de reproduction sur papier ou sur format électronique.

L'auteur conserve la propriété du droit d'auteur qui protège cette thèse. Ni la thèse ni des extraits substantiels de celle-ci ne doivent être imprimés ou autrement reproduits sans son autorisation.

0-612-30376-4

Canada

ABSTRACT

The high incidence of pulmonary disease in critically ill patients necessitates new and improved techniques for pulmonary monitoring and thoracic imaging. To investigate pulmonary monitoring techniques using pressure and flow signals, I developed a comprehensive computational model of subjects breathing spontaneously or with the support of an assist-ventilator. The model was used to quantitatively assess measurement techniques for dynamic intrinsic positive end-expiratory pressure (PEEP_i) and inspiratory work of breathing. The results demonstrate that some means of correction for both expiratory muscle activity and cardiogenic oscillations on esophageal pressure is necessary if dynamic PEEP_i and work of breathing are to be measured accurately on-line. I also conclude that the discrepancies between static and dynamic PEEP_i are caused by heterogeneity of the expiratory flow limitation. An adaptive filter to reduce the cardiogenic oscillations on esophageal pressure was developed and validated in a computer simulation. In four intensive care patients, the adaptive filter markedly attenuated the apparent cardiogenic oscillations and reduced the standard deviation of the measured PEEP_i by 57%. Investigation of the interactions between patients and a pressure support ventilator using the computer model confirmed our present understanding of patient-ventilator asynchrony and indicated that patient and ventilator form a highly nonlinear dynamic system, so that the optimal ventilator settings most likely vary between

patients and with time. In the second part of this thesis, I investigated the importance of inaccuracies in conventional Finite Elements for thoracic Electrical Impedance Tomography (EIT) imaging. Augmenting the number of first-order Finite Elements did not efficiently reduce these inaccuracies. A computer simulation suggested that the accuracy of the forward solution needs to be improved by at least 30 dB before useful static EIT images can be obtained and showed that neighbouring currents outperform other single-source current patterns. The potential usefulness of a central reference electrode was demonstrated. Finally, I derived higher-order isoparametric Finite Elements with space-variant conductivity for EIT. In a preliminary study, a simple implementation of these Finite Elements improved the accuracy of the EIT forward solution by up to 15 dB.

ABREGE

La forte incidence des maladies pulmonaires entre les patients de soins intensif nécessite des nouvelles techniques pour le monitoring pulmonaire et l'imagerie thoracique. Pour étudier les techniques du monitoring pulmonaire utilisant les signaux de pression et de débit, j'ai développé un modèle informatisé d'un sujet respirant spontanément ou en ventilation assistée. Ce modèle a été utilisé pour étudier quantitativement les techniques de mesure de la dynamique pression positive intrinsèque de fin d'expiration (intrinsic positive end-expiratory pressure, PEEP_i) et le travail inspiratoire. Les résultats démontrent qu'une correction est nécessaire aussi bien pour l'activité des muscles expiratoires que pour les oscillations cardiogéniques sur la pression œsophageale si la PEEP_i dynamique et le travail inspiratoire doivent être mesurés avec précision en temps réel. Il résulte aussi que l'écart entre la PEEP_i statique et dynamique est lié à l'hétérogénéité de la limitation du débit expiratoire. Afin de réduire les oscillations cardiogéniques sur la pression œsophageale, un filtre adaptable a été développé et validé en simulation. Sur quatre patients en soins intensifs, ce filtre a considérablement atténué les oscillations cardiogéniques et réduit de 57% l'écart type de la PEEP_i mesurée. La recherche des interactions entre patient et ventilateur en support de pression utilisant le modèle informatisé confirme notre compréhension de l'asynchronie entre patient et ventilateur et indique que l'ensemble patient-ventilateur forme un système

sévèrement non-linéaire. Par conséquent, la mise au point du ventilateur varie probablement entre les sujets et avec le temps. Dans la deuxième partie de cette thèse, j'ai recherché l'importance de l'inexactitude des éléments finis conventionnels pour l'imagerie thoracique utilisant la tomographie d'impédance électrique (TIE). Une augmentation du nombre d'éléments finis n'a pas réduit suffisamment ces imprécisions. Une simulation a suggéré que la précision des éléments finis doit être améliorée d'au moins 30 dB avant que des images valables de TIE puissent être obtenues et a montré que l'injection du courant par électrodes adjacentes est meilleure que les autres méthodes d'injection utilisant une seule source de courant. Le potentiel d'une électrode de référence centrale a été démontré. Puis, j'ai dérivé des éléments finis isoparamétriques d'ordre élevé avec une conductivité variant dans l'espace pour la TIE. Dans une étude préliminaire, une implémentation simple de ces éléments finis a amélioré la précision par environ 15 dB.

ACKNOWLEDGMENTS

The role that Dr. Jason H.T. Bates has played in my life over the past years is probably best summarized by the German term *Doktorvater* - the doctoral father. I would like to thank Jason very much not only for supervision of the work described in this thesis, but also for the motivation, encouragement and guidance he provided.

My deep thanks to my friends Geoff Maksym, Gail Dechman, William Thorpe, Carlo Volta and Rute Gomez, to Andy Adler, Eve Bija, Norihiro Shinozuka, Tadashi Nemoto and Mohsen Ahmadi, and to all other people who around the Meakins-Christie Labs who helped and encouraged me and made life in and outside the lab enjoyable. Thanks to the staff off the Meakins-Christie labs who keep us all going, especially Serge Filiatrault and Whitney de Vries. I would also like to thank Drs. Stewart B. Gottfried and Peter Goldberg for fruitful collaborations and discussions.

Needless to say, I am always thankful to my parents and my sister for supporting and encouraging me in many late-night long distance calls, and for making all of this possible.

Dear Gail, I want to thank you for your love and support over most of the time I spent working towards completion of this thesis. I'm sorry it didn't work out in the end.

This work was supported by the Montreal Chest Institute Research Fund, the J.T. Costello Memorial Fund, the Canadian Respiratory Health Network of Centres of

Excellence (Inspiraplex), and by a McGill Major Fellowship in the academic year 1993/94.

TABLE OF CONTENTS

| | |
|--|----------|
| Abstract | i |
| Abrégé..... | iii |
| Acknowledgments..... | v |
| Table of Contents | vii |
| List of Figures | xiii |
| List of Tables | xvii |
| List of Symbols | xviii |
| Preface..... | xxv |
| | |
| 1. INTRODUCTION | 1 |
| | |
| 2. LITERATURE REVIEW | 3 |
| 2.1 The respiratory system | 3 |
| 2.1.1 Basic respiratory physiology | 3 |
| Overview | 3 |
| Mechanical properties..... | 5 |

| | |
|--|----|
| The respiratory pump..... | 6 |
| Control of breathing..... | 6 |
| 2.1.2 Relevant pulmonary pathophysiology | 7 |
| Chronic Obstructive Pulmonary Disease (COPD) | 7 |
| Acute respiratory failure | 7 |
| 2.1.3 Expiratory flow limitation | 8 |
| 2.1.4 Dynamic hyperinflation, intrinsic PEEP and work of breathing | 10 |
| 2.2 Measurements of pulmonary function | 11 |
| 2.2.1 Basic diagnostic techniques | 11 |
| Physical examination..... | 11 |
| Blood gases..... | 11 |
| Lung function tests | 12 |
| 2.2.2 Esophageal pressure measurement | 12 |
| 2.2.3 Measurement of PEEPi and Winsp..... | 13 |
| Static PEEPi..... | 13 |
| Dynamic PEEPi | 13 |
| Inspiratory work of breathing | 15 |
| 2.2.4 Thoracic radiography | 16 |
| 2.3 Assisted positive pressure ventilation..... | 17 |
| 2.3.1 Positive pressure ventilation | 17 |
| 2.3.2 Modes of assisted mechanical ventilation | 17 |
| Continuous positive airway pressure (CPAP) | 17 |
| Synchronized intermittent mechanical ventilation (SIMV)..... | 17 |
| Assist-control ventilation (ACV)..... | 17 |
| Pressure support ventilation (PSV)..... | 18 |
| Proportional assist ventilation (PAV)..... | 18 |
| 2.3.3 Positive end-expiratory pressure (PEEP)..... | 18 |
| 2.3.4 Trigger mechanisms..... | 18 |

| | |
|--|-----------|
| Pressure trigger | 18 |
| Flow trigger | 19 |
| 2.3.5 Weaning | 19 |
| 2.4 Electrical Impedance Tomography | 20 |
| 2.4.1 Imaging electrical tissue properties of the thorax | 20 |
| 2.4.2 The EIT system | 21 |
| Overview | 21 |
| Current injection | 22 |
| Voltage measurement | 24 |
| Static and dynamic imaging | 25 |
| Multifrequency and complex-valued imaging | 26 |
| Three-dimensional EIT | 27 |
| 2.4.3 Image reconstruction | 27 |
| Forward and inverse problem | 27 |
| Weighted backprojection along equipotential lines | 28 |
| Image reconstruction using Newtonian optimization techniques | 30 |
| Other image reconstruction techniques | 37 |
| 2.4.4 Pulmonary applications of EIT | 37 |
| Monitoring lung inflation | 37 |
| Pneumothorax and pleural effusion | 38 |
| Detection of increased lung water | 38 |
| Other pulmonary applications | 39 |
| 2.4.5 Non-pulmonary applications of EIT | 39 |
| 3. PULMONARY MONITORING | 41 |
| 3.1 A computer model of the spontaneously breathing patient | 42 |
| 3.1.1 Motivation | 42 |
| 3.1.2 Implementation | 42 |

| | |
|--|-----------|
| Overview | 42 |
| Lung and chest wall | 43 |
| Airways..... | 46 |
| Patient effort | 48 |
| Cardiogenic oscillations | 51 |
| Endotracheal tube | 52 |
| Determination of flow | 52 |
| 3.1.3 Performance | 54 |
| Sample traces | 54 |
| Pulmonary function measurements | 58 |
| 3.1.4 Discussion..... | 59 |
| 3.2 Quantitative assessment of measurement techniques for intrinsic PEEP | |
| and work of breathing | 61 |
| 3.2.1 Motivation..... | 61 |
| 3.2.2 Methods | 62 |
| Protocol..... | 62 |
| Data analysis..... | 62 |
| 3.2.3 Results..... | 63 |
| 3.2.4 Discussion..... | 69 |
| 3.3 An adaptive filter to reduce the cardiogenic oscillations in esophageal pressure..... | 73 |
| 3.3.1 Motivation..... | 73 |
| 3.3.2 Methods | 73 |
| The adaptive filter..... | 73 |
| Computer simulations..... | 78 |
| Patient data | 79 |
| 3.3.3 Results..... | 80 |
| Simulated data | 80 |
| Patient data | 80 |

| | |
|---|------------|
| 3.3.4 Discussion..... | 86 |
| 3.4 Assessment of patient-ventilator asynchrony during pressure support ventilation..... | 88 |
| 3.4.1 Motivation..... | 88 |
| 3.4.2 Methods | 88 |
| 3.4.3 Results..... | 90 |
| 3.4.4 Discussion..... | 97 |
| | |
| 4. THORACIC IMAGING USING ELECTRICAL IMPEDANCE TOMOGRAPHY | 101 |
| 4.1 A critical analysis of the Finite Element method for static EIT..... | 102 |
| 4.1.1 Motivation..... | 102 |
| 4.1.2 Methods | 102 |
| Analytical solution..... | 102 |
| FEM phantoms | 105 |
| Quantification of the FEM inaccuracies | 106 |
| Protocols | 108 |
| 4.1.3 Results..... | 108 |
| 4.1.4 Discussion..... | 111 |
| 4.2 Effects of current patterns and central electrodes on static EIT images of the thorax | 115 |
| 4.2.1 Motivation..... | 115 |
| 4.2.2 Methods | 116 |
| Phantoms and simulation..... | 116 |
| Image reconstruction | 117 |
| Convergence criterion..... | 118 |
| Reconstruction error | 119 |
| Protocols | 120 |
| 4.2.3 Results..... | 122 |
| 4.2.4 Discussion..... | 129 |

| | |
|--|------------|
| 4.3 Higher-order Finite Elements for the forward solution in static EIT | 135 |
| 4.3.1 Motivation..... | 135 |
| 4.3.2 Methods | 136 |
| Two-dimensional isoparametric Finite Elements with variable conductivity | 136 |
| Curvilinear one-dimensional Finite Elements for the boundary condition | 139 |
| Protocol..... | 140 |
| 4.3.3 Results..... | 140 |
| 4.3.4 Discussion..... | 143 |
| | |
| 5 CONCLUSION | 147 |
| 5.1 Summary and conclusions | 147 |
| 5.2 Original contributions | 151 |
| 5.3 Suggestions for future work..... | 155 |
| 5.3.1 Pulmonary monitoring..... | 155 |
| 5.3.2 Thoracic imaging using EIT | 156 |
| Bibliography | 157 |
| Appendix: Implementation of the model described in section 3.1 | 175 |

LIST OF FIGURES

- Fig. 2.1: Iso-volume pressure-flow curves and maximum expiratory flow-volume curve describing expiratory flow limitation.
- Fig. 2.2: Measurement of static intrinsic positive end-expiratory pressure.
- Fig. 2.3: Measurement of dynamic intrinsic positive end-expiratory pressure.
- Fig. 2.4: Measurement of the patient's inspiratory work of breathing.
- Fig. 2.5: Overview of an Electrical Impedance Tomography system.
- Fig. 2.6: Arrangement of induction coils for induced current Electrical Impedance Tomography.
- Fig. 2.7: Weighted backprojection along equipotential lines.
- Fig. 2.8: Illustration of the Compensation theorem.
- Fig. 3.1: Schematic representation of the computer model used to simulate patients breathing spontaneously or with the support of an assisting ventilator.
- Fig. 3.2: Iso-volume pressure-flow relationships of the airway compartment of the model during expiration.

- Fig. 3.3: Simulated flow-volume loop with all model parameters adjusted to their population means.
- Fig. 3.4: Time course of the neural output with all model parameters adjusted to their population means.
- Fig. 3.5: Modeled volume dependence of the pressure generated by the respiratory muscles.
- Fig. 3.6: Feedback of the airway opening pressure for different modes of breathing.
- Fig. 3.7: Sample traces of the simulated pressure and flow waveforms for spontaneous breathing and Constant Positive Airway Pressure ventilation.
- Fig. 3.8: Sample traces of the simulated pressure and flow waveforms for Assist-Control ventilation and Pressure Support ventilation.
- Fig. 3.9: Relationship of the measured and the true dynamic positive end-expiratory pressure.
- Fig. 3.10: Relationship of the measured and the true inspiratory work of breathing.
- Fig. 3.11: Measurement errors in dynamic positive end-expiratory pressure and inspiratory work of breathing as functions of the peak expiratory muscle pressure.
- Fig. 3.12: Comparison of static and dynamic positive end-expiratory pressure.
- Fig. 3.13: Structure of the adaptive filter to reduce cardiogenic oscillations on esophageal pressure traces.
- Fig. 3.14: Sample traces of simulated pleural pressure and esophageal pressure, and the output of the adaptive filter.
- Fig. 3.15: Sample traces of the unfiltered and adaptively filtered esophageal pressure signals in four ICU patients.

- Fig. 3.16: Fourier transforms of the unfiltered and adaptively filtered esophageal pressure signals in four ICU patients.
- Fig. 3.17: Asynchrony between patient and ventilator for the simulated average COPD patient.
- Fig. 3.18: Sample traces of pressure and flow for the simulated average COPD patient.
- Fig. 3.19: Asynchrony between patient and ventilator for the simulated COPD patient with very severe expiratory flow limitation.
- Fig. 3.20: Sample traces of pressure and flow for the simulated COPD patient with very severe expiratory flow limitation at a pressure support level of 20 cmH₂O and a PEEP of 0.
- Fig. 3.21: Sample traces of pressure and flow for the simulated COPD patient with very severe expiratory flow limitation at a pressure support level of 20 cmH₂O and a PEEP of 5 cmH₂O.
- Fig. 4.1: Illustration of the circular geometry for which an analytical solution was computed.
- Fig. 4.2: Five first-order Finite Element meshes compared to the analytical solution.
- Fig. 4.3: Inaccuracies of the five Finite Element Meshes as a function of the number of nodes.
- Fig. 4.4: Computational phantoms mimicking a small centered object and a cross section of the human thorax.
- Fig. 4.5: Illustration of electrode configurations using a Central Reference Electrode or 32 boundary electrodes.
- Fig. 4.6: Samples of reconstructed images and illustration of the reconstruction error.
- Fig. 4.7: Performance of the convergence estimator.

- Fig. 4.8: Effects of the separation between the current source and sink on the convergence rate and the reconstruction error at four noise levels.
- Fig. 4.9: Effects of the central reference electrode on the convergence rate and the reconstruction error as functions of the noise levels.
- Fig. 4.10: Illustration of second-order square and isoparametric Finite Elements
- Fig. 4.11: Four isoparametric Finite Element meshes compared to the analytical solution.
- Fig. 4.12: Inaccuracies of standard and isoparametric Finite Element meshes
- Fig. 4.13: Approximation functions for a one-dimensional second-order Finite Element

LIST OF TABLES

- Table 2.1: Electrical resistivities of biological tissues in the thorax in the range from 20 to 100 kHz.
- Table 3.1: Means and standard deviations of the parameter values used to simulate a population of 100 COPD patients.
- Table 3.2: Pulmonary function data for the population of 100 simulated COPD patients.
- Table 3.3: Heart rates and respiratory rates of eight patients simulated to test the adaptive filter.
- Table 3.4: Characteristics of four intensive care patients studied using the adaptive filter.
- Table 3.5: Comparison of the mean and standard deviation of intrinsic PEEP measured with and without the adaptive filter.
- Table 4.1: Characteristics of the five Finite Element meshes compared to the analytical solution.
- Table 4.2: Inaccuracies of the five Finite Element meshes for different centered targets.
- Table 4.3: Characteristics of the four isoparametric Finite Element meshes compared to the analytical solution.

LIST OF SYMBOLS

| | | |
|-------------------|---|-------|
| PEEPi | Intrinsic positive end-expiratory pressure | i/1 |
| EIT | Electrical impedance tomography | ii/20 |
| ICU | Intensive care unit | 1 |
| COPD | Chronic obstructive pulmonary disease | 1 |
| W_{insp} | Inspiratory work of breathing of the patient..... | 1 |
| P_{O_2} | Partial pressure of oxygen | 5 |
| FRC | Functional residual capacity | 5 |
| V_t | Tidal volume..... | 5 |
| IC | Inspiratory capacity | 5 |
| TLC | Total lung capacity | 5 |
| ER | Expiratory reserve | 5 |
| RV | Residual volume | 6 |
| VC | Vital capacity..... | 6 |
| FEV_1 | Volume expired over the first second of a forced expiration | 7 |
| FVC | Forced vital capacity | 7 |
| ARF | Acute respiratory failure..... | 7 |
| IVPF | Iso-volume pressure-flow curve | 8 |
| MEFV | Maximum expiratory flow-volume curve | 9 |

| | | |
|--------------------|---|-------|
| P_{CO_2} | Partial pressure of carbon dioxide | 11 |
| RR | Respiratory rate | 12 |
| \dot{V}_e | Minute ventilation | 12 |
| P_{es} | Esophageal pressure | 12 |
| P_{pl} | Pleural pressure | 12 |
| $PEEP_{i,dyn}$ | Dynamic PEEP _i | 12 |
| $PEEP_{i,stat}$ | Static PEEP _i | 13 |
| $P_{es,0}$ | End-expiratory relaxation value of P_{es} | 13 |
| $W_{insp,lung}$ | Fraction of W_{insp} required to inflate the lungs | 15 |
| CPAP | Continuous positive airway pressure | 17 |
| SIMV | Synchronized intermittent mechanical ventilation | 17 |
| ACV | Assist control ventilation | 17 |
| PSV | Pressure support ventilation | 18 |
| PAV | Proportional assist ventilation | 18 |
| PEEP | Applied positive end-expiratory pressure | 18 |
| P_{aw} | Airway opening pressure | 19 |
| N_e | Number of electrodes of an EIT system | 22 |
| j | Current density | 27 |
| E | Electric field | 27 |
| ϕ | Scalar electric potential | 27 |
| γ, γ^* | Admittivity distribution, true admittivity distribution in Ω | 27/28 |
| Ω | Space of interest of the EIT problem | 27 |
| S | Surface of Ω | 27 |
| j_s | Current density normal to S | 27 |
| n_s | Normal vector of S | 27 |
| v_b | Measured boundary voltages | 28 |
| x_m | Locations of the voltage measurement sites | 28 |
| N_p | Number of projections | 28 |

| | | |
|---------------------------|--|-------|
| \mathbf{v}_m | Vector of all measured voltages in one data set. | 28 |
| ρ, ρ_0 | Resistivity distribution, initial resistivity distribution..... | 28/29 |
| σ | Conductivity distribution..... | 28 |
| $\hat{\mathbf{v}}$ | Estimate of \mathbf{v}_m obtained from the forward solution..... | 29 |
| \mathbf{W}_B | Weight matrix of the Weighted Backprojection technique | 29 |
| x_p | Locations of an image pixel | 29 |
| x_j | Locations of the current injection sites..... | 29 |
| FE | Finite Element | 30 |
| α_i | FE approximation functions | 30 |
| Θ | Energy-related functional of the Helmholtz equation | 30 |
| ϕ_n, i_n | Vectors of node values for potential and current, respectively | 31 |
| \mathbf{S} | System matrix of the connected FEM | 31 |
| N_n | Number of nodes in the connected FEM..... | 31 |
| \mathbf{S}_{el} | System matrix for a single FE | 31 |
| σ_{el} | Element conductivity..... | 31 |
| $\tilde{\mathbf{S}}_{el}$ | Preliminary, conductivity independent \mathbf{S}_{el} matrix..... | 31 |
| FEM | Finite Element Mesh | 31 |
| \mathbf{S}_{dis} | System matrix of the disconnected FEM | 31 |
| \mathbf{C} | Connectivity matrix of the FEM | 31 |
| λ | Iteration step with factor..... | 31 |
| \mathbf{X}_v | Boundary voltage extraction matrix | 32 |
| N_b | Number of boundary voltages per projection..... | 32 |
| σ^* | Desired conductivity distribution (“true” image)..... | 32 |
| Φ | Objective function of the nonlinear EIT inverse problem..... | 32 |
| N_v | Number of voltage data points in one data set | 32 |
| \mathbf{W} | Weight matrix..... | 32 |
| \mathbf{I} | Identity matrix | 32 |
| SDM | Steepest descent method..... | 32 |

| | | |
|---|--|-------|
| Φ', Φ'' | First and second derivative of Φ with respect to σ | 32/33 |
| $\Delta\sigma_i$ | Conductivity update at iteration I..... | 33 |
| N_σ | Number of conductivity parameters in an EIT image | 33 |
| GNM | Gauss-Newton method | 33 |
| LMM | Levenberg-Marquardt method..... | 33 |
| H | Hessian matrix of the EIT inverse problem..... | 33 |
| μ | Parameter of the Levenberg-Marquardt method | 33 |
| J | Jacobian matrix of the EIT inverse problem | 34 |
| Φ_{reg} | Regularized objective function of the EIT inverse problem | 36 |
| P | Penalty function..... | 36 |
| η | Weight of the penalty function..... | 36 |
| $\bar{\sigma}$ | Mean conductivity of the EIT image..... | 36 |
| ETT | Endotracheal tube | 42 |
| \dot{V} | Air flow | 42 |
| V | Total lung volume | 42 |
| P_{musc} | Pressure generated by the respiratory musculature | 42 |
| SD | Standard deviation | 43 |
| V-P | Volume-pressure [relationship/curve]..... | 43 |
| A_L, B_L, K_L | Parameters of the static V-P curve of the lung..... | 43 |
| $P_{\text{el,L}}$ | Elastic recoil pressure of the lung | 43 |
| $A_{\text{cw}}, B_{\text{cw}}, K_{\text{cw}}$ | Parameters of the static V-P curve of the chest wall | 43 |
| $P_{\text{el,cw}}$ | Elastic recoil pressure of the chest wall | 43 |
| $R_{2,L}, \tau_{2,L}$ | Viscoelastic parameters of the lung..... | 46 |
| $R_{2,CW}, \tau_{2,CW}$ | Viscoelastic parameters of the chest wall..... | 46 |
| ΔP_{aw} | Pressure drop across the airways..... | 46 |
| $K_{\text{aw},1}, K_{\text{aw},2}$ | Rohrer's coefficients for nonlinear airway resistance | 46 |
| α, β, χ | Parameters of the expiratory flow limitation model | 46 |
| P_{neur} | Neural output (in units of pressure)..... | 48 |

| | | |
|---------------------------|---|----|
| T_i/T_{tot} | Respiratory duty cycle..... | 48 |
| P_{exp} | Expiratory peak value of P_{neur} | 49 |
| P_{CGO} | Cardiogenic oscillation pressure waveform | 51 |
| C_{CP} | Cardio-pulmonary coupling factor | 51 |
| C_{CE} | Cardio-esophageal coupling factor..... | 51 |
| P_{ETT} | Pressure drop across the endotracheal tube | 52 |
| κ, ν | Parameters of the endotracheal tub model | 52 |
| d | Nominal diameter of the endotracheal tube..... | 52 |
| $P_{es,baseline}$ | End-expiratory baseline value of esophageal pressure..... | 63 |
| $PEEP_{i,meas}$ | Measured dynamic intrinsic PEEP | 63 |
| W_{meas} | Measured inspiratory work of breathing of the patient | 63 |
| P_{resp} | Respiratory component of esophageal pressure | 73 |
| C_p | Series of impulses generated by the cardiac pacemaker in the SA node.... | 73 |
| $h_1(\tau), h_2(\tau)$ | Impulse response functions | 73 |
| HR | Heart rate | 73 |
| EKG | Electrocardiogram | 74 |
| \bar{x}_k | Mean value of x up to sample k , estimated recursively with exponentially weighted finite memory..... | 75 |
| ζ | Forgetting factor of the recursive estimator with exponentially weighted finite memory | 75 |
| \hat{P}_{CGO} | Estimate of P_{CGO} calculated by the adaptive filter | 75 |
| \hat{C}_p | Estimate of C_p calculated by the adaptive filter | 75 |
| $P_{es,HP}$ | High-pass filtered P_{es} signal | 75 |
| $h_3(\tau)$ | Impulse response function..... | 76 |
| \hat{P}_{resp} | Estimate of P_{resp} calculated by the adaptive filter..... | 76 |
| Δ | Helper function for the determination of the forgetting factor of the adaptive filter..... | 77 |
| ξ, κ_1, κ_2 | Forgetting factor and parameters for the calculation of Δ | 77 |

| | | |
|-------------------------|--|-----|
| k_1, k_2 | Constant parameters of the volume dependence of P_{CGO} | 78 |
| \bar{P}_{CGO} | Preliminary, volume independent cardiogenic oscillation pressure | 78 |
| VAF | Variance accounted for | 78 |
| FT | Fourier transform..... | 79 |
| PVA | Patient-ventilator asynchrony | 88 |
| RR_{spont} | Spontaneous respiratory rate of the patient | 88 |
| RR_{vent} | Respiratory rate of the ventilated patient..... | 88 |
| PS | Pressure Support level | 89 |
| Δt_{trig} | Trigger delay | 89 |
| P_{stress} | Maximal pressure across the parenchyma | 89 |
| φ_b | Electrical potential on the boundary of Ω | 102 |
| r_0 | Diameter of the circular analytical phantom | 102 |
| σ_{bg} | Background conductivity | 102 |
| r_{obj}, σ_{obj} | Radius and conductivity of the centered object, respectively | 102 |
| C_n, S_n | Fourier coefficients..... | 103 |
| R | Relative radius of the centered object (r_{obj}/r_0) | 103 |
| D | Electrode size parameter..... | 103 |
| Θ_b | Functional for the boundary condition in the Helmholtz equation | 103 |
| φ_b | Electrical potential at the boundary nodes..... | 105 |
| j_b | Boundary node values of j_s | 105 |
| T_b | System matrix for the one-dimensional FEs for the boundary condition..... | 105 |
| U | Matrix relating injection currents to injection current densities..... | 105 |
| C_b | Mapping of the one-dimensional boundary FEs onto the FEM | 105 |
| Δv_{rms} | Root-mean-squared difference between φ_n and φ_e at the boundary | 106 |
| SNR | Signal-to-noise ratio | 106 |
| CRE | Central reference electrode..... | 115 |
| Φ_0, Φ_1 | Objective function of the GNM at $\lambda = 0$ and at $\lambda = 1$ respectively | 117 |
| Φ'_0 | First derivative of Φ_0 with respect to λ | 117 |

| | | |
|--|--|-----|
| $\overline{\Delta\sigma_i^2}$ | Relative mean squared change in the image at iteration i | 118 |
| \mathbf{W}_A | Diagonal weight matrix containing the relative areas of each FE..... | 118 |
| $\Delta\Phi_i$ | Relative change of the objective function at iteration i..... | 119 |
| Ψ | Convergence estimator function..... | 119 |
| ϑ | Forgetting factor for the convergence estimator function | 119 |
| ψ_g | Threshold for detection of convergence to the global minimum | 119 |
| ψ_l | Threshold for detection of convergence to a local minimum..... | 119 |
| ε | Normalized root-means-squared image error | 119 |
| $\varepsilon_{\min}, \varepsilon_{\text{final}}$ | Minimal value of ε , value of ε after the maximal number of iterations ... | 120 |
| N_{conv} | Number of cases that converged to the global minimum..... | 120 |
| N_{local} | Number of cases that converged to a local minimum | 120 |
| $\varepsilon_{\text{conv}}$ | Value of ε when convergence was detected | 120 |

PREFACE

The motivation of the research described in this thesis is the continued need for improved methods and techniques to assess the status of the diseased respiratory system.

Chapter one of this thesis provides a brief introduction to the clinical context of this work and states the goals of my research. In the literature review in chapter two, the relevant aspects of respiratory physiology, pulmonary pathophysiology and ventilatory support are reviewed, and the literature pertinent to monitoring dynamic hyperinflation and to thoracic imaging using Electrical Impedance Tomography is discussed in detail.

In the research that I have conducted over the past three years, two methodically distinct approaches were used. Chapter three describes advances in the field of pulmonary monitoring, i.e., the analysis of pressure and flow data. Specifically, I developed a computer model of the spontaneously breathing or assist-ventilated patient that is described in detail in section 3.1. In section 3.2, this model is used to test the sensitivity of measurement techniques for intrinsic positive end-expiratory pressure ($PEEP_i$) and inspiratory work of breathing to expiratory muscle activity and cardiogenic oscillations, and to investigate the physiologic cause for discrepancies between static and dynamic measurements of $PEEP_i$. In section 3.3, an adaptive filter is developed to suppress the measurement problems caused by cardiogenic oscillations that were identified in section 3.2. This filter was tested both on simulated data and on *in vivo* patient data. Finally, the

computer model was used to investigate mechanisms that compromise the synchrony between the patient and an assisting ventilator in section 3.4. Much of the research described in chapter 3 of this thesis was conducted in collaboration with Dr. Stewart B. Gottfried, who contributed his clinical expertise and exhaustive knowledge of the clinical literature. Dr. Robert E. Kearney contributed his experience in the field of time-domain identification techniques to the adaptive filter described in section 3.3. The patient data used to test this filter were provided by Drs. Stewart. B. Gottfried and Peter Goldberg.

Chapter four of this thesis is concerned with the reconstruction of static Electrical Impedance Tomography (EIT) images. EIT is a novel medical imaging technique that could potentially provide a direct measure of dynamic hyperinflation in patients suffering from severe airway obstruction, or of increased lung water due to congestion of the pulmonary vasculature. Section 4.1 presents a critical analysis of the first-order Finite Elements that are commonly used for EIT image reconstruction. In section 4.2, the effects of the current pattern on the image quality and the utility of a central reference electrode in the esophagus are investigated in a computer simulation. The results are discussed in the context of the results of section 4.1. Finally, section 4.3 presents a modification of the initial algorithm using a novel type of Finite Elements that are expected to overcome some of the limitations of first-order Finite Elements.

The work described in chapters three and four represents original contributions to knowledge in the fields of pulmonary monitoring and thoracic imaging. Each section of these chapters is structured into sub-sections describing the motivation for the study, the methods employed, the resulting data, and a discussion of these results in their individual scientific context. Chapter five concludes the thesis and provides a list of the original contributions that I have made.

The publications listed below have resulted from the work described in this thesis.

Refereed journal papers:

- A-1. **Schuessler, T.F.**, S.B. Gottfried and J.H.T. Bates: "A model of the spontaneously breathing patient: Applications to intrinsic PEEP and work of breathing", *J. Appl. Physiol.*, in press.
- A-2. **Schuessler, T.F.**, and J.H.T. Bates: "Current patterns and electrode types for single source Electrical Impedance Tomography of the thorax", *Annals of Biomedical Eng.*, submitted August 1996.
- A-3. **Schuessler, T.F.**, S.B. Gottfried, P. Goldberg, R.E. Kearney, and J.H.T. Bates: "An adaptive filter to reduce cardiogenic oscillations on esophageal pressure signals", submitted January 1997.

Conference papers:

- B-1. **Schuessler, T.F.**, C.A. Volta, P. Goldberg, S.B. Gottfried, R.E. Kearney and J.H.T. Bates: "An adaptive filter for the reduction of cardiogenic oscillations on esophageal pressure signals", *Proc. 17th Int. Ann. Conf. IEEE EMBS*, paper no. 792, Montréal 1995.
- B-2. **Schuessler, T.F.** and J.H.T. Bates: "Utility of an esophageal reference electrode for thoracic electrical impedance tomography", *Proc. 17th Int. Ann. Conf. IEEE EMBS*, paper no. 793, Montréal 1995.
- B-3. **Schuessler, T.F.** and J.H.T. Bates: "A convergence estimator for the iterative reconstruction of electrical impedance tomography images", *18th Int. Ann. Conf. IEEE EMBS*, Amsterdam 1996, paper no. 381.

Abstracts:

- C-1. **Schuessler, T.F.** and J.H.T. Bates: "Effects of expiratory effort and cardiogenic oscillations on the measurement of work of breathing", *Am. J. Resp. Crit. Care Med.*, **151(4)**: A332, Seattle, 1995.

- C-2. **Schuessler, T.F.** and J.H.T. Bates: "True and measured intrinsic PEEP in the presence of expiratory effort", *Am. J. Resp. Crit. Care Med.*, **151(4)**: A332, Seattle, 1995.
- C-3. **Schuessler, T.F.**, C.A. Volta, P. Goldberg, R.E. Kearney and J.H.T. Bates: "Suppression of cardiogenic oscillations on esophageal pressure: Effect on the measurement of intrinsic PEEP", *Conf. Royal Col. of Physicians & Surgeons of Canada*, Montréal 1995.
- C-4. **Schuessler, T.F.** and J.H.T. Bates: "Model-based analysis of patient-ventilator desynchronization during pressure support ventilation", *Am. J. Resp. Crit. Care Med.*, **153(4)**: A372, New Orleans 1996.

1.

INTRODUCTION

Approximately 85% of the patients admitted to the intensive care unit (ICU) of the Royal Victoria Hospital in Montreal are treated for pulmonary disease during their ICU stay. Some of these patients remain mechanically ventilated over very long periods of time, so that 10% of the ventilated patients account for as much as 90% of the ventilator days. Severe chronic airway obstruction, usually as a consequence of chronic obstructive pulmonary disease (COPD), is the most common cause for this long-term ventilator dependence, and is one of the dominant causes for long term hospitalization. Understanding and accurately monitoring the mechanical status of the respiratory system of these patients is thus an important task in modern medicine.

Severe airway obstruction commonly leads to dynamic hyperinflation, which has profound physiologic consequences that eventually lead to acute respiratory failure and long term ventilator dependence. The precise physiologic mechanisms that are involved in this process are reviewed in more detail in section 2.1. Dynamic hyperinflation can be assessed either directly via thoracic imaging, or more indirectly by computing the associated intrinsic positive end-expiratory pressure ($PEEP_i$) and inspiratory work of breathing (W_{insp}) from pressure and flow data. The goal of the research described in this thesis was to investigate and improve methods for assessing dynamic hyperinflation and its consequences. Specifically, this included the quantitative assessment of measurement

techniques for $PEEP_i$ and W_{insp} , the development of a data processing technique that overcomes some of the problems associated with these techniques, and the investigation of patient-ventilator asynchronies that are caused by dynamic hyperinflation. The investigation of factors that limit the reconstruction of static Electrical Impedance Tomography (EIT) images and the development of reconstruction techniques that may overcome some of these restrictions were also part of this goal. In the long-term, I envisage EIT as a technique for direct and non-invasive monitoring and visualization of dynamic hyperinflation and its changes over time, e.g., following a change in the ventilator settings or as a consequence of a medical intervention.

2.

LITERATURE REVIEW

2.1 The respiratory system

2.1.1 *Basic respiratory physiology*

Overview

The respiratory system consists of the upper airways, the lung and the chest wall. Its prime duty is the exchange of oxygen and carbon dioxide between the atmosphere and the blood. This function is absolutely essential for life; malfunction at the very least limits exercise capacity, and may in extreme cases even be fatal.

Air enters the respiratory system through the upper airways, namely the nose, the mouth and the larynx. The larynx assures that larger solid particles such as food do not accidentally enter the lung by rapidly closing the glottis and opening the esophagus. The upper airways humidify and warm the air to body temperature and provide a basic immunodefense mechanism.

After passing the glottis, the air is conducted through the airway tree towards the lung periphery. The human airways bifurcate on average 23 times from the trachea to the terminal bronchioles, forming a right lung with three and a left lung with two distinct lobes. In the upper 16 generations of airways, bulk flow is the dominant mechanism of

gas transport. These airways are not lined with alveoli and are thus called conducting airways. The four most distal generations of airways contain numerous alveoli and are referred to as the respiratory zone or alveolar duct region. At this level, diffusion is the dominant gas transport mechanism. The intermediate three generations form a gradual transition zone from the conducting airways to the alveolar duct region. The airway walls contain smooth muscle that presumably contributes to the adaptation of the respiratory system to varying environmental conditions. Constriction of the smooth muscle narrows the airways and increases their resistance to flow. The airway smooth muscle is controlled by the autonomic nervous system and endocrine factors, and airway smooth muscle hyperresponsiveness is thought to play an important role in Asthma.

Gas exchange between the air and the blood occurs solely by a passive diffusion process, and a large surface area is required at the blood-gas barrier in order to exchange sufficient quantities of gas. The lung provides such a large area within a relatively small volume by aggregating the area of about 300 million gas exchange chambers (alveoli) with an average diameter of 0.3 mm. This produces a total surface area of approximately 85 square meters (145). The stability of this configuration is assured by the release of surfactant in the smaller alveoli that lowers the local coefficient of surface tension. Without the surfactant, small alveoli would have a higher internal pressure than bigger ones because the pressure within a sphere due to the surface tension is inversely proportional to its radius. Therefore, the alveoli would coalesce into a few big air spaces having a similar total volume, but a much smaller surface area.

The alveolar walls are lined with a close network of pulmonary capillaries. While venous blood is conducted through these capillaries, oxygen diffuses from the alveoli into the blood and carbon dioxide (CO₂) diffuses in the opposite direction. In the blood, only a small fraction of the oxygen is transported in a dissolved state in the plasma, while the majority is bound by hemoglobin in the red blood cells. This mechanism allows the blood to transport more than an order of magnitude more oxygen per unit volume than would be

possible by solution only. CO_2 is much more soluble in the plasma than oxygen and can be transported in sufficient quantities in a dissolved state and as bicarbonate ions.

The partial pressure of oxygen (Po_2) in the venous blood that reaches the alveolar blood-gas interface is substantially lower than that in the lumen of the alveolus. In resting normals, diffusion of oxygen into the blood is so rapid that the Po_2 levels of blood and alveolar air are equilibrated in a fraction of the time the blood takes to pass through the pulmonary capillaries. However, during exercise or in disease, the transfer time of the blood may become smaller than the diffusion time, and oxygenation may be incomplete. If some alveolar regions are not ventilated at all or in the presence of an extreme diffusion impairment, some venous blood may be able to reach the left ventricle completely without being oxygenated. This condition is called a *true shunt*.

Mechanical properties

From an engineering point of view, the airway tree and alveoli can be viewed as a fluid mechanical system that can be characterized by pressure-flow relationships. Despite the enormous complexity of the system, the lungs are often regarded as a single resistive pipe with an elastic or viscoelastic balloon at its end. More complex models have been postulated and discussed in the literature, but only very simple models have found their way to a wider application so far.

The elastic forces of the parenchymal tissue are always inbound, i.e., they oppose expansion of the lung. In contrast, the elastic forces of the chest wall point outwards over a wide range of lung volumes. The total lung volume at which the elastic forces of lung and chest wall balance is called *relaxation volume*, while the total lung volume at the end of a normal expiration in a quietly breathing subject is termed *Functional Residual Capacity (FRC)*. In normal adults, FRC and relaxation volume are essentially equal. At FRC, the pressure in the virtual space between the lungs and the chest wall (pleural space) becomes slightly subatmospheric, with its precise value depending on various factors including body position. The volume inspired during a regular breath is called *Tidal Volume (V)*. The maximal volume that a patient can inspire is named *Inspiratory*

Capacity (IC), and the sum of IC and FRC is the *Total Lung Capacity (TLC)*. The maximal volume below FRC that a patient can expire in a forced expiration is called *Expiratory Reserve (ER)*, and the amount of air that remains in the lungs after maximal expiration is the *Residual Volume (RV)*. The sum of IC and ER, i.e., the range of lung volumes that can be covered by voluntary inspiration and expiration, is called *Vital Capacity (VC)*.

The respiratory pump

The lungs and the chest wall are not rigidly attached to each other. Rather, a virtual space between the membranes of the pleura allows the lung and chest wall to slide past each other, but nevertheless forces the lung to closely follow the volume and shape changes of the chest wall.

The most important muscle for inspiration is the dome-shaped diaphragm. As it contracts, the pressure in the thoracic cavity is reduced to a value below its equilibrium level, and inspiratory flow is initiated. The external intercostal muscles support inspiration by lifting and expanding the rib cage. In a healthy resting subject, expiration is passive and complete, i.e., air is forced out of the lungs solely by the elastic energy stored during inspiration until the equilibrium volume is reached. The primary mediator of active expiration, as it occurs for example during exercise, is the abdominal wall musculature. It compresses the abdominal cavity and, since the diaphragm is relaxed during expiration, increases intrathoracic pressure, pressing air out of the lungs. This process is supported by the internal intercostal muscles that reduce the diameter of the rib cage.

Control of breathing

The frequency and depth of respiration is usually controlled subconsciously in the central nervous system, but can be consciously altered within certain limits. The precise location and structure of the respiratory pattern generator in the brainstem remains unclear to date. The partial pressure of CO₂ measured via a central chemoreceptor in the brain stem is the most important respiratory feedback mechanism. Secondary feedback

pathways include peripheral chemoreceptors for oxygen as well as stretch receptors in the lungs and the thorax.

2.1.2 Relevant pulmonary pathophysiology

Chronic Obstructive Pulmonary Disease (COPD)

COPD is an ill-defined but commonly used term that is generally applied to patients suffering from Chronic Bronchitis and/or Emphysema. Symptomatically, a patient is considered to have COPD when the volume expired over the first second of a forced expiration (FEV_1) and the forced vital capacity (FVC) are less than a certain percentage of the normal predicted values. Chronic Bronchitis is associated with enlarged mucous glands and excessive mucus production in the bronchial tree. Both factors contribute to the narrowing and obstruction of airways. Emphysema is characterized by structural changes in the alveolar duct region, leading in particular to a loss of alveolar walls and an enlargement of air spaces. There is evidence that excessive breakdown of the elastin fibers within the parenchyma due to an overproduction of lysosomal elastase is the underlying mechanism for these structural changes (146). The structural changes in the lungs in Emphysema also affect the airway walls and reduce the maximal expiratory flow that the patient can achieve. As a consequence, expiratory flow limitation occurs at comparatively low flows in these patients. Expiratory flow limitation and its consequences are discussed in detail in sections 2.1.3 and 2.1.4.

Acute respiratory failure

Acute respiratory failure (ARF) occurs when the respiratory system is no longer able to maintain adequate gas exchange. According to general guidelines, a patient is considered to be in ARF when the partial pressures of O_2 and CO_2 in the arterial blood fall outside certain limits for an extended period of time (146).

2.1.3 Expiratory flow limitation

The flow resistance of airways differs between inspiration and expiration. While during inspiration, an increased driving pressure almost always results in increased flow, Fry *et al.* showed in 1954 that expiratory flow reaches a limit above which an increase in driving pressure does not significantly change the flow (44). This phenomenon can be demonstrated by plotting expiratory flow as a function of the driving pressure at a fixed lung volume, producing the so-called iso-volume pressure-flow (IVPF) curves. Fig. 2.1 shows an illustration of three typical IVPF curves, with the lung volume decreasing from curve A to curve C (71). While at very high lung volumes, the expiratory flow increases with driving pressure over most of its physiologic range, the expiratory flow rate clearly plateaus at intermediate and low lung volumes. At the lowest lung volume (curve C), very moderate expiratory pressures of less than 10 cmH₂O are already sufficient to produce the maximal expiratory flow. The plateau values of expiratory flow can be plotted against

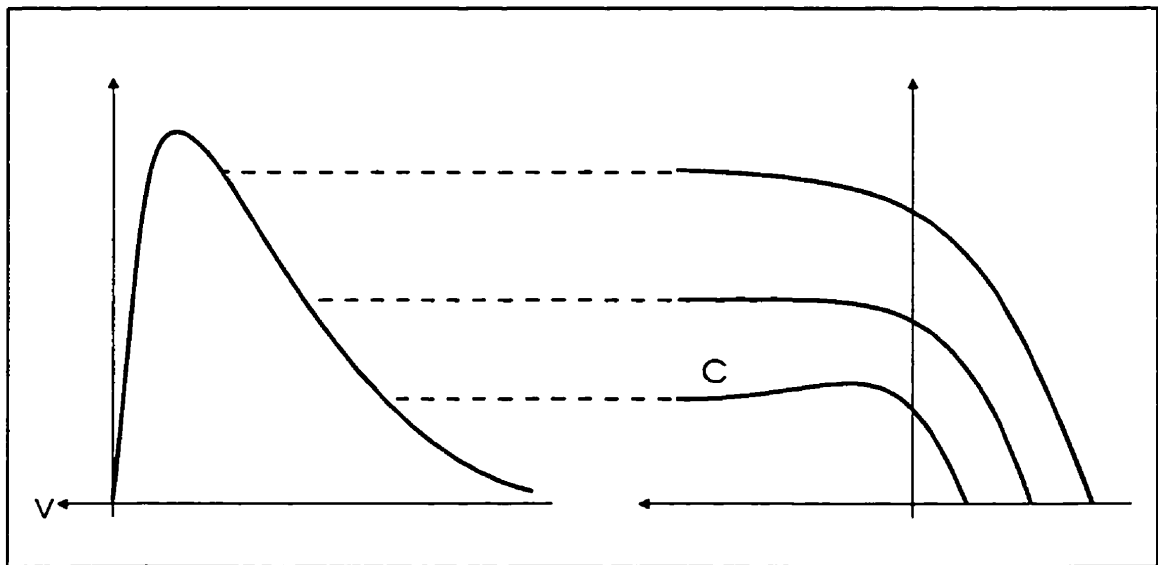


Fig. 2.1

Right panel: Stylized IVPF curves describing expiratory flow limitation. A: high lung volume; B: intermediate lung volume; C: lower lung volume. Left panel: MEFV curve constructed from the plateau values of the IVPF curves. Illustration according to (71). See text for details.

lung volume to obtain the maximum expiratory flow volume (MEFV) curve (71), as also shown in Fig. 2.1. Beyond the maximum, the IVPF curves may also exhibit a drop in expiratory flow with increasing driving pressure, in particular at lower lung volumes. This “negative effort dependence” (93) is illustrated in curve C of Fig. 2.1.

The explanation of the expiratory flow limitation phenomenon turned out to be a complex issue. First, it was realized that the pressure along the airway tree during forced expiration exhibits a pressure “waterfall”, i.e., a large pressure drop over a short segment of the airways, and that changing the pressure on the downstream side of the waterfall does not alter expiratory flow (110). The pressure waterfall occurs because of two mechanisms. Under certain circumstances, the compressive forces on the airway due to flow-related pressure losses in the airway lumen balance the elastic forces distending the airway (71,82,102). Such an equilibrium of forces presents an intrinsic negative feedback mechanism, since small increases in flow augment the viscous pressure losses and thus further compress the airway, which in turn counteracts the increase in flow. Furthermore, elastic tubes cannot conduct fluids at a velocity greater than the speed at which pressure waves propagate along the wall of the tube, the so-called wave speed (30). If the wave speed is reached at any point along an airway, communication between the upstream and downstream sides of this “choke-point” is lost, and flow through the airway becomes independent of the driving pressure. Lambert *et al.* showed in a detailed computer simulation (83) that in normals, the wave speed phenomenon is the dominant flow limiting mechanism at higher and intermediate lung volumes, while the coupling between the viscous pressure losses and airway wall compliance limits expiratory flow at low lung volumes.

The wave speed of an elastic tube depends on the viscosity of the conducted fluid, the mechanical properties of the tube wall, the geometry of the tube and the pressures in and around the tube. In general, a stiff tube has a higher wave speed than a compliant tube. In COPD patients, the compliance of the airway walls is increased, which reduces

the wave speed and the maximal possible expiratory flow in any particular airway. Expiratory flow limitation is also increased in asthmatics (71).

2.1.4 Dynamic hyperinflation, intrinsic PEEP and work of breathing

In patients with severe airway obstruction, e.g., in COPD, expiratory flow is often slowed to the extent that expiration cannot be completed and inspiratory flow is initiated before the equilibrium volume has been reached. The volume above FRC that remains in the lungs at end-expiration in these patients is called dynamic hyperinflation, and the elastic recoil pressure of the lungs and the chest wall that is associated with a given level of dynamic hyperinflation is the patient's $PEEP_i$. $PEEP_i$ represents a threshold load that needs to be overcome by the patient's inspiratory muscles before inspiratory flow can be initiated during both spontaneous breathing and assisted modes of mechanical ventilation (51,52,105,119,135). The additional W_{insp} required to overcome this threshold load is thought to be a major contributing factor to the development of inspiratory muscle fatigue, particularly in the face of the inherently disadvantageous operating conditions of the inspiratory muscles during dynamic hyperinflation (122). Consequently, determining the presence and magnitude of both $PEEP_i$ (51,120) and W_{insp} (10,41,129) is of great clinical importance for the management of critical care patients.

2.2 Measurement of pulmonary function

2.2.1 Basic diagnostic techniques

Physical examination

Physical examination receives great attention in many respiratory care textbooks. Besides observation of the patient for obvious signs of respiratory distress, physical examination includes passive tactile examination of the thorax (palpation), percussion techniques and the stethoscopic analysis of breath sounds. Physical examination techniques frequently rely on the subjective perception by the physician, e.g., the identification of a “dull” percussion note or a “rumbling sound” with a “musical quality” (127). Furthermore, they in general only provide qualitative results, and often the nature of the disease can only be inferred from the combination of several tests. The practical importance of these techniques despite their shortcomings illustrates the enormous need and potential for Biomedical Engineers to develop advanced methods and techniques that permit rapid, precise and quantitative evaluation of the patient status.

Blood gases

The analysis of the P_{O_2} and the partial pressures of CO_2 (P_{CO_2}) in arterial blood is considered to provide a direct measure of the adequacy of the pulmonary ventilation and the oxygenation of the blood. Respiratory distress is almost always associated with an increase in P_{CO_2} . In the case of an acute exacerbation of the patient, the change in P_{CO_2} also causes a reduction of the blood pH. Since the kidneys compensate this acidosis over a period of roughly 24 hours, the combination of P_{CO_2} and pH can be used to distinguish acute events from chronic disease processes.

Blood gases are taken several times a day in the ICU and can be analyzed in a few minutes. Devices that detect the blood gases from a single drop of arterial blood instantaneously at the bedside have recently become available.

Lung function tests

In the majority of hospitals, lung function tests are restricted to measurements that can be obtained from a conventional spirometer. Beside V_t , respiratory rate (RR) and minute ventilation (\dot{V}_e), this device can be used to evaluate FVC and FEV₁, provided that the patient is willing and able to perform a forced expiration maneuver. These tests are considered relatively robust, but are not very specific because each parameter is influenced by a number of physiological factors and may be modulated by conscious inputs.

In recent years, computerized pulmonary monitoring equipment has become available that continuously monitors pressures and flow across the respiratory system and computes parameters such as V_t and RR on-line. More advanced measurements such as respiratory system resistance and elastance, intrinsic PEEP and work of breathing can also be monitored. The introduction of these pulmonary monitoring devices is a great step towards better pulmonary monitoring and patient management. However, many of the algorithms employed have not been properly validated or suffer from known shortcomings. The quantitative assessment of some of these measurement techniques forms part of the work for this thesis and is described in section 3.2.

2.2.2 Esophageal pressure measurement

Respiratory pressure swings in the esophagus (P_{es}) can be measured using an esophageal balloon, i.e., a small elastic balloon attached to the end of a small plastic catheter placed in the mid-thoracic section of the esophagus via the nose (15,21). Provided that the esophageal balloon is adequately placed and inflated, swings in P_{es} reflect swings in pleural pressure (P_{pl}) with sufficient accuracy over the range of frequencies that are relevant during spontaneous breathing (15,22,32). Measurements of P_{es} can be used to separate estimates of respiratory mechanics into lung and chest wall compartments (29,33,57), to evaluate variables of clinical importance such as dynamic

PEEP_i (PEEP_{i,dyn}) and W_{insp} (see section 2.2.3), and to estimate the patient's muscular and/or neural drive (148).

Since the esophageal balloon is placed in close proximity to the heart, P_{es} recordings often contain cardiogenic oscillations. These are components of P_{es} that are not directly related to respiration, but originate from pressure changes within the pericardium and the aorta that are communicated to the esophageal balloon. Cardiogenic oscillations can assume amplitudes that are large enough to significantly complicate processing of the P_{es} signal.

2.2.3 Measurement of PEEP_i and W_{insp}

Static PEEP_i

In passive patients, static PEEP_i (PEEP_{i,stat}) can be measured by occluding the patient's airway opening at end-expiration (Fig. 2.2). PEEP_{i,stat} equals the pressure that can be measured on the patient side of the occlusion after any transients have vanished (119). PEEP_{i,stat} is difficult to measure in distressed patients because they are often not able to remain passive for a sufficiently long period of time. Prolonged relaxation can be achieved by sedating or paralyzing the patient. However, sedatives also change the general muscle tone and alter the breathing pattern. The value of PEEP_{i,stat} obtained under sedated conditions may thus differ significantly from the value of PEEP_{i,stat} during spontaneous breathing.

Dynamic PEEP_i

During spontaneous breathing or assisted mechanical ventilation, PEEP_{i,dyn} can be estimated from P_{es} and flow traces. As illustrated in Fig. 2.3, PEEP_{i,dyn} equals the negative deflection in P_{es} from its end-expiratory relaxation value ($P_{es,0}$) that is necessary to initiate inspiratory flow (107). PEEP_{i,dyn} was initially considered a reasonable approximation of the value of PEEP_{i,stat} (107,119). However, recent studies indicate that PEEP_{i,dyn} can substantially underestimate PEEP_{i,stat} and suggest that these discrepancies originate from time constant inhomogeneities and/or tissue viscoelasticity (62,88).

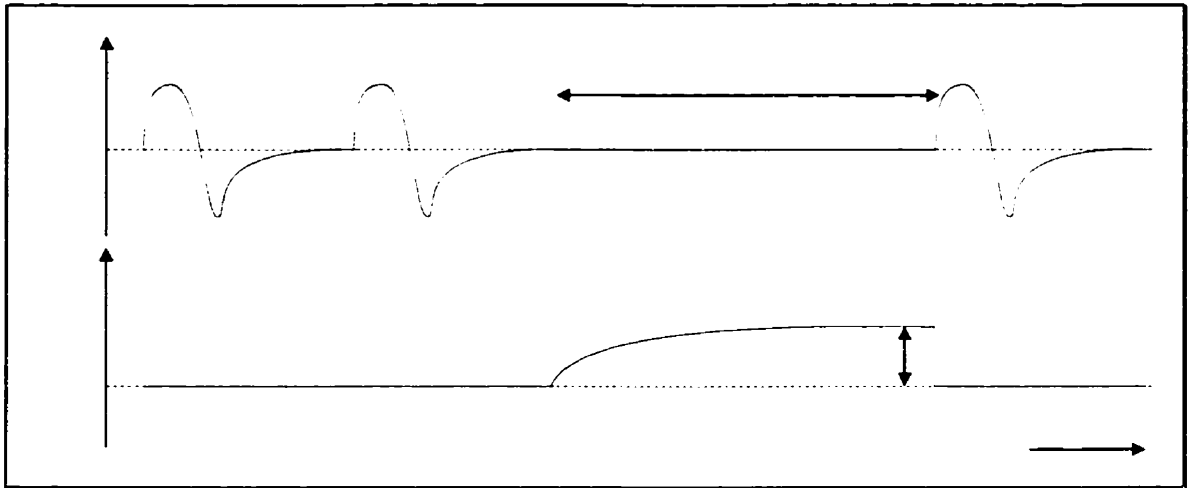


Fig. 2.2:
Measurement of static $PEEP_i$. $PEEP_{i,stat}$ equals the value at which airway opening pressure plateaus after a prolonged end-expiratory airway occlusion

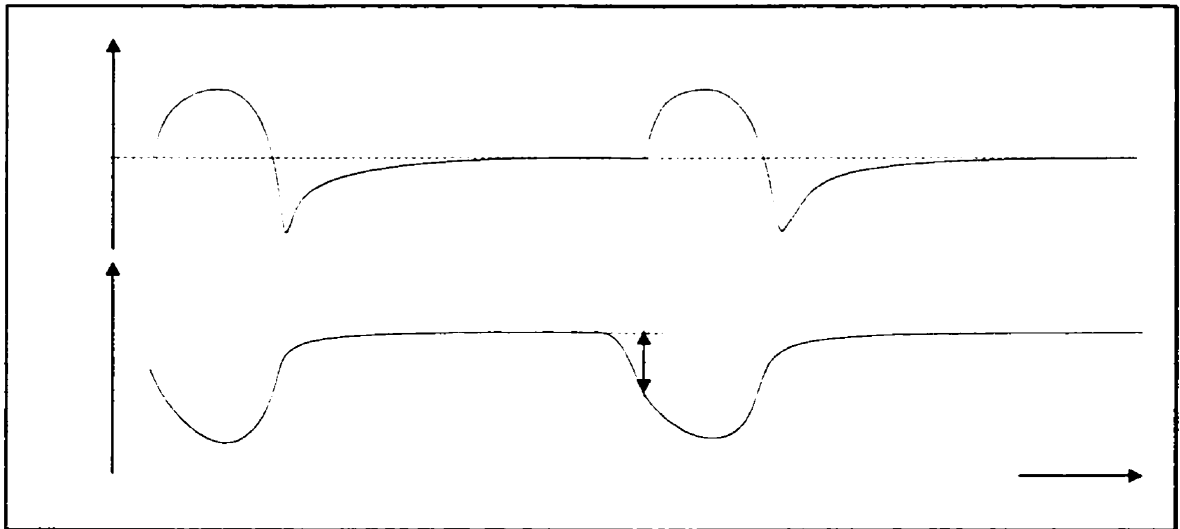


Fig. 2.3:
Measurement of dynamic $PEEP_i$. $PEEP_{i,dyn}$ equals the deflection in P_{ao} with respect to its end-expiratory baseline value prior to the onset of inspiratory flow.

Inspiratory work of breathing

The fraction of W_{insp} required to overcome the resistance of the airways and distend the lungs can be estimated from P_{es} and flow or volume traces according to

$$W_{\text{insp, lung}} = \int_{V_i} (P_{\text{es},0} - P_{\text{es}}) dV \quad (2.1)$$

as the integral of the inspiratory deflection in P_{es} from $P_{\text{es},0}$ over inspired volume. To obtain the complete W_{insp} , the work required to distend the chest wall must also be taken into account. One possibility is to obtain the passive inflation waveform of P_{es} from the sedated patient and subsequently integrate the difference between the active and the passive P_{es} , as illustrated in Fig. 2.4 (90). However, sedation is likely to alter the properties of the chest wall, and a significant uncertainty is associated with the passive inflation curve obtained in this manner. Therefore, some investigators have taken a simpler approach to estimate the chest wall component of W_{insp} by assuming a constant value for the chest wall elastance *a priori*. In this case, W_{insp} can be expressed as

$$W_{\text{insp}} = \int_{V_i} (P_{\text{es},0} - P_{\text{es}}) dV + \frac{1}{2} E V_i^2. \quad (2.2)$$

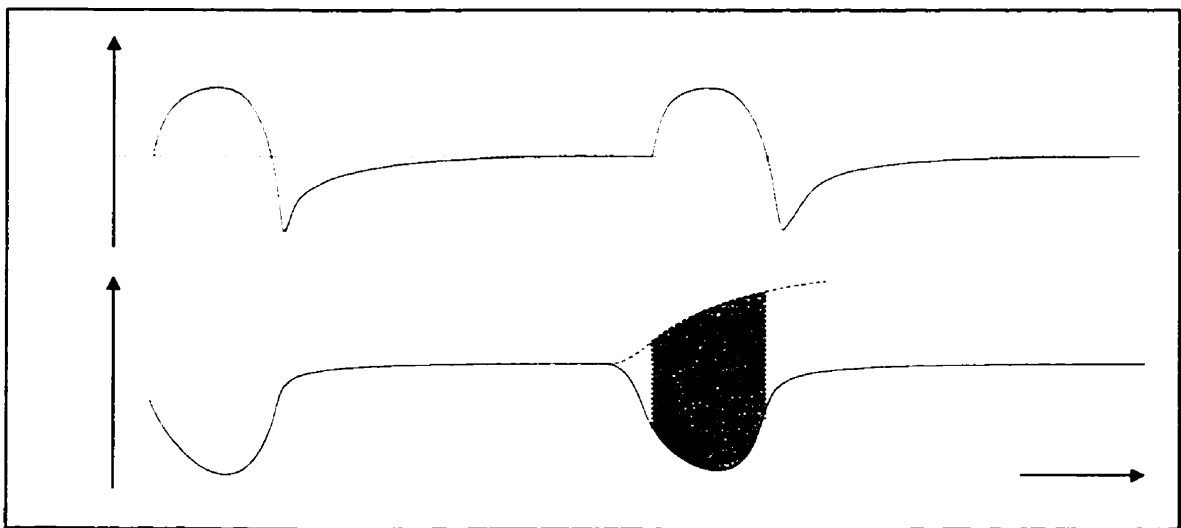


Fig. 2.4: Measurement of inspiratory work of breathing according to (90). The difference between P_{es} and the previously measured passive inflation curve, indicated by the shaded area, is integrated over inspired volume.

The Bicare CP-100 commercial pulmonary monitor (Bicare Corp., Irvine, CA) employs this algorithm, assuming a constant linear chest wall elastance of 5 cmH₂O for all patients.

2.2.4 Thoracic radiography

Radiography plays an important role in the diagnosis of pulmonary diseases. Typically, mobile, so-called *portable* x-ray units are used to obtain thoracic x-rays without removing the distressed patients from their beds or disconnecting vital sign monitors, mechanical ventilators and other equipment. However, these portable x-ray images suffer from a number of shortcomings. First, the geometry between tube, patient and film is restricted, and the photographic quality of the images is generally inferior to chest x-rays obtained from stationary equipment (127). Second, all equipment and tubing attached to the patient become part of the image and may conceal the sometimes very translucent reflections of abnormalities in the lungs. Finally, the patient position is usually restricted to the anteroposterior view, which results in a comparatively larger and less sharp cardiac shadow.

Chest radiography permits assessment of the diaphragm shape, which reflects the level of dynamic hyperinflation. Furthermore, pneumothoraces, pleural effusions and localized, severe airway closures (atelectases) can usually be detected in radiographic images. However, many abnormalities are only visible when the disease has reached a significant level of severity. Similar to physical examination techniques, the analysis of chest x-rays to a large extent is based on the subjective interpretation by the attending physician. The development of a non-invasive imaging technique that can be used continuously at the bedside, and that provides a variety of views of the thorax would present a great contribution to the improvement of respiratory care.

2.3 Assisted positive pressure ventilation

2.3.1 Positive pressure ventilation

Positive pressure ventilators apply a supra-atmospheric pressure to the airway opening in order to force air into the lungs. In general, the ventilator can take complete control of the breathing pattern, e.g., during open chest surgery when the respiratory pump is impaired. However, prolonged ventilation of intensive care patients under complete machine control causes muscular atrophy. Candidates for long-term ventilation are thus ventilated in assisting ventilator modes where ventilator and patient share the work of breathing. Since the monitoring of intensive care patients is the focus of this work, only assisted modes of positive pressure ventilation are discussed here.

2.3.2 Modes of assisted mechanical ventilation

Continuous positive airway pressure (CPAP)

In CPAP, a constant positive pressure is applied to the airway opening throughout the entire breath. CPAP effectively forces the patient to breathe at a higher lung volume, which is considered advantageous in the presence of severe airflow obstruction (6,106,107). CPAP is also frequently used in the treatment of sleep apnea.

Synchronized intermittent mechanical ventilation (SIMV)

In SIMV, the ventilator intermittently delivers controlled mechanical breaths at a very low respiratory rate. In the intervals between these machine breath, the patient is allowed to breathe spontaneously. SIMV was the first assisted mode of ventilation.

Assist-control ventilation (ACV)

In ACV, the ventilator does not initiate a mechanical breath until an inspiratory effort from the patient is sensed. Once the ventilator is triggered, a complete mechanical

breath is delivered as specified by the ventilator settings. The patient can thus control the respiratory rate, but not the tidal volume, inspiratory flow rate or inspiratory time.

Pressure support ventilation (PSV)

Pressure support ventilation is a more recent mode of ventilation. Similar to CPAP, a constant pressure is applied to the airway opening. However, the pressure level is increased during inspiration in order to actively support inspiration. Within limits, the patient can control the respiratory rate, the tidal volume, and the inspiratory time and flow.

Proportional assist ventilation (PAV)

PAV is a novel mode of ventilation (157,158) that has only very recently become commercially available. Similar to PSV, the airway opening pressure is controlled during PAV. However, the set point of the inspiratory pressure level is not fixed, but is computed in real time as the sum of two components. One of these components is proportional to the actual inspiratory flow (Flow assist), while the other component is proportional to the volume that has been inspired in the present breath (Volume assist). PAV thus allows specific and independent compensation for part of the resistive and elastic load that the respiratory pump is facing. The patient has complete control of the respiratory waveform, and the pressure generated by the ventilator increases with the patient effort.

2.3.3 Positive end-expiratory pressure (PEEP)

PEEP is a constant pressure that is applied to the airway opening during expiration. Similar to CPAP, the intention is to increase the mean lung volume in patients with severe airflow obstruction. PEEP is usually combined with SIMV, ACV, PSV or PAV.

2.3.4 Trigger mechanisms

A ventilator operating in an assisted mode of ventilation must recognize the patient effort before inspiratory flow is initiated. At present, two techniques are widely used for this purpose.

Pressure trigger

In this mode, the patient expires through a one-way valve. When expiration is terminated and the inspiratory effort begins, the valve closes and the patient's airways are temporarily occluded, which causes the airway opening pressure (P_{aw}) to drop rapidly. Once P_{aw} becomes more negative than a specified threshold, the ventilator is triggered and inspiratory flow is initiated.

This trigger mechanism is problematic because the patient does not receive flow immediately at the onset of an inspiratory effort. Rather, the onset of flow is delayed by the closing time of the one-way valve and the time required to detect and react to a sub-threshold pressure. Also, the generation of sufficient negative pressure to trigger the ventilator may impose a significant work load on the patient (40,135).

Flow trigger

More recent ventilators do not use a one-way valve, but permit the patient to inspire while the ventilator is in its expiratory phase. As soon as inspiratory flow is detected, the ventilator is switched to its inspiratory phase and the commenced inspiration is actively supported.

2.3.5 Weaning

The process of getting a ventilated patient back to breathing spontaneously and without the aid of a ventilator is termed *weaning*. Many physiologic parameters have been reported as predictors of weaning outcome, but often the results have been contradictory. An overall consensus about how to wean a patient does not exist in the literature, and a number of experts consider weaning an art rather than a science. However, more formalized weaning protocols and the use of knowledge-based algorithms in computerized weaning aids have been suggested (36,86). The development of methods and tools that permit more rapid and reliable weaning is one of today's challenges for Biomedical Engineering research in the field of respirology.

2.4 Electrical Impedance Tomography

2.4.1 Imaging electrical tissue properties of the thorax

Biological tissues contain large amounts of ion-rich fluids. Because the relative amount of body fluid, the ion balance and the nature and geometry of the membrane structures that confine the body fluids differ from organ to organ, biological tissues exhibit a wide variety of complex, frequency-dependent electrical properties (26,47,126). A summary of the electrical resistivities of some biological tissues, i.e., the real parts of their impedances, is given in Table 2.1 for the frequency range from 20 to 100 kHz.

Table 2.1:
Approximate electrical resistivities of tissues in the thorax in the range from 20 to 100 kHz according to (11).

| Tissue | Resistivity ($\Omega\cdot\text{cm}$) |
|-----------------|--|
| Bone | 16600 |
| Fat | 2500 |
| Lung tissue | 727 - 2363 |
| Skeletal muscle | 530 |
| Blood | 150 |
| Plasma | 66 |

Electrical Impedance Tomography (EIT) is a medical imaging modality that estimates the spatial distribution of the electrical tissue properties. Often, the imaginary part of the tissue impedance is ignored and only the resistivities or conductivities are measured (3,12,24,155), although imaging of the complex tissue impedance has received increased attention in the recent literature (54,75,114,115). Because the tissues that compose the human thorax exhibit a wide range of resistivities, thoracic EIT images should permit clear delineation of the various tissues and the many disease processes that significantly alter the tissue conductivity (e.g., due to the increased volume of highly

conductive fluid in the usually rather resistive lungs during pulmonary edema or congestion of the pulmonary vasculature). EIT is relatively inexpensive and minimally invasive and is thus potentially well-suited for continuous bedside monitoring of pulmonary function (19,34,60,124,138). However, there is much room for improvement in the resolution and contrast of current EIT systems.

2.4.2 The EIT system

Overview

An overview of a typical EIT system is provided in Fig. 2.5. In order to determine the transfer impedances between a number of electrodes on the body surface, small-amplitude high-frequency currents are injected into the body segment under consideration and the resulting voltages are measured (12,56,115,134). The current sources are controlled by a computer to apply the desired current patterns, and all data are digitized and transferred to the computer which reconstructs the tissue impedance distribution from the measured transfer impedances. All front-end electronics are electrically isolated from all other equipment to assure patient safety. EIT systems that apply potentials to the body

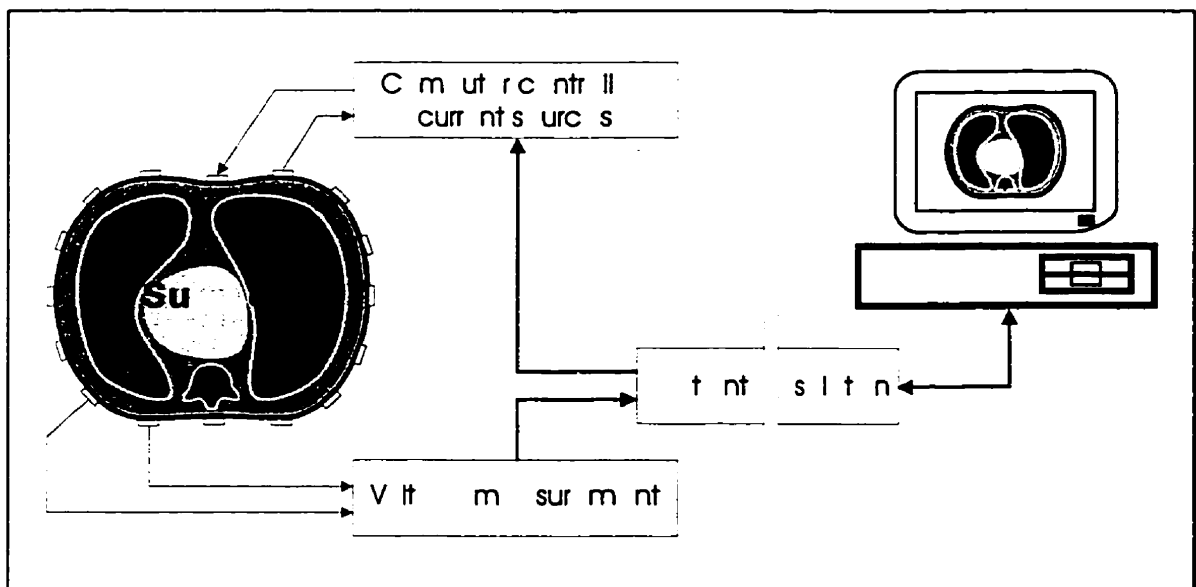


Fig. 2.5:
Overview of an EIT system

surface and measure the resulting currents have been used less frequently (112,160) because they are more sensitive to changes in the impedance of the electrode-skin interface (117).

Current injection

The pattern in which current is injected into the body has an important influence on the quality of the resulting image (23,65,104). The following is a summary of the current patterns that are frequently used to collect EIT data.

(i) Neighbouring currents

When neighbouring currents are used, a single current source and sink are placed on adjacent electrodes on the circumference of the body segment under consideration (12). Both the source and sink are incrementally rotated around the body to obtain the maximal number of $N_e - 1$ linearly independent projections, where N_e is the number of electrodes. Neighbouring currents have been used frequently in EIT (7,12,14,56). Compared to other current patterns, neighbouring currents produce a low current density in the center of the body segment to be imaged and a very inhomogeneous current density distribution.

(ii) Opposite currents

Similar to neighbouring currents, opposite currents utilize only a single current source and sink. In this case, the sink is placed diametrically opposed to the source (104), and the maximal number of linearly independent projections equals $N_e/2$. Opposite currents provide a higher current density to the center than neighbouring currents, although the current density distribution remains somewhat inhomogeneous.

(iii) Current patterns using multiple sources

In general, the current density distribution can be controlled best when current is injected through multiple sources rather than through a single source-sink pair. The most popular of these approaches is the optimal current pattern (49). It can be shown that the distinguishability, defined as the normalized change of the measured voltages in response to a conductivity change in a small central region of a cylindrical body, is maximal when the amplitudes of equidistantly spaced current sources are adjusted according to

trigonometric basis functions (73). From this starting point, the optimal current patterns are adjusted iteratively such that the distinguishability is maximized for the conductivity distribution in the most recently reconstructed image. Thus, unlike other current patterns, optimal currents take the nature of the image into account. Unfortunately, this method requires that all current sources present in the system are calibrated precisely with respect to each other, which adds to the complexity of the device.

Other current patterns using multiple sources, e.g., the multireference method (65) and current injection according to Walsh functions (23,73), have been suggested in the literature without attaining any practical significance.

(iv) *Induced currents*

In 1990, Purvis *et al.* (111) suggested replacing the injection of current through boundary electrodes by induction of high-frequency rotary currents through a set of coils placed around the object to be imaged, as shown in Fig. 2.6. This approach has been subject to numerous studies in the recent EIT literature (46,111,123) since it possesses several technical advantages. Because no current is injected into the patient, less stringent safety requirements apply to the equipment design. Furthermore, the quality of the voltage measurements is improved since no multiplexing circuitry is required to switch electrodes between current injection and voltage measurement modes. Also, the maximal number of independent projections, now determined by the number of induction coils, becomes independent of the number of boundary electrodes, which

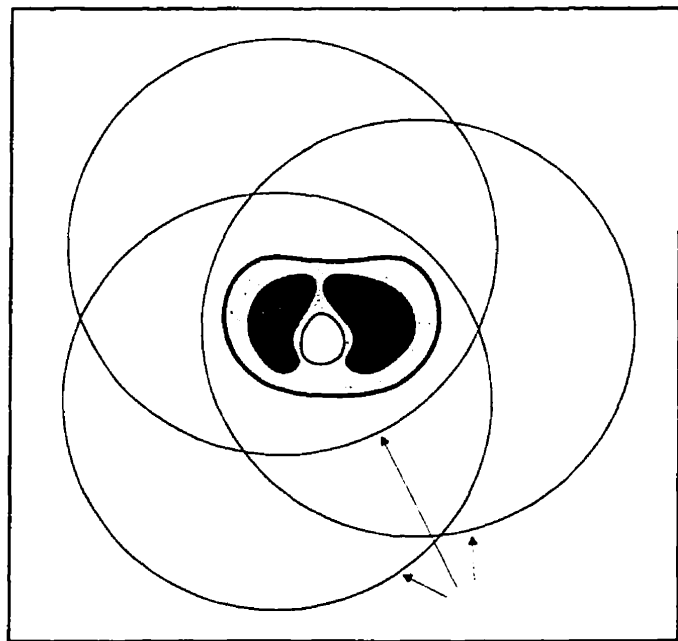


Fig. 2.6:
Arrangement of induction coils for induced current EIT around the object to be imaged.

introduces a new degree of freedom to EIT system design. Despite these advantages, however, induced current EIT has not been able to dramatically improve the resolution of EIT images, and the significantly more cumbersome equipment remains the drawback of this technique.

Voltage measurement

(i) Parallel versus serial data collection

To collect an EIT projection, a set of boundary voltages is measured on the body surface. Ideally, these voltages should be measured at exactly the same point in time, i.e., using a parallel data collection strategy, to minimize the overall duration of the data collection cycle. However, this method requires independent instrumentation amplifier and demodulator circuits for each channel (76,118,140) and is thus comparatively expensive. Alternatively, many investigators have employed a serial data collection strategy, using multiplexers to consecutively connect each electrode to a single instrumentation amplifier and demodulator circuit (12,56,81,137).

(ii) Electrode contact impedance

Electrode skin interfaces are known to have a significant and time-varying contact impedance. Thus, the voltages measured at the electrodes that conduct current are influenced by the contact impedances as well as by the conductivity distribution within the body, which introduces a significant measurement error to EIT (117).

When neighbouring or opposite currents are used, this problem can be overcome by excluding the voltages measured at the injection electrodes (104), which reduces the number of linearly independent data points that can be obtained per projection by two. When current patterns with multiple current sources are used, however, “compound electrodes” consisting of pairs of independent voltage and current electrodes (68,160) are necessary to avoid the contact impedance problem.

(iii) Geselowitz's theorem

The number of independent measurements that can be obtained in an EIT measurement situation is limited by symmetry of the measurements. According to

Geselowitz's theorem (48), the voltage measured at a pair of electrodes, i and j , when a current is injected through a different pair of electrodes, n and m , is exactly equivalent to the voltage measured at electrodes n and m when a current of equal amplitude is injected through electrodes i and j . This reduces the total number of independent measurements, e.g., when neighbouring currents are used and the voltage measurements at the injection electrodes are excluded, to $N_e/2(N_e-3)$.

(iv) Esophageal reference electrodes

In a standard EIT setup, currents are applied and voltages are measured (or vice versa) exclusively on the periphery of the body segment to be imaged. In order to provide more information about the central regions of thoracic images, Pilkington *et al.* (108) suggested the placement of a reference electrode in the thoracic section of the esophagus. They argued that such an esophageal reference electrode increases the distinguishability, defined above as the normalized change of the measured voltages in response to a conductivity change in a small central region of a cylindrical body, by a factor of six in a two-dimensional thoracic imaging situation (108). However, the effect of an esophageal reference electrode on the reconstruction error, i.e., the normalized difference between the reconstructed image and a known physical or computational phantom, has not been examined to date.

Static and dynamic imaging

The long-term goal of EIT is to obtain a static image, i.e., an image of the absolute values of the tissue conductivities in the body segment under consideration. However, the reconstruction of static EIT images is problematic, presumably because of systematic errors of the image reconstruction schemes (12). Static images of low resolution have been obtained from physical phantoms (67,152) and, very recently, *in vivo* (91).

Dynamic EIT imaging does not attempt to reconstruct the absolute values of the tissue conductivities. Rather, two sets of data are obtained before and after an event, e.g., at the beginning and the end of inspiration, and the difference between the two data sets is used to reconstruct the dynamic (difference) image. In this case, the systematic errors

cancel out and an image of the change in conductivities can be reconstructed (12). Dynamic EIT images have been used for a number of applications, such as monitoring of the depth of ventilation, measuring gastric emptying and secretion, monitoring microwave hyperthermia treatment in cancer therapy and cancer screening (7,14,19,89,109,152).

Unfortunately, dynamic imaging is of limited use for many applications because the event to be monitored has already occurred when the patient enters the hospital or clinic, so that no reference data set can be obtained. To overcome this problem, a recent study employed the average of a large number of data sets obtained from numerous normal subjects as a reference data set to monitor the presence of increased lung water in a small number of patients with pulmonary hypertension (100). However, the specificity of this technique remains to be established in a larger number of subjects.

The difficulties in reconstructing static images were initially thought to relate to the unknown position of the electrodes on the body surface (12). However, simulation studies with variable electrode positions as well as the performance of the above averaging technique show that the electrode position error is not as important as previously thought, and that other systematic errors must play a role for the difficulty of static imaging (1,100).

Multifrequency and complex-valued imaging

While early EIT systems were only able to measure the magnitudes or the real parts of the transfer impedances, more recent designs permit evaluation of the complex transfer impedances over a wide range of frequencies. Because the impedance of biological tissues is frequency-dependent, it is possible to obtain a so-called multifrequency EIT image from two data sets acquired simultaneously or in rapid succession, but at different frequencies (55,115). Similar to dynamic imaging, systematic errors cancel out in this approach, but a change in tissue properties between the two data acquisitions is not necessary for multifrequency imaging. However, multifrequency images differ fundamentally from static EIT images because they do not estimate the absolute tissue conductivities, but the dissociation of the tissue conductivities at the two measurement

frequencies. Furthermore, using the complex transfer impedances to reconstruct complex-valued EIT images (54,115) may help to distinguish tissues that have similar conductivities but different permittivities, e.g., to distinguish carcinogenic from adipose tissue (42,43).

Three-dimensional EIT

Unlike x-rays in a Computed Tomography system, electrical currents are not restricted to the cross-sectional plane in which the electrodes are placed. In current practice, many investigators assume a cylindrical geometry in which two-dimensional treatment is valid despite the generally three-dimensional nature of the EIT problem. However, while this assumption may be acceptable for some applications, e.g., to image the depth of ventilation (19,60), reduced contrast and cancellation effects are encountered as soon as objects with a finite longitudinal dimension are located in or near the image plane (94). Truly three-dimensional EIT images of the thorax obtained from a 64 electrode system with four electrode planes have recently been presented (94,95) and demonstrate that significantly improved resolution and contrast can be obtained.

2.4.3 Image reconstruction

Forward and inverse problem

We assume biological tissues to produce linear relationships between voltage and current density, so that the EIT forward problem is governed by Ohm's law. Using \mathbf{j} for the current density, \mathbf{E} for the electric field, ϕ for the electrical potential, and γ for the complex admittivity of the medium, Ohm's law can be expressed as

$$\mathbf{j} = \gamma \mathbf{E} = -\gamma \nabla \phi, \quad (2.3)$$

where ∇ is the gradient operator and \mathbf{j} , γ , \mathbf{E} and ϕ vary with position in the space of interest (Ω). At the boundary of Ω , we inject current into the medium, so that the current density normal to the surface of Ω (S) becomes

$$\mathbf{j}_S = \mathbf{j} \cdot \mathbf{n}_S = -\gamma \frac{\partial \phi}{\partial n_S}, \quad (2.4)$$

where n_s is the vector normal to S . To assure continuity, the net current injected must vanish, i.e.,

$$\oint j_s dS = 0. \quad (2.5)$$

We can now find the voltages that are measured on the boundary (v_b) as a function of γ , j_s and the positions at which the measurements are obtained (x_m), from

$$v_b = \varphi(x_m, \gamma, j_s), \quad (2.6)$$

which solves the EIT forward problem. While v_b is a linear function of j_s , it is significantly nonlinear in γ (73,96).

EIT image reconstruction poses the inverse problem because we want to find the admittivity distribution γ^* that reproduces the measured v_b for each projection p in a data set of N_p projections, i.e.,

$$v_b^{(p)} \equiv \varphi(x_m, \gamma^*, j_s^{(p)}). \quad (2.7)$$

This is a nonlinear inverse problem that, in general, requires iterative solution (96).

In the following discussion of commonly used EIT image reconstruction techniques, v_m denotes the vector of all measured voltages in one data set that has been obtained by concatenating the measured $v_b^{(p)}$ for all N_p projections. Furthermore, the imaginary part of γ is neglected and the reconstruction algorithms are written in terms of resistivity (ρ) or conductivity (σ). Image reconstruction is restricted to the real part or magnitude of γ in most EIT image reconstruction schemes documented in the literature. In any case, the reconstruction methods discussed below can be adapted to reconstructing complex images without much difficulty.

Weighted backprojection along equipotential lines

Weighted backprojection along equipotential lines (11,12) is a two-dimensional single-step reconstruction technique that employs an analytical solution for the forward problem with neighbouring current injection. Assuming a homogeneous initial resistivity, ρ_0 , and a cylindrical geometry, the equipotential lines are computed analytically for each projection, and an estimate of the voltages at the measurement sites (\hat{v}) is obtained. Subsequently, each element of the vector v_m is compared to the analogous element

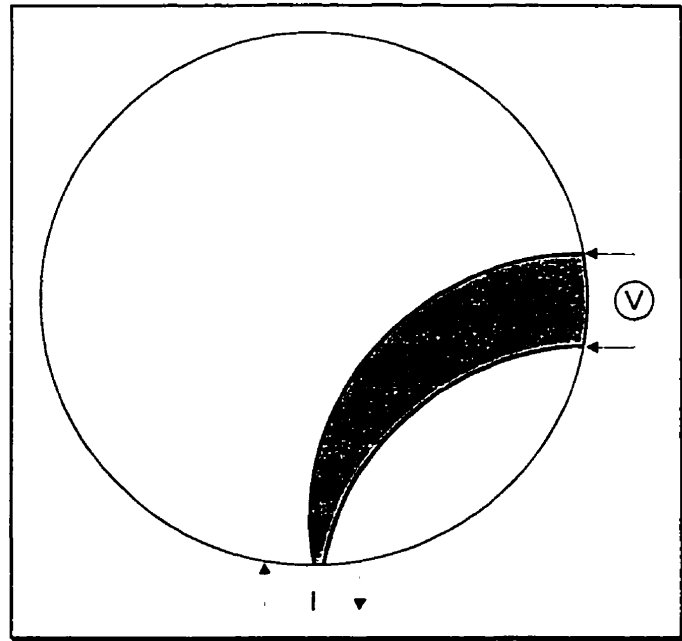


Fig. 2.7:
Weighted backprojection along equipotential lines.
The area enclosed by the predicted equipotential lines (shaded) is updated according to the measured voltage, V .

of \hat{v} . The resistivities of all image pixels that lie between the equipotential lines passing through the voltage electrodes (Fig. 2.7) are now updated according to

$$\rho = W_B(x_p, x_j, x_m) \cdot \rho_0 \cdot \frac{v_m}{\hat{v}}, \quad (2.8)$$

where W_B is a weight that depends on the positions of the pixel (x_p), the injection electrodes (x_j), and on x_m . W_B is necessary to compensate for geometric effects that without weighing produce a non-uniform point-spread function (13).

Besides the assumption of a circular geometry, the above algorithm is exact only for small changes in conductivity, i.e., when $(\rho - \rho_0)/\rho_0 \ll 1$ (12). Since in general, both assumptions are not valid in a practical imaging situation, the pixel values of the reconstructed images bear little relation to the absolute changes in conductivity. However,

the technique is very fast and has been shown to provide useful images for a number of clinical applications (7,14,19,100).

Image reconstruction using Newtonian optimization techniques

(i) Forward solution using Finite Elements

The Finite Element (FE) method provides an approximation of the EIT forward problem that has fewer restrictions than the analytic solution discussed above because it allows almost arbitrary boundaries and conductivity distributions as well as large changes in the element conductivities. FEs have frequently been used to solve the EIT forward problem (3,24,96,123,153,154).

The EIT forward problem can be expressed as a special case of the more general Helmholtz equation. Any scalar potential function that can be expressed by the Helmholtz equation assumes its minimum energy configuration exactly when a functional Θ containing the integral of the Helmholtz equation over Ω is minimal (131). For the EIT forward problem, Θ can be written as

$$\Theta = \frac{1}{2} \int \sigma(\nabla\phi)^2 d\Omega + \oint \phi j_s dS. \quad (2.9)$$

The FE method approximates the first integral by dividing Ω into a large number of elements of finite size. In the first-order FEs that are used almost exclusively in EIT, σ is assumed to be constant throughout the element and ϕ is assumed to vary linearly between the nodes of each FE, i.e.,

$$\phi(x) = \sum_{i=1}^{N_{n,e}} \phi_i \alpha_i(x) \quad (2.10)$$

where $N_{n,e}$ is the number of nodes per element, the subscript i denotes the node number, the α_i represent linear approximation functions that assume a value of 1 at node i and vanish at all other nodes (131). Dividing Ω into a large number of two-dimensional FEs and substituting each element's $\phi(x)$ by Eq. 2.10, the first integral in Eq. 2.9 can be expressed as a matrix product. Similarly, the second integral in Eq. 2.9 can be turned into an algebraic expression by substituting both ϕ and j_s by one-dimensional approximation functions. Then, Eq. 2.9 can be written as

$$\Theta = \frac{1}{2} \varphi_n^T \mathbf{S} \varphi_n - \varphi_n^T \mathbf{T} \mathbf{i}_n, \quad (2.11)$$

where T denotes transposition, φ_n is the vector of the values of φ at the nodes of the FEM, and \mathbf{i}_n is the vector of the currents injected at the nodes. In Eq. 2.11, \mathbf{S} and \mathbf{T} are a symmetric (N_n, N_n) matrices that represent the properties of the medium and map the boundary condition, respectively, with N_n being the number of nodes in the FEM. \mathbf{S} is assembled from the individual element system matrices \mathbf{S}_{el} , as follows. Because σ is considered constant across the element, each \mathbf{S}_{el} can be expressed as

$$\mathbf{S}_{el} = \sigma_{el} \tilde{\mathbf{S}}_{el}, \quad (2.12)$$

where σ_{el} represents the element conductivity. The preliminary matrix $\tilde{\mathbf{S}}_{el}$ contains the integrals of the α_i over the element area and essentially captures the geometry of the FE. In order to assemble the FEs into a Finite Element mesh (FEM), the individual \mathbf{S}_{el} matrices are arranged along the main diagonal of the system matrix of the disconnected mesh, \mathbf{S}_{dis} , and the connectivity of the elements is expressed in a connectivity matrix, \mathbf{C} (131). Then, the system matrix of the assembled mesh can be written as

$$\mathbf{S} = \mathbf{C}^T \mathbf{S}_{dis} \mathbf{C}. \quad (2.13)$$

The \mathbf{T} matrix is assembled in an analagous fashion from the element matrices of the individual one-dimensional FEs that are used to approximate the boundary condition. However, in the EIT literature first-order FEMes are often interpreted as resistor networks and the injection of current into the FEM is often modeled by point sources located on the element nodes, i.e., with approximation functions that consist of Dirac's δ -functions at the nodes rather the linear α_i shown in Eq. 2.10 (96,154). In this case, \mathbf{T} becomes the (N_n, N_n) identity matrix.

When the potential distribution in Ω represents the minimal energy configuration for any given \mathbf{i}_n , the first derivative of Eq. 2.11 with respect to φ_n must vanish, i.e.,

$$\frac{\partial}{\partial \varphi_n} \left(\frac{1}{2} \varphi_n^T \mathbf{S} \varphi_n - \varphi_n^T \mathbf{T} \mathbf{i}_n \right) = \mathbf{S} \varphi_n - \mathbf{T} \mathbf{i}_n = 0, \quad (2.14)$$

which yields the node potentials

$$\varphi_n = \mathbf{S}^{-1} \mathbf{T} \mathbf{i}_n. \quad (2.15)$$

Now, an estimate of the boundary voltages at the measurement sites for each projection p ($\hat{v}^{(p)}$) can be computed by extracting the node voltages at the sites of the voltage measurements from φ_n , i.e.,

$$\hat{v}^{(p)} = \mathbf{X}_v^{(p)} \varphi_n^{(p)} = \mathbf{X}_v^{(p)} \mathbf{S}^{-1} \mathbf{T} i_n^{(p)}. \quad (2.16)$$

Here, \mathbf{X}_v is the (N_b, N_n) matrix that reproduces the way in which the EIT hardware obtains differential voltage measurements from the body surface, with N_b being the number of boundary voltages per projection. Finally, the boundary voltages of all projections are concatenated into the desired \hat{v} according to

$$\hat{v} = \begin{bmatrix} \hat{v}^{(1)} \\ \hat{v}^{(2)} \\ \vdots \\ \hat{v}^{(N_p)} \end{bmatrix}. \quad (2.17)$$

(ii) *Newtonian optimization*

To solve the inverse EIT problem, we want to find the conductivity distribution σ^* that equals the best possible mapping of the true conductivity distribution in the body or phantom to be imaged onto the FEM used for the forward solution. We hence define the scalar objective function of the inverse problem as

$$\Phi = \frac{1}{2} [\hat{v}(\sigma) - \mathbf{v}_m]^T \mathbf{W} [\hat{v}(\sigma) - \mathbf{v}_m], \quad (2.18)$$

where \mathbf{W} is a symmetric (N_v, N_v) -matrix and N_v is the number of data points in \mathbf{v}_m ($N_v = N_b \cdot N_p$). \mathbf{W} can be used to implement *a priori* knowledge, e.g., to attenuate the data obtained from a faulty electrode. For the remainder of this derivation, we shall consider \mathbf{W} to be the identity matrix (\mathbf{I}). Furthermore, we assume that the point $\sigma = \sigma^*$ represents the global minimum of $\Phi(\sigma)$.

The steepest descent method (SDM) is the simplest approach to finding the minimum of $\Phi(\sigma)$. Using the first derivative of Φ with respect to σ , i.e., the gradient of Φ in σ -space (Φ'), σ is updated recursively according to

$$\sigma_{i+1} = \sigma_i + \Delta\sigma_i \quad (2.19)$$

with

$$\Delta\sigma_i = -\lambda \Phi'(\sigma_i), \quad (2.20)$$

where λ is a step size parameter. Both Φ' and σ are $(N_\sigma, 1)$ -vectors, where N_σ is the number of conductivity parameters in the image. The SDM is known to converge slowly, so that large numbers of iterations are necessary.

The Gauss-Newton method (GNM) is derived from the requirement that $\Phi'(\sigma^*)$ must vanish. Using a Taylor expansion and truncating after the second term, we can write

$$\Phi'(\sigma^*) \approx \Phi'(\sigma) + \Phi''(\sigma) \cdot \Delta\sigma = 0, \quad (2.21)$$

where $\Delta\sigma$ is the difference between σ and σ^* , and Φ'' is a square (N_σ, N_σ) -matrix representing the second derivative of Φ with respect to σ that is often referred to as the Hessian matrix (\mathbf{H}). Solving for $\Delta\sigma$ yields

$$\Delta\sigma = -\mathbf{H}^{-1}\Phi'(\sigma). \quad (2.22)$$

However, because the Taylor series was truncated in Eq. 2.21 it is often useful to employ the more conservative estimate

$$\Delta\sigma = -\lambda \mathbf{H}^{-1}\Phi'(\sigma), \quad (2.23)$$

where λ again is a step size parameter that usually ranges between 0 and 1. In the GNM, this value of $\Delta\sigma$ is used in Eq. 2.19 to recursively update σ . The GNM converges very rapidly in the neighborhood of the global minimum, but is known to be less robust than the SDM at a greater distance from σ^* .

The Levenberg-Marquardt method (LMM) is an attempt to combine the advantages of the SDM and the GNM by calculating $\Delta\sigma$ according to

$$\Delta\sigma = -\lambda [\mathbf{H} + \mu \mathbf{I}]^{-1} \Phi'(\sigma), \quad (2.24)$$

where μ is a positive real parameter. If μ is zero, Eq. 2.24 equals Eq. 2.23, so that the LMM performs like the GNM. In the limit of large values of μ , Eq. 2.24 equals Eq. 2.20, which causes the LMM to behave like the SDM. The LMM thus permits a compromise between the rapid convergence of the GNM and the robustness of the SDM.

(iii) *Jacobian and Hessian matrices*

Implementation of the Newtonian optimization techniques requires the evaluation of Φ' and \mathbf{H} . Because \mathbf{v}_m is independent of σ , application of the derivative operator to Eq. 2.18 yields

$$\Phi'(\sigma) = \hat{\mathbf{v}}'^T \cdot (\hat{\mathbf{v}} - \mathbf{v}_m) = \mathbf{J}^T \cdot (\hat{\mathbf{v}} - \mathbf{v}_m), \quad (2.25)$$

where \mathbf{J} is an (N_v, N_σ) matrix that is often referred to as the Jacobian matrix. Using the product rule, we find the second derivative to be

$$\mathbf{H} = \mathbf{J}^T \mathbf{J} + \hat{\mathbf{v}}''^T [\mathbf{I} \otimes (\hat{\mathbf{v}} - \mathbf{v}_m)], \quad (2.26)$$

where \otimes denotes the Kronecker matrix product. The second term in this equation is computationally expensive to evaluate and has been shown to be negligible (154), such that we can use the local linearization of the forward problem,

$$\mathbf{H} = \mathbf{J}^T \mathbf{J}, \quad (2.27)$$

instead of Eq. 2.26.

The Jacobian matrix can be evaluated from the FE equations. From Eq. 2.17 it follows that we can evaluate \mathbf{J} by partitions for each projection, $\mathbf{J}^{(p)}$, and subsequently assemble \mathbf{J} according to

$$\mathbf{J} = \begin{bmatrix} \mathbf{J}^{(1)} \\ \mathbf{J}^{(2)} \\ \vdots \\ \mathbf{J}^{(N_p)} \end{bmatrix}. \quad (2.28)$$

For one partition, application of the differential operator to Eq. 2.16 yields

$$\mathbf{J}^{(p)} = \frac{d\hat{\mathbf{v}}^{(p)}}{d\sigma} = \mathbf{X}_v^{(p)} \frac{d}{d\sigma} (\mathbf{S}^{-1}) \mathbf{T} \mathbf{i}_n^{(p)} = \mathbf{X}_v^{(p)} \mathbf{S}^{-1} \frac{d\mathbf{S}}{d\sigma} \mathbf{S}^{-1} \mathbf{T} \mathbf{i}_n^{(p)}. \quad (2.29)$$

Substitution using Eqs. 2.13 and 2.15 results in the final form of the Jacobian partition,

$$\mathbf{J}^{(p)} = \mathbf{X}_v^{(p)} \mathbf{S}^{-1} \mathbf{C}^T \frac{d\mathbf{S}_{\text{dis}}}{d\sigma} \mathbf{C} \varphi_n^{(p)}. \quad (2.30)$$

Because the individual S_{ei} matrices are well separated in S_{dis} , the derivative of S_{dis} is easily evaluated.

Alternatively, the Jacobian matrix can be evaluated by applying the Compensation theorem to a discrete network (96,154). Consider the network in Fig. 2.8(a). The voltage at port 2 (v_2) that results from injection of the current i_1 at port 1 can be written as

$$v_2 = z_{12} i_1, \quad (2.31)$$

where z_{12} is the transfer impedance between ports 1 and 2. Furthermore, assume that for the forward solution we use a first-order FEM that is equivalent to a network of resistors connecting the nodes of the FEM (96), where v_3 is assumed to be the voltage between two neighbouring nodes of the FEM, i.e., the voltage across one network branch of the admittance y . Increasing the admittance of this branch from y to $y+\Delta y$ causes a change in v_2 that can be expressed as

$$v_2 + \Delta v_2 = (z_{12} + \Delta z_{12}) i_1 = v_2 + \Delta z_{12} i_1. \quad (2.32)$$

However, according to the compensation theorem, the initial v_2 can be reestablished if port 3 is paralleled by a current source $i_3 = -\Delta y v_3$, as shown in Fig. 2.8(b). The effect of i_3 on v_2 is denoted by $\Delta v'_2$ and can be expressed as

$$\Delta v'_2 = z_{23'} i_3, \quad (2.33)$$

with port 3' as illustrated in Fig. 2.8(b). For i_3 to reestablish the initial v_2 , its influence must compensate exactly for Δv_2 , i.e.,

$$\Delta v_2 + \Delta v'_2 = \Delta v_2 + z_{23'} i_3 = \Delta v_2 - z_{23'} \Delta y v_3 = 0. \quad (2.34)$$

Solving for Δv_2 and dividing by Δy yields

$$\frac{\Delta v_2}{\Delta y} = z_{23'} v_3. \quad (2.35)$$

For $\Delta y \rightarrow 0$, the port 3' becomes equivalent to port 3 and we find

$$\frac{\partial v_2}{\partial y} = z_{23} v_3. \quad (2.36)$$

This represents a single entry of the Jacobian matrix for the element y and the current pattern i_1 . This method for evaluating J has been shown to be more numerically efficient than the direct method described above (154).

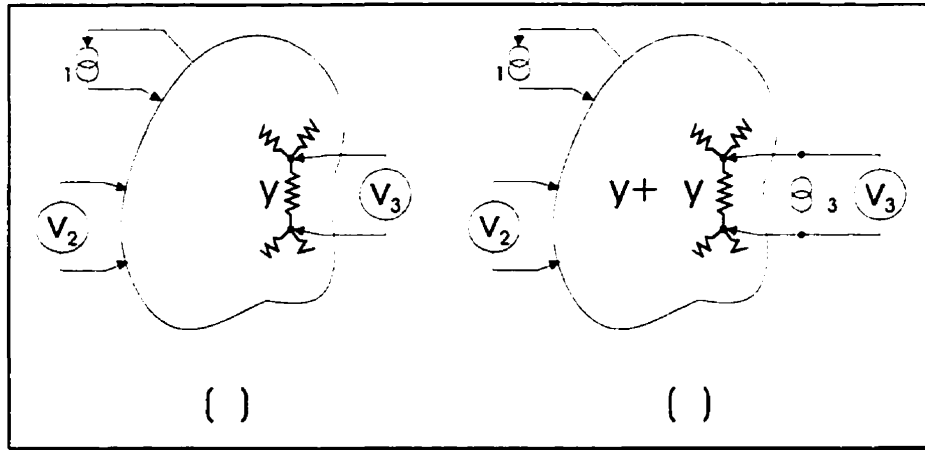


Fig. 2.8:
Illustration of the Compensation theorem method to evaluate the Jacobian matrix. See text for details.

(iv) Regularization

Direct application of the nonlinear optimization techniques outlined above frequently results in unstable numerical behavior or in convergence to a local minimum where the image does not reflect the true conductivities in the body. However, a physically and physiologically meaningful image can be enforced by incorporating *a priori* knowledge in the reconstruction algorithm (3,66). This is often achieved by adding a penalty function P to the initial objective function that assumes large values when undesired behavior occurs, i.e.,

$$\Phi_{\text{reg}} = \Phi + \eta P, \quad (2.37)$$

where η is a positive real constant that controls the relative weight of the penalty function. The simplest form of P is

$$P = (\sigma - \bar{\sigma})^T (\sigma - \bar{\sigma}), \quad (2.38)$$

where $\bar{\sigma}$ is the mean conductivity of the image and equals zero in the case of dynamic imaging (17,66,154). This penalty function imposes a bounding constraint that favors a homogeneous image.

In a more general approach, the penalty function can be expressed as

$$P = \sigma^T W \sigma, \quad (2.39)$$

where W is a positive-definite weight matrix that can, for example, be chosen to impose a continuity constraint that penalizes a large first spatial derivative of σ , or a smoothing constraint that penalizes a large second spatial derivative of σ (66). An approach that effectively limits the spatial frequency content within the image has also been suggested (3). However, all of these penalty functions alter the objective function in the entire conductivity space, including the neighborhood of the global minimum, and are thus likely to result in substantially reduced contrast and blurring of the image, as demonstrated in (3).

(v) Single-step implementations

In general, the solution of nonlinear inverse problems requires an iterative implementation of the techniques described above (96). However, the implementation of iterative optimization techniques is often associated with stability and convergence problems. To overcome this problem, some investigators only perform a single iteration of a Newtonian optimization technique (3,24). Images obtained using this method do not reproduce the full contrast of the conductivity distribution in the body to be imaged, but are more stable than truly iterative implementations.

Other image reconstruction techniques

Numerous other algorithms have been suggested for the reconstruction of EIT images, including the perturbation technique, the double constraint method and Neural Networks (2,78,79,147,154,155). However, none of them has been employed frequently in the literature. Therefore, a detailed discussion of these methods is omitted.

2.4.4 Pulmonary applications of EIT

Monitoring lung inflation

The inflation and deflation of the lungs is ideally suited for EIT monitoring for a number of reasons. First, the electrical impedance of the lungs is known to change significantly with the degree of lung inflation. Furthermore, the reconstruction of dynamic rather than static images is adequate for monitoring a periodic process such as respiration.

Finally, the limited resolution and the two-dimensional nature of today's EIT systems are less critical for the monitoring of ventilation than for other applications because of the approximately cylindrical anatomy of the lungs and their comparatively large size. The feasibility of EIT for monitoring the depth of ventilation has been demonstrated in a number of studies (19,60,136,151).

Pneumothorax and pleural effusion

The influx of extremely resistive air or highly conductive body fluid into the pleural space as a result of pneumothorax or pleural effusion, respectively, causes a substantial change in the electrical tissue properties of the affected area. It would thus seem likely that these conditions could clearly be identified in an EIT image. Unfortunately, static *in vivo* EIT images have proven difficult to reconstruct to date. However, recent progress suggests that static or quasi-static images may soon be available at a resolution that would be sufficient to detect and monitor these disorders (see section 2.4.2) (91,100). It may also be possible to infer the existence of pleural effusions and pneumothoraces from dynamic EIT images because these conditions are likely to cause unilateral ventilatory disturbances.

Detection of increased lung water

A recent studies investigated the utility of EIT to detect pulmonary edema induced by instillation of oleic acid in laboratory animals (98) and found that severe bilateral and unilateral edema can be reflected adequately in the EIT images. Furthermore, increased lung water was reflected in quasi-static EIT images in patients suffering from pulmonary hypertension (100,124). With the recent progress in (quasi-)static and three-dimensional EIT (91,94,100), it is likely that the resolution and specificity of EIT for monitoring lung water will be further increased in the near future. A distinction between increased blood volume in the pulmonary circulation and pulmonary edema, i.e., fluid entering the alveolar spaces, is not possible at present. However, we may speculate that as multifrequency and complex-valued EIT images become more common and better

understood, they may provide a means of distinction between different mechanisms of increased lung water.

Other pulmonary applications

Many disease processes cause substantial biochemical and structural changes in the lungs. It is intriguing to speculate to what extent these alterations would be reflected in static, three-dimensional and complex-valued images that are obtained over a wide range of frequencies. For example, substantial structural changes have occurred in the lungs of patients suffering from emphysema and COPD that may alter the complex electrical tissue properties over a certain range of frequencies. Similarly, carcinogenic tissues may become detectable in complex-valued images. From today's perspective, the ability to detect such disease processes would not only require significant improvements in the EIT hardware technology, but also necessitate exhaustive clinical research in order to permit adequate understanding and interpretation of these EIT images.

2.4.5 Non-pulmonary applications of EIT

The following non-pulmonary applications of EIT are listed for the sake of completeness.

(i) Gastric applications

EIT has repeatedly been used to non-invasively measure the transfer times of food through parts of the digestive system and to monitor gastric secretions and gastro-esophageal reflux (7,14,19,89). In these applications, EIT replaced invasive techniques involving radioactive tracers.

(ii) Cancer detection

Carcinogenic tissues have electrical properties that differ substantially from those of adipose tissues (42,43), so that EIT may provide a non-invasive, painless scanning tool for many forms of cancer including breast carcinomas (74,109).

(iii) Cardiological applications

EIT has been suggested as a non-invasive method to estimate the stroke volume, cardiac output and blood flow (20,37).

(iv) Dose monitoring for microwave hyperthermia therapy

Several studies have investigated the use of EIT for dose monitoring during microwave hyperthermia treatment for cancer patients (5,16,27,28,53,101).

3.

PULMONARY MONITORING

Pulmonary monitoring, i.e., the computation of clinically valuable parameters from pressure and flow data in real time, is an important aid for the management of patients suffering from severe pulmonary disease in the ICU. The first section of this chapter describes a computer model of a spontaneously breathing or assist-ventilated patient that forms a methodological basis for the subsequent sections. In section 3.2, this model is used to investigate the susceptibility of conventional measurement techniques for $PEEP_i$ and W_{insp} to two important confounding factors, and to investigate a physiological hypothesis that explains inconsistencies between static and dynamic measurements of $PEEP_i$. An adaptive filter that attenuates the adverse effects of cardiogenic oscillations on measurements of $PEEP_i$ and W_{insp} is developed in section 3.3. The performance of this filter is demonstrated both in simulated data and in pressure and flow signals obtained from four intensive care patients. Finally, in section 3.4 the computer model developed in section 3.1 is used to study the interactions between flow-limited patients and an assisting flow-triggered pressure support ventilator.

3.1 A computer model of the spontaneously breathing patient

3.1.1 Motivation

This section describes a comprehensive model of respiratory mechanics that permits the simulation of patients breathing spontaneously or with the support of an assisting ventilator. The motivation to develop such a model initially originated from the insight that several measurement techniques that are frequently used in clinical practice have not been properly validated and are extremely difficult to validate in patients. In contrast, the validation of measurement techniques is comparatively easy using a computer model, since many variables that are inaccessible in patients become available in simulation.

However, the range of possible applications of the model described in this section exceeds the validation of measurement techniques. For example, it can be used to test hypotheses in a very controlled environment by studying the exact same population of patients under two sets of conditions that differ only in the value of a single parameter. The modified parameter can either be part of the model, e.g., the viscoelasticity of the lungs, or represent a setting or design aspect of an assisting ventilator, e.g., the trigger threshold, pressure support level or response time of a valve. The model can thus be valuable to address both physiological questions and ventilator design criteria. Furthermore, this computer model could be a valuable teaching tool.

3.1.2 Implementation

Overview

An overview of the nonlinear, viscoelastic model of the actively breathing subject is shown in Fig. 3.1. The pressure drops across each passive compartment of the respiratory system and the endotracheal tube (ETT) were computed as functions of tracheal flow (\dot{V}) and total lung volume (V). A predefined neural output signal was used to generate a volume- and flow-dependent muscular pressure (P_{musc}). The individual pressures were summed as illustrated in Fig. 3.1 to yield P_{aw} . P_{aw} was fed back into an active numerical

controller that controlled \dot{V} and/or P_{aw} according to the desired mode of breathing (see *Determination of flow*). For all studies performed to date, the mean and standard deviation (SD) of each model parameter were chosen according to the literature to generate a population of 100 random hypothetical adult patients with severe COPD (Table 3.1). However, the model could easily be parameterized to simulate different diseases, normal subjects, infants or neonates, provided that sufficient data are tabulated in the literature.

The model was implemented using the Matlab 4.2/Simulink 1.3 mathematical and simulation software package (The MathWorks Inc., Natick, MA). It was solved using Matlab's fourth order Runge-Kutta integration routine with a precision setting of 10^{-6} . Complete diagrams of the Simulink implementation of the model are provided in the appendix.

Lung and chest wall

The nonlinear static volume-pressure (V-P) relationship of the lung was modeled using an exponential equation (125) of the form

$$V = A_L - B_L e^{-K_L P_{cl,L}}, \quad (3.1)$$

where $P_{cl,L}$ is the static elastic recoil pressure of the lungs. The values of the parameters A_L , B_L and K_L were set to the ones reported by Pare *et al.* (103) for COPD patients with an emphysema score of greater than 20 (see Table 3.1).

The static V-P curve of the chest wall was modeled by an analogous equation,

$$V = A_{cw} + B_{cw} e^{K_{cw} P_{cl,cw}}, \quad (3.2)$$

where $P_{cl,cw}$ is the static elastic recoil pressure of the chest wall. This equation was fit to previously reported data for the elastic recoils of the rib cage and the passive diaphragm in normal supine subjects (133) to determine A_{cw} , B_{cw} and K_{cw} ($V = 1.36 + 2.31.e^{0.05.P}$, $r^2 = 0.94$). These parameters were not modified for the COPD patients, since available evidence suggests that the chest wall V-P relationship is not altered in COPD (57).

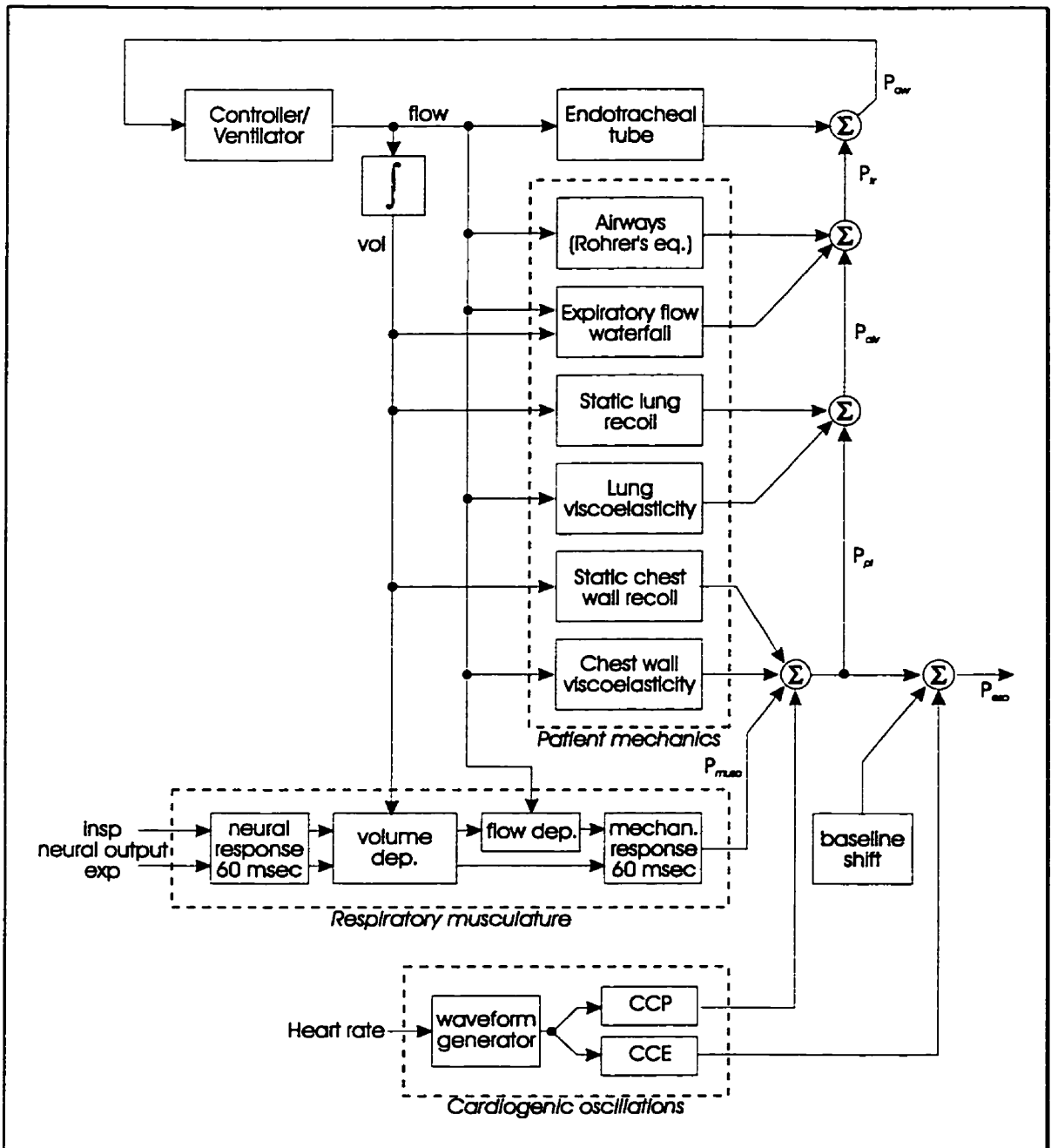


Fig. 3.1
Schematic representation of the computer model used to simulate patients breathing spontaneously or with the support of an assisting ventilator.

Table 3.1:
Means and standard deviations of the parameter values used to simulated a population of 100 COPD patients.

| Compartment | Parameter (units) | Mean | SD | Source / comment |
|--------------------------|---|-------|-------|---|
| Lung | A_L (L) | 7.41 | 1.18 | Pare <i>et al.</i> (103), Group III |
| | B_I/A_L | 1.02 | 0.44 | Pare <i>et al.</i> (103), Group III |
| | K_L (cmH ₂ O ⁻¹) | 0.249 | 0.079 | Pare <i>et al.</i> (103), Group III |
| | $R_{2,L}$ (cmH ₂ O'sL ⁻¹) | 8.75 | 1.21 | Guerin <i>et al.</i> (57) |
| | $T_{2,L}$ (s) | 1.4 | 0.19 | Guerin <i>et al.</i> (57) |
| Chest wall | A_{CW} (L) | 1.36 | 0.2 | fit to Smith and Loring (133) |
| | B_{CW}/A_{CW} | 1.699 | 0.3 | fit to Smith and Loring (133) |
| | K_{CW} (cmH ₂ O ⁻¹) | 0.05 | 0.01 | fit to Smith and Loring (133) |
| | $R_{2,CW}$ (cmH ₂ O'sL ⁻¹) | 3.25 | 0.6 | Guerin <i>et al.</i> (57) |
| | $T_{2,CW}$ (s) | 2.49 | 0.48 | Guerin <i>et al.</i> (57) |
| Airways | $K_{aw,1}$ (cmH ₂ O'sL ⁻¹) | 5.03 | 0.45 | Guerin <i>et al.</i> (57) |
| | $K_{aw,2}$ (cmH ₂ O's ² L ⁻²) | 2.69 | 0.63 | Guerin <i>et al.</i> (57) |
| | χ/χ_0 | 3 | 0.25 | to produce typical FEV ₁ & FVC |
| Endotracheal tube | Diameter (mm) | 8 | 0.5 | empirical |
| Neural output | Breath Rate (min ⁻¹) | 21.1 | 5.9 | Appendini <i>et al.</i> (6) |
| | duty cycle | 0.41 | 0.04 | Appendini <i>et al.</i> (6) |
| | rate of increase (cmH ₂ O's ⁻¹) | 20 | 5 | to match V _t from (6) |
| | P_{exp} (cmH ₂ O) | 4 | 2 | see text |
| Noise | Heart rate (min ⁻¹) | 100 | 20 | empirical |
| | C_{CP} (cmH ₂ O) | 0.5 | 0.2 | empirical |
| | C_{CE} (cmH ₂ O) | 3 | 1 | empirical |
| | P_{es} shift (cmH ₂ O) | 3 | 2 | empirical |

Stress adaptation of both the lung and the chest wall was modeled by assigning a Maxwell body in parallel to their respective static elastances (Fig. 3.1). The parameter values for the Maxwell bodies ($R_{2,L}$, $R_{2,CW}$, $\tau_{2,L}$, and $\tau_{2,CW}$) were chosen according to recently reported data for severe COPD patients (57) (see Table 3.1). Stress adaptation can be interpreted to reflect time constant inhomogeneities within the lung, viscoelastic tissue properties or a combination of the two, since both phenomena have been shown to have identical mathematical representations (132).

Airways

The pressure drop across the airways during inspiration was modeled using Rohrer's equation (116),

$$\Delta P_{aw} = K_{aw,1} \dot{V} + K_{aw,2} \dot{V} |\dot{V}|, \quad (3.3)$$

and previously reported values for $K_{aw,1}$ and $K_{aw,2}$ were used (57). Unfortunately, this equation is not sufficient to describe the behavior of the airways during expiration in the presence of flow limitation. While the mechanisms of expiratory flow limitation have been extensively investigated (71,83), an empirical description of flow limitation in the lung as a whole has not been previously proposed. I therefore incorporated an empirical description into the model such that FEV₁, FVC and PEEP_i assumed values similar to those reported in the literature (6). An exponential function of flow with a hyperbolic volume dependence was employed to account for the pressure drop across the site of expiratory flow limitation. The resulting equation for the expiratory pressure drop across the airways,

$$\Delta P_{aw} = K_{aw,1} \dot{V} + K_{aw,2} \dot{V} |\dot{V}| + \alpha \left(e^{\beta(V/V_0)^{\chi_0} \dot{V}} - 1 \right), \quad (3.4)$$

was then fit to the family of IVPF curves shown by Lambert (83), setting $K_{aw,1}$ equal to Lambert's airway resistance for very small flows. As illustrated in Fig. 3.2, Eq. 3.4 was able to reproduce the principal characteristics of the IVPF curves when constants $K_{aw,2}$, α , β_0 , and χ_0 equaled $0.34 \text{ cmH}_2\text{O}\cdot\text{L}^{-2}\cdot\text{s}^2$, $1.83\cdot 10^{-4} \text{ cmH}_2\text{O}$, $1.227 \text{ L}^{-1}\cdot\text{s}$ and 1.823, respectively, and the volume V_0 was set to TLC. The expiratory flow limitation mechanism was placed in parallel with the block representing Rohrer's equation (Fig.

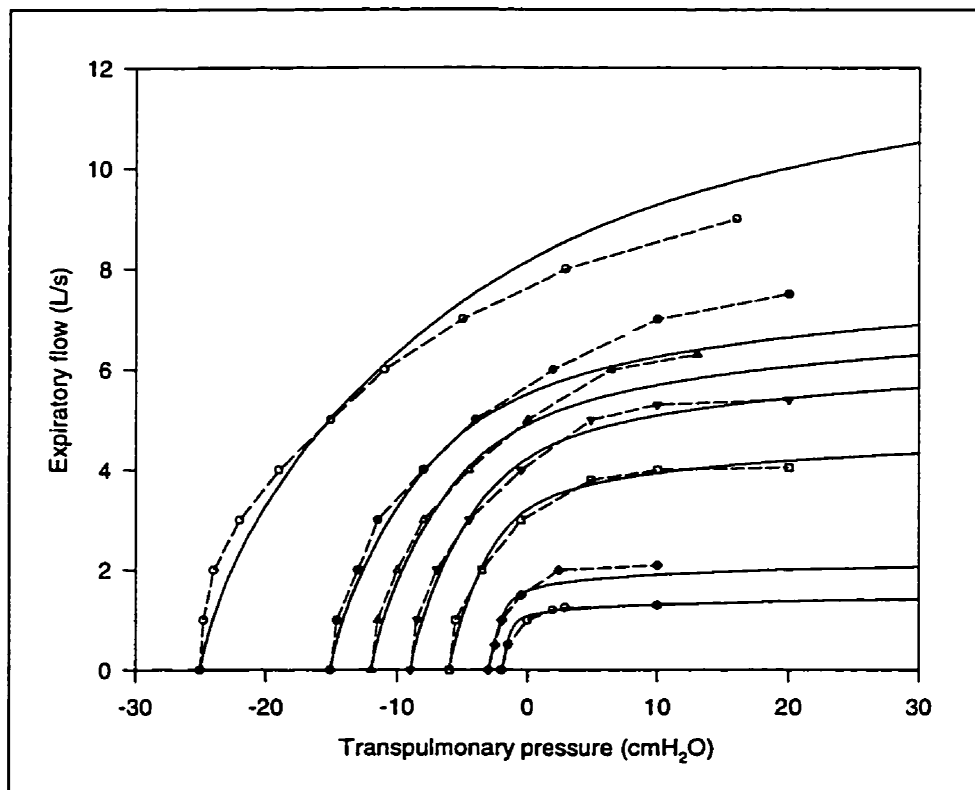


Fig. 3.2:

Iso-volume pressure-flow relationships of the airway compartment during expiration. The empirical representation used in the model (solid lines, see text for details) reproduced the principal features of the data by Lambert *et al.* (83) (dashed lines).

3.1). A 100 msec time constant was assigned to the waterfall compartment in order to produce the supramaximal flow transients at the onset of expiration.

Flow limitation is more pronounced in COPD patients. In my model, FEV_1 , FVC and $PEEP_i$ assumed appropriate values for COPD patients and flow limitation during tidal breathing was achieved (Fig. 3.3) when χ was raised to $\chi/\chi_0 = 3$. In this case, the average simulated patient was described by $FEV_1 = 0.81$ L, $FVC = 2.36$ L, $FEV_1/FVC = 34\%$, $PEEP_{i,stat} = 4.8$ cmH₂O and $PEEP_{i,dyn} = 4.5$ cmH₂O. In contrast, flow limitation during tidal breathing could not be achieved when β was raised while χ was maintained equal to χ_0 .

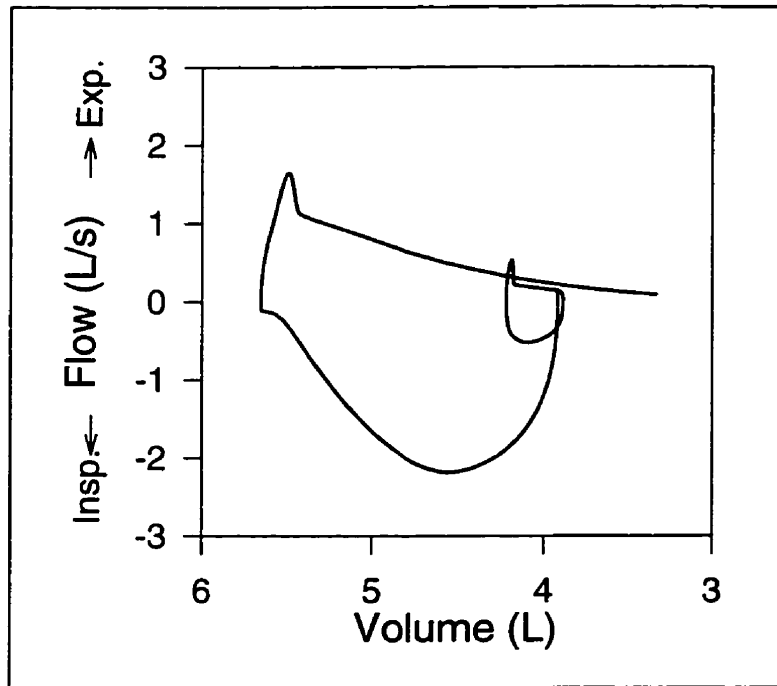


Fig. 3.3:

Sample flow-volume loop of the average subject for one tidal breath with a passive expiration and a subsequent forced expiratory maneuver with a peak expiratory effort of 200 cmH₂O . The expiratory flow amplitude is almost independent of the magnitude of the patient's expiratory effort, indicating that expiratory flow limitation during tidal breathing was achieved.

Patient effort

The central neural output to the respiratory musculature (P_{neur} , in pressure units) is modulated by a variety of factors, such as the physiological needs of the body as well as psychological and voluntary factors that are beyond the scope of this model. For all studies described in this chapter, inspiratory and expiratory P_{neur} were assumed to be piecewise linear as shown in Fig. 3.4. Breathing frequency and duty cycle (T_i/T_{tot}) were chosen according to the data of Appendini *et al.* for spontaneously breathing patients with severe COPD in acute respiratory failure (6). Inspiratory P_{neur} was assumed to increase at a constant rate up to an end-inspiratory plateau of 200 ms. The rate of increase of P_{neur} was chosen such that when all other model parameters were set to their population means (Table 3.1), a tidal volume of 330 mL was achieved (6). At the beginning of expiration, the inspiratory activity decreased linearly to zero by 200 msec. Subsequently, expiratory

P_{neur} increased linearly to an end-expiratory plateau of 200 msec. The expiratory peak value of P_{neur} (P_{exp}) was set to 4 ± 2 cmH₂O, which approximately averages the values reported in the recent literature (6,85,99). Expiratory P_{neur} linearly returned to zero over the last 200 msec of each tidal breath.

In order to reproduce the length-tension relationship that has been reported for the diaphragm (128), a bi-exponential volume-dependence was employed for inspiratory P_{musc}/P_{neur} , as shown in Fig. 3.5 (solid line). The volume dependence of P_{musc} during maximal inspiration and expiration has been shown to be approximately inverse (4). In the absence of a more detailed description, a mirrored version of the bi-exponential function was used to implement the volume dependence of P_{musc}/P_{neur} during expiration (dashed line, Fig. 3.5). For both inspiration and expiration, P_{musc}/P_{neur} was scaled to unity at FRC.

The flow dependence of the inspiratory P_{musc}/P_{neur} was implemented according to the model of Younes and Riddle (113,159) (see Fig. 3.1). Since flow dependence of the expiratory musculature has not been quantitatively described in the literature, this feature was omitted from the model. Both the inspiratory and expiratory muscles were assigned a neural response time constant of 60 msec and a mechanical response time constant of 100 ms (113,159).

In some situations, it may be desirable to append a forced expiratory maneuver to a sequence of spontaneous breaths. When this was the case, the neural output was altered as shown on the right side of Fig. 3.4. In order to simulate truly maximal effort during the forced expiration maneuver, the peak values of P_{neur} were set to 100 cmH₂O for inspiration and to 200 cmH₂O for expiration. The P_{neur} waveform was altered such that these plateau values were reached more rapidly than in the tidal breaths, namely within 500 msec. The inspiratory time was doubled during the forced breath, and the total expiratory time was fixed at 8 sec.

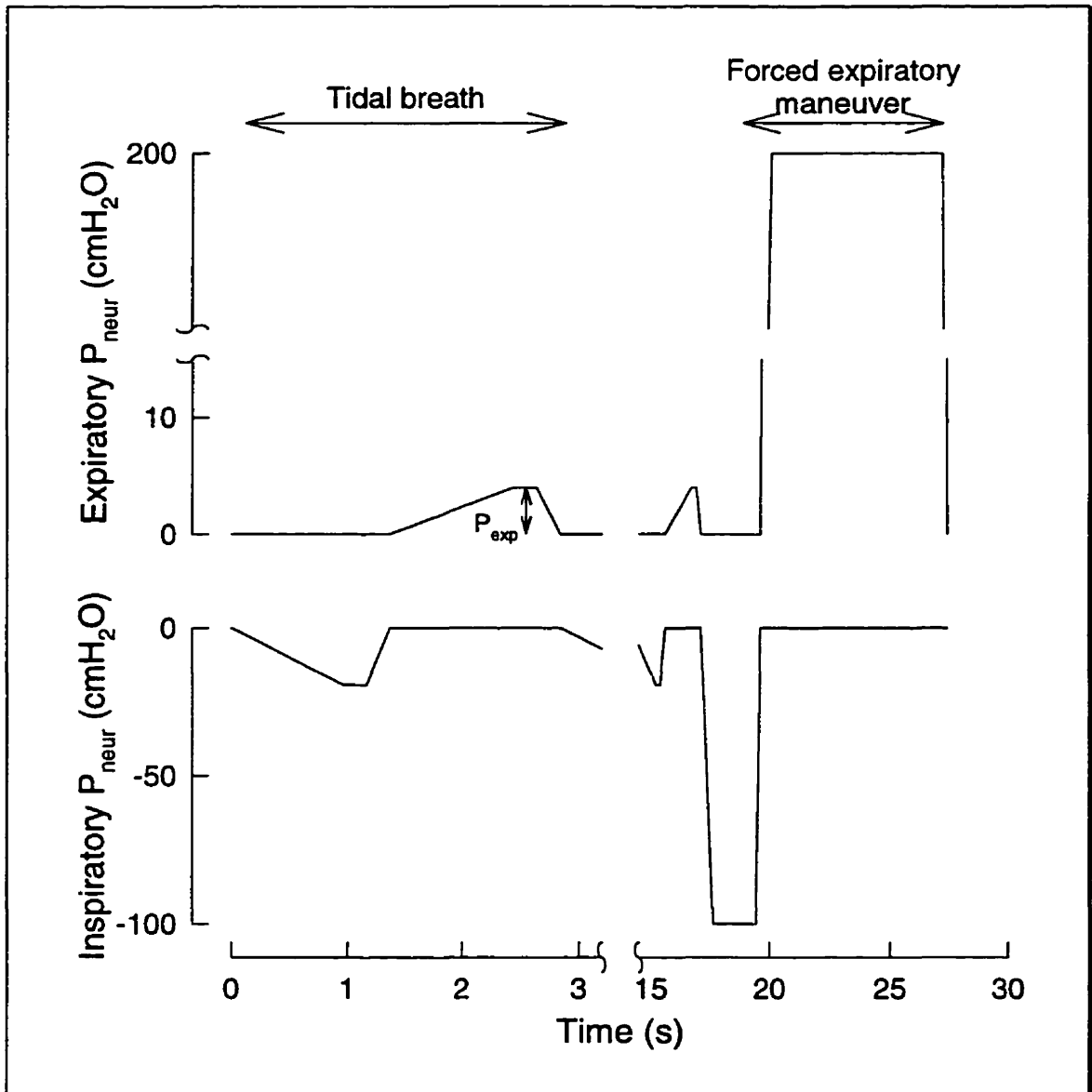


Fig. 3.4:

Time course of expiratory (top) and inspiratory (bottom) neural output with all neural output parameters adjusted to their population means (see text for details) for one tidal breath (left) and a deep inflation/forced expiration maneuver (right). The neural output was expressed in units of the driving pressure it generates at functional residual capacity under isovolume conditions.

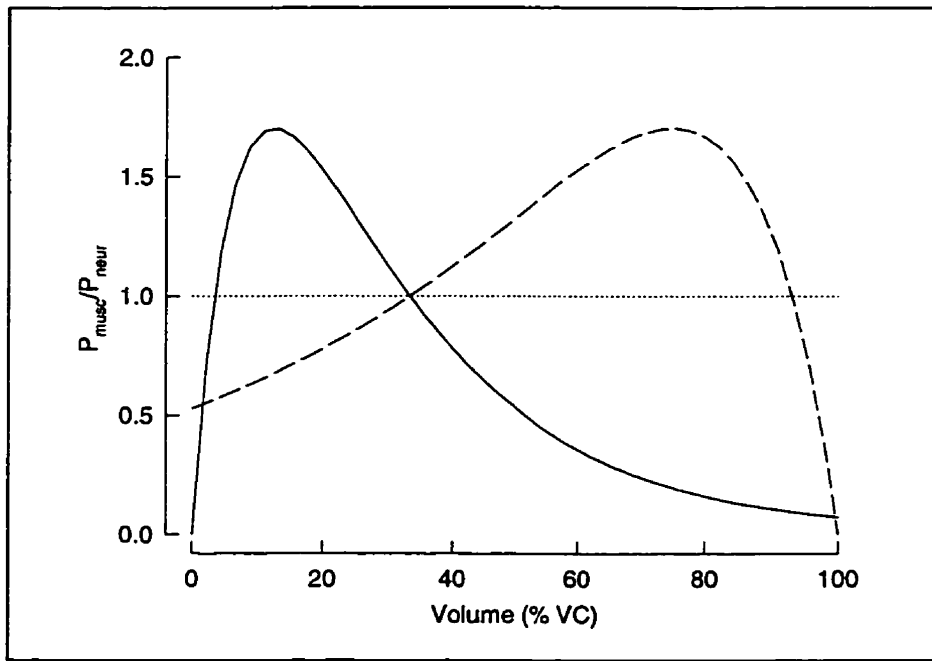


Fig. 3.5:
Volume dependence of the inspiratory (solid line) and expiratory (dashed line) muscles used in the model simulation. See text for details.

Cardiogenic oscillations

A waveform for the cardiogenic oscillations was generated by passing a train of impulses representing the basic heart beat through a linear low-pass filter with a cutoff frequency of 100 Hz and a resonance at 10 Hz. This filter was adjusted such that at the average heart rate, the mean value of the cardiogenic oscillation pressure (P_{CGO}) equaled zero. The effect of the beating heart on pleural pressure was modeled by multiplying P_{CGO} with a cardio-pleural coupling factor (C_{CP}) and adding the result to P_{pl} (Fig. 3.1). However, strong cardiogenic oscillations on P_{es} concurrent with mild cardiogenic oscillations on flow and P_{aw} , as often observed under true physiological conditions, could only be achieved after a second, cardio-esophageal coupling factor (C_{CE}) was introduced between P_{CGO} and P_{es} (Fig. 3.1). Both the heart rate and the values for C_{CP} and C_{CE} were randomized as shown in Table 3.1.

Endotracheal tube

The significant flow resistance of the ETT connecting the ventilator to the patient's airway opening had to be taken into account in the model. The pressure drop across ETTs has been shown to fit the equation

$$P_{ETT} = \kappa \cdot \dot{V}^{\nu}, \quad (3.5)$$

where κ and ν depend on the tube dimensions (59). An analysis of the values for κ and ν documented in the literature for ETTs from 7.5 to 9 cm diameter (59) showed that ν remains roughly constant at a mean value of 1.738, while the variations of κ with the nominal tube diameter, d , fit the equation

$$\kappa = 301 \frac{\text{cmH}_2\text{O}\cdot\text{s}}{\text{L}} \cdot e^{-0.489\text{cm}^{-1}\cdot d}. \quad (3.6)$$

When intubated patients were simulated, these equations were used to compute P_{ETT} from the randomly chosen ETT diameter (see Table 3.1) and flow. The effects of variations in tube length and of reductions in the tube diameter due to depositions have not been described quantitatively in the literature and were neglected.

Determination of flow

To date, four modes of breathing have been implemented, namely spontaneous breathing, CPAP, ACV and PSV (see section 2.3). In the most simple cases of spontaneous breathing and CPAP, \dot{V} was adjusted such that P_{aw} remained constant at atmospheric pressure or assumed a constant positive value, respectively (Fig. 3.6a).

During flow-triggered PSV (Fig. 3.6b), P_{aw} was maintained equal to a chosen PEEP level during expiration. When inspiratory flow became greater than a preset trigger threshold, the ventilator was switched to its inspiratory phase, and the setpoint for P_{aw} was raised above PEEP level by a preset pressure support level. When the inspiratory flow fell to a value less than a preset off-trigger threshold, the setpoint for P_{aw} was lowered back to PEEP level. The transducer measuring flow was modeled to have single-pole behaviour with a cutoff frequency of 20 Hz, and the ventilator was allowed to switch between the two pressure setpoints with a time constant of 20 ms.

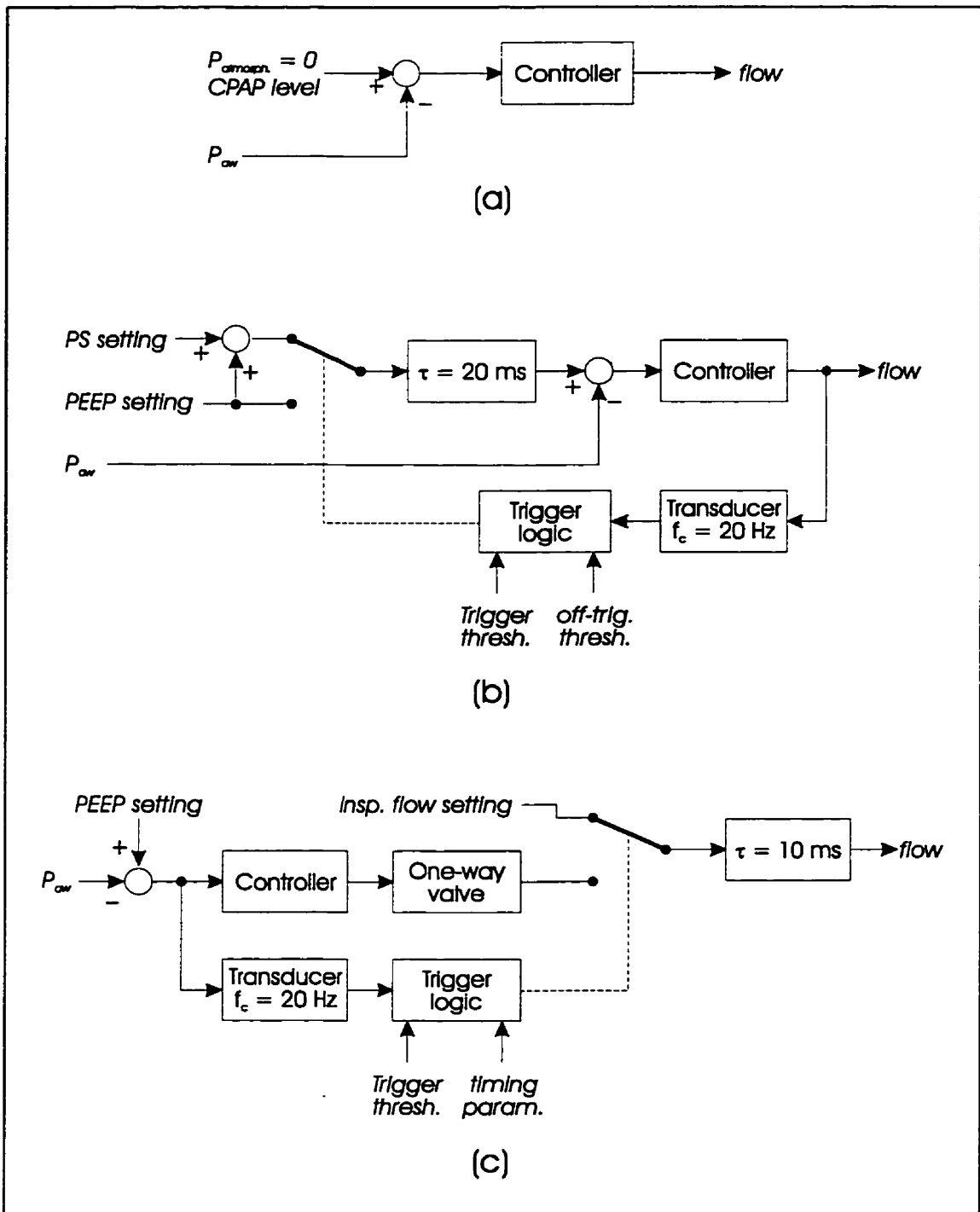


Fig. 3.6:
Feedback of P_{aw} to control inspiratory flow according to a chosen mode of breathing. (a) Spontaneous breathing and CPAP, (b) Pressure Support Ventilation, (c) Assist Control Ventilation.

Pressure-triggered ACV was simulated using the ventilator model shown in Fig. 3.6c. During expiration, PEEP was applied as described for PSV. However, a one-way valve was implemented such that no inspiratory flow was possible during the ventilator's expiratory phase. At the onset of an inspiratory effort, the patient thus inspired against an occlusion, and P_{aw} dropped rapidly. When $PEEP - P_{aw}$ became greater than a preset threshold value, the ventilator was switched to inspiratory mode. Unlike the other modes of breathing described above, inspiratory flow then became independent of P_{aw} and was set to a constant rate. After a preset inspiratory time had passed, the ventilator was switched back to expiratory mode. The trigger was disabled for a preset minimum expiratory time before a new inspiration was allowed. The pressure transducer measuring P_{aw} was modeled to have a cutoff frequency of 20 Hz, and a small single time constant of 10 ms was used to model the mechanical properties of the ventilator and to assure numerical stability.

3.1.3 Performance

Sample traces

To illustrate the performance of this model, eight breaths were simulated for the average COPD patient, i.e., with all parameters adjusted to their population means (see Table 3.1), for the following modes of breathing.

- Spontaneous breathing;
- CPAP at a level of 5 cmH₂O;
- pressure-triggered ACV, constant inspiratory flow of 0.5 L/s, inspiratory time of 1 s, trigger threshold at 2 cmH₂O, plus PEEP of 5 cmH₂O; and
- flow-triggered PSV (Fig. 3.6b) at 5 cmH₂O plus 5 cmH₂O PEEP, trigger threshold at 0.05 L/s, off-trigger at 0.02 L/s.

In all four cases, the first six breaths were discarded to assure that a steady state had been reached and dynamic hyperinflation was fully developed. The level of dynamic hyperinflation and V_t was evaluated from the volume traces of breaths seven and eight,

and $PEEP_{i,stat}$ was evaluated as the difference between the sum of the static elastic recoil pressures of lung and chest wall and P_{aw} at the seventh end-expiration.

The left panels of Fig. 3.7 show sample traces of the simulated flow, volume, P_{aw} and P_{es} waveforms during spontaneous breathing. At the onset of expiration, the simulated patient exhibited the characteristic supramaximal flow transients that are frequently observed in flow limited COPD patients. The patient was dynamically hyperinflated with an end-expiratory lung volume of 477 mL above FRC, while $PEEP_{i,stat}$ and V_t amounted to 4.72 cmH₂O and 341 mL, respectively. Cardiogenic oscillations were present both on P_{es} and, to a lesser extent, on the flow trace. P_{aw} showed its greatest deflections at the onset of expiration when the highly nonlinear expiratory flow limitation phenomenon began to dominate the model behavior. With an rms-value of less than 0.05 cmH₂O, these deflections were negligible compared to the amplitudes of physiologic pressures associated with respiration.

The right-hand side panels of Fig. 3.7 display traces for the same patient during CPAP ventilation. In this case, the patient became considerably more hyperinflated with an end-expiratory lung volume of 710 mL above FRC. The tidal volume was slightly increased to 380 mL, and $PEEP_{i,stat}$ was reduced to 1.8 cmH₂O.

Fig. 3.8 shows equivalent traces for ACV and PSV ventilation. During ACV (left panels of Fig. 3.8), inspiratory flow was fixed and did not contain any cardiogenic oscillations. However, cardiogenic oscillations could be observed on P_{aw} in this case. At the onset of inspiration, the patient inspired against an occlusion for a period of roughly 300 ms before the ventilator was triggered and inspiratory flow was initiated. The end-expiratory lung volume ranged 841 mL above FRC, while $PEEP_{i,stat}$ equaled 2.9 cmH₂O. In the case of flow-triggered PSV, the simulated patient achieved a V_t of 513 mL at an end-expiratory lung volume of 867 mL above FRC and a $PEEP_{i,stat}$ of 3.1 cmH₂O.

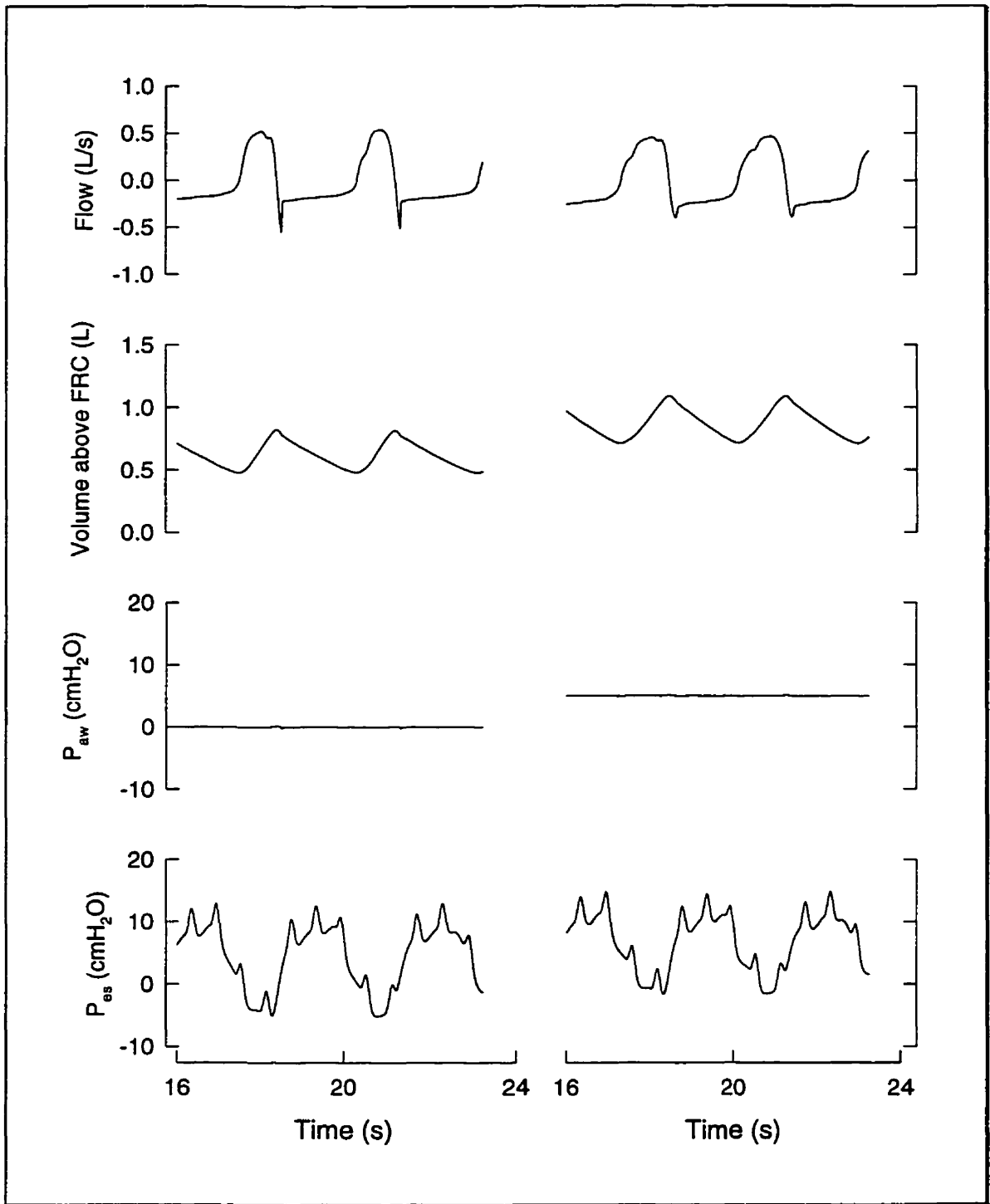


Fig. 3.7:
Sample traces of the simulated waveforms of flow, volume above FRC, P_{aw} and P_{es} .
Left: Spontaneous breathing; right: Continuous Positive Airway Pressure (CPAP).

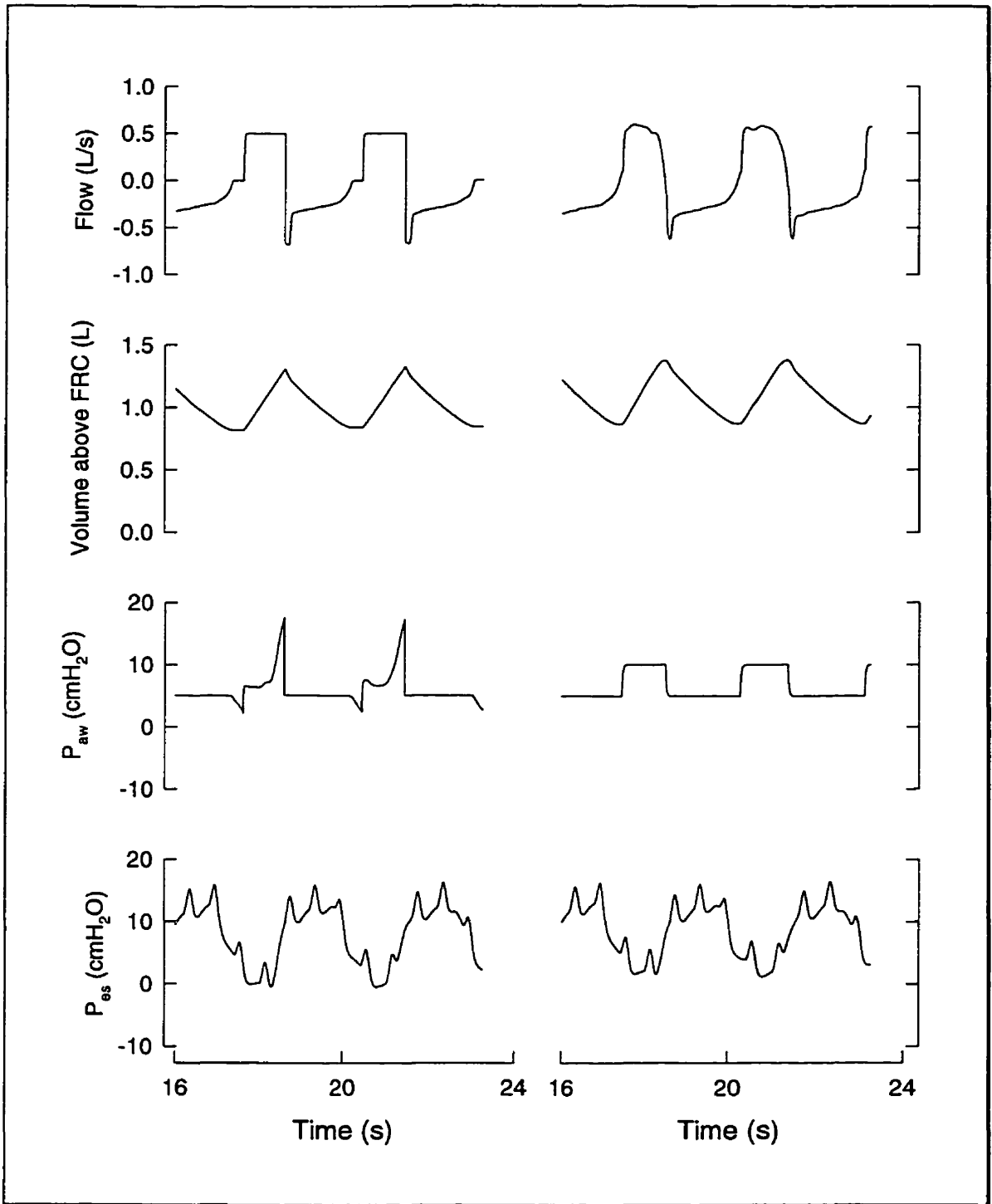


Fig. 3.8:
**Sample traces of the simulated waveforms of flow, volume above FRC, P_{aw} and P_{es} .
 Left: Assist-Control Ventilation (ACV); right: Pressure Support Ventilation (PSV).**

Pulmonary function measurements

In a second test experiment, a population of 100 COPD patients was generated with the specific parameter values drawn randomly from normal distributions having the means and standard deviations shown in Table 3.1. For each patient, six spontaneous breaths and a subsequent forced expiratory maneuver were simulated. To accelerate convergence of the simulation towards a stable breathing pattern, an estimate of the expected dynamic hyperinflation was employed as the initial lung volume for these patient simulations. The change in end-expiratory lung volume between breaths four and five averaged 1.2% of the dynamic hyperinflation volume at the end of breath five, indicating that steady state breathing had essentially been achieved and dynamic hyperinflation was completely developed.

For each patient, V_t was then evaluated as the volume inspired in breath six, and \dot{V}_e was computed by multiplying V_t by the patient's RR. FEV₁ and FVC were evaluated as the volumes expired over the first second and the over the full eight seconds of the forced expiratory maneuver. The means and standard deviations of all four

Table 3.2:
Means and standard deviations of pulmonary function data obtained from the population of 100 simulated COPD patients.

| Parameter | Value | Units |
|-----------------------|-----------------|---------------------|
| V_t | 0.34 ± 0.19 | L |
| \dot{V}_e | 6.8 ± 3.1 | L·min ⁻¹ |
| FEV ₁ | 0.82 ± 0.31 | L |
| FVC | 2.34 ± 0.55 | L |
| FEV ₁ /FVC | 33.8 ± 6.0 | % |

parameters are given in Table 3.2 and were in good agreement with the ones reported in the literature for COPD patients (6,57,107).

3.1.4 Discussion

In this section, I have described a comprehensive computational model of the actively breathing patient that can be used to simulate spontaneously breathing patients as well as patients breathing with the support of an assisting mechanical ventilator. Computer simulations are particularly well-suited for many tasks in biomedical research because they provide access to variables that are impossible to measure in patients and because the simulated experimental conditions can be manipulated at will. This allows the effects of various factors to be evaluated independently of all others. Also, computer simulations allow an essentially unlimited number of subjects to be studied, and under conditions that would be unacceptable in real patients. Indeed, with the growing awareness of the ethical issues involved in human and animal experimentation, we may expect computer simulations to play an increasingly important role in future biomedical research.

The results of any computer simulation are always open to question in that the underlying model will never completely reproduce human physiology. However, the structure and parameters used for this model were taken from the recent literature wherever possible, although some aspects of the model required extrapolation of published data (such as the formula used for expiratory flow limitation, Eq. 3.4). The pressure and flow waveforms and the values of FEV₁ and FVC obtained when simulating spontaneously breathing patients were consistent with clinical observations in patients. Similarly, changes in the ventilator settings during assisted modes of ventilation produced changes in pressure and flow waveforms and ventilation parameters that were in accordance with clinical observation and the literature. However, the waveforms of flow and/or P_{aw} appeared idealized compared to clinical data during assisted modes of ventilation because the simulated ventilators provided much faster rise and fall times and controlled the inspiratory flow and/or P_{aw} with much greater accuracy than commercial clinical ventilators.

The model described in this section is based on general respiratory physiology and is thus not specific to the study of any particular disease. However, the model parameters to date have always been set to represent a population of COPD patients (Table 3.1). This disease group was chosen because dynamic hyperinflation is generally well developed in COPD patients. Furthermore, the model parameters could be drawn from a vast literature, since COPD has received great attention in the clinical and respiratory mechanics literature.

In its present form, my model has a multitude of uses. The remainder of this chapter describes research that I have conducted using this model to analyse measurement and data processing techniques for pulmonary monitoring, to address physiological questions, and to investigate the synchronization between patient and ventilator during PSV. Other potential applications as well as possible extensions to the model that would further increase its range of uses are discussed briefly in section 5.3.

3.2 Quantitative assessment of measurement techniques for intrinsic PEEP and work of breathing

3.2.1 Motivation

In dynamically hyperinflated patients in the ICU, it would be of great benefit to be able to automatically assess $PEEP_{i,dyn}$ and W_{insp} breath-by-breath using computerized monitoring equipment. Although this is straightforward in principle (see section 2.2.3), the breath-by-breath estimation of $P_{es,0}$, which is used to compute both $PEEP_{i,dyn}$ and W_{insp} , is complicated in practice by cardiogenic oscillations on P_{es} . Furthermore, any expiratory muscle activity that might be present at the end of a breath can potentially cause overestimation of $P_{es,0}$ and hence corrupt measurements of $PEEP_{i,dyn}$ and W_{insp} . A quantitative analysis of the measurement errors due to cardiogenic oscillations and expiratory muscle activity requires knowledge of the true values of $PEEP_{i,dyn}$ and W_{insp} , which is essentially impossible in patients. I therefore decided to investigate these measurement errors using the computer model described in the previous section, where the true values of $PEEP_{i,dyn}$ and W_{insp} are known accurately and confounding factors can be precisely controlled.

As described in section 2.2.3, $PEEP_i$ can also be measured under static conditions. $PEEP_{i,dyn}$ is often considered a reasonable approximation of the value of $PEEP_{i,stat}$ (107,119), although recent studies indicate that $PEEP_{i,dyn}$ can substantially underestimate $PEEP_{i,stat}$ (62,88,107). Taking advantage of the computer model described in section 3.1, I further investigated the hypothesis that time constant inhomogeneities and/or tissue viscoelasticity are responsible for the discrepancies observed between $PEEP_{i,dyn}$ and $PEEP_{i,stat}$ during severe airway obstruction (62,88).

3.2.2 Methods

Protocol

To test the sensitivity of measurement techniques for $PEEP_{i,dyn}$ and W_{insp} to cardiogenic oscillations and expiratory muscle activity, a Monte-Carlo simulation of a population of 100 COPD patients was performed as described above (see *Pulmonary function measurements* in section 3.1.3). Each patient was simulated in four configurations: (a) with neither expiratory effort nor cardiogenic oscillations (C_{CE} , C_{CP} , and $P_{exp} = 0$; Control); (b) with P_{exp} as shown in Table 3.1 and no cardiogenic oscillations; (c) with no expiratory effort and C_{CE} and C_{CP} as shown in Table 3.1; and (d) with both expiratory effort and cardiogenic oscillations, i.e., with all parameters as shown in Table 3.1. Finally, to investigate whether increased time constant inhomogeneities alter the ratio of $PEEP_{i,dyn}$ to $PEEP_{i,stat}$ as previously suggested (62,88), the control experiment was repeated with the model parameters altered such that the effects of stress adaptation in the lung were amplified, i.e., simulating a more heterogeneous and/or viscoelastic lung (e). This was achieved by multiplying $R_{2,L}$ by a factor of five, i.e., setting its mean value to $43.75 \text{ cmH}_2\text{O}\cdot\text{L}^{-1}\cdot\text{s}$.

All patients were simulated without any ventilatory support and without an ETT. Each simulation consisted of six spontaneous breaths and a subsequent forced expiratory maneuver. An estimate of the expected dynamic hyperinflation was employed as the initial lung volume for each patient simulation to accelerate convergence of the simulation towards a stable breathing pattern. The change in end-expiratory lung volume between breaths four and five averaged 1.2% of the dynamic hyperinflation volume at the end of breath five, indicating that steady state breathing had essentially been achieved and dynamic hyperinflation was completely developed.

Data analysis

At the end of the fifth breath, the true $PEEP_{i,stat}$ was evaluated as the total static recoil pressure. The true $PEEP_{i,dyn}$ was evaluated as the sum of the static recoil pressures and the pressures across the Maxwell bodies of lung and chest wall at the onset of the

sixth inspiratory effort. V_t was the volume inspired in breath six, and \dot{V}_c was computed by multiplying V_t by the patient's RR. In the same breath, the true W_{insp} was computed by integrating $P_{musc,insp}$ over the inspired volume and dividing the result by V_t . FEV₁ and FVC were evaluated as the volumes expired over the first second and the over the full eight seconds of the forced expiratory maneuver.

Over the period in which expiratory flow was present, the derivative of P_{es} (dP_{es}/dt) was evaluated. The baseline value of P_{es} at end-expiration ($P_{es,baseline}$) was identified automatically at the point closest to the end of expiratory flow at which dP_{es}/dt did not exceed its minimum by more than 5% of its range over that expiratory period. The threshold for the detection of $P_{es,baseline}$ was thus not fixed, but depended on the P_{es} waveform during the breath under consideration. The measured dynamic PEEP_i (PEEP_{i,meas}) was obtained from the deflection from $P_{es,baseline}$ to the value of P_{es} at the onset of inspiratory flow in breath six. When the value identified at the onset of inspiratory flow exceeded $P_{es,baseline}$, which occasionally occurred in the presence of cardiogenic oscillations, PEEP_{i,meas} was set to zero. A measurement of W_{insp} (W_{meas}) was evaluated as the integral of the difference between $P_{es,baseline}$ and P_{es} over inspired volume plus the work done to distend the chest wall, divided by V_t . A constant linear chest wall elastance of 5 cmH₂O.L⁻¹ was used to calculate the work done to distend the chest wall.

3.2.3 Results

Fig. 3.9 shows PEEP_{i,meas} with respect to PEEP_{i,dyn} for configurations (a) to (d). Without expiratory effort and cardiogenic oscillations (Fig. 3.9a), PEEP_{i,meas} reproduced PEEP_{i,dyn} with a good degree of accuracy ($y = 0.96x - 0.03$, $r = 0.999$). In the presence of expiratory effort (Fig. 3.9b), PEEP_{i,meas} systematically overestimated PEEP_{i,dyn} ($y = 1.08x + 4.79$, $r = 0.85$). As anticipated, the measurement error (PEEP_{i,meas} - PEEP_{i,dyn}) was closely correlated with P_{exp} (Fig. 3.11a) ($y = 1.13x + 0.008$, $r = 0.98$). In Fig. 3.9c, cardiogenic oscillations introduced a random error in PEEP_{i,meas} which effectively obliterated the correlation between PEEP_{i,meas} and PEEP_{i,dyn} ($r = 0.29$). The mean error was 0.51 cmH₂O which is 12.5% of the mean PEEP_{i,dyn} (4.1 cmH₂O), while the standard

deviation of the error was 3.54 cmH₂O. With both expiratory effort and cardiogenic oscillations (Fig. 3.9d), the scatter in PEEP_{i,meas} was even more pronounced ($r = 0.18$). It should be noted that data points representing a small number of simulated patients that were able to expire below their equilibrium volumes when their expiratory muscles were active were excluded from Fig. 3.9b and d, since they did not develop dynamic hyperinflation and PEEP_i under those conditions.

W_{meas} is plotted with respect to W_{insp} in Fig. 3.10 for configurations (a) to (d). Under control conditions (Fig. 3.10a), W_{meas} slightly underestimated the true W_{insp} ($y = 0.99x - 0.04$, $r = 0.97$), although the average relative error remained smaller than 5%. In the presence of expiratory effort (Fig. 3.10b), W_{meas} systematically overestimated W_{insp} ($y = 1.36x + 0.15$, $r = 0.81$). As above for PEEP_{i,dyn}, the measurement error of W_{insp} ($W_{\text{meas}} - W_{\text{insp}}$) was closely correlated with P_{exp} (Fig. 3.11b) ($y = 0.11x - 0.015$, $r = 0.91$). The correlation between W_{meas} and W_{insp} was lost when cardiogenic oscillations were present (Fig. 3.10c, $r = 0.38$). The error due to the oscillations was $-0.018 \pm 0.29 \text{ J.L}^{-1}$ (mean \pm SD), compared to a mean W_{insp} of 0.92 J.L^{-1} . The scatter became even greater when both expiratory effort and cardiogenic oscillations were present (Fig. 3.10d, $r = 0.27$).

The open circles in Fig. 3.12 display the relationship between PEEP_{i,stat} and PEEP_{i,dyn} under control conditions (configuration (a)). At higher levels of PEEP_i, the data points are scattered about the line of identity, while PEEP_{i,dyn} increasingly underestimated PEEP_{i,stat} as PEEP_{i,stat} decreased. In contrast, PEEP_{i,dyn} underestimated PEEP_{i,stat} in a larger number of cases and to a greater extent when the stress adaptation of the lung was increased five-fold (configuration (e), solid circles in Fig. 3.12).

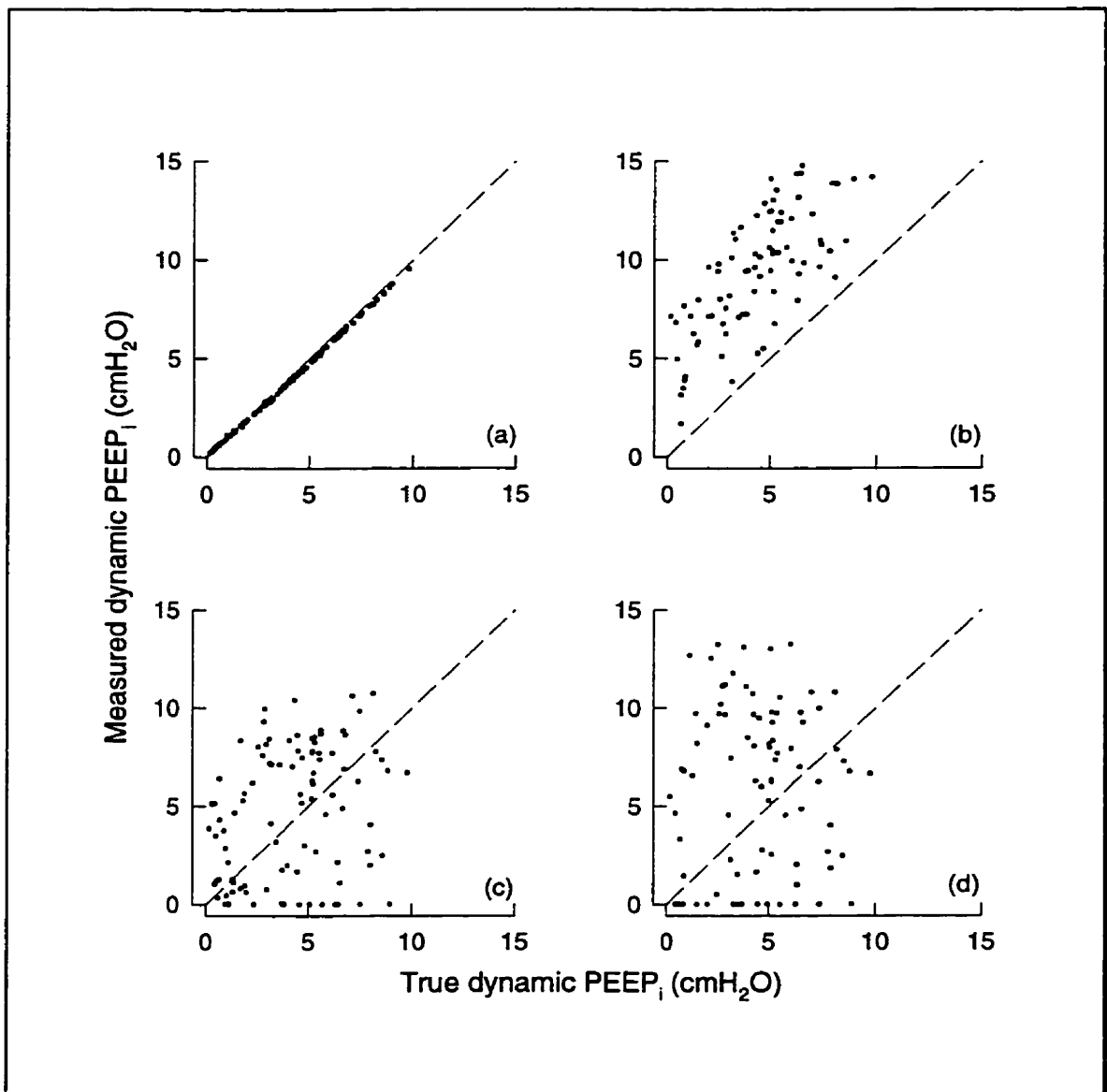


Fig. 3.9:

Identity plots relating the measured and the true dynamic PEEP_i in four different configurations: (a) no expiratory effort or cardiogenic oscillations ; (b) expiratory effort alone; (c) cardiogenic oscillations alone; and (d) both expiratory effort and cardiogenic oscillations. The dashed lines are lines of identity.

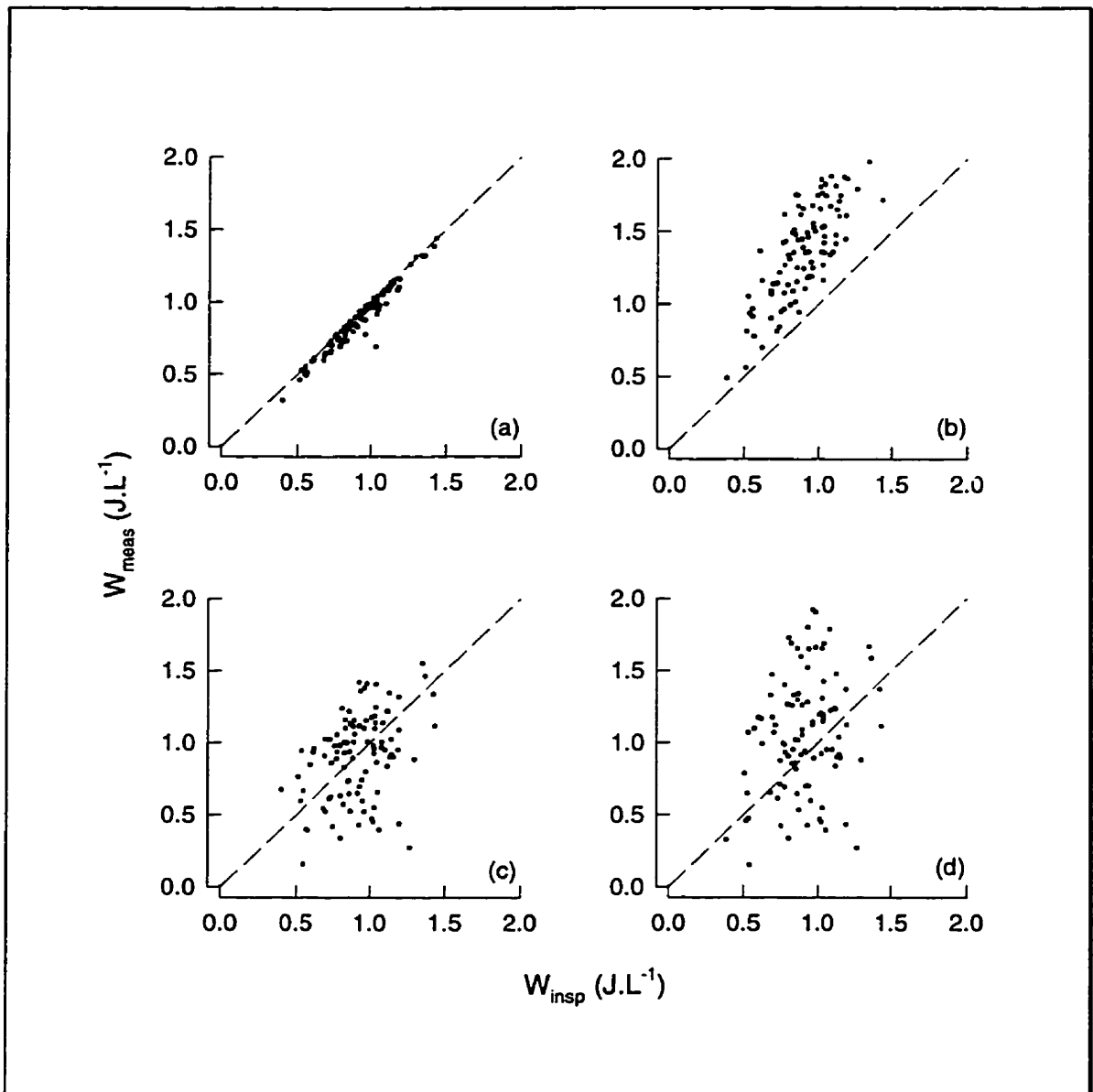


Fig. 3.10:
Identity plots relating the measured and the true inspiratory work of breathing in four different configurations: (a) no expiratory effort and cardiogenic oscillations; (b) expiratory effort alone; (c) cardiogenic oscillations alone; and (d) both expiratory effort and cardiogenic oscillations. The dashed lines are lines of identity.

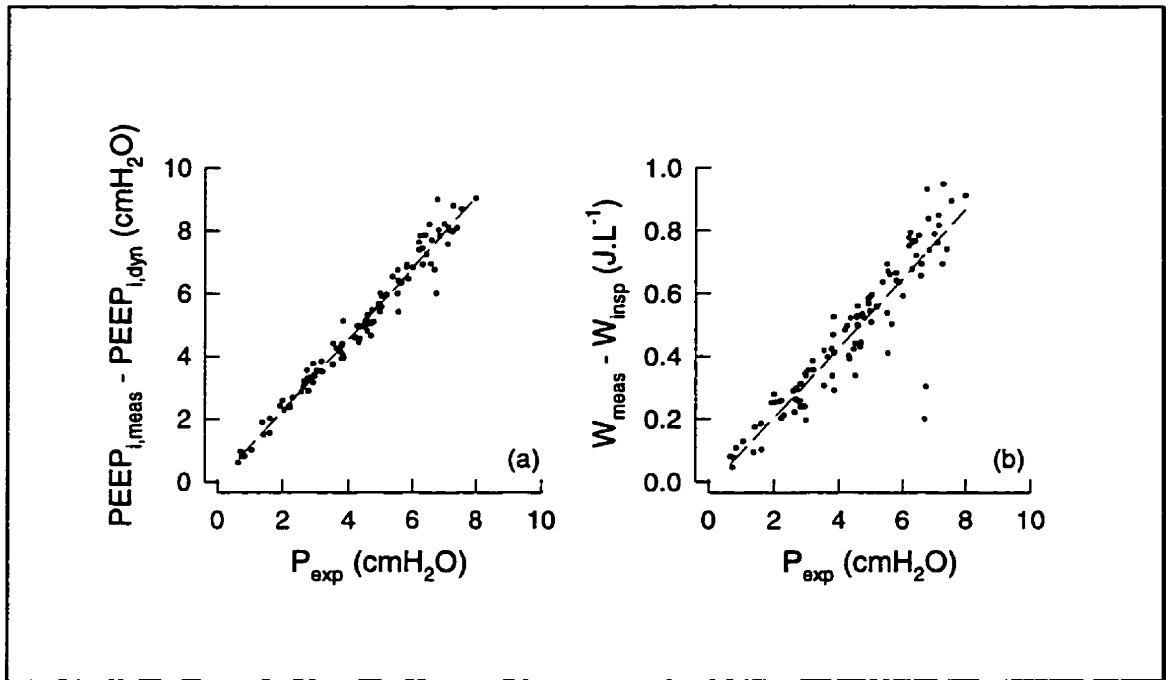


Fig. 3.11:
The measurement errors in both $PEEP_i$ (a) and W_{insp} (b) versus the peak expiratory effort. The dashed lines are regression lines.

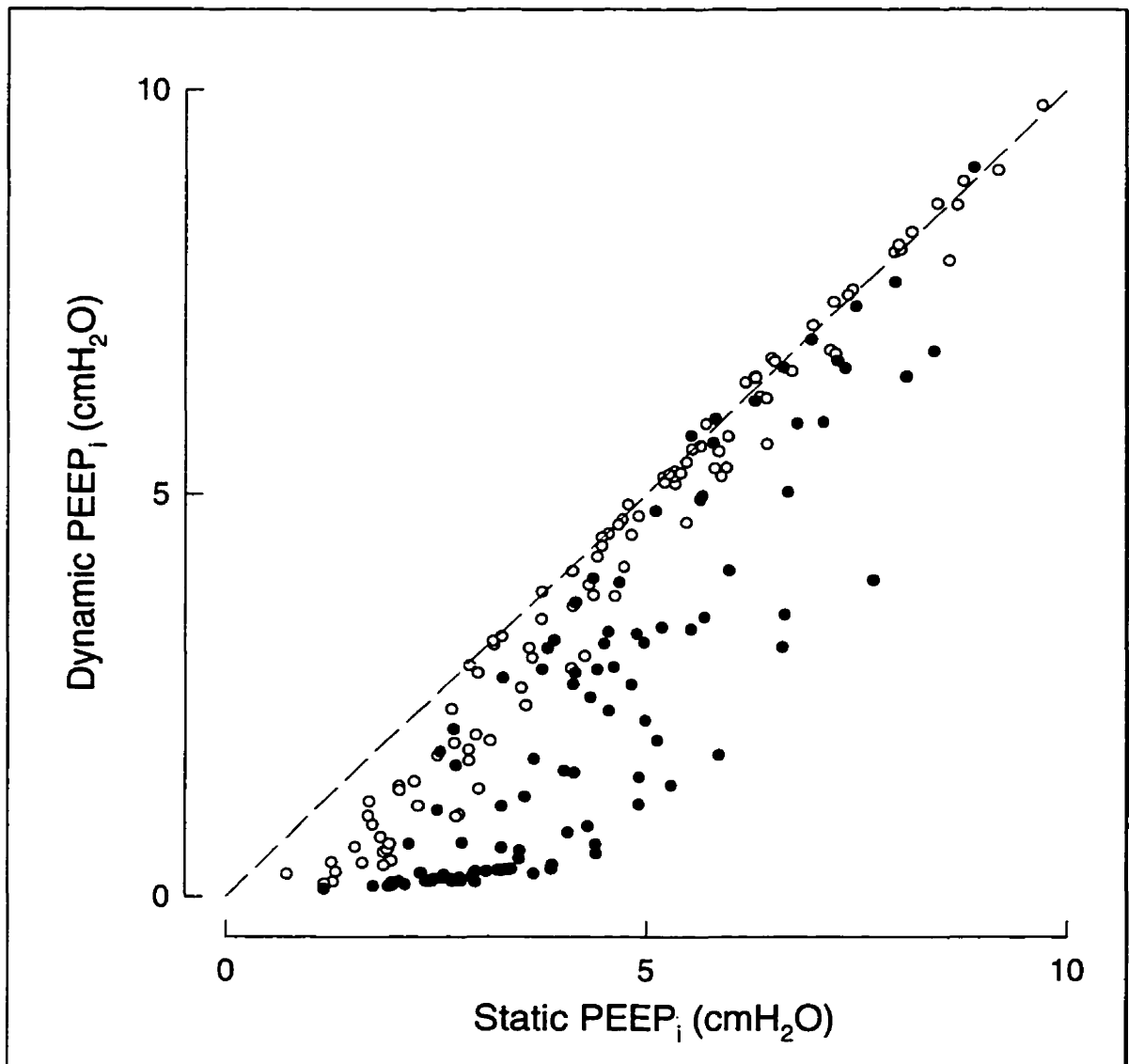


Fig. 3.12:

Identity plot comparing static and dynamic $PEEP_i$. In the initial population of COPD patients (open circles), $PEEP_{i,dyn}$ underestimated $PEEP_{i,stat}$ at lower levels of $PEEP_{i,stat}$, whereas the two were comparable at higher $PEEP_{i,stat}$ values. After stress adaptation within the lungs was increased five-fold (closed circles), $PEEP_{i,dyn}$ consistently underestimated $PEEP_{i,stat}$ at all levels of $PEEP_{i,stat}$. The dashed line is the line of identity.

3.2.4 Discussion

In the present study, I have employed the computational model of the actively breathing patient developed in section 3.1 to quantitatively analyze measurement errors in $PEEP_{i,dyn}$ and W_{insp} during spontaneous breathing. Computer simulations are particularly well-suited for this kind of analysis, because they provide access to variables that are impossible to measure in patients and because the effects of various confounding factors can be evaluated independently.

As discussed in section 3.1.4, the results of any computer simulation study are always open to question in that the underlying model will never completely reproduce human physiology. However, even if the mechanism that determined the true $PEEP_{i,dyn}$ and W_{insp} in these simulations was not entirely realistic, a robust algorithm should still have estimated them correctly. Also, the employed scheme for identifying $P_{es,baseline}$ was based on the derivative of P_{es} . This approach works well in a computer simulation where random measurement noise is absent, but is likely to perform less well in a practical measurement situation where numerical differentiation amplifies measurement noise and necessitates further signal processing that may introduce additional errors to $P_{es,baseline}$. In this sense, the data presented in Fig. 3.9 to Fig. 3.11 are a best-case scenario, whereas poorer performance would be expected in a true measurement situation.

The results of this study demonstrate the extent to which automated breath-by-breath measurements of both $PEEP_{i,dyn}$ and W_{insp} are susceptible to errors due to expiratory muscle activity and cardiogenic oscillations. In the absence of expiratory effort and cardiogenic oscillations, both $PEEP_{i,dyn}$ (Fig. 3.9a) and W_{insp} (Fig. 3.10a) were well estimated. The slight systematic error in $PEEP_{i,meas}$ (Fig. 3.9a) was presumably due to small changes in the pressure drop across the stress adaptation compartments that occurred during the time required to evaluate $PEEP_{i,meas}$. The random error in $PEEP_{i,meas}$ was negligible. W_{insp} exhibited a slight systematic error with a small degree of random scatter (Fig. 3.10a). Comparison of these results to estimates of W_{insp} obtained using each patient's individual chest wall mechanics showed that most of the error in W_{meas} under

control conditions was due to the assumption of a fixed chest wall elastance of $5 \text{ cmH}_2\text{O}\cdot\text{L}^{-1}$. This strategy is motivated by the fact that chest wall elastance is not easily obtained in actively breathing patients and, as a result, a normal predicted value is commonly used (9,18,106). A fixed chest wall elastance of $5 \text{ cmH}_2\text{O}\cdot\text{L}^{-1}$ has also been employed in the W_{insp} algorithm of a commercially available pulmonary monitoring device (CP-100, Bicore Corp., Irvine, CA). In any case, this study indicates that the errors introduced by assuming a fixed chest wall elastance for all patients are minor.

With the introduction of expiratory effort, significant errors were encountered in both $\text{PEEP}_{\text{i,meas}}$ (Fig. 3.9b) and W_{meas} (Fig. 3.10b). The measurement errors for both quantities correlated linearly with P_{exp} (Fig. 3.11), indicating that the measurement errors are predominantly determined by the expiratory muscle activity and do not depend on the level of dynamic hyperinflation itself. Several investigators have suggested using changes in gastric pressure to estimate the magnitude of the expiratory muscle pressure, which may then be employed to correct $\text{PEEP}_{\text{i,meas}}$ (6,85). Although the pressure generated by the expiratory muscles of the rib cage may not be completely reflected in gastric pressure (31,99), this method is certain to be better than no correction at all. Presumably, gastric pressure could also be used to make a corresponding correction in W_{meas} , although to the best of my knowledge this has not yet been investigated. Unfortunately, I was unable to investigate the use of gastric pressure in my model because of the lack of published data showing quantitatively how the abdominal wall and contents contribute to respiratory mechanics.

I also found that cardiogenic oscillations produced large errors in both $\text{PEEP}_{\text{i,meas}}$ and W_{meas} (Fig. 3.9c and Fig. 3.10c). These errors can be reduced by averaging estimates from many breaths, provided that the cardiogenic oscillations are not entrained with the breathing cycle. However, a statistical analysis showed that over 1145 breaths would need to be averaged to reduce the standard deviation of $\text{PEEP}_{\text{i,meas}} - \text{PEEP}_{\text{i,dyn}}$ to less than 5% of the mean $\text{PEEP}_{\text{i,dyn}}$ with 95% confidence (63). An analogous computation showed that a similar level of confidence would be obtained for W_{insp} by averaging over 152 breaths. In my opinion, these numbers of breaths are too large to allow either $\text{PEEP}_{\text{i,dyn}}$ or W_{insp} to

be accurately estimated in anything close to real time. On the other hand, single breath estimates of both quantities are far too noisy to be useful. Furthermore, standard filtering techniques are not capable of reducing the confounding effects of cardiogenic oscillations because the frequency spectra of respiratory and cardiac pressure waveforms overlap too much. Obviously, more sophisticated processing of P_{es} , such as the adaptive filter technique described in the next section, is required in order to ameliorate the effects of cardiogenic oscillations. Almost no attention has been given to this matter in previous reports (6,9,85,99,107), yet it is clearly crucial to the successful estimation of both $PEEP_{i,dyn}$ and W_{insp} , in particular when these quantities are to be evaluated automatically on a breath-by-breath basis. Not surprisingly, the errors were even greater when both expiratory muscle activity and cardiogenic oscillations were present (Fig. 3.9d and Fig. 3.10d).

Under the control condition (configuration (a), open circles in Fig. 3.12), i.e., in absence of expiratory effort and cardiogenic oscillations and with R_{2L} as given in Table 3.1, it was not possible to reproduce the significant differences that have been observed between $PEEP_{i,stat}$ and $PEEP_{i,dyn}$ in the setting of severe airway obstruction (62,88,107), especially when $PEEP_{i,stat}$ was large. Presumably, this is because central airway flow limitation was the main determinant of expiratory flow in my simulations, which would have reduced the magnitude of the end-expiratory pressure in the stress adaptation compartment. In other words, expiratory flow was slowed in the central airways to an extent that much of the energy stored in viscoelastic tissues and in local pressure differences due to peripheral time constant inhomogeneities could dissipate before end-expiration. I was able to simulate differences between $PEEP_{i,dyn}$ and $PEEP_{i,stat}$ similar to those reported in patients only after the degree of stress adaptation in the lung compartment had been increased five-fold (configuration (e), solid circles in Fig. 3.12) over that reported for COPD patients during inspiration (57). This suggests that COPD patients exhibit more stress adaptation during expiration than during inspiration. Presumably, the only way this can happen is if these patients are inhomogeneously flow limited during expiration, so that their lungs expire like a parallel arrangement of flow

limited compartments emptying at relatively different rates. Inhomogeneous emptying during flow limitation has been described previously in dogs (92,139,149). Because the degree of inhomogeneity in flow limitation is likely to vary considerably from patient to patient, the relationship between $PEEP_{i,dyn}$ and $PEEP_{i,stat}$ is in general extremely difficult to predict in any particular individual. This may account for the wide range of $PEEP_{i,dyn}$ to $PEEP_{i,stat}$ ratios reported in the literature (62,88,107,119).

In summary, I employed the computer model described in section 3.1 to examine the extent to which automated breath-by-breath measurement techniques for $PEEP_{i,dyn}$ and W_{insp} are susceptible to errors due to expiratory muscle activity and cardiogenic oscillations. The results of this study demonstrate that both quantities are highly sensitive to these phenomena, such that in general, some means of correction for expiratory muscle activity and cardiogenic oscillations are necessary if $PEEP_{i,dyn}$ and W_{insp} are to be measured accurately on-line. Furthermore, my simulations suggest that the discrepancies between $PEEP_{i,stat}$ and $PEEP_{i,dyn}$ are caused by the heterogeneity of the expiratory flow limitation throughout the lung.

3.3 An adaptive filter to reduce the cardiogenic oscillations in esophageal pressure

3.3.1 Motivation

In the previous section, I have demonstrated in a computer simulation that cardiogenic oscillations in P_{es} may introduce substantial errors in estimates of $PEEP_{i,dyn}$ and W_{insp} . Similarly, cardiogenic oscillations reduce the goodness of model fits when the mechanical properties of the lungs and chest wall are identified using P_{es} . Unfortunately, cardiogenic oscillations cannot be removed from P_{es} signals by simple low-pass filtering because their frequency content overlaps that of the respiratory signal.

This section describes an adaptive filter to suppress cardiogenic oscillations that I developed to reduce the adverse effects of cardiogenic oscillations. The filter is validated using both data obtained from the computer model described in section 3.1 and records from four patients in a respiratory ICU. The effects on measurements of $PEEP_{i,dyn}$ are investigated.

3.3.2 Methods

The adaptive filter

In order to develop the adaptive filter presented in this study, we model P_{es} as the sum of pressure swings due to respiration (P_{resp}) and the undesired cardiogenic oscillation pressure (P_{CGO}), as illustrated in Fig. 3.13a. The linear dynamic system described by the impulse response function $h_1(\tau)$ relates P_{CGO} to the series of impulses generated by the cardiac pacemaker in the SA node (C_p). P_{CGO} contains very little power at frequencies below the heart rate (HR), while P_{resp} is likely to contain significant power below the HR because the RR is generally less than the HR. Therefore, P_{es} can be considered to be entirely determined by P_{resp} in the frequency band from 0 Hz to slightly below the HR, but to contain significant cardiogenic oscillations at and above the HR. A second impulse

response, $h_2(\tau)$, translates C_p into voltage swings on the body surface that can be measured as an electrocardiogram (EKG).

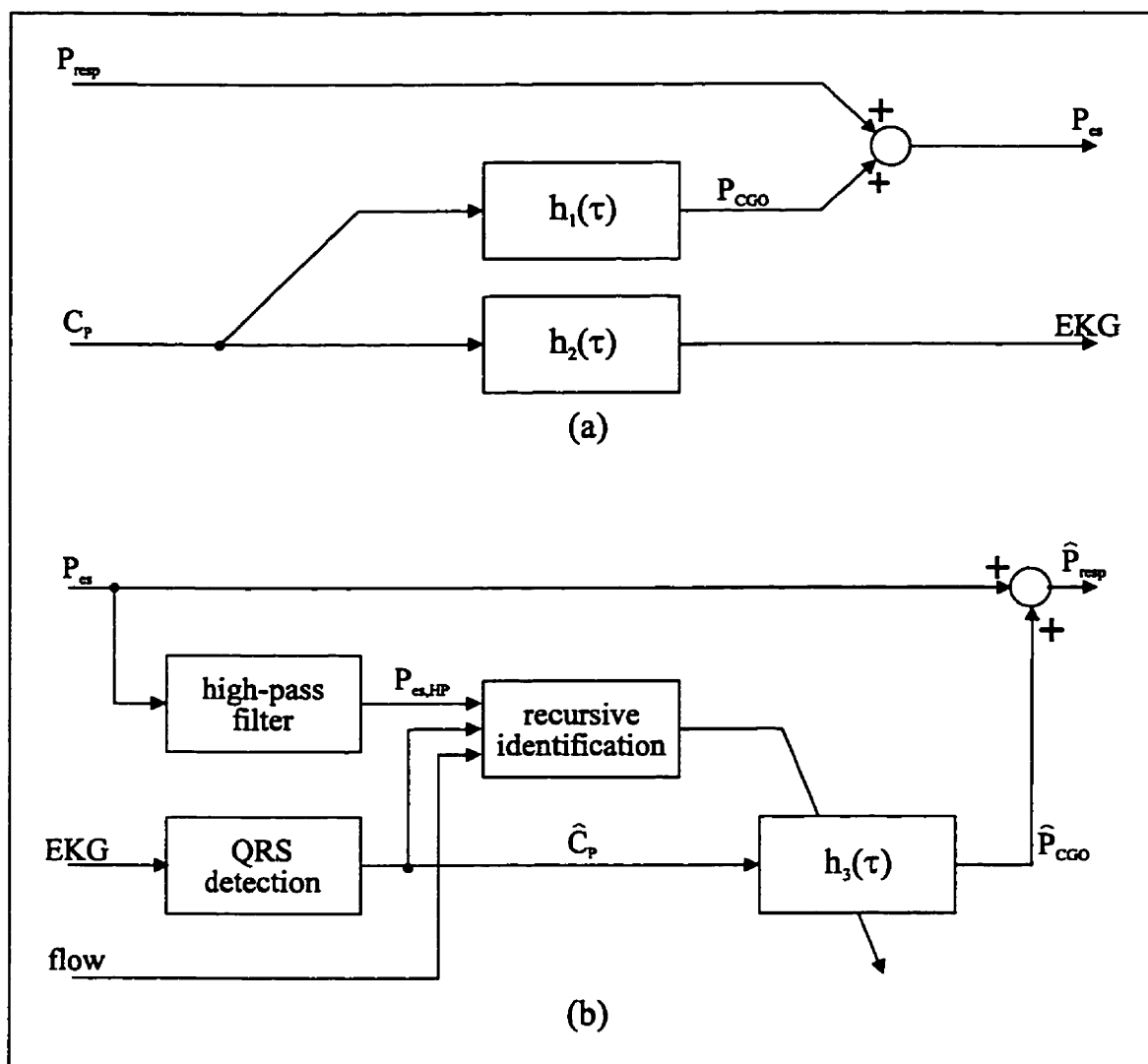


Fig. 3.13:

- (a) Model of the origin of cardiogenic oscillations employed to develop the adaptive filter.
 (b) Structure of the adaptive filter. See text for details.

In the adaptive filter, a number of quantities are smoothed by recursively calculating an exponentially weighted running mean according to

$$\bar{x}_k = \zeta \bar{x}_{k-1} + (1 - \zeta)x_k, \quad (3.7)$$

where \bar{x}_k is the estimate of the mean obtained up to sample k . ζ is often referred to as a forgetting factor, and must range between 0 and 1. If x is sampled uniformly, this estimator becomes equivalent to a single-pole low-pass filter, and ζ is related to the time constant of the finite memory, τ , by the equation

$$\tau = -\frac{\Delta t}{\ln(\zeta)}, \quad (3.8)$$

where Δt is the sampling interval. If ζ is adequately chosen, this recursive estimator tracks slow changes in x but averages out rapid fluctuations and measurement noise.

The structure of the adaptive filter is shown in Fig. 3.13b. In order to compute an estimate of P_{CGO} (\hat{P}_{CGO}), a sequence of impulses representing the cardiac R-waves from a lead II EKG was generated by thresholding the negative deflections of the EKG. The threshold value for the R-wave detection was set to 1.7 times the RMS value of the EKG signal, which was smoothed recursively as described above with a forgetting factor of 0.97. Provided that $h_2(\tau)$ is stationary, this sequence of impulses represents an estimate of C_p , i.e.,

$$\hat{C}_p \approx C_p(t - \tau_2), \quad (3.9)$$

where τ_2 is the delay between the initiation of a heart beat in the SA node and its manifestation in the EKG. The HR was computed from the inverse R-R intervals and smoothed recursively using a forgetting factor of 0.9.

Next, P_{es} was high-pass filtered using a two-sided 256th-order FIR filter with a constant group delay. The cutoff frequency (f_c) of this filter was adjusted to 0.6 times the identified HR. Thus, the high-pass filtered P_{es} signal ($P_{es,HP}$) still contained the complete and undistorted P_{CGO} , but suppressed the low frequency components of P_{resp} that in some cases would complicate the following processing steps. The two sided high-pass filter introduced a delay of 128 data points from the moment that data were sampled to the

point when filtered values were available. Since all data were sampled at 100 Hz, the time delay amounted to 1.28 seconds.

Assuming linearity, we have that

$$P_{CGO} = h_1(\tau - \tau_2) * \hat{C}_P, \quad (3.10)$$

where * denotes convolution. In order to calculate \hat{P}_{CGO} , a third impulse response, $h_3(\tau)$, was estimated recursively according to

$$h_3^{(k+1)}(\tau) = \zeta h_3^{(k)}(\tau) + (1 - \zeta) P_{es,HP}^{(k)}(t), \quad (3.11)$$

where ζ again is the forgetting factor, and $P_{es,HP}^{(k)}$ is the segment of $P_{es,HP}$ that falls into the k -th R-R interval. Assuming that there is no phase-locking between the heart rate and the breathing cycle, and provided that ζ is sufficiently large, components of $h_3(\tau)$ that originate from P_{resp} are averaged out so that $h_3(\tau)$ effectively provides an estimate of $h_1(\tau - \tau_2)$. Using $h_3(\tau)$, \hat{P}_{CGO} was computed and subtracted from P_{es} in order to obtain the final estimate of P_{resp} , i.e.,

$$\hat{P}_{resp} = P_{es} - \hat{P}_{CGO} = P_{es} - h_3(\tau) * \hat{C}_P. \quad (3.12)$$

The choice of the forgetting factor ζ in Eq. 3.11 is a crucial determinant of the algorithm's performance. If ζ is chosen too small then $h_3(\tau)$ becomes sensitive to measurement noise, and contributions to $P_{es,HP}$ that originate from P_{resp} are not effectively averaged out. On the other hand, large values of ζ limit the filters ability to adapt to changes in $h_1(\tau)$ over time. Part of this problem can be overcome by using the adaptive scheme of Wellstead and Sanoff (144) to update ζ at each iteration. Briefly, this scheme recursively tracks the residuals with a finite memory. When the residuals are persistently large, a change in the underlying dynamics is assumed and ζ is decreased. Conversely, ζ is increased to reduce the sensitivity to measurement noise in the case of consistently small residuals. This scheme has been applied successfully to fitting models of respiratory mechanics to pressure and flow data (84).

While the scheme of Wellstead and Sanoff alters ζ appropriately in the case of changing underlying dynamics, it fails in the presence of increased band overlap, i.e.,

when the frequency content of P_{CGO} increasingly overlaps that of P_{resp} . Band overlap also increases the variability between \hat{P}_{CGO} and $P_{es,HP}$, but requires an increase rather than a reduction of ζ in order to properly average out the contributions of P_{resp} in Eq. 3.11. We are thus faced with conflicting possibilities when \hat{P}_{CGO} and $P_{es,HP}$ do not match well: it may be that the underlying dynamics are varying in which case ζ should be decreased, or it may be due to band overlap in which case ζ should be increased. However, some *a priori* information to estimate the prominence of band overlap can be obtained from the relative values of the HR and the respiratory rate (RR). We can develop a modified scheme to adaptively update ζ at each interval k that encapsulates this *a priori* information starting with an expression similar to the scheme by Wellstead and Sanoff, i.e.,

$$\zeta_k = 1 - \frac{\Delta_k}{1 + \Delta_k}. \quad (3.13)$$

However, Δ in this case is a function of the residuals, the heart rate and the respiratory rate that is recursively updated according to

$$\Delta_k = \xi \Delta_{k-1} + (1 - \xi) \frac{\|P_{es,HP}^{(k)} - h_3^{(k)}\|}{\|h_3^{(k)}\|} e^{\kappa_1 \frac{HR}{RR} + \kappa_2}, \quad (3.14)$$

where ξ is another forgetting factor, and $\|\cdot\|$ denotes a quadratic norm. The exponential term in Eq. 3.14 was chosen empirically on the basis of preliminary computer simulations and effectively determines the range over which the scheme can modify ζ . When the HR is close to the RR, the exponential term in Eq. 3.14 is small. This in turn causes Δ_k to remain small, so that ζ_k in Eq. 3.13 is close to unity, biasing the algorithm towards long memory. The effects of band overlap can thus be averaged out. Conversely, as the HR becomes much greater than the RR, the exponential term in Eq. 3.14 increases. This allows Δ_k to be large and the memory to be short when $P_{es,HP}$ consistently differs significantly from h_3 . The filter can then adapt rapidly to changes in P_{CGO} . The constants in Eq. 3.14 were set to $\xi = 0.8$, $\kappa_1 = 0.5$ and $\kappa_2 = -5$. Small changes in these parameters hardly affected the overall outcome, indicating that this scheme is robust towards slight

misadjustments of ξ , κ_1 and κ_2 . The RR was computed from the intervals between the onset of inspiratory flow and smoothed recursively with a forgetting factor of 0.6.

The adaptive filter was implemented using the Matlab 4.2/Simulink 1.3 mathematical software package (The Mathworks, Nattick, MA).

Computer simulations

To test the adaptive filter, P_{es} signals contaminated with cardiogenic oscillations were simulated using the model described in section 3.1. In order to introduce a physiologically reasonable variability in P_{CGO} over time, this model was extended by making the magnitude of P_{CGO} volume-dependent according to

$$P_{CGO} = k_1 \cdot e^{k_2 \frac{FRC - V(t)}{FRC}} \cdot \tilde{P}_{CGO}. \quad (3.15)$$

Here, \tilde{P}_{CGO} is the preliminary, volume independent cardiogenic oscillation waveform. The constants k_1 and k_2 were chosen to be 10 cmH₂O and 5, respectively. This volume dependence can be interpreted as one possible mechanism to introduce variability of P_{CGO} over time.

Eight spontaneously breathing patients were simulated with the RRs and HRs shown in Table 3.3. These values were chosen to produce degrees of band overlap spanning the range likely to be observed in real patients. The inspiratory drive was adjusted to produce minute ventilations between 5.5 and 7.2 L/min, and expiratory muscle activity was absent in all eight simulated patients. All other model parameters were chosen equal to the population means listed in Table 3.1. Patients 1 to 4 had very rapid shallow breathing patterns with a RR of 40 min⁻¹. The simulations were designed such that band overlap was most pronounced in patient 1, where the HR with 54.7 min⁻¹ was only 37% higher than the RR. In contrast, patients 5 to 8 breathed deeply with a RR of 10 min⁻¹. In these patients, band overlap was less prominent, but the effects of the volume dependence of P_{CGO} became more important due to the larger V_t . Three minutes of data were simulated for each patient, and the first two minutes of data were discarded in order to assure that the steady state of the simulation had been reached, and to allow the filter to adapt. From the last minute of data, I evaluated the variance accounted for (VAF) by both

P_{es} and \hat{P}_{CGO} with respect to the true P_{resp} in order to quantify the reduction of the cardiogenic oscillation achieved by the adaptive filter.

Patient data

The adaptive filter was also applied to recordings of P_{es} , \dot{V} and EKG that had been obtained from four patients receiving ventilatory support in the ICU of the Montreal Chest Hospital. Each data collection protocol was approved by the local ethics committee, and informed consent had been obtained from all subjects. All signals were amplified and anti-aliasing filtered at 30 Hz using 6th-order Bessel low-pass filters and digitized at a sampling rate of 100 Hz. The correct position of the esophageal balloon was verified prior to data collection by a standard occlusion test (15). Table 3.4 summarizes the characteristics of each patient.

From each patient record, a data segment was chosen for further analysis that (i) started a minimum of 60 seconds after the beginning of data collection to permit time for the filter to adapt, (ii) showed a relatively stable breathing pattern over a period of at least 10 breaths, and (iii) did not contain any esophageal spasms or EKG artifacts. For each analysis segment, the magnitude of the 2048-point Fourier Transform (FT) was computed for both the unfiltered and the filtered P_{es} using a Hamming window with 50% overlap. Using the same segments, $PEEP_{i,dyn}$ was estimated automatically for each breath as described in section 3.2.2. $PEEP_{i,dyn}$ was corrected for the trigger threshold of the ventilator by subtracting the deflection in airway opening pressure that occurred simultaneously with the deflection in P_{es} . The onset of inspiratory flow was identified by extrapolating backwards to zero flow from the points at which inspiratory flow amounted to 50 and 100 mL/sec. This procedure was carried out using both the unfiltered and the filtered P_{es} , and the mean and standard deviation of $PEEP_{i,dyn}$ were computed in each case.

3.3.3 Results

Simulated data

Fig. 3.14 shows samples of the simulated P_{resp} and P_{es} and the resulting \hat{P}_{resp} traces for simulated patients 1 (top) and 8 (bottom). In both patients, the unfiltered P_{es} (center) differed significantly from the simulated P_{resp} (left). In patient 1 where band overlap was most pronounced, the effects of the cardiogenic oscillations were suppressed to a large extent, but not entirely in the filtered P_{es} signal (top right). In the filtered P_{es} trace of patient 8 where volume dependence was more pronounced (bottom right), most of the cardiogenic oscillations were suppressed.

The VAFs for both P_{es} and \hat{P}_{resp} are shown in the bottom two rows of Table 3.3. When the RR was 10 breaths per minute, P_{es} accounted for 89 to 94% of the variance of P_{resp} . This number dropped as low as 55% when the RR was raised to 40 breaths per minute and band overlap became more prominent. \hat{P}_{resp} produced a substantially greater VAF in all eight cases, with a minimum of 98.5% at a RR of 10 and a minimum of 95.4% at a RR of 40.

Patient data

Fig. 3.15 shows samples of the unfiltered (dashed lines) and filtered (solid lines) P_{es} for each of the four ICU patients studied. In all four graphs, the filtered P_{es} trace was shifted downward by 5 cmH₂O to separate the graphs. Except for patient C, the data shown in Fig. 3.15 lie completely within the segments used to compute the power spectrum and to estimate PEEP_i. For patient C, the analysis segment ended at t=290 sec., when the patient was switched from Proportional Assist Ventilation to Pressure Support Ventilation. At this point, the RR of patient C dropped from 32 breaths per minute to 8.3 breaths per minute. Fig. 3.15 shows this transition to illustrate the performance of the adaptive filter over a change in ventilatory conditions. Patient D had a large tidal volume at a very low RR of 4.7 and showed abnormal positive deflections in P_{es} . Analysis of concurrently recorded P_{aw} and \dot{V} traces suggested that these were busts of expiratory muscle recruitment.

In Fig. 3.16, the magnitudes of the FT of the unfiltered (dashed lines) and filtered (solid lines) P_{es} signals of all four patients are plotted against the frequency normalized to the heart rate. Thus, on the abscissa of each plot, the heart rate occurs at a value of one and its harmonics occur at integer values greater than one. In all cases, the FT of the unfiltered P_{es} signal showed spikes at the heart rate and its harmonics. These were essentially eliminated in the FT of the filtered P_{es} signal.

The mean and standard deviation of $PEEP_{i,dyn}$ for each patient are shown in Table 3.5. The standard deviation of $PEEP_{i,dyn}$ was less for the filtered than for the unfiltered P_{es} signal in all patients. The mean $PEEP_{i,dyn}$ dropped in three patients and increased in one patient when the filtered P_{es} signal was used.

Table 3.3:
Heart rate and respiratory rate of eight simulated patients, and variance accounted for (VAF) of the unfiltered and filtered P_{es} with respect to P_{resp} .

| Simulated patient | 1 | 2 | 3 | 4 | 5 | 6 | 7 | 8 | |
|-------------------|------|------|-------|-------|------|------|-------|-------|-------------------|
| Heart rate | 54.7 | 74.7 | 139.3 | 199.3 | 54.7 | 74.7 | 139.3 | 199.3 | min ⁻¹ |
| Respiratory rate | 40 | 40 | 40 | 40 | 10 | 10 | 10 | 10 | min ⁻¹ |
| VAF unfiltered | 57.9 | 54.5 | 64.5 | 76.2 | 90.2 | 89.4 | 91.7 | 94.4 | % |
| VAF filtered | 95.4 | 97.7 | 97.8 | 97.9 | 98.5 | 98.7 | 98.9 | 99.4 | % |

Table 3.4:
Characteristics of the four intensive care patients studied.

| Patient | Sex | Age | Diagnosis | Ventilator mode | Heart rate | Resp. rate |
|----------|-----|-----|--------------------|--|-----------------------|-----------------------|
| <i>A</i> | m | 66 | COPD/ Pneumonia | CPAP 5 cmH ₂ O | 126 min ⁻¹ | 22 min ⁻¹ |
| <i>B</i> | f | 57 | COPD | PAV + PEEP 3 cmH ₂ O | 104 min ⁻¹ | 15 min ⁻¹ |
| <i>C</i> | m | 64 | COPD | PAV + PEEP 4 cmH ₂ O | 87 min ⁻¹ | 32 min ⁻¹ |
| <i>D</i> | f | 69 | COPD | PSV 12 cmH ₂ O + PEEP 5 cmH ₂ O | 106 min ⁻¹ | 4.7 min ⁻¹ |

Table 3.5:
Dynamic intrinsic PEEP (mean ± standard deviation) for four intensive care patients, obtained using the unfiltered and the filtered esophageal pressure signal.

| | Length of analyzed data segment | PEEP _{i,dyn} (unfiltered P _{es}) | PEEP _{i,dyn} (filtered P _{es}) |
|------------------|---------------------------------|--|--|
| Patient <i>A</i> | 100 sec (36 breaths) | 0.54 ± 1.06 cmH ₂ O | 0.18 ± 0.31 cmH ₂ O |
| Patient <i>B</i> | 100 sec (25 breaths) | 1.54 ± 1.59 cmH ₂ O | 1.11 ± 0.57 cmH ₂ O |
| Patient <i>C</i> | 50 sec (24 breaths) | 2.06 ± 1.11 cmH ₂ O | 1.06 ± 0.56 cmH ₂ O |
| Patient <i>D</i> | 120 sec (10 breaths) | 2.56 ± 1.64 cmH ₂ O | 3.76 ± 0.92 cmH ₂ O |

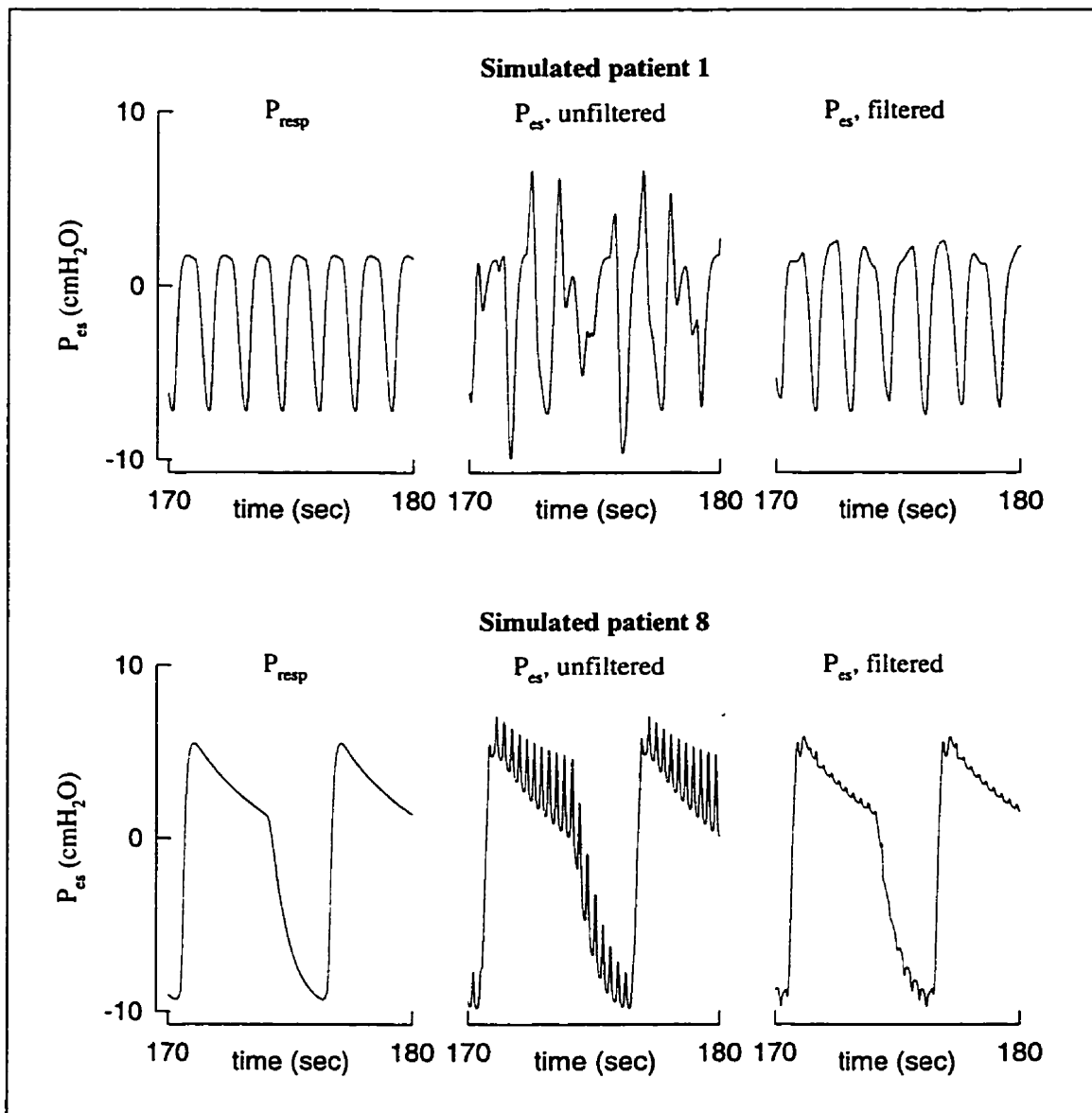


Fig. 3.14:
Simulated data for simulated patients 1 (top) and 8 (bottom). The filtered P_{es} traces (right panels) reproduce the simulated P_{resp} traces (left panels) with much greater accuracy than the unfiltered P_{es} traces (center panels).

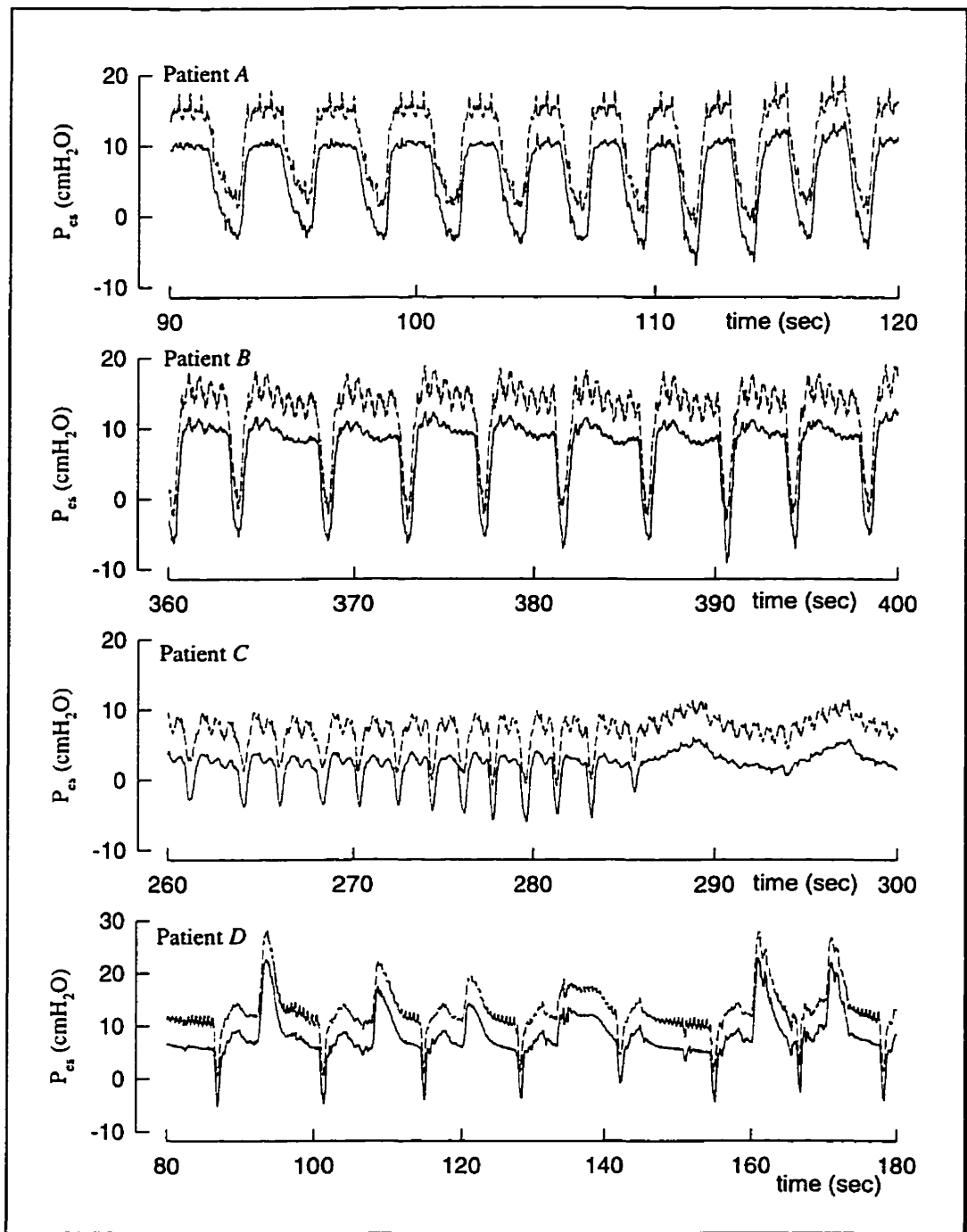


Fig. 3.15:

Sample traces from the four patients studied. Dashed lines: Unfiltered P_{es} signals. Solid lines: Adaptively filtered P_{es} signal (shifted downward by 5 cmH_2O to separate the curves). Patient characteristics see Table 3.4. Patient C was switched to from PAV to PSV at $t=290$ sec., causing the respiratory rate to instantaneously drop from 32 to 8 breaths per minute. Patient D showed an abnormal recruitment of expiratory muscles.

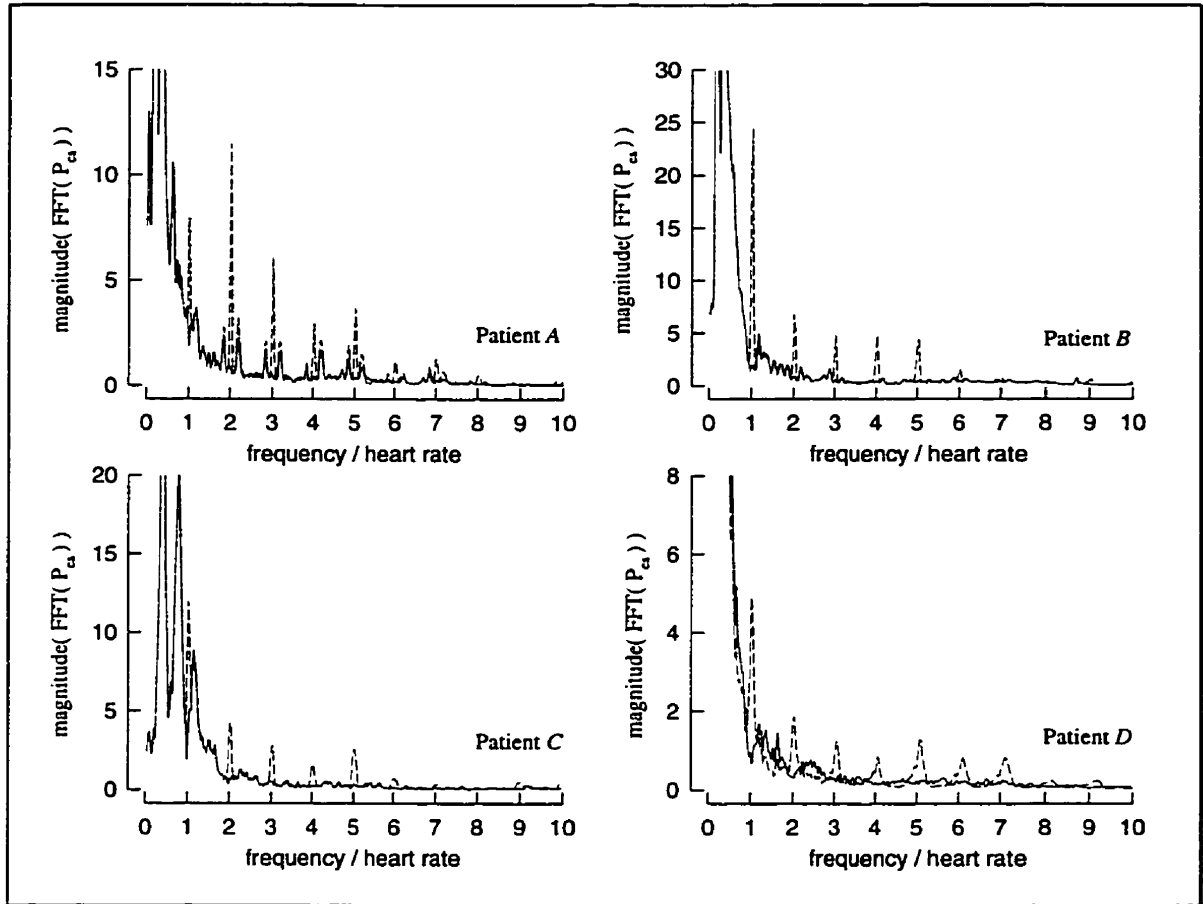


Fig. 3.16:
Magnitude of the Fourier Transform of both the unfiltered (dashed lines) and filtered (solid lines) esophageal pressure traces for all four patients, plotted against the frequency normalized to the heart rate. The Fourier Transform was computed using a moving 2048-point Hamming window with 50% overlap. The filter removed transients in the Fourier Transform at the heart rate and its harmonics (at integer values on the abscissa).

3.3.4 Discussion

In the present study, I have described in detail an adaptive filter to suppress the cardiogenic oscillations that complicate the processing of P_{es} signals. This filter was tested in eight simulated patients with a wide range of heart and respiratory rates. In all eight cases, \hat{P}_{resp} reproduced the P_{resp} with substantially greater accuracy than the unfiltered P_{es} . The VAF of \hat{P}_{resp} with respect to P_{resp} was lowest in simulated patient 1 where band overlap was most pronounced, but exceeded 95% in all simulated patients (Table 3.3).

I also tested the adaptive filter in four patients receiving mechanical ventilatory support in the ICU. The performance of the adaptive filter is more difficult to evaluate in patients because P_{resp} is unknown and cannot be used as a reference. However, the filter always reduced the apparent cardiogenic oscillations without noticeably distorting the sharp deflections due to respiration (Fig. 3.15). In the Fourier domain, the filter suppressed transients at integer multiples of the heart rate that presumably represent the harmonics of P_{CGO} (Fig. 3.16). Otherwise, the FT of the filtered P_{es} signal closely resembled the FT of the unfiltered P_{es} signal. These results indicate that the adaptive filter adequately reduces the cardiogenic oscillations in P_{es} without unduly distorting the respiratory pressure swings.

Finally, I applied the adaptive filter to the computerized estimation of $PEEP_{i,dyn}$ using the algorithm described in section 3.2.2. The mean $PEEP_{i,dyn}$ was reduced in three patients and increased in one patient. However, the standard deviation of $PEEP_{i,dyn}$ was reduced by 44 to 71% (mean 57%) in all four patients when the filtered P_{es} was used. This suggests, as one would expect, that part of the variability of the $PEEP_{i,dyn}$ obtained from the unfiltered P_{es} was not due to variability in the patient's breathing pattern, but rather to the cardiogenic oscillations. As it is improbable that the patients were perfectly stable over the analysis period, it seems likely that part of the remaining variability must have been physiologic.

To develop the adaptive filter, P_{es} was assumed to represent the sum of two independent and uncorrelated pressure signals, namely P_{resp} and P_{CGO} . Clearly, this is not a

precise account of events. First, the coupling between the heart and the esophageal balloon is likely to be volume dependent. This would cause P_{CGO} to be entrained with respiration in patients with large tidal volumes. However, the adaptive filter performed well in my computer simulations even when the simulated P_{CGO} was markedly volume dependent (simulated patients 5 to 8). The filter also performed well in patient D where the amplitude of the cardiogenic oscillations appeared to increase during expiration as lung volume decreased.

Second, since the beating heart is located within the thoracic cavity, cardiac pressure swings are not only communicated directly to the esophageal balloon, but also contribute to the pleural pressure swings. Depending on the application, this indirect contribution of the heart to P_{es} may be considered part of the respiratory pressure swings because it contributes to the transpulmonary pressure and hence influences flow. Alternatively, it may be considered artifactual because it does not originate from the respiratory musculature. In any case, this indirect contribution of the heart is likely to contribute much less to the cardiogenic oscillations on P_{es} than the direct coupling from the heart to the esophageal balloon.

The identification of the transfer function $h_3(\tau)$ would, in general, require the utilization of time-domain system identification techniques (70,143) between P_{es} and \hat{C}_p . However, the input signal to h_3 is reduced to a single impulse function when each R-R interval is processed independently. Provided that the delay between a cardiac event and its manifestation in P_{es} is much shorter than the duration of an R-R interval, the segment of P_{es} that corresponds to the R-R interval constitutes the impulse response, obliterating the need for computationally expensive deconvolution.

In summary, I have described an adaptive filter that reduces the cardiogenic oscillations on esophageal pressure traces. I have validated its performance in a computer simulation and shown its effect in both the time and the frequency domain on data obtained from four ICU patients. Furthermore, I found the standard deviation of breath-by-breath estimates of $PEEP_{i,dyn}$, obtained from periods with apparently stable breathing patterns, to be substantially reduced when the adaptive filter was used.

3.4 Assessment of patient-ventilator asynchrony during pressure support ventilation

3.4.1 Motivation

PSV is frequently administered to patients suffering from acute respiratory failure to unload the respiratory pump. Several investigators have suggested the RR as a possible criterion for the determination of the optimal ventilator settings during PSV (18,77,80,87), and one study explicitly argues that the optimal ventilator setting is the one that minimizes the RR (87). On the other hand, the clinical literature also reports cases in which patients failed to trigger the ventilator on every inspiratory effort (39,58,69). In these cases, the reduction in the apparent RR of the ventilator (RR_{vent}) may reflect patient-ventilator asynchrony (PVA) rather than unloading of the respiratory pump. The mechanisms leading to PVA have been studied in some detail in a computer simulation (156). However, that study employed a comparatively simple model of respiratory mechanics with a single respiratory system resistance for inspiration and expiration and was focused primarily on patients with muscle weaknesses or severely decreased respiratory drive.

The motivation for the study described in this section was to use the computer model described in section 3.1 to examine the mechanisms and determining factors of asynchrony between a mechanical ventilator in flow-triggered PSV mode and patients with adequate respiratory drive, but severe airway obstruction and expiratory flow limitation.

3.4.2 Methods

Two actively breathing COPD patients were simulated using the computer model described in section 3.1. The spontaneous respiratory rate was fixed at $RR_{spont} = 30 \text{ min}^{-1}$ and cardiogenic oscillations were absent ($C_{CE} = C_{CP} = 0$) in both patients. The rate of increase in P_{neur} determining the patient's respiratory drive was adjusted as described

below. In subject 1, all other model parameters were set to the mean values given in Table 3.1 in order to simulate an average COPD patient. Patient 2 differed from patient 1 in that χ was increased by 30% to simulate very severe flow limitation.

Both simulated patients breathed with the support of a flow-triggered pressure support ventilator as described in section 3.1.2 using four PEEP levels from 0 to 7.5 cmH₂O and 20 PS levels from 1 to 20 cmH₂O. The ventilator's trigger and off-trigger thresholds were set to 0.05 L/s and 0.02 L/s, respectively. Each simulation consisted of 36 breathing efforts. The rate of increase in P_{neur} was set to 20 cmH₂O s⁻¹ and resulted in a peak inspiratory P_{neur} of 12 cmH₂O, which equaled approximately 40% of the maximal inspiratory effort of an average patient requiring ventilatory support (156). As in my previous simulations, the initial lung volume was set equal to an estimate of the expected dynamic hyperinflation to accelerate convergence towards a stable breathing pattern, and the first six breaths were discarded to assure that dynamic hyperinflation was completely developed (see section 3.2.2).

Over the remaining 30 breathing efforts, comprising one minute of data, the respiratory rate of the ventilator (RR_{vent}) was obtained from the flow trace and the average delay from the onset of a triggering inspiratory effort to the onset of inspiratory flow (Δt_{trig}) was computed. Δt_{trig} included both delays due to neuromuscular dynamics (approximately 100 msec) and the trigger delay caused by dynamic hyperinflation. \dot{V}_e was determined, and the parenchymal stress was evaluated (in units of pressure) according to

$$P_{stress} = \max(P_{alv} - P_{es}) \quad (3.16)$$

as an index for the risk of barotrauma.

3.4.3 Results

The results for patient 1 breathing without PEEP are shown by the solid circles in Fig. 3.17. At low values of PS, RR_{vent} was equal to RR_{spont} (Fig. 3.17a). As PS exceeded a threshold of 13 cmH₂O, RR_{vent} suddenly deviated from RR_{spont} and dropped to 15 min⁻¹. Analysis of the pressure and flow waveforms showed that for PS greater than 14 cmH₂O, this patient only succeeded in triggering the ventilator with every second inspiratory effort, as shown in Fig. 3.18 for a PS of 15 cmH₂O.

At PS levels below 14 cmH₂O, Δt_{trig} increased monotonically with increasing PS (Fig. 3.17b). At PS = 13 cmH₂O, i.e., just below the PVA threshold, Δt_{trig} was 0.78 sec, which is only slightly less than the duration of the inspiratory effort (0.82 sec). As PS increased further, Δt_{trig} dropped to a minimum of 0.5 sec at PS = 15 cmH₂O and subsequently increased slowly with increasing PS. As shown in Fig. 3.17c, \dot{V}_e generally increased with increasing PS. However, a slight decrease occurred when PS ranged from 13 to 15 cmH₂O, i.e., around the PVA threshold.

The application of PEEP shifted the PVA threshold slightly towards higher values of PS (other symbols in Fig. 3.17a). Furthermore, Δt_{trig} was reduced substantially at most values of PS and \dot{V}_e increased considerably in all cases as PEEP was increased (Fig. 3.17b and c, respectively).

P_{stress} showed a step increase of approximately 20% whenever an PVA occurred, but increased only mildly with increasing PS and PEEP otherwise (Fig. 3.17d). In general, P_{stress} in this patient remained far below the upper deflection point of the static V-P curve of the lungs and hence did not indicate an important risk of barotrauma (121).

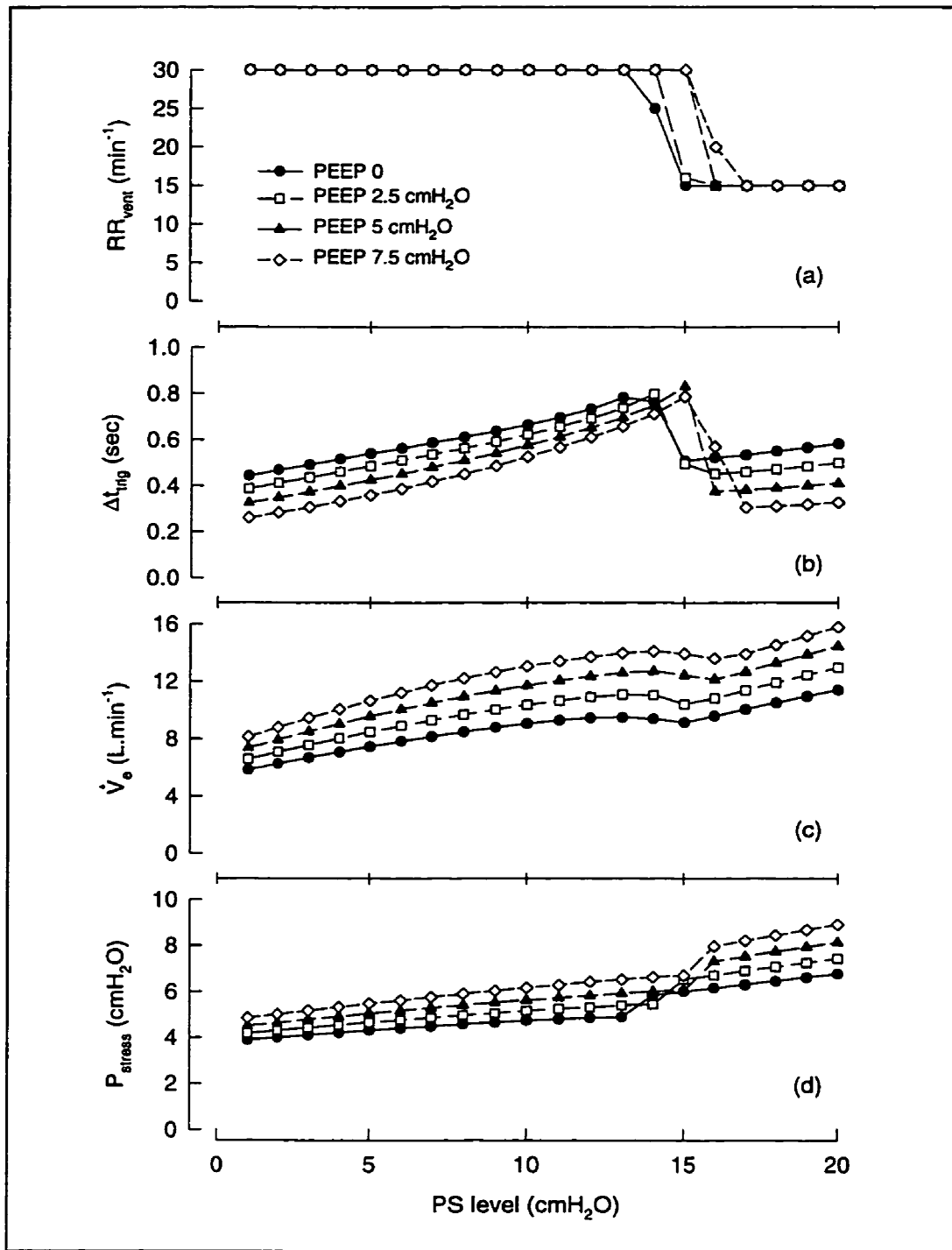


Fig. 3.17: RR_{vent}, trigger delay, minute ventilation and trans-alveolar pressure in the simulated average COPD patient (patient 1). See text for details.

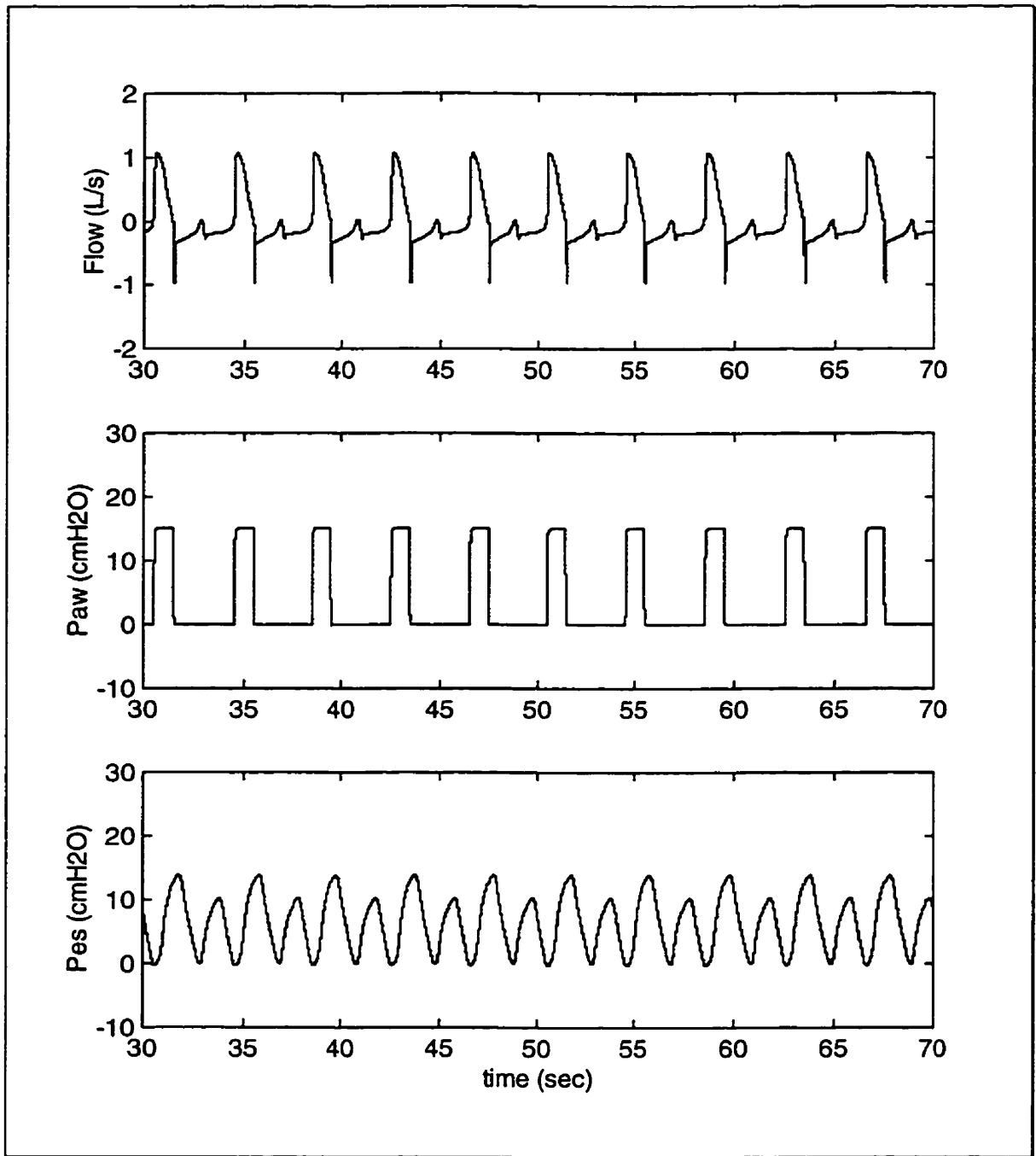


Fig. 3.18:
Sample traces for the simulated average COPD patient (patient 1) at a PS of 15 cmH₂O and a PEEP of 0. The patient only managed to trigger the ventilator with every second inspiratory effort.

At low levels of PS, the more severely flow limited patient 2 behaved similarly to patient 1 (Fig. 3.19). However, the PVA threshold was shifted towards lower PS levels and showed a stronger PEEP dependence than in patient 1. As shown in Fig. 3.19a, PVA occurred at as low a PS level as 8 cmH₂O when no PEEP was applied. Not surprisingly, Δt_{trig} was increased and \dot{V}_e was reduced in patient 2 relative to patient 1. P_{stress} differed very little between patients 1 and 2 at low levels of PS.

At higher levels of PS, patient 2 exhibited behavior that was not observed in patient 1. At a PEEP of 0 (solid circles in Fig. 3.19), RR_{vent} dropped to one third of RR_{spont} as PS was raised beyond 14 cmH₂O. As before, this drop in RR_{vent} was associated with a considerable drop in Δt_{trig} , a slight reduction of \dot{V}_e and a step increase in P_{stress} of approximately 20%. Analysis of the pressure and flow traces showed that in the range of PS from 15 to 19 cmH₂O, this patient only managed to trigger the ventilator with every third inspiratory effort. As PS was raised to 20 cmH₂O, RR_{vent} dropped again to 8 min⁻¹. However, both Δt_{trig} and \dot{V}_e failed to drop in this case, while P_{stress} increased by 30% to a value exceeding 10 cmH₂O. In this case, the ventilator sometimes failed to switch from inspiration to expiration over an entire expiratory phase of the patient. Thus some ventilator inspirations extended over more than one full period of patient effort (Fig. 3.20). The duration of the ventilator expiration was variable, and up to four inspiratory efforts were necessary before the patient succeeded in triggering the next inspiration.

At lower levels of PS, the effects of PEEP in patient 2 were similar to those in patient 1. When a PEEP of 2.5 cmH₂O was applied, a second drop in RR_{vent} occurred at a PS of 18 cmH₂O. In this case, only every third effort triggered the ventilator, but no off-trigger problems were observed. In contrast, at PEEPs of 5 and 7.5 cmH₂O the second drop in RR_{vent} was associated with off-trigger problems. These cases resulted in complex phasic breathing patterns, as illustrated in Fig. 3.21 for the case of a PS of 20 cmH₂O and a PEEP of 5 cmH₂O.

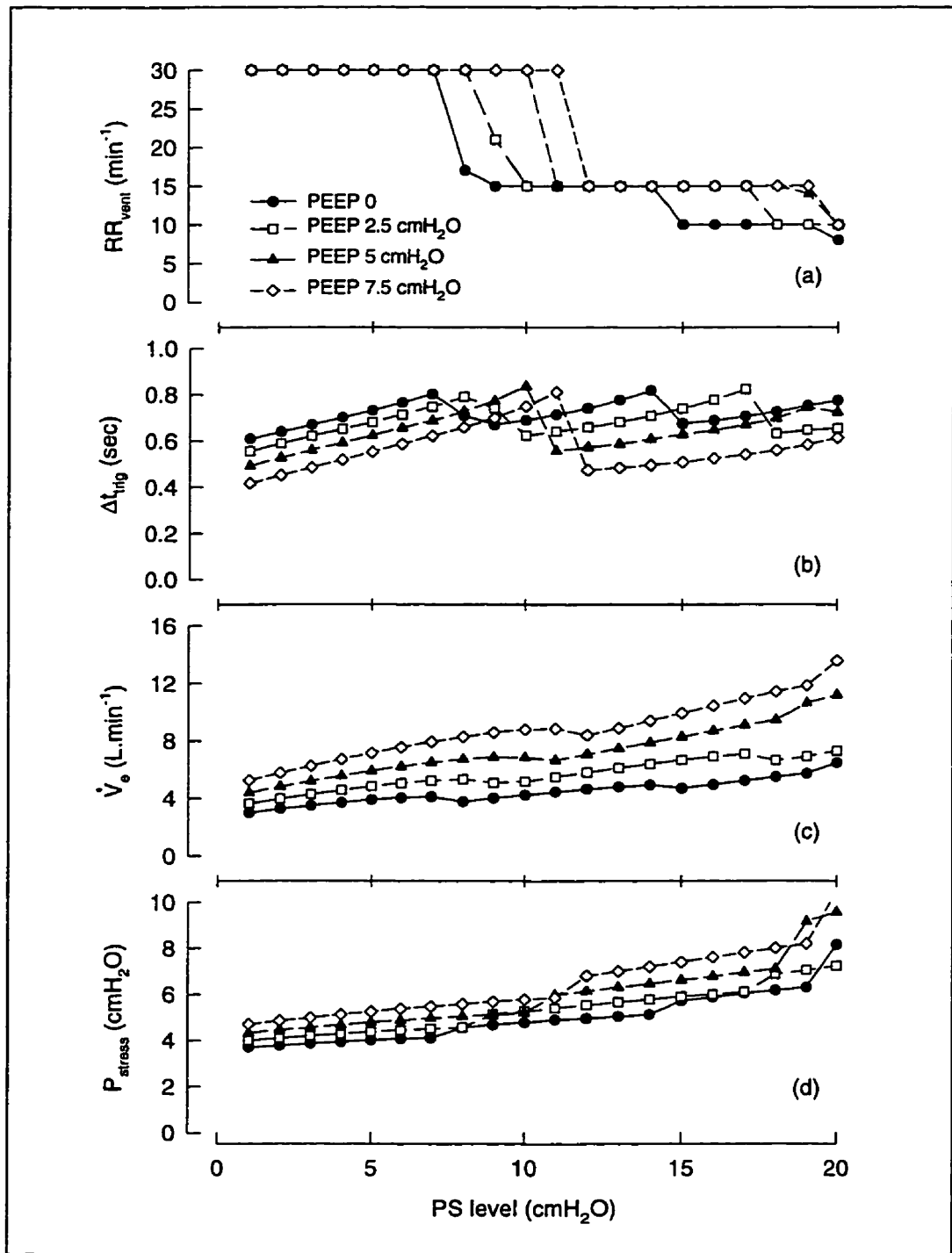


Fig. 3.19: RR_{vent}, trigger delay, minute ventilation and trans-alveolar pressure in the simulated very severely flow limited COPD patient (patient 2). See text for details.

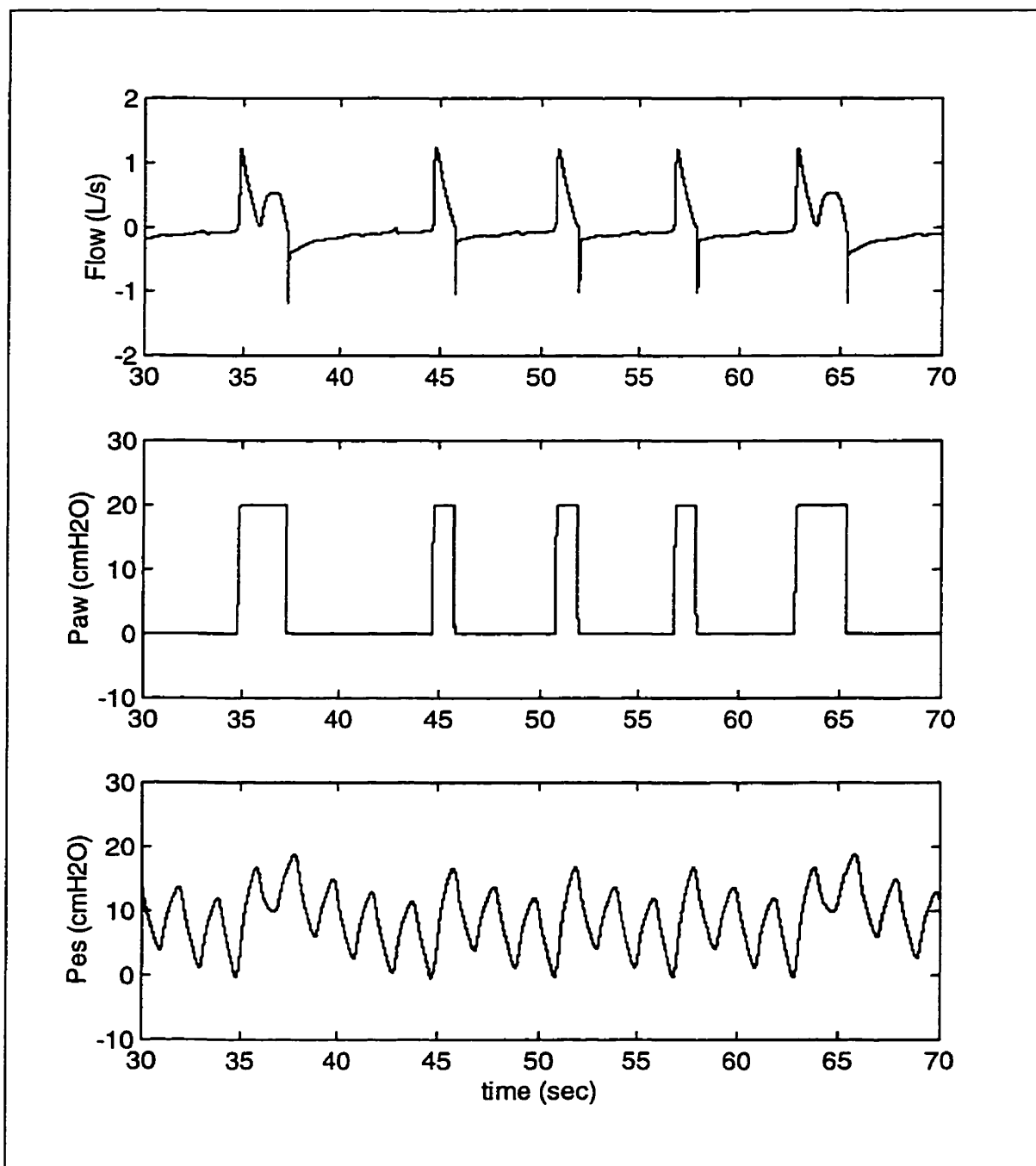


Fig. 3.20:
Sample traces for the simulated very severely flow limited COPD patient (patient 2) at a PS of 20 cmH₂O and a PEEP of 0. In this case, the patient was unable to properly trigger or off-trigger the ventilator, resulting in a phasic breathing pattern.

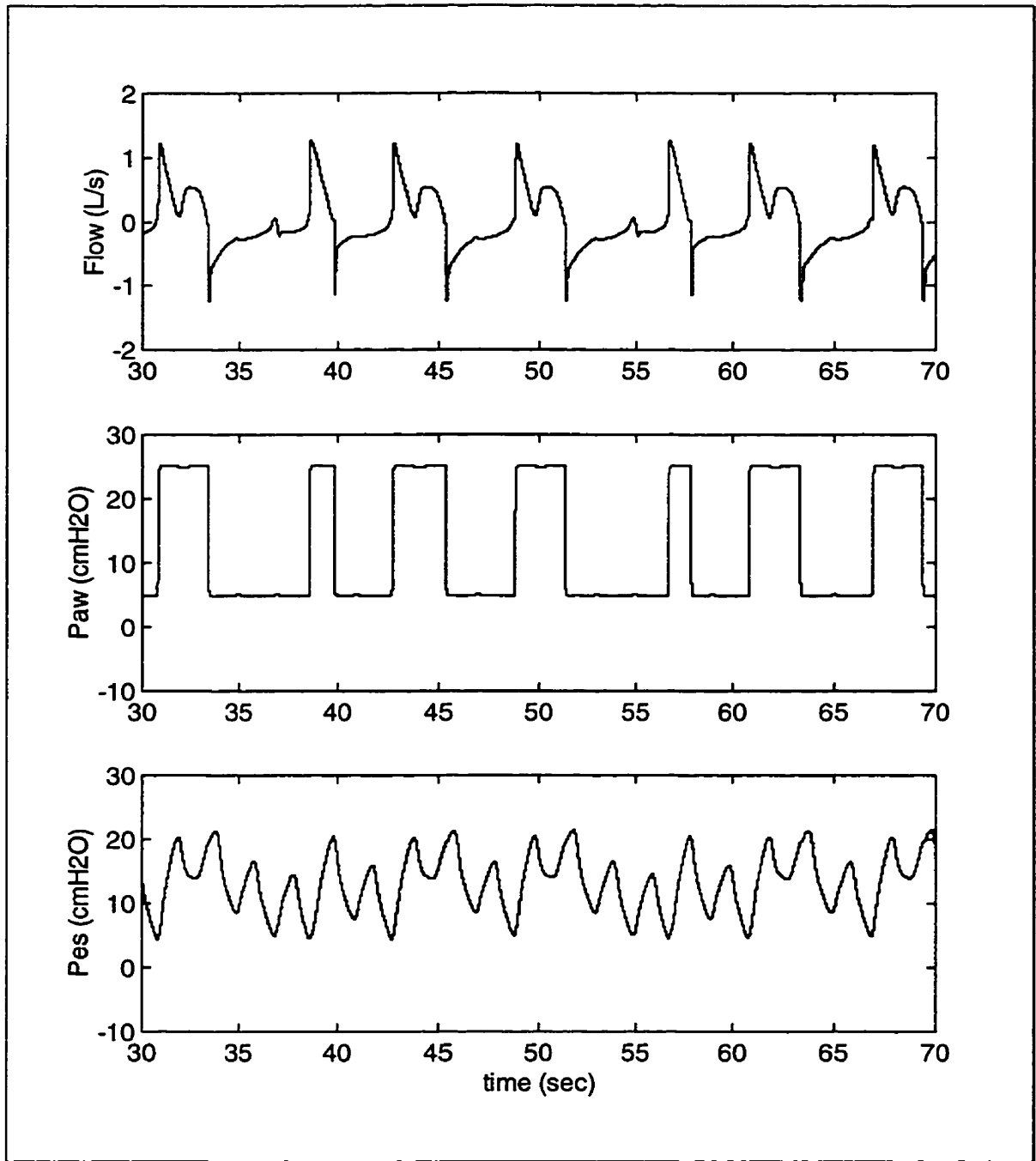


Fig. 3.21:

Sample traces for the simulated very severely flow limited COPD patient (patient 2) at a PS of 20 cmH₂O and a PEEP of 5 cmH₂O. The patient is frequently unable to off-trigger the ventilator, resulting in a complete loss of synchrony between the patient and the ventilator.

3.4.4 Discussion

Rapid shallow breathing is a characteristic sign of respiratory distress. Thus, the reduction of RR_{vent} during PSV was initially interpreted as an indication of relief of the patient's distress and hence considered beneficial (87). On the other hand, several more recent studies have demonstrated both in critically ill patients (39,58,69) and in a computer simulation (156) that the reduction in RR_{vent} during PSV may be related to asynchronies between the patient and the ventilator rather than to true reduction of RR_{spont} . The results of this simulation study confirm the previous findings in a more systematic and quantitative fashion and permit some additional insights.

When PVA are studied *in vivo*, some uncertainties remain as to what extent the observed PVA are caused or amplified by an adaptation of the patient's respiratory controller to the periodic unloading of the respiratory pump by the ventilator. For example, it is conceivable that the inspiratory effort following an assisted breath is weaker than the inspiratory effort following an episode of trigger failure. Also, PVA may in part be caused by technological limitations of the mechanical ventilator employed. Practical limitations of the ventilatory equipment can, for example, be observed in Figure 2 of (39). The ventilator employed in that study failed to produce a square waveform in P_{aw} , and the rise time and steady state error amounted to approximately 500 msec and 3 cmH₂O, respectively. For these reasons, it is useful to investigate the mechanisms of PVA in computer simulations, where neural feedback can be excluded and RR_{spont} can be fixed.

The principal mechanisms of PVA have previously been investigated in a computer simulation by Younes (156). However, this study focused on patients with muscle weaknesses or severely decreased respiratory drive and employed a comparatively simple model of respiratory mechanics. Specifically, a single linear respiratory system resistance was employed for inspiration and expiration, stress adaptation in the lung and chest wall were neglected, no PEEP was applied and expiration was assumed to be entirely passive. In comparison, the present study of PVA uses a computer simulation of COPD patients

with severe expiratory flow limitation in the presence of expiratory muscle activity at various PEEPs.

The basic mechanisms that led to PVA in the present study follow the discussion in (156). Briefly, progressively raising the PS level increased V_t and hence \dot{V}_e (Fig. 3.17 and Fig. 3.19). This augmented the amount of air left in the lungs and hence the threshold load at the onset of subsequent inspiratory efforts. With P_{musc} rising approximately linearly during most of the patient inspiration, Δt_{trig} increased and eventually became close to the total neural inspiratory time, so that the simulated patients only triggered the ventilator during the last fraction of their inspiratory efforts. In other words, the ventilator breaths were essentially almost 180° out of phase with the patients' efforts. With the next increase in PS, each ventilator breath inflated the patient by a small additional amount that sufficed to raise the threshold load at the onset of the next inspiratory effort to the point that the patient was no longer able to trigger the ventilator. Then, expiration was continued over an additional period of the neural output, causing RR_{vent} to drop to half of its initial value. At the end of this prolonged expiration, the threshold load was significantly reduced, so that the patient now succeeded in triggering the ventilator with a much smaller Δt_{trig} . This decrease in Δt_{trig} allowed for an increased inspiratory time that also raised V_t . Consequently, \dot{V}_e remained almost constant around the PS where PVA occurred (Fig. 3.17c and Fig. 3.19c). This result suggests that the pronounced drop in \dot{V}_e associated with PVA in a previous case study (39) must have been associated with secondary influences over the $2^{1/2}$ hour observation period in that study.

In the very severely flow limited patient 2, further drops in RR_{vent} were encountered at higher levels of PS. Some of these represented a reoccurrence of trigger problems discussed above so that only every third or fourth inspiratory effort triggered a machine breath. However, in three cases a qualitatively different behaviour was observed when the ventilator failed to off-trigger during the patient's entire expiratory phase of the patient, so that those ventilator inspirations extended over more than one full period of the patient effort (Fig. 3.20 and Fig. 3.21). In fact, patient data showing this exact behaviour were presented in Figure 3 (breaths 5 and 8) of (39), although the authors did not explicitly

address this issue. Similar episodes of complex or entirely aperiodic breathing patterns have also been reported in a number of very severely diseased COPD patients who were transferred to the ICU of the Montreal Chest Hospital because of failure to wean from mechanical ventilation (Dr. Peter Goldberg, personal communication). Presumably, the balance between the pressure applied by the ventilator and the elastic recoil of the respiratory system in these cases was such that even the sum of the pressures generated by the elastic lung recoil and the expiratory musculature was not sufficient to slow inspiratory flow below the off-trigger threshold. When such prolonged inspirations occurred, P_{stress} increased to approximately twice its baseline value, generating an increased risk of barotrauma, while P_{stress} remained uncritical under all other circumstances (Fig. 3.17d and Fig. 3.19d).

In earlier studies, it has been argued repeatedly that PVA during PSV can be detected by observing P_{aw} or flow traces because non-triggering inspiratory efforts retard expiratory flow (39,156). However, this was not always true in my simulations of the more severely flow-limited patient 2 (Fig. 3.20 and Fig. 3.21). Presumably, in some cases the “pressure waterfall” of expiratory flow limitation was large enough to completely conceal any effect of the inspiratory effort. Also, at very high lung volumes following a machine inspiration the inspiratory muscles may be operating under such mechanically disadvantageous conditions that the deflections in P_{musc} are very small in the first place (159). In the latter case, missed inspiratory efforts may even be difficult to detect from esophageal pressure traces. Clearly, the missed breaths should not be reflected in P_{aw} because a properly functioning ventilator should accurately control P_{aw} .

The ultimate question to be addressed in the context of PVA is how to optimally choose the PSV settings. The present study shows, however, that even when an almost ideal implementation of a pressure support ventilator is used, PVA may still arise. This means that the problem of PVA during PSV cannot be overcome by simply improving the design of pressure support ventilators. Thus, we are left with the choice of adjusting the ventilator settings above or slightly below the PVA threshold. In the first case, a considerable fraction of the patient efforts are wasted because they fail to trigger the

ventilator, but the patient is externally stabilized, i.e., respiration is slower and deeper. In the second case, RR_{vent} matches RR_{spont} , but Δt_{trig} is high and patient and ventilator breathe almost 180 degrees out of phase. In a recent clinical study comparing both options (97), the patients' blood gases were worst at the lowest PS level where PVA were least pronounced. The best blood gases were obtained at an intermediate PS level, which was equivalent to an intermediate prevalence of PVA.

In summary, these findings confirm the conclusion of an earlier study that patient-ventilator interactions in patients with COPD are a complex matter (77). In general, an assisting mechanical ventilator together with a severely flow limited patient forms a dynamic system with multiple degrees of freedom and several strong nonlinearities, e.g., the patient's expiratory flow limitation and V-P relationship and the ventilator's trigger and off-trigger mechanisms. Such higher-order nonlinear dynamic systems can exhibit complex period or chaotic behaviour and are extremely difficult to control because a small change in one of the parameters can significantly alter the overall system behaviour (50). Thus, a globally valid way of determining the optimal PSV settings in patients with severe expiratory flow limitation may not exist. Most likely, the best choice of the ventilator settings depends of the actual characteristics of the patient and varies quite considerably with time. This suggests that in clinical practice, the ventilator settings during PSV should be verified and updated as frequently as possible.

4.

THORACIC IMAGING USING ELECTRICAL IMPEDANCE TOMOGRAPHY

The potential of EIT as a method to provide clinically useful images of the thorax has repeatedly been demonstrated (see section 2.4.6). However, the poor resolution of EIT and the restrictions of dynamic imaging remain limiting factors for the precision and clinical usefulness of the images obtained. This chapter describes research that I have conducted to investigate factors limiting the quality of static EIT images, and to develop improved static EIT image reconstruction techniques. In section 4.1, the magnitude of inaccuracies of first-order Finite Elements is investigated and the implications for static EIT are discussed. In section 4.2, a computer simulation is introduced that employs a computational phantom and a reconstruction algorithm based on the Finite Element method and Gauss-Newton optimization. This simulation is used to examine the effects of the current pattern and of a central reference electrode on the reconstruction error. Finally, higher-order isoparametric Finite Elements for the EIT forward solution are derived in section 4.3, and the accuracy of the simplest version of this type of element is evaluated.

For all of this chapter, the body to be imaged was assumed to be of cylindrical geometry with a large enough extension in the axial direction that a central slice could be modeled with sufficient accuracy in two dimensions.

4.1 A critical analysis of the Finite Element method for static EIT

4.1.1 Motivation

The accuracy of the forward solution is of great importance for the iterative solution of nonlinear inverse problems because the repetitive evaluation of the forward solution allows even small errors to accumulate. As described in section 2.4.3, FEs are advantageous for the EIT forward solution because of their geometrical flexibility. However, the accuracy of the FE method may still be a limiting factor for static EIT. The purpose of this study was to evaluate the accuracy of the FE method by comparing the boundary voltage estimates obtained from a circular FEM to an analytical solution for the same geometry.

4.1.2 Methods

Analytical solution

In order to compute the analytical solution of the electrical potential on the boundary (φ_b), consider a circular phantom of radius r_0 and background conductivity σ_{bg} with a centered circular object of radius r_{obj} and conductivity σ_{obj} (Fig. 4.1). Furthermore, let the Fourier series

$$j_s(\theta) = \sum_{n=1}^{\infty} C_n \cos(n\theta) + S_n \sin(n\theta) \quad (4.1)$$

represent a current pattern that satisfies Eq. 2.5 for θ as shown in Fig. 4.1. Then, according to (45,73), φ_b can be computed from

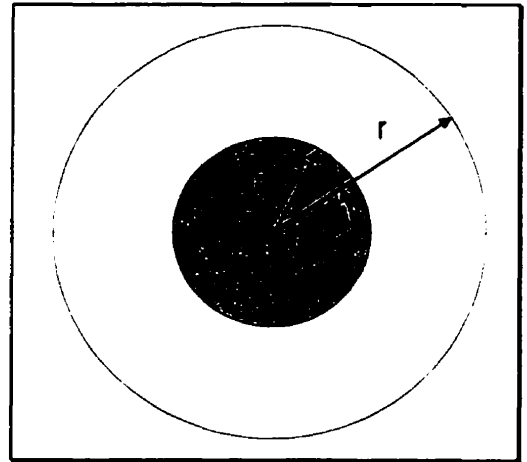


Fig. 4.1:
Circular geometry for the analytical solution.

$$\varphi_b(\theta) = -\sum_{n=1}^{\infty} \frac{1}{\sigma_{bg} n} \cdot \frac{1 - \sigma_{rel} R^{2n}}{1 + \sigma_{rel} R^{2n}} [C_n \cos(n\theta) + S_n \sin(n\theta)], \quad (4.2)$$

where $R = r_{obj}/r_0$, and

$$\sigma_{rel} = \frac{\sigma_{obj} - \sigma_{bg}}{\sigma_{obj} + \sigma_{bg}}. \quad (4.3)$$

An approximate numerical solution for φ_b is possible if the sum in Eq. 4.2 is finite and can be approximated by a manageable number of terms. If the electrodes are assumed to be very small, the first projection of the opposite current pattern can be expressed by

$$j_s(\theta) = \delta(\theta) - \delta(\theta - \pi), \quad (4.4)$$

where δ represents the Dirac delta function. Because this is an even function in θ , all S_n vanish and the Fourier series is completely described by the C_n coefficients that are found to be

$$C_n = \frac{1}{\pi} [\cos(n\pi) - 1] = \begin{cases} -\frac{2}{\pi}, & n \text{ odd;} \\ 0, & n \text{ even.} \end{cases} \quad (4.5)$$

Substitution of these Fourier coefficients into Eq. 4.2 yields the infinite series representation of φ_b . Unfortunately, the resulting φ_b is not finite for all combinations of R and θ . For example, at $R = 0$ and $\theta = 0$, we find

$$\varphi_b \propto \sum_{n=1}^{\infty} \frac{1}{2n-1}, \quad (4.6)$$

which is infinite.

However, φ_b is finite for all combinations of R and θ if the electrodes are modeled to have a finite dimension and j_s is written as

$$j_s(\theta) = \frac{D}{2\pi} [\Pi(\frac{D}{2\pi}\theta) - \Pi(\frac{D}{2\pi}(\theta - \pi))]. \quad (4.7)$$

Here, D is a parameter that prescribes the finite size of the electrode as a fraction of the phantom perimeter, and the rectangular function

$$\Pi(x) = \begin{cases} 0, & |x| > \frac{1}{2} \\ 1, & |x| \leq \frac{1}{2} \end{cases} \quad (4.8)$$

models the electrodes such that in the interval $-\pi/D < \theta < \pi/D$ the current density is uniform and positive and a current of 1 mA is injected, while an equal and opposite current density is applied to the interval $\pi-\pi/D < \theta < \pi+\pi/D$. Because j_s as described by Eq. 4.7 is even all the S_n vanish, so that its Fourier series is completely described by the C_n coefficients. Using Eq. 4.7, the integral that defines the C_n can be written as

$$C_n = \frac{1}{\pi} \int_0^{2\pi} \frac{D}{2\pi} \left[\Pi\left(\frac{D}{2\pi}\theta\right) - \Pi\left(\frac{D}{2\pi}(\theta - \pi)\right) \right] \cos(n\theta) d\theta, \quad (4.9)$$

which reduces to the integrals over the electrode segments. Thus, we can write

$$C_n = \frac{D}{2\pi^2} \left[\int_{-\frac{\pi}{2}}^{\frac{\pi}{2}} \cos(n\theta) d\theta - \int_{\pi-\frac{\pi}{2}}^{\pi+\frac{\pi}{2}} \cos(n\theta) d\theta \right]. \quad (4.10)$$

Making use of the symmetry of the trigonometric functions, we find

$$C_n = \frac{D}{n\pi^2} \left[\sin\left(\frac{n\pi}{D}\right) - \sin\left(n\pi + \frac{n\pi}{D}\right) \right] \\ = \begin{cases} 0, & n \text{ even;} \\ \frac{2D}{n\pi^2} \sin\left(\frac{n\pi}{D}\right), & n \text{ odd.} \end{cases} \quad (4.11)$$

Substitution of the odd terms into Eq. 4.2 and rearranging the terms yields

$$\varphi_b(\theta) = -\frac{2D}{\sigma_{bg}\pi^2} \sum_{n=1}^{\infty} \frac{\cos[(2n-1)\theta]}{(2n-1)^2} \cdot \frac{1 - \sigma_{rel}R^{4n-2}}{1 + \sigma_{rel}R^{4n-2}} \sin\frac{(2n-1)\pi}{D}. \quad (4.12)$$

The finiteness of φ_b for the current pattern defined by Eq. 4.7 can be established as follows. First,

$$\lim_{n \rightarrow \infty} \left\{ \frac{\cos[(2n-1)\theta]}{(2n-1)^2} \cdot \frac{1 - \sigma_{rel}R^{4n-2}}{1 + \sigma_{rel}R^{4n-2}} \right\} = 0. \quad (4.13)$$

Furthermore, because of the periodicity of the sine function there exists a bound B such that

$$\left| \sum_{n=N_1}^{N_2} \sin\left(\frac{(2n-1)\pi}{D}\right) \right| < B \quad (4.14)$$

for any N_1 and N_2 . Together, these conditions are sufficient to ensure that Eq. 4.12 is finite as per Dirichlet's convergence criterion (141).

In the present study, the sum in Eq. 4.12 was approximated by the sum over the first 1024 terms. Under all conditions that were used in this study, doubling the number of terms changed the rms-value of φ_b by less than 0.1%.

FEM phantoms

In this study, the EIT boundary condition (Eq. 2.4) was modeled by linear approximation functions that were defined in analogy to Eq. 2.10. Hence, unlike other EIT studies (3,96,154), the \mathbf{T} matrix in Eq. 2.11 did not equal the identity matrix, but was derived as follows.

Let the boundary of the FEM be represented by a ring of N_b one-dimensional first-order FEs. In analogy to the FEM derivation in section 2.4.3, the functional of the Helmholtz equation (Eq. 2.9) for the boundary condition (Θ_b) can be expressed as

$$\Theta_b = \oint \varphi_b j_s dS = \varphi_{nb}^T \mathbf{T}_b \mathbf{j}_{nb}, \quad (4.15)$$

where φ_{nb} and \mathbf{j}_{nb} denote the values of φ and j_s at the boundary nodes, respectively, and \mathbf{T}_b captures the geometry of the ring of one-dimensional FEs. Furthermore, the vector of the currents injected at the boundary nodes can be expressed as

$$\mathbf{i}_{nb} = \mathbf{U} \mathbf{j}_{nb}, \quad (4.16)$$

where \mathbf{U} is a diagonal matrix that contains the integrals of the linear approximation functions and the connectivity of the boundary FEs. Then, Eq. 4.15 can be written as

$$\Theta_b = \varphi_{nb}^T \mathbf{T}_b \mathbf{U}^{-1} \mathbf{i}_{nb}. \quad (4.17)$$

Finally, the boundary nodes are mapped onto the nodes of the FEM by the (N_b, N_n) matrix \mathbf{C}_b , which yields

$$\Theta_b = \varphi_n^T \mathbf{C}_b^T \mathbf{T}_b \mathbf{U}^{-1} \mathbf{C}_b \mathbf{i}_n \quad (4.18)$$

and

$$\mathbf{T} = \mathbf{C}_b^T \mathbf{T}_b \mathbf{U}^{-1} \mathbf{C}_b. \quad (4.19)$$

The five circular FEMs that were used in this study are shown in Fig. 4.2, and their characteristics are summarized in Table 4.1. In Fig. 4.2, the small solid circles denote the locations of the electrodes ($N_e = 16$) on the FEM boundary. The admittance of each

triangular FE was assumed to be constant and real, such that the tissue properties in each phantom were completely described by the vector of the element conductivities, σ_p .

Table 4.1:
Characteristics of the five FEMs used in this study.

| Mesh | N_σ | N_n | N_b | N_e |
|------|------------|-------|-------|-------|
| (a) | 38 | 28 | 16 | 16 |
| (b) | 86 | 60 | 32 | 16 |
| (c) | 182 | 124 | 64 | 16 |
| (d) | 374 | 252 | 128 | 16 |
| (e) | 758 | 508 | 256 | 16 |

Quantification of the FEM inaccuracies

In this study, the inaccuracies of the FEM were quantified both by computing the root-mean-square (rms) potential difference between φ_n and φ_b at the electrode locations (Δv_{rms}), and in terms of the signal-to-noise ratio (SNR) they produce according to

$$SNR = 20 \cdot \log_{10} \frac{\varphi_{e,rms}}{\Delta v_{rms}}. \quad (4.20)$$

where, φ_e represents the values of φ_b at the electrode locations. The current density on the boundary was set as described by Eq. 4.7. Unless otherwise stated, D equaled 256, which is equivalent to an electrode diameter of 3.7 mm for a phantom diameter of 30 cm.

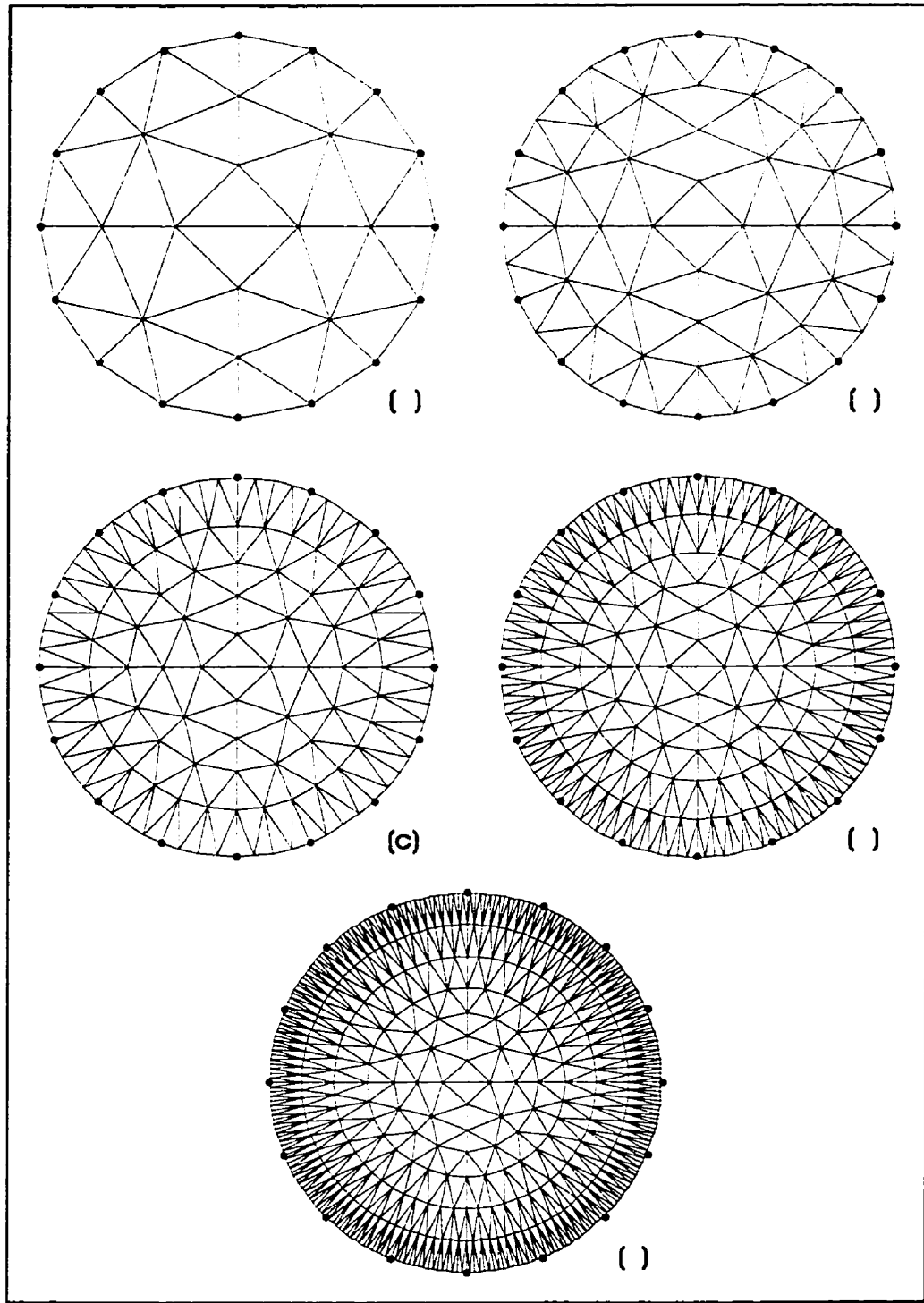


Fig. 4.2:
The five phantom FEMs. The small solid circles denote the sixteen electrode locations.
See Table 4.1 for details.

Protocols

(i) *Boundary voltages of a homogeneous phantom*

The FEM inaccuracies were evaluated for all five phantoms using a homogeneous conductivity distribution of $\sigma_{bg} = \sigma_p = 1$ mS. Because the greatest errors are likely to occur at the site of current injection where the current density is largest, Δv_{rms} and SNR were computed twice for each FEM. First, all N_e data points were used, which is equivalent to the two-electrode method (142). Subsequently, Δv_{rms} and SNR were evaluated from $N_e - 2$ data points, excluding the potentials at the boundary nodes where the current source and sink were located (four-electrode method). To investigate the effects of the electrode size, the complete protocol was repeated with a value of $D = 512$, which is equivalent to an electrode diameter of 1.85 mm on a 30 cm phantom.

(ii) *Centered targets in a circular phantom*

The inaccuracies of FEM (b) (Fig. 4.2/Table 4.1) were evaluated for four circular targets that were centered in a medium of $\sigma_{bg} = 1$ mS. For targets A and B, the radius r_{obj} was chosen such that R assumed a value of 0.1862, so that the target area equaled the area of the two central elements of the FEM. Target A represented a small object that was more conductive than the background ($\sigma_{obj} = 10$ mS), while target B was chosen 10 times more resistive than the background ($\sigma_{obj} = 0.1$ mS). For targets C and D, r_{obj} was increased such that R became 0.4744, which matched the area of the two innermost layers of FEs. The object conductivities were again set to 10 mS and 0.1 mS for targets C and D, respectively. As in the previous protocol, Δv_{rms} and SNR were evaluated for both the two-electrode and the four-electrode methods.

4.1.3 Results

The results for protocol (i) are shown in Fig. 4.3. In general, Δv_{rms} dropped and the SNR became larger with increasing N_n . However, the rate at which the accuracy of the FEM improved dropped considerably as N_n became larger. Both Δv_{rms} and the SNR demonstrated substantially larger inaccuracies for the two-electrode method than for the

four-electrode method in all five FEMs, indicating that the greatest errors were encountered at the sites of current injection. For the two-electrode method, the SNR was further reduced and Δv_{rms} was further increased when D was raised from 256 to 512, halving the electrode size in the analytical solution. In contrast, altering D had a negligible effect on the FEM inaccuracies when the four-electrode method was used.

The values of Δv_{rms} and the SNR for the four targets of protocol (ii) are shown in Table 4.2 together with their values for the homogeneous case (first row in Table 4.2). The values of both Δv_{rms} and SNR did not change substantially for any of the targets, although the fluctuation in SNR were somewhat greater for the four-electrode method. As above, the FEM inaccuracies were reduced dramatically as the four-electrode method was used in lieu of the two-electrode method.

Table 4.2:
Inaccuracies of the FEM shown in Fig. 4.2(b) for the homogeneous case and
when four centered, circular targets were modeled. See text for details.

| Target | R | σ_{obj} (mS) | two-electrode | | four-electrode | |
|--------|--------|----------------------------|------------------------------|----------|------------------------------|----------|
| | | | Δv_{rms} (mV) | SNR (dB) | Δv_{rms} (mV) | SNR (dB) |
| none | 1 | 1 | 313.5 | 7.83 | 18.8 | 24.9 |
| A | 0.1862 | 10 | 319.0 | 7.45 | 11.0 | 29.0 |
| B | 0.1862 | 0.1 | 315.4 | 8.02 | 14.9 | 27.6 |
| C | 0.4744 | 10 | 316.7 | 6.39 | 15.3 | 22.4 |
| D | 0.4744 | 0.1 | 324.9 | 9.31 | 11.7 | 33.0 |

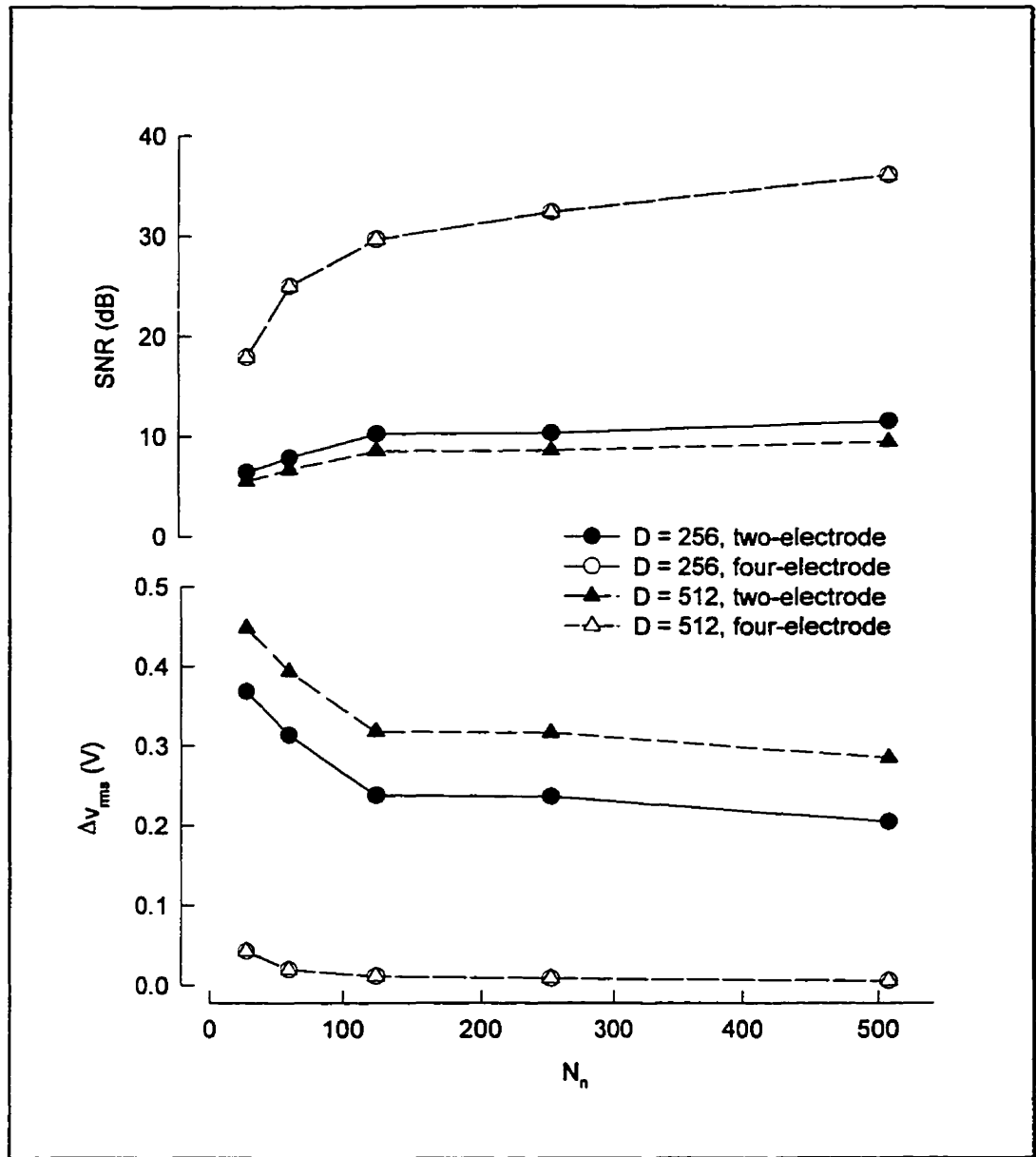


Fig. 4.3:

FEM inaccuracies with respect to the analytical solution for the homogeneous case. The circles represent data points where the standard finite element size was used for the analytical solution ($D = 256$), while the triangles represent smaller current electrodes ($D = 512$). Solid and open symbols represent the two- and four electrode method, respectively.

4.1.4 Discussion

The FE method has frequently been used to solve the EIT forward problem (3,24,96,123,153,154) because it provides good geometrical flexibility and does not require assumptions about the magnitude of the change in σ (as does, for example, the weighted backprojection method, see section 2.4.3). However, the data presented in this section show that the first-order FEs that are usually employed for EIT produce significant inaccuracies in the forward solution. These inaccuracies persisted even when FEMs with very large numbers of elements were used, and they were not altered substantially by conductive or resistive targets in the medium. In contrast, both Δv_{rms} and the SNR differed dramatically between the two-electrode method and the four-electrode method. This indicates that the largest differences between φ_n and φ_b were encountered at the sites of current injection. Strictly speaking, the results of this section are only valid for the opposite current pattern. However, because similar or even greater current densities occur near the electrodes when other current patterns with a single source and sink (such as neighbouring currents), the results of this study most likely are relevant for all single-source current patterns.

The accuracy of the FE forward solution is best evaluated by comparing the estimate of the boundary voltages to an analytical solution. However, it is important to assure that the analytical solution is accurate and reflects the real measurement situation as closely as possible. While the general analytical solution used in this study (Eq. 4.2) is valid for any current pattern that fulfills Eq. 2.5, it cannot be solved for point current sources because the value of the sum in Eq. 4.2 is infinite. This occurs because such electrodes produce a singularity in the current density, which would require infinite power and result in an infinite value of φ_b at the site of injection. To overcome this problem, I derived the analytical solution for a finite electrode size and opposite currents (Eq. 4.12). Provided that D is finite which is equivalent to a finite electrode size, Eq. 4.12 results in a finite-valued boundary potential vector.

The assumption of infinitesimally small current electrodes is also frequently made when the FEM for the EIT forward solution is developed. However, because this assumption is not valid in practice, I employed linear approximation functions for modeling the current density normal to the boundary of the first-order FEM. This approach does not assume an infinite power configuration and, in general, is more consistent with the FE methodology.

A finite and exact analytical solution exists for any current pattern that is based on trigonometric functions, such as the optimal current pattern (49), because these result in only a small number of non-zero Fourier coefficients. Trigonometric current patterns can also be modeled fairly accurately in the FEM if linear approximation functions are used for the current density normal to the boundary. Unfortunately, trigonometric current patterns are difficult to apply in practice. For example, if a limited number of small electrodes is used, significant gaps occur between the electrodes, such that the true j_s is a cosine-weighted set of impulses rather than a true cosine pattern. On the other hand, large electrodes impose a piecewise constant approximation of the cosine function and essentially short-circuit the potentials over considerable parts of the boundary. Also, the simultaneous use of multiple current sources requires precise calibration of all current sources to assure proper mutual phase-locking. Thus, the use of trigonometric current patterns is inadequate for evaluating the accuracy of the FE method because it is likely to result in an agreement between the analytic solution and the FEM that cannot be reproduced in practice.

The inaccuracies of the FEM are systematic errors, in contrast to the effects of random measurement noise. Nonetheless, they are quantified in terms of a SNR in this study in order to maintain a consistent terminology with subsequent sections of this chapter. In all scenarios that were examined in this study, the inaccuracies of the FEM produced SNRs of less than 40 dB. In comparison, the SNR due to the electrical characteristics of present EIT hardware amounts to approximately 60 dB (56,61). Thus, it is likely that in most EIT systems, the errors in static EIT image reconstruction are

dominated by the inaccuracies of the FEM rather than by the measurement errors of the EIT hardware.

As shown in Fig. 4.3, the FEM inaccuracies were reduced as the number of elements in the mesh was increased. However, the rate at which the accuracy of the FEM improved dropped considerably as N_n became larger. This may be counter-intuitive because, in general, the accuracy of estimates of electrical potentials obtained from FEMs are known to improve as the number of elements in the mesh increases. Indeed, increasing the number of FEs substantially reduces the average estimation error in Ω . However, as this study demonstrates, the effect of the mesh size is much weaker if the errors are evaluated only at the nodes representing the electrodes. In EIT, we employ only the potentials at these nodes to reconstruct images. Furthermore, the computational complexity increases as $N_n^{1.85}$ when sparse matrix techniques are used (150), so that the solution of FEM (e) takes approximately 213 times as long as the solution of FEM (a). For these reasons, increasing the number of elements in the FEM is not an efficient strategy for improving the precision of the EIT forward solution.

The SNR and Δv_{rms} remained roughly constant when centered conductive or resistive targets were used (Table 4.2). Presumably, this means that at least part of the FEM inaccuracies are independent of the conductivity distribution to be imaged. In a dynamic imaging situation (see section 2.4.2), these inaccuracies would cancel out, making the difference signal obtained from the FE forward solution more accurate than the absolute boundary voltage estimate. This may be one of the factors that explains why dynamic EIT imaging has been more successful than static EIT imaging to date.

In general, Δv_{rms} and the SNR were considerably improved when the four-electrode method was used instead of the two-electrode method, i.e., when the voltages at the sites of current injection were neglected. An analysis of the boundary voltage estimates showed that the errors at these nodes were always an order of magnitude larger than at any other point along the FEM boundary. Also, the error at the sites of current injection depended on the electrode size that was assumed for the analytical solution (solid symbols in Fig. 4.3), while no such dependence was noticeable for the four-electrode data (open symbols

in Fig. 4.3). This means that first-order FEMs are particularly bad at modeling the high current densities that occur in the vicinity of the current electrodes. In the literature, the four electrode method is often favored because it eliminates the effects of unknown impedances of the electrode-skin interface (117,142). However, the inaccuracies of the FEM approximation represent a second reason why the voltages at the sites of current injection should not be used for static EIT image reconstruction.

In summary, the data presented in this section show that first-order FEs are associated with numerical inaccuracies that are large enough to significantly disturb the reconstruction of static EIT images. These inaccuracies are particularly pronounced at the sites of current injection, and their effects can be diminished by neglecting the boundary potentials at the sites of current injection for the image reconstruction, i.e., by using the four-electrode method. In contrast, the data presented show that increasing the number of elements in the FEM is not an efficient way of improving the precision of the forward solution. Because the errors associated with first order FEMs present one of the important error sources for static EIT, it is likely that the accuracy of the forward solution needs to be improved considerably before high resolution static EIT images can be obtained.

4.2 Effects of current patterns and central electrodes on static EIT images of the thorax

4.2.1 Motivation

Most of today's EIT systems use 16 or 32 electrodes that are placed equidistantly in a linear array around the body segment to be imaged, with a single current source and sink being used to drive current through the body while the remaining electrodes measure the resulting voltages (12,56,72,134). The relative position of the current source with respect to the sink is arbitrary and can be anything from neighbouring to opposite currents (see section 2.4.2). It has been argued that opposite currents are advantageous because they provide a higher current density to the central regions (23,104). However, the ultimate current density distribution and hence the optimal current pattern depends on the nature of the objects to be imaged and the reconstruction algorithm employed (23). For dynamic imaging using weighted backprojection, it has been shown that neighbouring currents produce better-conditioned projection matrices than opposite currents (8). The effect of the source-sink constellation on the reconstruction error has not yet been systematically examined for static EIT image reconstruction using Newtonian optimization techniques, and for source-sink configurations other than opposite or neighbouring currents.

As described in section 2.4.2, the exclusive placement of electrodes on the body surface is thought to result in a relative lack of information about the central regions of the body, which contributes to the ill-conditioning of the inverse EIT problem. Consequently, it has been suggested that an additional central reference electrode (CRE) in the esophagus, i.e., close to the center of the thorax, could substantially improve the quality of thoracic EIT images (108). A CRE could also be placed in the stomach or the duodenum.

The goal of the work described in this section was to use a computer simulation to investigate the effects of single-source current patterns and a CRE on the convergence

rate and reconstruction error of static thoracic EIT images. Computer simulations are well-suited for this kind of analysis because the experimental parameters are under complete control and the reconstruction error can be evaluated accurately.

4.2.2 Methods

Phantoms and simulation

The FEM shown in Fig. 4.2(b) was used as a computational phantom to simulate an EIT measurement. This FEM was parameterized using two different conductivity distributions, as shown in Fig. 4.4. The phantom shown in Fig. 4.4(a) modeled a small central conductive target with a conductivity of 7 mS against a background with a conductivity of 1 mS (Central object phantom). For the phantom shown in Fig. 4.4(b), σ_p was chosen according to the literature to reproduce the principal features of the conductivity distribution in a cross-section of the human thorax (Thoracic phantom). The vector \mathbf{v}_m was computed by solving the phantom FEM for each projection and extracting and concatenating the boundary voltage measurements in analogy to Eqs. 2.16 and 2.17.

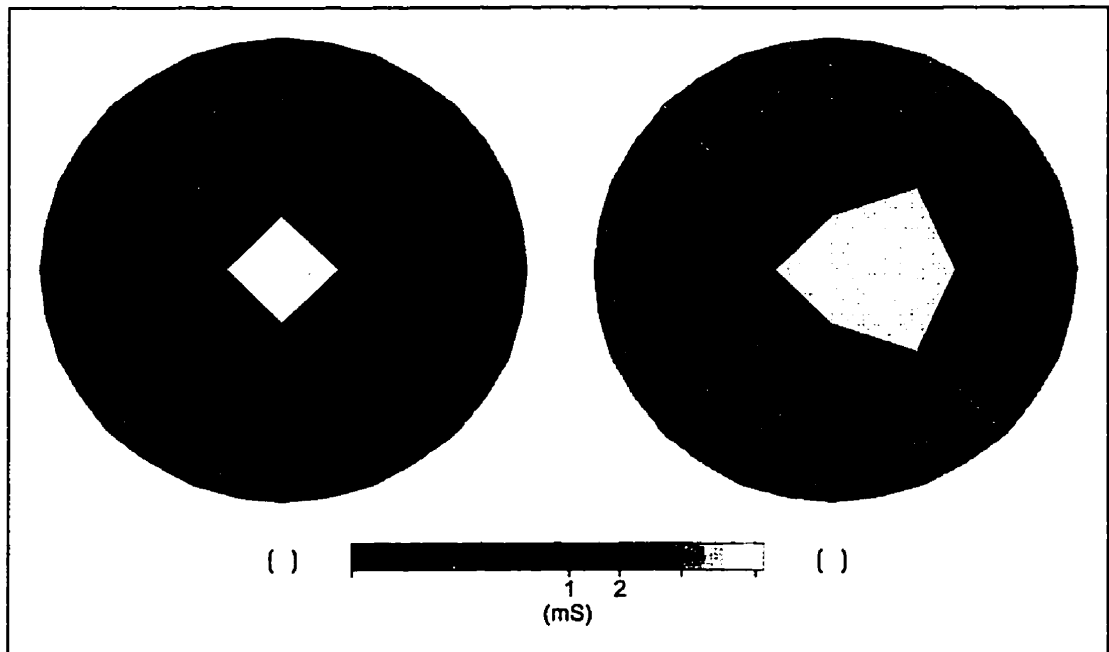


Fig. 4.4:
(a) Central object phantom. (b) Thoracic phantom.

Various levels of Gaussian white noise were added to \mathbf{v}_m in order to produce SNRs between 30 and 80 dB.

For all images shown in this section, a nonlinear mapping of σ onto a gray scale was employed in order to enhance the contrast. This mapping is illustrated at the bottom of Fig. 4.4.

Image reconstruction

Images were reconstructed from the simulated data as described in section 2.4.3. The forward problem was solved using a FEM that was topologically identical to the phantom FEM (Fig. 4.2b). To solve the inverse problem, the Jacobian matrix was computed according to Eqs. 2.28 and 2.30, and the GNM was employed as stated in Eq. 2.23. The step size parameter λ was adjusted by a quadratic line search, as follows.

If Eq. 2.23 is substituted into Eq. 2.19 and the result is substituted into Eq. 2.18, the objective function Φ can be expressed as a function of λ , i.e.,

$$\Phi = \Phi(\lambda). \quad (4.21)$$

Thus, Eq. 2.23 maps the multidimensional EIT optimization problem onto a one-dimensional optimization problem that is easier to solve. From the preceding major iteration i , we already know the value of Φ at $\lambda=0$ (Φ_0). Furthermore, the GNM employs derivatives up to second order, which means that it essentially fits a quadratic function to the multi-dimensional gradient information provided by \mathbf{J} and \mathbf{H} that possesses a minimum at $\lambda = 1$. Assuming that Φ at $\lambda = 1$ (Φ_1) vanishes completely, the one-dimensional $\Phi(\lambda)$ is parabolic and fully defined, so that we can estimate the slope of $\Phi(\lambda)$ at $\lambda = 0$ according to

$$\Phi'_0 = \left. \frac{\partial \Phi}{\partial \lambda} \right|_{\lambda=0} = 2\Phi_0. \quad (4.22)$$

In practice, of course, Φ_1 will not vanish because the Taylor series in Eq. 2.21 was truncated. However, we can now evaluate Φ_1 and use it with Φ_0 and Φ'_0 to fit a second order polynomial to $\Phi(\lambda)$. The location of the minimum of this polynomial (λ^*) is our new estimate of the optimal λ that minimizes $\Phi(\lambda)$.

Because the EIT optimization problem is highly nonlinear, this line search is faced with two potential problems. First, λ^* may still be too large to assure convergence. However, a measure of confidence can be obtained by comparing the actual value of $\Phi(\lambda^*)$ to its prediction obtained from the second order polynomial. If the two values differ significantly, another iteration of the line search (also termed subiteration) can be invoked, now fitting a second order polynomial to Φ_0 , Φ'_0 and $\Phi(\lambda^*)$. Second, Φ_1 may be so large that λ^* immediately becomes extremely small, which may produce unacceptably slow convergence rates. It is hence useful to specify a limit for the amount by which λ can be reduced in one subiteration.

In the present study, a maximal number of 20 major iterations was used for each image reconstruction. For each major iteration, the quadratic line search was started with an initial value of $\lambda = 1$ and was not allowed to reduce λ by more than 80% of its value within one subiteration. The line search was terminated when the true value of $\Phi(\lambda^*)$ exceeded its predicted value by less than 5%, or after five subiterations were completed.

Convergence criterion

In general, the iterative image reconstruction technique derived above may behave in three distinct ways. First, the algorithm may fail to reduce Φ , i.e., diverge. Second, the solution may converge towards a local minimum in Φ where σ does not reproduce σ^* . Finally, the solution may converge as intended towards the global minimum where σ approximates σ^* within the limits of the FEM grid. Divergence of the reconstruction process is easily detected because Φ is evaluated at each iteration. In contrast, it is more difficult in a practical measurement situation to distinguish between convergence to local and global minima because σ^* is usually unknown. In this study, convergence to local and global minima was detected as follows.

We define the relative mean squared image update at major iteration i as

$$\overline{\Delta\sigma_i^2} = \frac{\Delta\sigma_i^T \mathbf{W}_A^T \mathbf{W}_A \Delta\sigma_i}{\sigma_i^T \mathbf{W}_A^T \mathbf{W}_A \sigma_i}, \quad (4.23)$$

where \mathbf{W}_A is a diagonal weight matrix of the relative areas of each FE that accounts for the size and topology of the FEM used. The relative change in Φ at each major iteration is defined as

$$\Delta\Phi_i = \frac{\Phi_i - \Phi_{i-1}}{\Phi_{i-1}}. \quad (4.24)$$

Now, a convergence estimator function Ψ can be computed according to

$$\Psi_i = \vartheta\Psi_{i-1} + (1 - \vartheta)\frac{\overline{\Delta\sigma_i^2}}{\Delta\Phi_i}. \quad (4.25)$$

This function assumes a very small value when a small conductivity change in the image causes a large change in the objective function Φ . On the other hand, Ψ becomes large when significant conductivity changes in the image cause only small changes in the Φ . Thus, Ψ represents a measure of the prominence of ill-conditioning at any given point in the iterative process. In order to suppress rapid fluctuations, Ψ is updated recursively in Eq. 4.25, with ϑ being a forgetting factor that ranges between 0 and 1.

The parameters of the convergence estimator for this study were chosen on the basis of preliminary experiments. Images were considered to have essentially converged to the global minimum when Ψ assumed a value of less than $\psi_g = 5 \cdot 10^{-7}$. In contrast, convergence to a local minimum was suspected when Ψ exceeded $\psi_l = 5 \cdot 10^{-4}$. The forgetting factor was set to $\vartheta = 0.5$. The reconstruction was terminated and considered divergent when the algorithm failed to reduce Φ below its initial value after three iterations.

Reconstruction error

The topological identity between the phantom and the reconstruction FEM permits precise evaluation of the reconstruction error at each iteration. We can hence define the normalized rms image error as

$$\varepsilon = 100\% \cdot \sqrt{\frac{(\sigma_i - \sigma^*)^T \mathbf{W}_A^T \mathbf{W}_A (\sigma_i - \sigma^*)}{\sigma^{*T} \mathbf{W}_A^T \mathbf{W}_A \sigma^*}}. \quad (4.26)$$

Because ε is weighted by the relative FE area and normalized by an equivalent expression of σ^* , it is independent of the size or topology of the phantom and its mean conductivity.

Protocols

(i) *Correlation of sample images and reconstruction error*

In order to illustrate the performance of the reconstruction algorithm and to demonstrate the way in which ε correlates with the visual appearance of the image, the thoracic phantom was simulated using neighbouring currents and without any measurement noise (SNR = ∞). An image reconstruction was performed executing 20 major iterations, and the image and ε were saved for each major iteration.

(ii) *Validation of the convergence estimator*

To validate the convergence estimator, images of both phantoms (Fig. 4.4) were reconstructed at 11 SNRs from 30 to 80 dB. For each phantom and noise level, the simulation was repeated 10 times in order to average out the influences of any particular noise implementation, resulting in a total of 220 simulations. Twenty iterations were performed for each image reconstruction, and both the minimal value of ε (ε_{\min}) over all 20 iterations and the value of ε after the 20th iteration ($\varepsilon_{\text{final}}$) were stored. The value of Ψ was computed for each iteration, and the numbers of cases in which convergence to the global minimum was detected and in which convergence to a local minimum was suspected (N_{conv} and N_{local} , respectively) were evaluated. In the simulations that converged to the global minimum according to Ψ , the value of ε at the point of convergence ($\varepsilon_{\text{conv}}$), i.e., when Ψ first was less than ψ_g , was saved.

(iii) *Effects of current patterns*

In this protocol, the influence of the relative position of the current source and sink on N_{conv} and $\varepsilon_{\text{conv}}$ was evaluated using the thoracic phantom. Initially, neighbouring currents were used, i.e., the current source was located at the electrode adjacent to the sink for each projection. Subsequently, the current source and sink were progressively separated until the source was diametrically opposed to the sink, which is equivalent to the opposite current pattern. At each separation setting and for SNRs of 50, 60, 70 and 80

dB, 10 images were reconstructed, yielding a total of 320 simulations. For each source-sink separation setting and noise level, N_{conv} , N_{local} and the mean and standard deviation of ϵ_{conv} were evaluated.

(iv) Effect of a central reference electrode

To investigate the effect of a CRE on N_{conv} and ϵ_{conv} , EIT measurements were simulated using the thoracic phantom with the neighbouring current pattern in three configurations: (A) with 16 boundary electrodes as above (Control16); (B) with a CRE located as shown in Fig. 4.5(a) in addition to the 16 boundary electrodes (CRE17); and (C) with 32 boundary electrodes but no CRE, as shown in Fig. 4.5(b) (Control32). For each configuration, measurements were simulated 10 times at each of 11 SNRs from 30 to 80 dB. As above, N_{conv} and the mean and standard deviation of ϵ_{conv} were evaluated for each simulation.

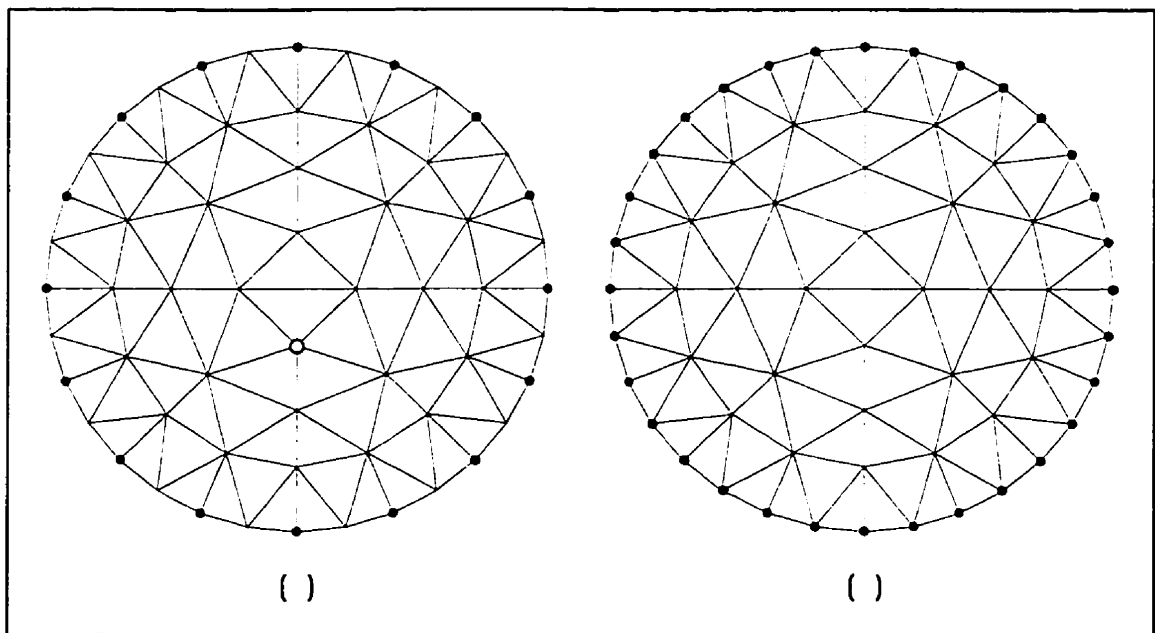


Fig. 4.5:
FEM used for protocol (iv). The open circle denotes the location of the CRE.

4.2.3 Results

Fig. 4.6(a) to (c) show reconstructed images for protocol (i) at iterations 3, 6 and 8, respectively. The image shown in Fig. 4.6(a) produced a value of $\varepsilon = 60\%$ and did not reflect the features of thoracic phantom. The principal features of the phantom were better reproduced in the image shown in Fig. 4.6(b), which corresponded to $\varepsilon = 15\%$. However, some visible differences remained between this image and the phantom. The image shown in Fig. 4.6(c) produced an error of $\varepsilon = 1.9\%$ and was essentially visually identical to the thoracic phantom. In general, the principal features of the phantom were reproduced in the images for $\varepsilon < 20\%$, and the images closely resembled the phantom when ε assumed a value of less than 5%.

In protocol (ii), convergence of images of the thoracic phantom to the global minimum was detected in 69 out of 110 reconstructions after an average of 13.3 iterations. In 22 cases, convergence to a local minimum was suspected after 7.5 iterations on average. For the remaining 19 simulations, Ψ ranged between ψ_g and ψ_l for all 20 iterations. The relationships between $\varepsilon_{\text{conv}}$ and ε_{min} and between $\varepsilon_{\text{conv}}$ and $\varepsilon_{\text{final}}$ for the thoracic phantom are denoted by the solid circles in Fig. 4.7. In Fig. 4.7(a), the data points are scattered slightly above the line of identity, indicating that $\varepsilon_{\text{conv}}$ exceeded ε_{min} by some small amount in most cases. On average, $\varepsilon_{\text{conv}}$ equaled $1.092\varepsilon_{\text{min}}$. The data points in Fig. 4.7(b) are scattered tightly around the line of identity, showing that $\varepsilon_{\text{conv}}$ was very close to $\varepsilon_{\text{final}}$ in all cases. On average, the mean of the ratio of $\varepsilon_{\text{conv}}$ to $\varepsilon_{\text{final}}$ amounted to 1.0001. The criterion for convergence to the global minimum was fulfilled for all image reconstructions for which ε_{min} was less than 20%, i.e., for all images that reproduced the principal features of the phantom. The value of ε increased by 202% on average in the first iteration for which Ψ exceeded ψ_l , indicating that these reconstructions were indeed not converging to the global minimum.

The central object phantom in protocol (ii) produced similar results to the thoracic phantom. In this case, convergence to the global and local minima was detected in 79 and 9 simulations, respectively. Both outcomes were detected after slightly more than 9

iterations on average. In the remaining 22 cases, 20 iterations were completed without either criterion being fulfilled. No numerical instability was encountered in the simulations performed for protocol (ii). The open triangles in Fig. 4.7(a) and (b) show ϵ_{conv} plotted over ϵ_{min} and ϵ_{final} for the central object phantom, respectively. The means of the $\epsilon_{\text{conv-to-}\epsilon_{\text{min}}}$ and $\epsilon_{\text{conv-to-}\epsilon_{\text{final}}}$ ratios were 1.085 and 0.986, respectively. Again, the criterion for convergence to the global minimum was fulfilled for all image reconstructions with an ϵ_{min} of less than 20%. For this phantom, ϵ increased by 89% in the first iteration at which Ψ exceeded ψ_1 .

For protocol (iii), N_{conv} and ϵ_{conv} are plotted as functions of the separation between the current source and sink and the SNR in Fig. 4.8(a) and (b), respectively. At comparatively high SNRs of 70 and 80 dB, nearly all simulations converged to the global minimum at all separation settings except for those using opposite currents (Fig. 4.8a). At a SNR of 60 dB, N_{conv} equaled 100% for source-sink separations of one and two electrodes but dropped as the source was progressively separated from the sink. When the SNR was further reduced to 50 dB, some images failed to converge to the global minimum at all small separation settings and N_{conv} was zero when the current source and sink were more than four electrodes apart. For all SNRs, the reconstructions diverged when opposite currents were used. This was in contrast to all other separation settings where reconstructions that failed to converge to the global minimum either approached a local minimum or completed the maximum number of iterations without fulfilling either criterion.

As shown in Fig. 4.8(b), the mean ϵ_{conv} was minimal for separation settings of 1 and 2 at each SNR. The mean ϵ_{conv} was less than 20% at a SNR of 80 dB for all separation settings except opposite currents. At SNRs of 60 and 70 dB, images that reproduced the principal features of the phantom (mean $\epsilon_{\text{conv}} < 20\%$) were obtained when source and sink were less than three electrodes apart. Images with a mean ϵ_{conv} of less than 5% were reconstructed for separations of 1 and 2 at a SNR of 80 dB and for neighbouring currents at a SNR of 70 dB.

For all three configurations used in protocol (iv), N_{conv} equaled 100% and 0% for SNRs greater than 55 dB and of less than 40 dB, respectively (Fig. 4.9a). The reconstruction error produced by configuration CRE17 in general ranged between those of the two control configurations (Fig. 4.9b). The mean ϵ_{conv} was less than 20% when SNR was equal or greater than 60, 55 and 50 dB for configurations Control16, CRE17 and Control32, respectively. Images that closely resembled the phantom (mean $\epsilon_{\text{conv}} < 5\%$) were obtained at SNRs of 70 dB and above for configuration Control16, and at SNRs of 65 dB and above for configurations CRE17 and Control32.

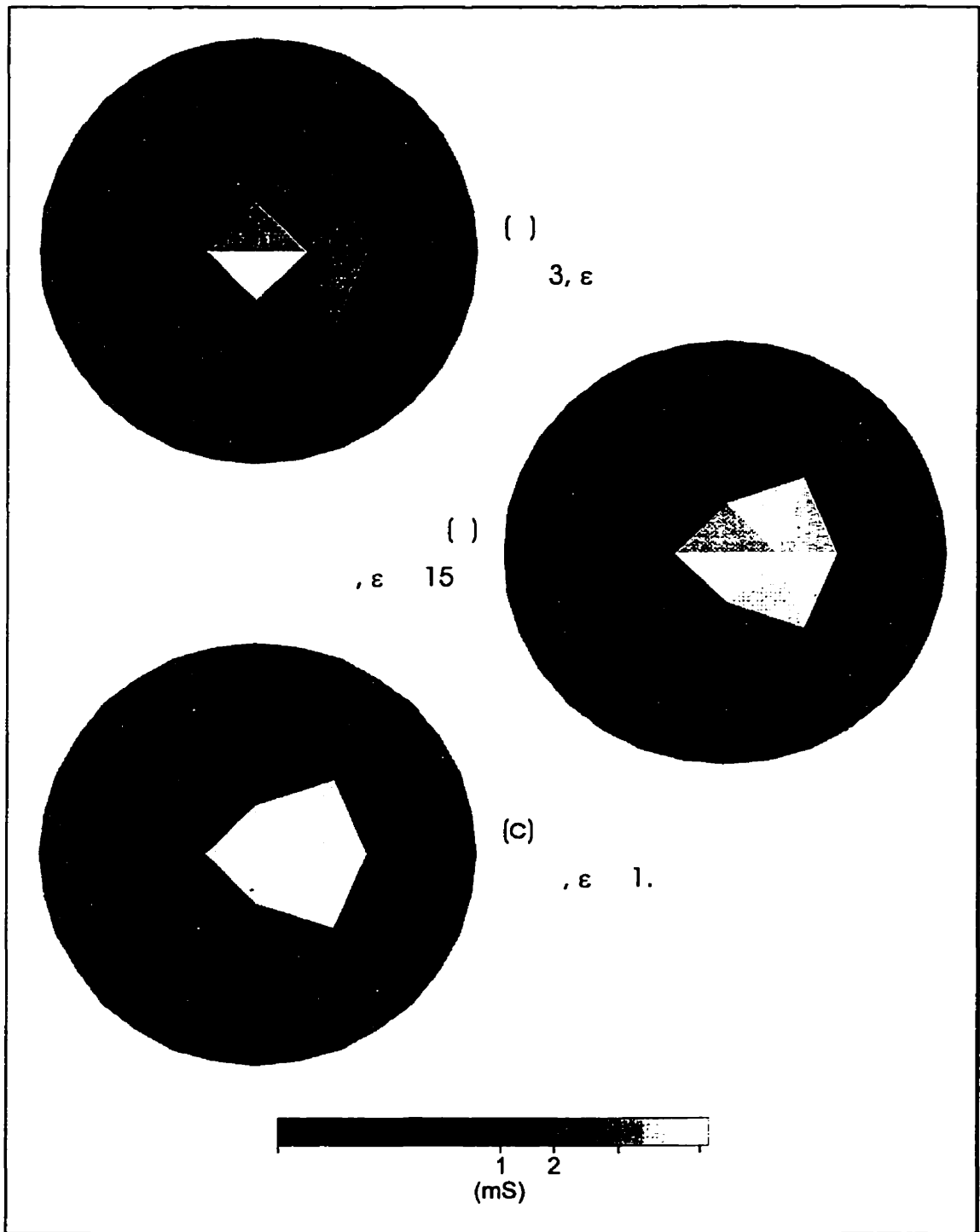


Fig. 4.6:
Images of the thoracic phantom reconstructed from noise-free data. The number of iterations (i) and the corresponding reconstruction error (ϵ) are given for each image.

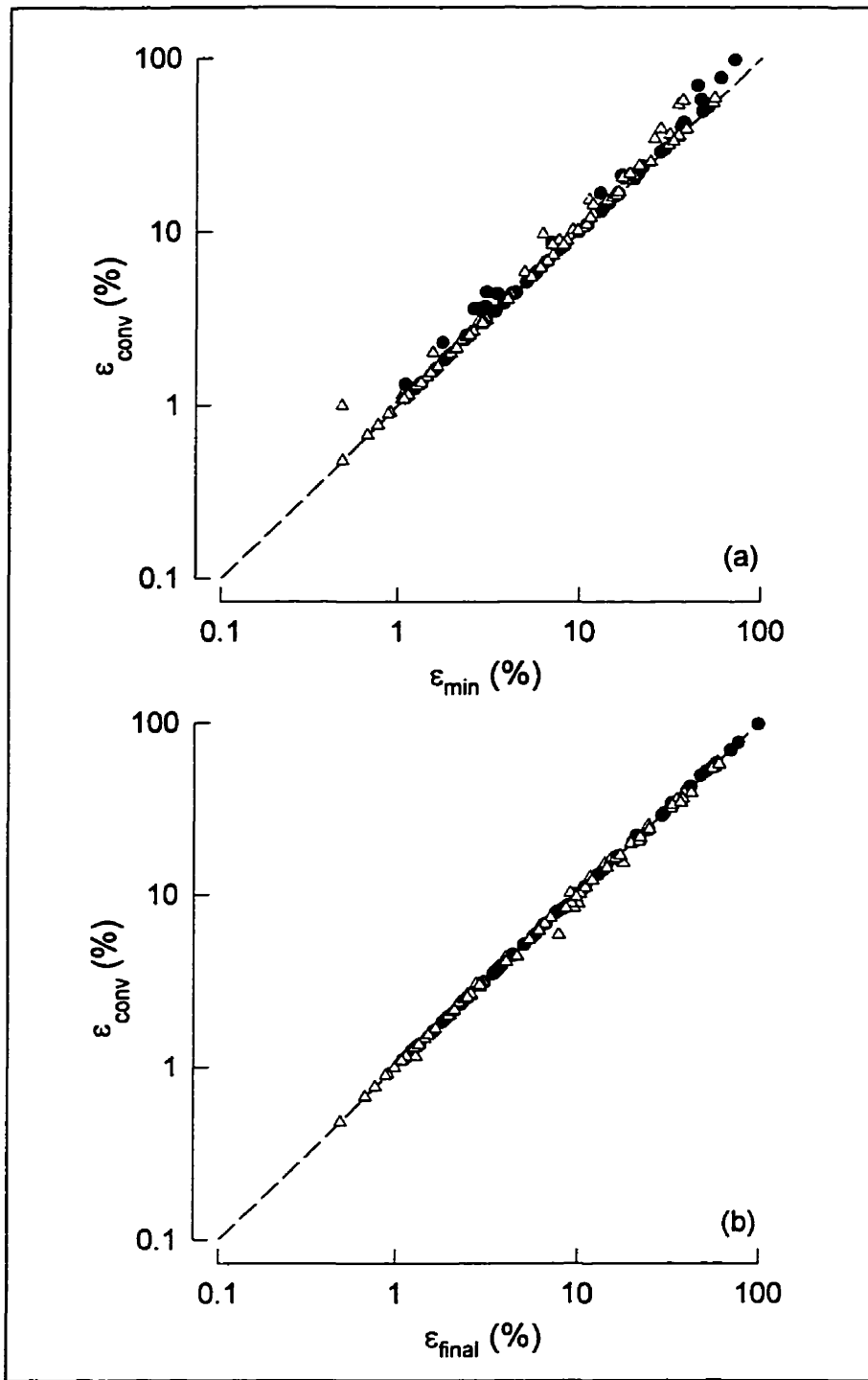


Fig. 4.7:

Reconstruction error at the point when convergence was detected plotted versus the minimal reconstruction error over 20 iterations (a) and the reconstruction error after 20 iterations (b). The circles and triangles represent reconstructions of the thoracic phantom and the central object phantoms, respectively. The dashed line is the line of identity.

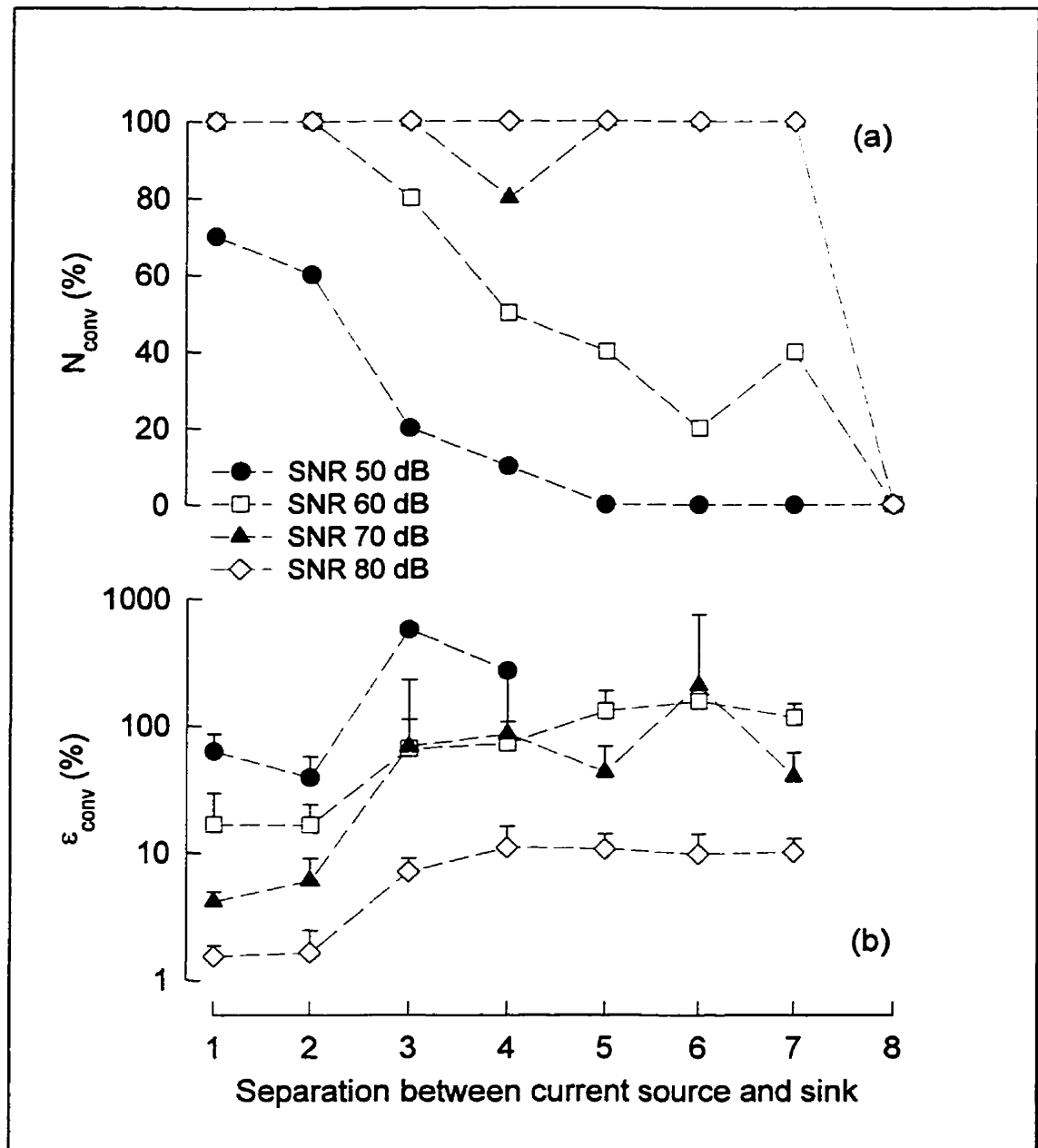


Fig. 4.8: Percentages of successful convergence to the global minimum (a) and reconstruction errors (b) as functions of the separation between the current source and sink for four signal-to-noise ratios. The error bars in plot (b) denote the standard deviation.

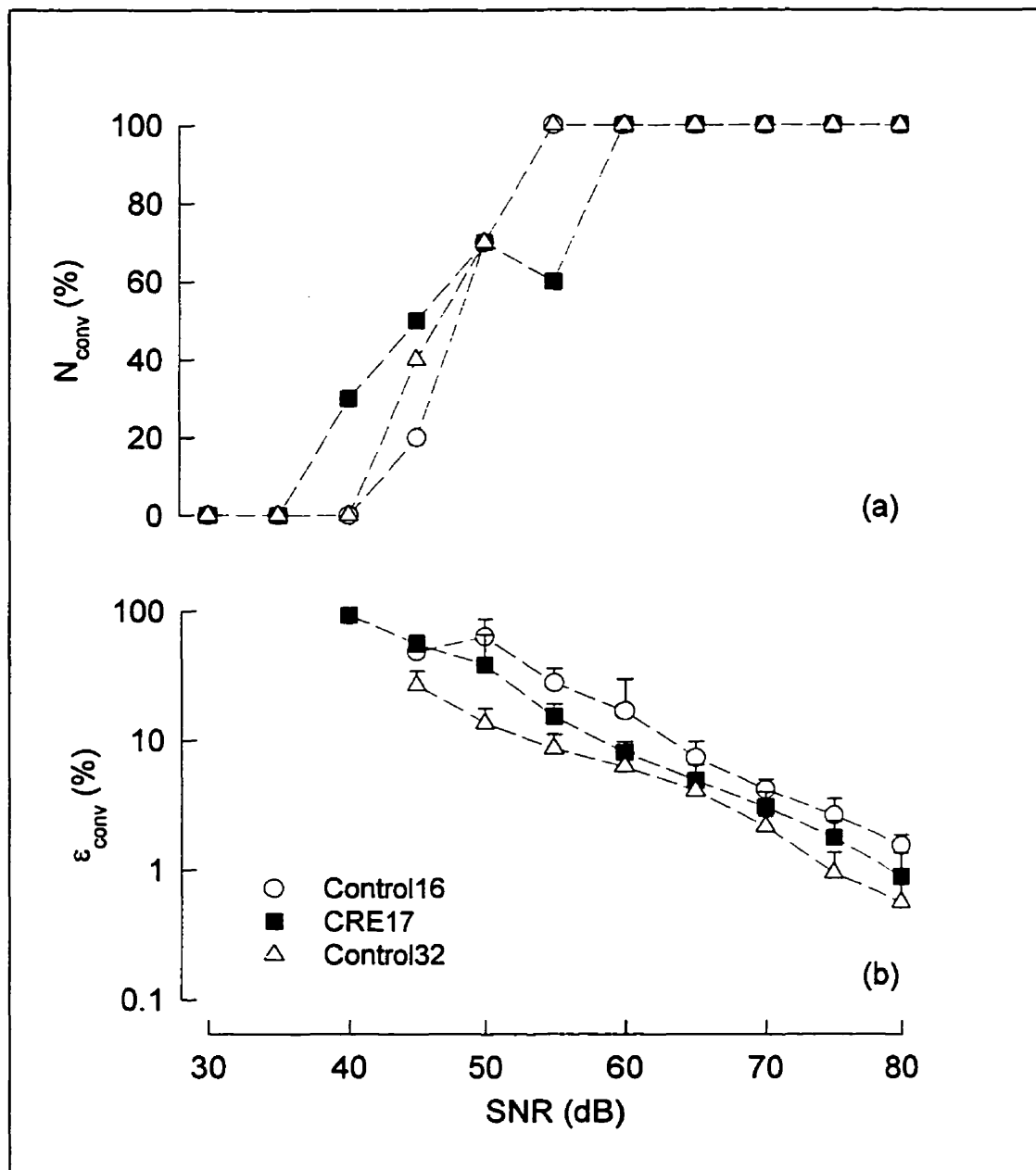


Fig. 4.9: Percentages of successful convergence to the global minimum (a) and reconstruction errors (b) as functions of the signal-to-noise ratio for the configuration using a central electrode (CRE17) and two control configurations with 16 and 32 boundary electrodes (Control16 and Control32, respectively). The error bars in plot (b) denote the standard deviation.

4.2.4 Discussion

In this section, I have developed a computer simulation of the static thoracic EIT measurement situation. This computer simulation was used to investigate how the choice of the current pattern and the placement of a CRE effect the probability of successful convergence to the global minimum and the reconstruction errors of images obtained using the GNM with a FE forward solution. The simulations showed that current patterns for which the current source was placed very close to the sink were best. The placement of a CRE did not significantly alter the likelihood of convergence of the reconstruction process to the global minimum, but noticeably reduced the reconstruction error. However, the reconstruction error was reduced even further when the number of boundary electrodes was doubled, but no CRE was used.

A circular FEM consisting of 86 first-order FEs was employed both for the computational phantom and to solve the forward problem for image reconstruction. This mesh has relatively few elements, compared to the FEMs used by some other investigators (3,24,68). However, in these studies the number of elements and hence the number of conductivity parameters in the image usually exceeds the number of independent measurements, which equals 104 when neighbouring currents are used (104). Thus, many investigators regularize the reconstruction process (3,17,155), e.g., using a smoothing constraint (see section 2.4.3). Regularization links the conductivity value of any element of the reconstruction mesh to its neighbours and hence effectively reduces the number of degrees of freedom of the reconstruction mesh to a value equal to or less than the number of independent measurements. Thus, increasing the number of FEs in the reconstruction mesh cannot overcome the fundamental restriction that is imposed on the resolution of EIT images by the limited number of independent measurements. For this study, I preferred a smaller FEM to the use of a smoothing constraint because regularization in itself may reduce the image quality and complicate the interpretation of the results.

Because the phantom and the image reconstruction FEM were topologically identical, the numerical inaccuracies of the FE method investigated in the previous section cancel out in this study. Therefore, the probabilities of convergence to the global minimum and the reconstruction errors obtained here differ substantially from those that would be obtained if the same reconstruction algorithm were used to reconstruct images from real static EIT data. However, the exclusion of confounding factors was desirable for the purposes of investigating only the influences of the current patterns and the CRE on the quality of the reconstructed images, which was the goal of this study. The topological identity of the phantom and reconstruction FEM also permitted precise evaluation of the reconstruction error, which would have been more problematic otherwise. Moreover, the elimination of the FEM error in the computer simulations permits an estimate of the extent to which the accuracy of the FE method must be improved before static images can be reconstructed. For example, in protocol (iii) of this section images with $\epsilon_{\text{conv}} < 20\%$ were successfully reconstructed only when the SNR was greater than 60 dB, and images with $\epsilon_{\text{conv}} < 5\%$ could not be obtained for SNRs less than 70 dB. In comparison, the FEM inaccuracies reported in section 4.1 produced SNRs of around 30 dB. Thus, it is necessary to reduce the FEM inaccuracies by at least 30 dB before static EIT images can be reconstructed.

The reconstruction algorithm used in this section employed a quadratic line search. For the derivation of this algorithm, it was assumed that for a step size of $\lambda = 1$, the objective function would vanish. However, the GNM only predicts a minimum of Φ at $\lambda = 1$ that, in general, can assume any positive value. Therefore, the estimate of the magnitude of Φ'_0 obtained from Eq. 4.22 represented an upper bound for Φ'_0 . Consequently, the minimum of the second-order polynomial that was fit to $\Phi(\lambda)$ was always closer to zero than it would have been if a smaller value of Φ'_0 had been used. This in turn caused the line search to produce comparatively small step sizes. Thus, the assumption that Φ vanishes completely for $\lambda = 1$ was conservative in the sense that it produced smaller step sizes, which is likely to render the iterative reconstruction algorithm more robust.

The sample images of the thoracic phantom for the noise-free case (Fig. 4.6) illustrate the performance of the reconstruction algorithm and the correlation of ϵ with the visual appearance of the images. The thresholds for ϵ of 20% and 5%, used to classify images that reproduced the principal features and the full detail of the phantom, respectively, were chosen empirically and are thus somewhat subjective. However, a slightly different choice of these thresholds would not have significantly altered the outcome of this study.

The value of the objective function of an iterative image reconstruction process does not directly correspond to the reconstruction error. Rather, Φ decreases when the solution converges to the global minimum as well as when a local minimum is approached and ϵ increases rapidly. In the case of convergence to the global minimum, the reconstruction error often plateaus, such that beyond a certain point additional iterations do not improve the image any further and may even result in a slight increase in ϵ . For these reasons, termination criteria that are based on only the objective function or on the termination of the reconstruction process after a fixed number of iterations are not satisfactory. The convergence estimator employed in this study used the ratio of the normalized change in the image to the change in the objective function at each iteration, which essentially provides an estimate of the ill-conditioning of the optimization problem. This convergence estimator successfully detected reconstructions that converged to the global minimum and indicated those that approached a local minimum. For all reconstructions that had the potential of reproducing the principal features of the phantom ($\epsilon_{\min} < 20\%$), Ψ became less than ψ_g before iteration 20 and ϵ_{conv} only slightly exceeded ϵ_{\min} (Fig. 4.7a). Moreover, ϵ_{conv} was generally very close to and sometimes even smaller than ϵ_{final} (Fig. 4.7a). This convergence estimator thus permitted excluding from the further analysis images that rapidly converged to a local minimum and would have produced large, meaningless values of ϵ . For images that converged to the global minimum, the convergence estimator helped in avoiding superfluous additional iterations that would not have improved the images.

The results of protocol (iii) in this section contradict a previous analytical study suggesting that current patterns with a low spatial frequency are advantageous because they produce a higher current density in central regions of the body (73). Using the same methodology, opposite currents were shown to resolve small central objects better than neighbouring currents (23). However, the outcome variable in these studies was not the reconstruction error, but a distinguishability function that was defined as the normalized change of the electrode voltages in response to a conductivity change in a small central region of a cylindrical body. This approach does not take into account the effect of the current pattern on the condition of the Hessian matrix. Also, the distinguishability function is defined in terms of a conductivity change rather than in terms of absolute conductivity and hence is relevant for the dynamic imaging situation only. Finally, the results of (23) are only valid for rotational symmetry in the volume to be imaged, and may differ significantly in cases where asymmetrical conductivity changes occur close to the periphery.

In an object with a homogeneous conductivity distribution, the current density in the center will clearly be greater for opposite currents than for neighbouring currents. However, as the object becomes inhomogeneous, the current densities become determined by the conductivity distribution to be imaged. In the thoracic phantom shown in Fig. 4.4(b), the minimal current density never occurred in the center, but always closer to the periphery in the highly resistive areas representing the lungs and the spine. In any case, a more homogeneous current density distribution is not necessarily numerically advantageous. When the current densities are homogeneously distributed, all element conductivities within the image contribute roughly equally to the boundary voltage vector of each projection, which means that all elements of the Jacobian matrix have approximately equal magnitudes. In this case, the Hessian is a full matrix. In contrast, if the current density distribution is highly heterogeneous, each element conductivity may contribute predominantly to one projection while its influence on all others is negligible. In this case, the Jacobian matrix is reduced to a sparse structure such as

$$\mathbf{J} = \begin{bmatrix} 0 & \mathbf{j}_{0,1} & \cdots & 0 \\ 0 & 0 & & \mathbf{j}_{1,N_\sigma} \\ \vdots & & \ddots & \vdots \\ \mathbf{j}_{N_p,0} & 0 & \cdots & 0 \end{bmatrix}, \quad (4.27)$$

where $\mathbf{j}_{p,i}$ is the $(N_b,1)$ vector that contains the derivatives of the boundary voltages of projection p with respect to the i -th element of σ . Then, the Hessian matrix

$$\mathbf{H} = \mathbf{J}^T \mathbf{J} = \begin{bmatrix} \mathbf{j}_{0,1}^T \cdot \mathbf{j}_{0,1} & 0 & \cdots & 0 \\ 0 & \mathbf{j}_{1,N_\sigma}^T \cdot \mathbf{j}_{1,N_\sigma} & & \\ \vdots & & \ddots & \vdots \\ 0 & 0 & \cdots & \mathbf{j}_{N_p,0}^T \cdot \mathbf{j}_{N_p,0} \end{bmatrix} \quad (4.28)$$

assumes a diagonal structure that is better conditioned than the full Hessian matrix in the case of homogeneous current densities. Thus, a comparatively localized current distribution such as occurs with neighbouring currents is likely to yield better images than more homogeneous current patterns in the presence of measurement noise. In general, these results suggest that the optimal choice of current pattern depends on both the conductivity distribution to be imaged and the reconstruction technique employed. As in this study, neighbouring currents have been shown to produce better images than opposite currents when filtered backprojection is used to reconstruct dynamic EIT images (8).

In protocol (iii), I did not consider current patterns with more than one source-sink pair (see section 2.4.2). As already discussed in section 4.1.4, these current patterns are difficult to implement in practice because precise matching of the output impedance of each current source in the system is required for the current patterns to be applied as desired. Also, only few currently existing EIT systems are capable of using more than one source-sink pair simultaneously. Furthermore, limiting the amount of current injected into

the body is more difficult when multiple current sources operate simultaneously, and the merit of these current patterns may be reduced when safety limitations are applied strictly (38). I envisage EIT ultimately to be a low-cost bedside monitoring tool and therefore focused this study on the simpler and more widely used single-source systems.

In protocol (iv), the use of a CRE shifted the graph of ϵ_{conv} as a function of the SNR towards lower SNRs by somewhat less than 5 dB (Fig. 4.9b). About twice as large an effect was obtained when the number of boundary electrodes was increased to $N_e = 32$ and no CRE was used, although this configuration may be biased because each boundary node of the FEM was used as an electrode. Considering that the Control32 configuration has a much greater number of independent measurements and takes much longer to solve, the CRE did produce a considerable improvement. However, the placement of a CRE is somewhat invasive, although in many ICU patients it may be possible to place the CRE together with an esophageal balloon or a endogastric feeding tube. It is also intriguing to speculate that a CRE may reduce the off-plane sensitivity and hence improve the specificity of two-dimensional EIT, but these effects have not yet been investigated.

In this section, I have developed a computer simulation of the static thoracic EIT measurement situation. A convergence criterion was introduced to terminate the iterative reconstruction of images from the simulated data. I have shown that this convergence criterion successfully distinguished between convergent and divergent images, and that the reconstruction error at the point when convergence was detected was close to its minimum while superfluous iterations were avoided. In protocol (iii), the best images were obtained when the current source and sink were placed in close proximity. These results were found to be related to the nature of the iterative reconstruction process employed because neighbouring currents accentuate the diagonal structure of the Hessian matrix. Moreover, I found that the use of a CRE reduces the reconstruction error and may be valuable despite its being somewhat more invasive. Finally, the comparison of the results of this study with those of the previous section suggests that the accuracy of the FE method needs to be improved by at least 30 dB before useful static EIT images can be obtained.

4.3 Higher-order Finite Elements for the forward solution in static EIT

4.3.1 Motivation

The previous sections of this chapter have demonstrated that first-order FEs are, in general, not accurate enough to be useful for the forward solution of static EIT problems. A possible approach for overcoming this problem is the use of higher-order FEs that have been shown to provide more accurate solutions than first-order FEs for comparable levels of computational complexity (131). Unfortunately, conventional higher-order FEs have the following two important shortcomings for their application in EIT: (i) Because the tissue properties are constant across conventional higher-order FEs, higher-order FEMs have fewer conductivity parameters than first-order FEM with similar values of N_n . Thus, the spatial resolution is reduced when conventional higher-order FEs are used instead of first-order FEs. (ii) For approximately constant inter-node distances, higher-order FEs have longer straight boundaries than first-order FEs. Therefore, conventional higher-order FEs do not approximate the irregular body shapes that need to be modeled in static EIT as well as first-order FEs. However, the approximation of the boundary shape is known to strongly effect the accuracy of the FEM solution (131). A poorer approximation of the boundary shape might thus counteract the improved polynomial accuracy of conventional higher-order FEs.

The aims of this study were to derive isoparametric curvilinear higher-order FEs with a space-variant conductivity that can approximate arbitrary continuous boundary shapes and conductivity distributions, to illustrate the potential of these elements for improving the accuracy of the EIT forward solution, and to discuss their theoretical advantages and limitations.

4.3.2 Methods

Two-dimensional isoparametric Finite Elements with variable conductivity

Higher-order isoparametric FEs with variable conductivity differ from the standard FEs described in the previous sections in three aspects. First, the increased order of the approximation functions necessitates additional nodes in the element. In two dimensions, a minimum of $(N + 1)(N + 2)/2$ nodes are required to completely describe a set of approximation functions of order N . Second, if the conductivity is modeled to vary across the element, the S matrix can no longer be assembled as outlined in section 2.4.3 (Eqs. 2.12 and 2.13). Thus, it is necessary to derive new element matrices for FEs with variable conductivity. Finally, curvilinear FEs require integration of the Helmholtz equation over curvilinear boundaries. This is best achieved by means of a coordinate transform that projects the curvilinear element onto a standard element of simpler geometry that can be integrated more easily. FEs that obey all three requirements can be derived, as follows.

In order to remain consistent with the FE methodology and for the sake of simplicity, we approximate the conductivity across the FE by the same approximation functions as the potential, i.e.,

$$\sigma(\mathbf{x}) = \sum_{i=1}^{N_{n,el}} \sigma_i \alpha_i(\mathbf{x}). \quad (4.29)$$

Substituting Eqs. 2.10 and 4.29 into Eq. 2.9, we can express the first functional of the Helmholtz equation (Θ_1) as

$$\Theta_1 = \frac{1}{2} \sum_i \sum_j \sum_k \sigma_i \varphi_j \varphi_k \int \alpha_i \nabla \alpha_j \nabla \alpha_k d\Omega. \quad (4.30)$$

Changing the order of summation and expressing two of the sums in matrix form yields

$$\Theta_1 = \frac{1}{2} \varphi_{n,el}^T \cdot \left[\sum_{i=1}^{N_{n,el}} \sigma_i \mathbf{S}_{el}^{(i)} \right] \cdot \varphi_{n,el} = \frac{1}{2} \varphi_{n,el}^T \mathbf{S}_{el} \varphi_{n,el}. \quad (4.31)$$

Thus, the \mathbf{S}_{el} matrix for a FE with variable conductivity is obtained from a conductivity-weighted sum over a family of $N_{n,el}$ distinct $\mathbf{S}_{el}^{(i)}$ matrices. Assembling the FEM in analogy to Eq. 2.13 and changing the order of summation, the first Helmholtz functional can be written as

$$\Theta_1 = \frac{1}{2} \boldsymbol{\varphi}_n^T \cdot \left[\sum_{i=1}^{N_n} \sigma_i \mathbf{S}^{(i)} \right] \cdot \boldsymbol{\varphi}_n = \frac{1}{2} \boldsymbol{\varphi}_n^T \mathbf{S} \boldsymbol{\varphi}_n. \quad (4.32)$$

This means that in contrast to FEs with constant conductivities, the FEM can be assembled before the conductivity-weighted sum over the $\mathbf{S}^{(i)}$ matrices is evaluated.

In general, the projection of a straight-bordered FE in the coordinate space (u,v) onto a the curvilinear FE in the coordinate space (x,y) is achieved by means of a coordinate transform of the form

$$\begin{aligned} x &= f_x(u, v), \\ y &= f_y(u, v). \end{aligned} \quad (4.33)$$

Because we want to actually define the element in (x,y) coordinates and then transform it back into (u,v) space where the element is straight-bordered and therefore easier to integrate, the coordinate transform used for our FEs must be reversible. This requires that it uniquely relates any point (u_i, v_i) to exactly one point (x_i, y_i) and vice versa and imposes some geometrical constraints in order to assure that the numerical inversion of the transform is well-conditioned (131). A suitable coordinate transform that is particularly consistent with the FE methodology is derived from the approximation functions themselves according to

$$\begin{aligned} x &= \sum_{i=1}^{N_{n,el}} x_i \alpha_i(u, v), \\ y &= \sum_{i=1}^{N_{n,el}} y_i \alpha_i(u, v). \end{aligned} \quad (4.34)$$

Curvilinear FEs that have been obtained using this transform are often referred to as isoparametric FEs. Now, the entries of the $\mathbf{S}_{el}^{(i)}$ matrices can be computed according to

$$\mathbf{S}_{el,k}^{(i)} = \iint \alpha_i (\mathbf{J}_C^{-1} \nabla \alpha_j)^T \cdot \mathbf{J}_C^{-1} \nabla \alpha_k \det(\mathbf{J}_C) du dv, \quad (4.35)$$

where ∇ now denotes the gradient in (u,v) coordinates and \mathbf{J}_C is the Jacobian matrix of the coordinate transform (131) that is defined as

$$\mathbf{J}_c = \begin{bmatrix} \frac{\partial x}{\partial u} & \frac{\partial x}{\partial v} \\ \frac{\partial y}{\partial u} & \frac{\partial y}{\partial v} \end{bmatrix}. \quad (4.36)$$

In the case of triangular FEs it is possible to express the $\mathbf{S}_{el}^{(i)}$ matrices such that all parameters defining the geometry of the element, i.e., all functions of the node coordinates, are no longer part of the integral (35,130,131). Then, the innermost kernels can be integrated and tabulated once and for all as global matrices, and the \mathbf{S}_{el} of any particular FE is rapidly evaluated by multiplication of these global matrices with comparatively simple functions of the element coordinates. Unfortunately, this is no longer possible for curvilinear elements because \mathbf{J}_c varies with position within the element and cannot be extracted from the integral. Thus, we must integrate the approximation functions of the curvilinear FEs numerically.

The integration of the FE matrices for triangular elements is best performed in Simplex coordinates (35,131) and can be solved using symbolic integration software. For curvilinear transformation, quadratic FEs are often preferred because they can be integrated in one dimension at a time, which simplifies the numerical implementation of Eq. 4.35 (131). However, quadratic FEs have the disadvantage that they are geometrically anisotropic. This means that their polynomial representation is supercomplete, i.e., that their polynomial basis contains some but not all terms of orders greater than the element order N (131). For example, the second-order FE shown in Fig. 4.10(a) can model only quadratic potential functions along any line parallel to the sides of the element, while cubic or quartic polynomials can be exactly represented along the diagonals. Because supercompleteness is of little practical benefit, the internal nodes of quadratic FEs are often omitted for $N < 5$ (131), which yields the boundary node FE shown in Fig. 4.10(b). This eliminates some of the supercomplete terms while all polynomials up to order N remain unaltered. Boundary nodes cannot be omitted because they are necessary to maintain inter-element continuity.

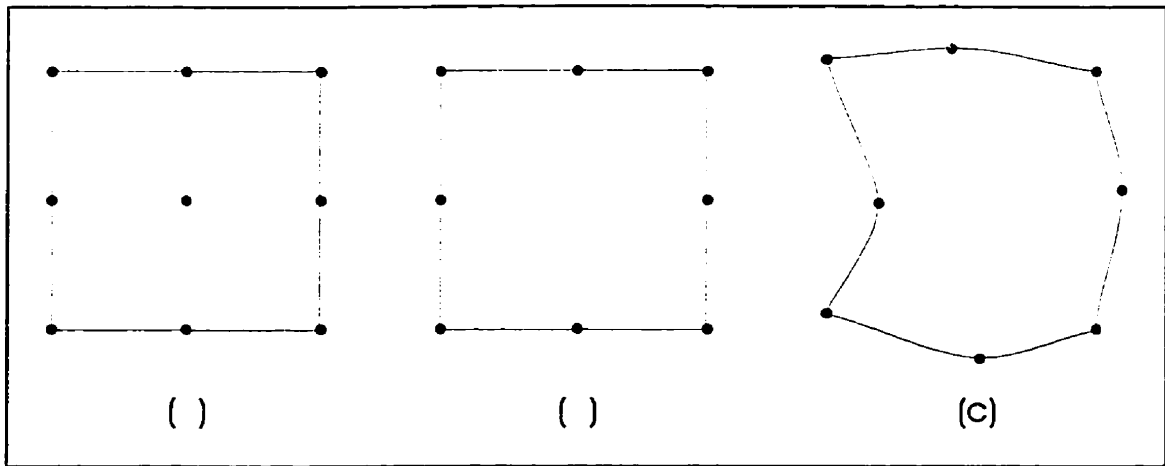


Fig. 4.10:

(a) Complete quadratic second-order FE, 9 nodes. (b) Quadratic second-order boundary node FE, 8 nodes. The internal node is omitted to reduce the supercompleteness. (c) Isoparametric second-order FE obtained from the boundary node FE shown in (b) using a coordinate transform.

For the computations performed in this section, the second-order boundary node FE shown in Fig. 4.10(b) was employed and transformed to any required shape using Eq. 4.34. An isoparametric curvilinear FE is illustrated in Fig. 4.10(c). The FE matrices were integrated using Gaussian quadrature. Because the polynomial order of the integrand in Eq. 4.35 equals 14 for each dimension, 8 quadrature points each in u and v were sufficient for exact numerical integration (64).

Curvilinear one-dimensional Finite Elements for the boundary condition

As in section 4.1.2, the boundary condition was modeled by a ring of one-dimensional FEs. Clearly, these line elements must be curvilinear and of an order equal to that of the two-dimensional FEs used to model the first term of the Helmholtz equation. The isoparametric coordinate transform for the one-dimensional line element is expressed by

$$\begin{aligned}
 x &= \sum_{i=1}^{N_{n,d}} x_i \alpha_i(u), \\
 y &= \sum_{i=1}^{N_{n,d}} y_i \alpha_i(u),
 \end{aligned}
 \tag{4.37}$$

and the elements of the \mathbf{T} matrix of a single one-dimensional element are easily found to be

$$\mathbf{T}_{e_{l,k}} = \int \alpha_j(u) \alpha_k(u) \sqrt{\left(\frac{\partial x(u)}{\partial u}\right)^2 + \left(\frac{\partial y(u)}{\partial u}\right)^2} du. \quad (4.38)$$

Because the polynomial order of the integrand is 6, four quadrature points along the element are sufficient for exact numerical integration of each element of \mathbf{T}_{e_l} . \mathbf{T}_b is assembled from the individual \mathbf{T}_{e_l} in analogy to Eq. 2.13, and the \mathbf{U} matrix is computed in direct analogy.

Protocol

The inaccuracies of the four second-order isoparametric FEMs shown in Fig. 4.11 were evaluated as described in section 4.1. A summary of the characteristics of these FEMs is given in Table 4.3. The electrode size parameter was adjusted to $D = 256$ and the four-electrode method was used in all cases. The results were compared to those obtained using standard first-order FEMs with the four-electrode method.

Table 4.3:
Characteristics of the four isoparametric FEMs used in this study.

| Mesh | N_σ | N_n | N_b | N_e |
|---------|------------|-------|-------|-------|
| (iso-a) | 69 | 69 | 16 | 16 |
| (iso-b) | 113 | 113 | 32 | 16 |
| (iso-c) | 193 | 193 | 48 | 16 |
| (iso-d) | 309 | 309 | 64 | 16 |

4.3.3 Results

Fig. 4.12 shows the inaccuracies of the higher-order FEMs shown in Fig. 4.11 in comparison with those of the FEMs shown in Fig. 4.2. When N_n was small (FEMs iso-a and iso-b), the inaccuracies of the isoparametric FEMs were somewhat greater than those of comparable first-order FEMs. However, at N_n greater than 100 the isoparametric FEMs (iso-c) and (iso-d) produced smaller values Δv_{rms} and larger SNRs than comparable first-order FEMs.

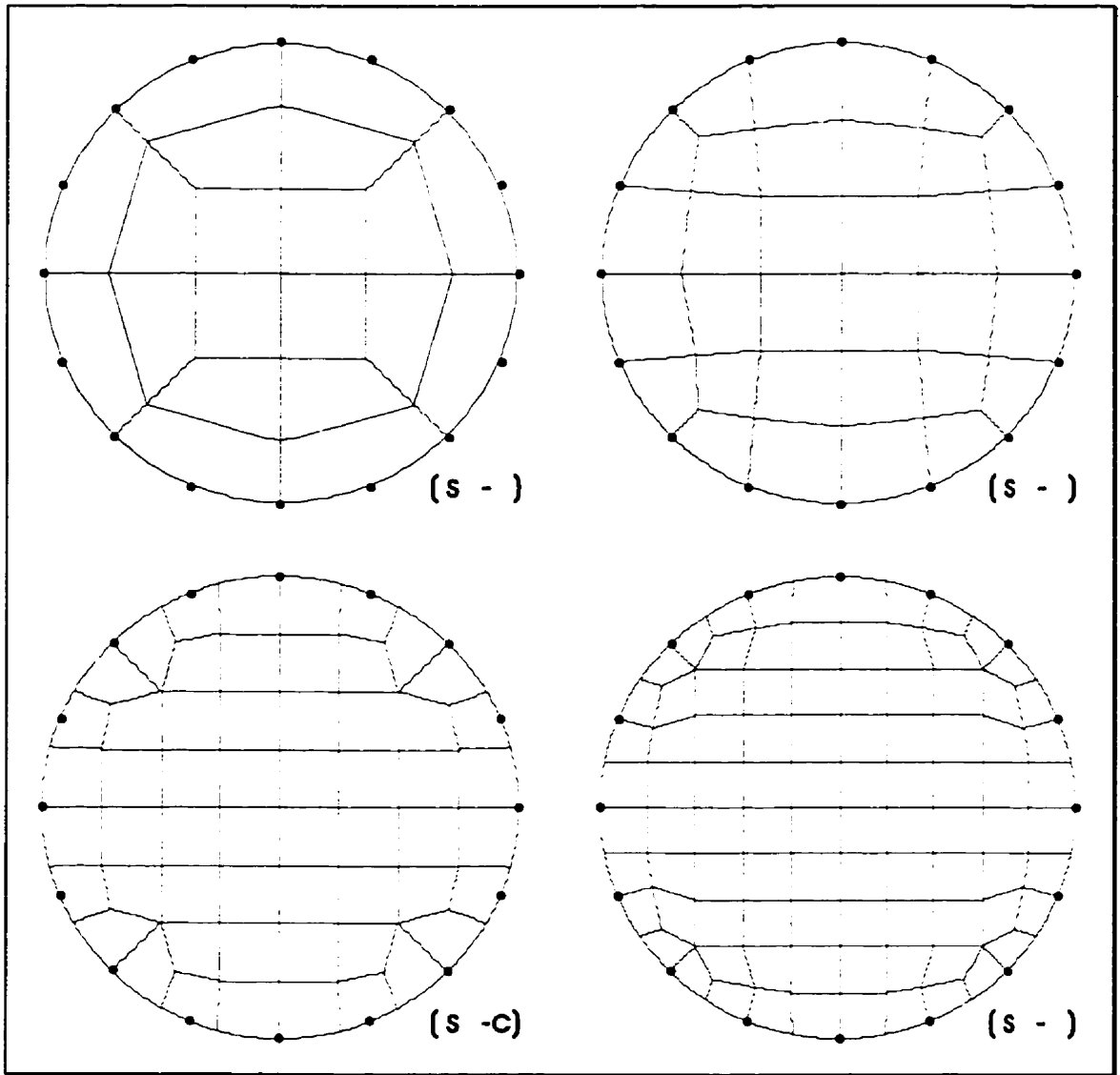


Fig. 4.11:
The four isoparametric Finite Element Meshes. The small solid circles denote the electrode locations. See Table 4.3 for details.

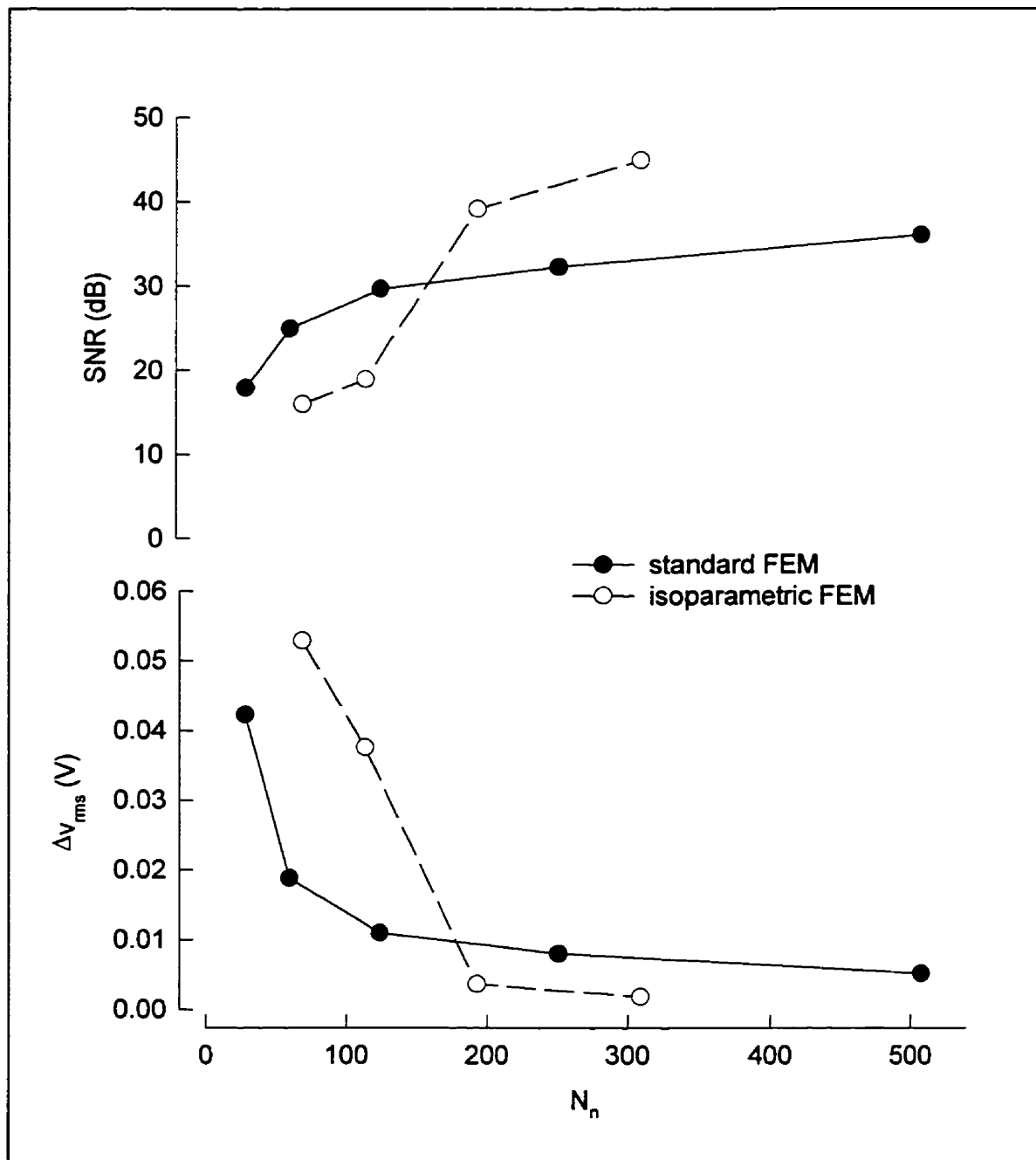


Fig. 4.12:
Inaccuracies of standard (solid circles) and isoparametric (open circles) FEMs.

4.3.4 Discussion

In this study, I have derived higher-order curvilinear FEs with space-variant conductivity across the element. This derivation (Eqs. 4.29 to 4.36) is of general validity for use with many kinds of two-dimensional FEs, i.e., for any element order as well as for various basic shapes, and could easily be extended to three spatial dimensions. However, the computations performed for this study were limited to isoparametrically distorted second-order square FEs with 8 boundary nodes (Fig. 4.10c). This is the type of isoparametric FE that is easiest to compute. The inhomogeneous boundary condition was modeled using second-order curvilinear line elements. The approximation functions for the standardized second-order line element before application of the coordinate transform are shown in Fig. 4.13.

Of the four FEMs that were used to investigate the accuracy of isoparametric FEs, the two smaller ones (iso-a and iso-b in Fig. 4.11) did not reproduce the analytical solution as well as comparable first-order FEMs. Presumably, these increased inaccuracies were caused by the side lobes of the approximation functions for the boundary condition. For example, the approximation function that models current injection into a node at the end of a second-order line element (solid line in Fig. 4.13) deviates considerably from zero close

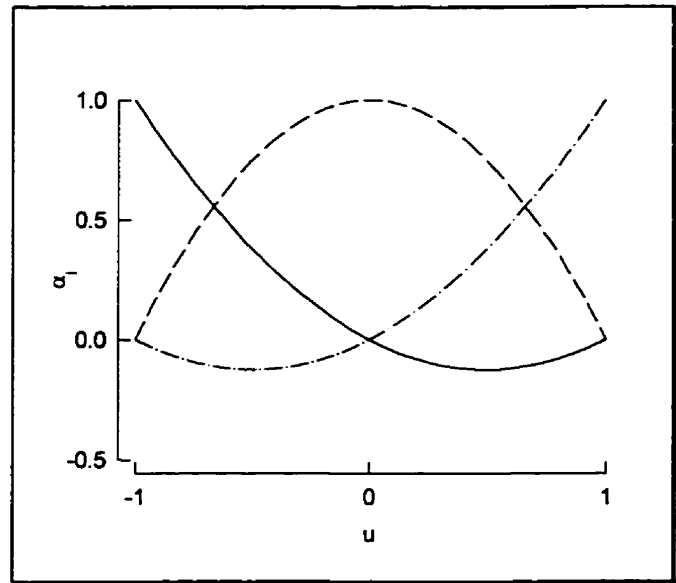


Fig. 4.13:
Approximation functions for a one-dimensional second-order Finite Element. The solid, dashed and dash-dotted lines represent the approximation functions for nodes placed at $u = -1$, $u = 0$ and $u = 1$, respectively.

to the node at the opposite end of that line element. In FEM (iso-a) where only 8 line elements were used to model the boundary condition, this was essentially equivalent to

unintentionally placing two current sources with small negative amplitudes at angles of $\pm 33.75^\circ$ relative to the position of the intended current source. The effects of these unintentional current sources are more pronounced in the FEMs (iso-a) and (iso-b) because they fall into close proximity of the voltage electrodes neighbouring the current electrodes. Therefore, a considerable error in φ_c was encountered at the voltage electrodes neighbouring the current electrodes. This analysis confirms a previous analytical study that demonstrated the importance of the accurate modeling of the boundary condition (25).

For meshes (iso-c) and (iso-d) in Fig. 4.11, the closest voltage electrode was always more than one complete line element away from the current electrode. This presumably explains the steep increase in the SNR from (iso-b) to (iso-c). The accuracy of the FEMs (iso-c) and (iso-d) exceeded that of first-order FEMs with a similar level of computational complexity by somewhat less than 15 dB. According to section 4.2.4, this improvement is not quite sufficient to permit the reconstruction of useful static EIT images. However, the FEs employed here were the simplest kind of higher-order isoparametric elements with space-variant conductivity. Most likely, the accuracy of the forward solution could be improved further by using third or fourth-order FEs and by an improved modeling of the boundary condition.

Theoretically, the fact that the conductivity of the isoparametric FEs was modeled to be space-variant may be advantageous in itself, for the following reason. The assumption of a constant conductivity across each element produces a piecewise constant conductivity distribution in the assembled FEM. If for simplicity we assume square FEs, this is equivalent to sampling and convolution with a two-dimensional square window. Because the spatial frequency content of a square window is not band limited, we must, in general, be concerned with the satisfaction of the sampling theorem when FEs with constant conductivity are used. In practice, however, the EIT reconstruction process is usually regularized (3,17,66,154) (see section 2.4.3), which effectively links the conductivities of neighbouring elements and hence imposes some degree of low-pass filtering. However, a piecewise constant conductivity distribution can only be truly band

limited in the limit of an infinitely large number of Finite Elements. In contrast, FEs with space-variant conductivity produce a continuous conductivity distribution in the assembled FEM, which in general has less power at high spatial frequencies than a piecewise constant conductivity distribution.

Although the spatial frequency content of the conductivity distribution in the isoparametric FEs derived above is band-limited, it may still be necessary to regularize the iterative image reconstruction process to assure convergence to the global minimum under all circumstances. At present, most reconstruction algorithms employ the penalty function described by Eq. 2.38. Formulations that penalize the first or second spatial derivative of σ have been shown to be advantageous (67) but cannot be implemented accurately in a standard first-order FEM because $\nabla\sigma$ vanishes within the element and is singular at the boundaries. In contrast, $\nabla\sigma$ is non-trivial at any point in the isoparametric FEs derived above. Furthermore, although the n -th derivative of an approximation function of order N is of order $N - n$, it can always be expressed exactly by a linear combination of the complete set of approximation functions of order N (130). Hence, the magnitude of $\nabla\sigma$ can be evaluated efficiently by multiplication of σ with a tabulated differential operator matrix (130). This permits more efficient and accurate gradient regularization than in a standard FEM, which may contribute to the reconstruction of EIT images with improved contrast. However, in cases where strong regularization is necessary, it may also be beneficial to alternatively reduce the order of the approximation functions for σ to a value less than the order of the approximation functions ϕ .

To the best of my knowledge, the preliminary study presented in this section is the first to investigate higher-order isoparametric FEs with space-variant conductivity for the EIT forward solution. Clearly, a great deal of work remains to fully investigate all aspects of these FEs, e.g., determining the ideal order and shape of the elements, the best modeling of the boundary condition and the effects of measurement noise and regularization of the reconstruction process. However, given the preliminary results of this section and the theoretical advantages that have been discussed, I expect higher-order isoparametric FEs with space-variant conductivity to improve the accuracy of the EIT

forward solution to an extent that FE inaccuracies are no longer a limiting factor for the reconstruction of clinically useful static EIT images.

5.

CONCLUSIONS

5.1 Summary and conclusions

The high incidence of pulmonary disease in critically ill patients necessitates the continued investigation of new and improved techniques for obtaining clinically valuable information from the diseased respiratory system. The research described in this thesis approaches this problem in two distinct ways. In chapter three, I investigate pulmonary monitoring techniques using conventional pressure and flow measurements. Many of the results of chapter three are immediately applicable in a clinical context. In chapter four, I investigate image reconstruction techniques for Electrical Impedance Tomography (EIT). This novel non-invasive medical imaging technique is still in its infancy, but has a great potential for continuous thoracic imaging because of the marked differences in the electrical properties of the tissues that compose the human thorax, and the pronounced changes that can be expected in disease.

In chapter three, I develop a comprehensive computational model of the actively breathing subject that can be used to simulate patients breathing spontaneously or with the support of an assisting mechanical ventilator. This model has a multitude of potential applications in respiratory research because the experimental conditions can be

manipulated at will and may be adjusted to simulate configurations that would be unacceptable in humans. Furthermore, variables that are inaccessible in patients can be accessed in computer simulations, and the number of subjects available for study is essentially unlimited. Therefore, I envisage this model to complement many clinical investigations and to contribute to the development of improved pulmonary monitoring techniques and mechanical ventilators.

In section 3.2, the computer model is used to quantitatively assess techniques to measure breath-by-breath a patient's dynamic intrinsic PEEP and inspiratory work of breathing, and to investigate the physiological reasons for the discrepancies that have been reported between values of intrinsic PEEP measured under static and dynamic conditions. Both measurement techniques performed well in the absence of expiratory muscle activity and cardiogenic oscillations. However, expiratory muscle activity at end-expiration introduced a substantial overestimation in both parameters, while cardiogenic oscillations caused large random errors that could not be reduced efficiently by ensemble averaging. These results demonstrate that some means of correction for both expiratory muscle activity and cardiogenic oscillations is necessary if dynamic intrinsic PEEP and work of breathing are to be measured accurately on-line. The kind of discrepancies seen experimentally between static and dynamic intrinsic PEEP could only be reproduced when the stress adaptation in the model was increased to five-fold the value that has been reported for COPD patients during inspiration, suggesting that these discrepancies are caused by heterogeneity of the expiratory flow limitation throughout the lung.

Cardiogenic oscillations on esophageal pressure signals cannot be removed by standard filtering because their frequency content overlaps that of respiratory pressure swings. In section 3.3, I develop an adaptive filter that employs an electrocardiogram to reduce the cardiogenic oscillations. In computer simulations, the variance of the simulated pleural pressure swings that was accounted for by the unfiltered and filtered esophageal pressure signal ranged between 55 and 94% and between 95 and 99%, respectively. In data obtained from four intensive care patients, the apparent cardiogenic oscillations were

markedly reduced without noticeable distortion of sharp deflections associated with respiration. The standard deviation of the measured intrinsic PEEP was reduced in all four patients by 44 to 71% (mean 57%), indicating that a considerable fraction of the variability of the measured dynamic intrinsic PEEP was entirely due to cardiogenic oscillations, and that the adaptive filter efficiently reduced this undesired variability.

In section 3.4, the effects of the interactions between a flow-triggered pressure support ventilator and patients with pronounced expiratory flow limitation are investigated in a computer simulation. The results of this study confirm Younes' earlier description of the basic mechanisms of patient-ventilator asynchrony (156) and indicated that a severely flow-limited patient receiving pressure support ventilation presents a highly nonlinear dynamic system in which small parameter changes can have a large impact on the overall system behaviour. Therefore, the optimal strategy for adjusting the ventilator is likely to depend on the subjects current condition and to vary considerably with time.

In chapter four, I investigate the inaccuracies of conventional first-order Finite Elements for EIT with respect to a specifically derived analytical solution. These inaccuracies produced SNRs of approximately 10 dB and between 18 and 35 dB for the two- and four-electrode method, respectively. Although the SNR increased somewhat when larger meshes were used, this study showed that augmenting the number of elements in a first-order Finite Element mesh is not an efficient means of improving the EIT forward solution. The great differences between the two- and four-electrode methods demonstrate that the voltages at the sites of current injection are badly estimated in a first-order Finite Element mesh and should not be used for static EIT image reconstruction even when the electrode-skin contact impedance is negligible. Comparison of the inaccuracies of the first-order Finite Element Meshes to the results of the simulation study in section 4.2 suggested that the accuracy of the forward solution needs to be improved by at least 30 dB before useful static EIT images can be obtained.

In a computer simulation of static EIT using only a single current source-sink pair, current patterns for which the current source was placed near the sink produced the smallest reconstruction errors and the greatest probabilities of convergence to the global minimum. Presumably, this was because they produced comparatively inhomogeneous current density distributions that favoured a diagonal structure of the Hessian matrix. The use of a central reference electrode produced approximately half the improvement in the quality of the reconstructed images that was obtained by doubling the number of boundary electrodes. This illustrates the general usefulness of central reference electrodes.

In the last section of chapter four, I derive higher-order isoparametric Finite Elements with space-variant conductivity for EIT. A comparatively simple second-order implementation of these Finite Elements improved the accuracy of the EIT forward solution by up to 15 dB over first-order Finite Elements. Higher-order isoparametric Finite Elements are also theoretically advantageous because they produce a conductivity distribution with less power at high spatial frequencies than standard Finite Elements, and because they permit a more accurate implementation of gradient regularization techniques. Thus, the further development of these higher-order Finite Elements for EIT is an important and promising area for future research.

Despite its present shortcomings, I envisage EIT to play an important role in future intensive care monitoring. For example, it is conceivable that a fairly accurate measure of lung volume may be obtained from a relatively simple three-dimensional EIT system. Simultaneous recordings of esophageal pressure signals would then allow the evaluation of clinically important parameters such as intrinsic PEEP and inspiratory work of breathing in spontaneously breathing patients without the discomfort of a direct flow measurement at the airway opening. Ultimately, the electrode grid of the EIT system may also be used for electrocardiographic measurements which, together with some measurements of physiological air and blood pressures, would permit the complete integration of cardio-respiratory monitoring equipment for critical care patients.

5.2 Original contributions

- (1) A multi-purpose nonlinear viscoelastic model of the actively breathing patient was developed. The model comprises four nonlinear dynamic subsystems that characterize the passive mechanical properties of the respiratory system, the properties of the respiratory musculature, the conditions at the airway opening (endotracheal tube and ventilator or atmospheric pressure), and the transmission of cardiogenic oscillations onto the respiratory system.
- (2) An empirical closed-form description of the expiratory flow limitation phenomenon was developed to permit efficient computational simulation of expiratory flow limitation.
- (3) In a computer simulation, the assumption of a fixed chest wall elastance of $5 \text{ cmH}_2\text{O}\cdot\text{L}^{-1}$ for the computation of the patient's inspiratory work of breathing from esophageal pressure and flow was found to be valid within a 5% error margin when no other confounding factors were present.
- (4) In a computer simulation, expiratory muscle activity at end-expiration was found to cause severe overestimation of the measured values of both dynamic intrinsic PEEP and the patient's inspiratory work of breathing.
- (5) In a computer simulation, cardiogenic oscillations on esophageal pressure were found to introduce substantial random errors to the measured values of both dynamic intrinsic PEEP and the patient's inspiratory work of breathing.
- (6) In a computer simulation based on a model with central expiratory flow limitation, the discrepancies between the values of intrinsic PEEP measured under static and dynamic conditions could be reproduced only after the stress adaptation in the lungs was increased five-fold over the values reported in the literature for COPD patients

during inspiration. This suggests that these discrepancies are caused by heterogeneity of the expiratory flow limitation throughout the lung.

- (7) An adaptive filter to reduce the cardiogenic oscillations on esophageal pressure signals was developed. In simulated data, this filter improved the variance of the true pleural pressure swings that was accounted for by the esophageal pressure signal from between 55 and 94% to between 95 and 99%. In *in vivo* patient data, the filter reduced the apparent cardiogenic oscillations without noticeably distorting the sharp deflections in esophageal pressure due to respiration. In the Fourier domain, the filter removed transients at integer multiples of the heart rate without significantly altering the remainder of the signals.
- (8) In four intensive care patients, the standard deviation of the dynamic intrinsic PEEP measured breath-by-breath over periods of 50 to 120 seconds was reduced by 44 to 71% (mean 57%) when the adaptive filter was used. This suggests that a considerable fraction of the variability of the measured dynamic intrinsic PEEP was entirely due to cardiogenic oscillations, and that the adaptive filter efficiently reduces this undesired variability.
- (9) The mechanisms of patient-ventilator asynchrony during pressure support ventilation were studied in a computer simulation that reproduces the diseased human respiratory system more closely than the model employed in an earlier study (156). The principal mechanisms of patient-ventilator asynchrony as described in that study were confirmed. The results suggest that a pressure support ventilator together with a severely diseased patient may form a highly nonlinear dynamic system that is difficult to control.
- (10) The analytical solution for the electrical potential on the boundary of a two-dimensional circular phantom and opposite current injection was shown to diverge when point current sources are assumed. A solution for finite size electrodes was

derived and shown to converge. This solution is applicable both for a homogeneous conductivity distribution and for centered circular targets.

- (11) The inaccuracies of first-order Finite Elements for the EIT forward solution were shown to produce SNRs of less than 35dB even when meshes with very large numbers of elements were used. The data suggest that the accuracy of the forward solution needs to be improved by approximately two orders of magnitude before good static EIT images can be obtained.
- (12) The inaccuracies of first-order Finite Elements for the EIT forward solution were more pronounced at the sites of current injection than anywhere else in the mesh. Thus, the voltages measured at these locations should not be used for the reconstruction of static EIT images even when the electrode-skin contact impedance is negligible.
- (13) A convergence criterion for the iterative reconstruction of EIT images was developed. This convergence criterion successfully identified image reconstructions that efficiently converged to the global minimum, thereby avoiding superfluous iterations that did not noticeably improve the image any further.
- (14) In a computer simulation, the reconstruction error of static EIT using a single current source-sink pair and iterative Gauss-Newton optimization was shown to be minimal when the current source and sink were placed in close vicinity. Presumably, this was because current patterns that produce relatively inhomogeneous current density distributions favour a diagonal structure of the Hessian matrix.
- (15) In a computer simulation, the reconstruction error of images obtained using a central reference electrode were found to range between those of a control configuration with an equal number of boundary electrodes and of a computationally more involved configuration with twice the number of boundary

electrodes, but no central electrode. This demonstrates the general value of a central reference electrode.

- (16) Higher-order isoparametric Finite Elements were derived for modeling electric fields in two-dimensional media with space-variant material properties.
- (17) Higher-order isoparametric Finite Elements with space-variant tissue properties were shown to reduce the inaccuracies of the EIT forward solution by up to 15 dB compared to first-order Finite Element Meshes of similar computational complexity.
- (18) The theoretical advantages and limitations of higher-order isoparametric Finite Elements with space-variant tissue properties for EIT image reconstruction were introduced.

5.3 Suggestions for future work

5.3.1 Pulmonary monitoring

As discussed elsewhere in this thesis, the computer model of the spontaneously breathing patient described in section 3.1 has a large number of potential applications. The following is a list of some examples.

Recent clinical studies advocate measuring the pressure-time integral (PTI, also referred to as pressure-time product) rather than W_{insp} . However, it is somewhat unclear whether the PTI can be measured any more accurately than W_{insp} and how PTI and W_{insp} relate. Also, the measurement of the PTI is ambiguous in that it can be measured between zero-flow points or between deflection points in P_{es} with both measurement techniques yielding markedly different results (Volta *et al.*, ATS intl. conf., New Orleans 1996). These issues could easily be addressed using the computer simulation described in section 3.1.

Younes (156) has previously compared PSV and PAV in a comparatively simple computer simulation. A more thorough investigation of the patient's ability to modulate ventilation for all existing assisting modes of mechanical ventilation including CPAP can be expected to be clinically valuable and to provide additional insights into patient-ventilator interactions. For this study, it might be interesting to parameterize the model of section 3.1 for various groups of simulated patients with different pulmonary diseases.

The effects of ventilator design aspects may be studied individually for different disease groups using my computer model. Hopefully, studies of this type will be conducted soon and may contribute to the design of improved mechanical ventilators.

The adaptive filter to reduce cardiogenic oscillations on P_{es} described in section 3.3 may permit an improved exploitation of the information contained in the esophageal pressure signal. One particularly interesting question is whether it may be possible to trigger an assisting mechanical ventilator off an adaptively filtered esophageal pressure

signal. Presumably, this would substantially reduce Δt_{trig} and hence overcome some of the problems of assisted mechanical ventilation that were addressed in section 3.4. The computer model developed in section 3.1 provides an ideal environment for the investigation of this issue.

5.3.2 Thoracic imaging using EIT

Although dynamic EIT imaging of the thorax has been shown to have several interesting applications, it is beyond question that static EIT imaging could ultimately provide a much greater amount of clinically valuable information. In my opinion, the long term goal of EIT research is the reconstruction of three-dimensional static complex-valued images at multiple frequencies in real time.

The most obvious continuation of the work presented in chapter four of this thesis is the further investigation of higher-order isoparametric FEs with variable conductivity. For solution of the inverse problem, however, I am inclined to speculate that meshes primarily based on the transformation of triangular elements may show better convergence behaviour because their polynomial basis is not supercomplete. The modeling of the boundary condition, especially in the context of very high-order FEs where the boundary condition may be modeled by only a few line elements, also merits further investigation. In this context, it may be useful to consider the use of other approximation functions than regular polynomials for j_s , since these might permit better modeling of finite-size electrodes.

In general, the FE method can easily be extended to three-dimensional, complex-valued isoparametric FEs with space-variant admittivity. Thus the FE method does not present any fundamental limitations for the reconstruction of three-dimensional static complex-valued images. However, a substantial amount of work will be necessary before this goal can be achieved.

BIBLIOGRAPHY

1. Adler, A., R. Guardo, and Y. Berthiaume, "Impedance imaging of lung ventilation: do we need to account for chest expansion?", *IEEE Trans Biomed Eng*, **43(4)**: 414-420, 1996.
2. Adler, A. and R. Guardo, "Neural network image reconstruction technique for electrical impedance tomography", *IEEE Trans Med Imaging*, **13(4)**: 593-600, 1994.
3. Adler, A. and R. Guardo, "Electrical Impedance Tomography: Regularized Imaging and Contrast Detection", *IEEE Trans Med Imaging*, **15(2)**: 170-179, 1996.
4. Agostoni, E. "Mechanics of the chest wall – statics". In: Campbell, E.J.M., E. Agostoni, and J. Newsom Davis (Eds), *The respiratory muscles, mechanics and neural control*. 2nd edition, Philadelphia: Saunders, 1970.
5. Amasha, H.M., A.P. Anderson, J. Conway, and D.C. Barber, "Quantitative assessment of impedance tomography for temperature measurements in microwave hyperthermia", *Clin Phys Physiol Meas*, **9**: Suppl A:49-53, 1988.

6. Appendini, L., A. Patessio, S. Zanaboni, M. Carone, B. Gukov, C.F. Donner, and A. Rossi, "Physiologic effects of positive end-expiratory pressure and mask pressure support during exacerbations of chronic obstructive pulmonary disease", *Am J Respir Crit Care Med*, **149(5)**: 1069-1076, 1994.
7. Avill, R., Y.F. Mangnall, N.C. Bird, B.H. Brown, D.C. Barber, A.D. Seagar, A.G. Johnson, and N.W. Read, "Applied potential tomography. A new noninvasive technique for measuring gastric emptying", *Gastroenterology*, **92(4)**: 1019-1026, 1987.
8. Avis, N.J. and D.C. Barber, "Adjacent or polar drive?: Image reconstruction implications in Electrical Impedance Tomography systems employing filtered backprojection", *Proc Ann Conf IEEE Eng Med Biol Soc*, **14**: 1689-1690, 1992.
9. Banner, M.J., M.J. Jaeger, and R.R. Kirby, "Components of the work of breathing and implications for monitoring ventilator-dependent patients. [Review]", *Crit Care Med*, **22(3)**: 515-523, 1994.
10. Banner, M.J., R.R. Kirby, A. Gabrielli, P.B. Blanch, and A.J. Layon, "Partially and totally unloading respiratory muscles based on real-time measurements of work of breathing. A clinical approach", *Chest*, **106(6)**: 1835-1842, 1994.
11. Barber, D.C. and B.H. Brown, "Applied potential tomography", *J Phys E: Sci Instr*, **17**: 723-733, 1984.
12. Barber, D.C., B.H. Brown, and I. Freeston, L, "Imaging spatial distributions of resistivity using applied potential tomography", *Elec Lett*, **19**: 933-935, 1983.
13. Barber, D.C. and A.D. Seagar, "Fast reconstruction of resistive images", *Clin Phys Physiol Meas*, **8 Suppl. A**: 47-54, 1987.
14. Baxter, A.J., Y.F. Mangnall, E.H. Loj, B. Brown, D.C. Barber, A.G. Johnson, and N.W. Read, "Evaluation of applied potential tomography as a new non-invasive gastric secretion test", *Gut*, **29(12)**: 1730-1735, 1988.

15. Baydur, A., P.K. Behrakis, W.A. Zin, M. Jaeger, and J. Milic-Emili, "A simple method for assessing the validity of the esophageal balloon technique", *Am Rev Respir Dis*, **126**: 788-791, 1982.
16. Blad, B., B. Persson, and K. Lindstrom, "Quantitative assessment of impedance tomography for temperature measurements in hyperthermia", *Int J Hyperthermia*, **8(1)**: 33-43, 1992.
17. Breckon, W.R. and M.K. Pidcock, "Data errors and reconstruction algorithms in electrical impedance tomography", *Clin Phys Physiol Meas*, **9, Suppl. A**: 105-109, 1988.
18. Brochard, L., A. Harf, H. Lorino, and F. Lemaire, "Inspiratory pressure support prevents diaphragmatic fatigue during weaning from mechanical ventilation", *Am Rev Respir Dis*, **139(2)**: 513-521, 1989.
19. Brown, B.H., D.C. Barber, and A.D. Seagar, "Applied potential tomography: possible clinical applications", *Clin Phys Physiol Meas*, **6(2)**: 109-121, 1985.
20. Brown, B.H., A. Leathard, A. Sinton, F.J. McArdle, R.W. Smith, and D.C. Barber, "Blood flow imaging using electrical impedance tomography", *Clin Phys Physiol Meas*, **13, Suppl A**: 175-9, 1992.
21. Buytendijk, H.J. *Oesophagusdruk en Longelasticiteit*, Dissertatie, Univ. Groningen, 1949.
22. Chartrand, D.A., T.E. Ye, J.M. Maarek, and H.K. Chang, "Measurement of pleural pressure at low and high frequencies in normal rabbits", *J Appl Physiol*, **63**: 1142-1146, 1987.
23. Cheney, M. and D. Isaacson, "Distinguishability in Impedance Imaging", *IEEE Trans Biomed Eng*, **39(8)**: 852-860, 1992.

24. Cheney, M., D. Isaacson, J.C. Newell, S. Simske, and J. Goble, "NOSER: An algorithm for solving the inverse conductivity problem", *Int J Imaging Systems & Technology*, **2**: 66-75, 1990.
25. Cheng, K.-S., D. Isaacson, J.C. Newell, and D.G. Gisser, "Electrode models for electric current computed tomography", *IEEE Trans Biomed Eng*, **36(9)**: 918-923, 1989.
26. Cole, K.S. and R.H. Cole, "Dispersion and absorption in dielectrics", *J Chem Phys*, **9**: 341-351, 1941.
27. Conway, J. "Electrical impedance tomography for thermal monitoring of hyperthermia treatment: an assessment using in vitro and in vivo measurements", *Clin Phys Physiol Meas*, **8**: Suppl A:141-6, 1987.
28. Conway, J., M. Hawley, Y. Mangnall, H. Amasha, and G.C. van Rhoon, "Experimental assessment of electrical impedance imaging for hyperthermia monitoring", *Clin Phys Physiol Meas*, **13**: Suppl A:185-9, 1992.
29. Coussa, M.L., C. Guerin, N.T. Eissa, C. Corbeil, M. Chasse, J. Braidy, N. Matar, and J. Milic-Emili, "Partitioning of work of breathing in mechanically ventilated COPD patients", *J Appl Physiol*, **75(4)**: 1711-1719, 1993.
30. Dawson, S.V. and E.A. Elliott, "Wave-speed limitation on expiratory flow - a unifying concept", *J Appl Physiol : Respirat Environ Exercise Physiol*, **43**: 498-515, 1977.
31. de Troyer, A., V. Ninane, J.J. Gilmartin, C. Lemerre, and M. Estenne, "Triangularis sterni muscle use in supine humans", *J Appl Physiol*, **62(3)**: 919-925, 1987.
32. Dechman, G.S., J. Sato, and J.H.T. Bates, "Factors affecting the accuracy of esophageal balloon measurement of pleural pressure in dogs", *J Appl Physiol*, **72(1)**: 383-388, 1992.

33. Dechman, G.S., J. Sato, and J.H.T. Bates, "Changes in dynamic elastance and resistance of the canine respiratory system with acute pleural effusion", *Eur Respir J*, **6**: 219-224, 1993.
34. Dijkstra, A.M., B.H. Brown, A.D. Leathard, N.D. Harris, D.C. Barber, and D.L. Edbrooke, "Clinical applications of electrical impedance tomography. [Review]", *J Med Eng Technol*, **17(3)**: 89-98, 1993.
35. Dufresne, M. and P.P. Silvester, "Universal matrices for the n-dimensional Finite Element", *Proc Int Conf Comput Electromagn*, **3**: Bath, U.K. 1996.
36. Esteban, A., F. Frutos, M.J. Tobin, I. Alia, J.F. Solsona, I. Valverdu, R. Fernandez, M.A. de la Cal, S. Benito, R. Tomas, et al. "A comparison of four methods of weaning patients from mechanical ventilation.", *New Engl J Med*, **332(6)**: 345-350, 1995.
37. Eyuboglu, B.M., B.H. Brown, D.C. Barber, and A.D. Seagar, "Localisation of cardiac related impedance changes in the thorax", *Clin Phys Physiol Meas*, **8**: Suppl A:167-73, 1987.
38. Eyuboglu, B.M. and T.C. Pilkington, "Comments on Distinguishability in Electrical Impedance Imaging", *IEEE Trans Biomed Eng*, **40(12)**: 1328-1330, 1993.
39. Fabry, B., J. Guttman, L. Eberhard, T. Bauer, C. Haberthur, and G. Wolff, "An analysis of desynchronization between the spontaneously breathing patient and ventilator during inspiratory pressure support", *Chest*, **107(5)**: 1387-1394, 1995.
40. Fernandez, R., S. Benito, J. Sanchis, J. Milic-Emili, and A. Net, "Inspiratory effort and occlusion pressure in triggered mechanical ventilation", *Intensive Care Med*, **14(6)**: 650-653, 1988.
41. Fiastro, J.F., M.P. Habib, B.Y. Shon, and S.C. Campbell, "Comparison of standard weaning parameters and the mechanical work of breathing in mechanically ventilated patients", *Chest*, **94(2)**: 232-238, 1988.

42. Foster, K.R. and H.P. Schwan, "Dielectric properties of tissue and biological materials", *Crit Rev Biomed Eng*, **17**: 25-104, 1989.
43. Fricke, H. and M. Morse, "The electrical capacity of tumour of the breast", *J Cancer Res*, **10**: 340-376, 1926.
44. Fry, D.L., R.V. Ebert, W.W. Stead, and C.C. Brown, "The mechanics of pulmonary ventilation in normal subjects and in patients with emphysema", *Am J Med*, **16**: 80-97, 1954.
45. Fuks, L.F., M. Cheney, D. Isaacson, D.G. Gisser, and J.C. Newell, "Detection and imaging of electric conductivity and permittivity at low frequency", *IEEE Trans Biomed Eng*, **38(11)**: 1106-1110, 1991.
46. Gencer, N.G., Y. Ziya, and S.J. Williamson, "Electrical impedance tomography: induced-current imaging achieved with a multiple coil system", *IEEE Trans Biomed Eng*, **43(2)**: 139-149, 1996.
47. Gersing, E., F. Bach, C. Brockhoff, M.M. Gebhard, G. Kehrer, A. Meissner, and H.J. Bretschneider, "Messung der elektrischen Impedanz von Organen", *Biomed Technik*, **36**: 70-77, 1991.
48. Geselowitz, D.B. "An application of electrocardiographic lead theory to impedance plethysmography", *IEEE Trans Biomed Eng*, **18(1)**: 38-41, 1971.
49. Gisser, D.G., D. Isaacson, and J.C. Newell, "Theory and performance of an adaptive current tomography system", *Clin Phys Physiol Meas*, **9, Suppl. A**: 35-41, 1988.
50. Glass, L. and M.C. Mackey, *From clocks to chaos*. Princeton: Princeton University Press, 1988.
51. Gottfried, S.B. "The role of PEEP in the mechanically ventilated COPD patient". In: Marini, J.J., C. Roussos, and J.L. Vincent (Eds), *Update in Intensive Care and Emergency Medicine*. Berlin: Springer, 1991.

52. Gottfried, S.B., A. Rossi, and J. Milic-Emili, "Dynamic hyperinflation, intrinsic PEEP, and the mechanically ventilated patient", *Intensive and Critical Care Digest*, **5**: 30-33, 1986.
53. Griffiths, H. and A. Ahmed, "Applied potential tomography for non-invasive temperature mapping in hyperthermia", *Clin Phys Physiol Meas*, **8**: Suppl A:147-53, 1987.
54. Griffiths, H. and J. Jossinet, "Bioelectrical spectroscopy from multi-frequency EIT", *Physiol Meas*, **15**, Suppl 2a: A59-A63, 1994.
55. Griffiths, H. and Z. Zhang, "A dual-frequency electrical impedance tomography system", *Phys Med Biol*, **34**(10): 1465-1476, 1989.
56. Guardo, R., C. Boulay, B. Murray, and M. Bertrand, "An experimental study in electrical impedance tomography using backprojection reconstruction", *IEEE Trans Biomed Eng*, **38**(7): 617-627, 1991.
57. Guerin, C., M.L. Coussa, N.T. Eissa, C. Corbeil, M. Chasse, J. Braidy, N. Matar, and J. Milic-Emili, "Lung and chest wall mechanics in mechanically ventilated COPD patients", *J Appl Physiol*, **74**(4): 1570-1580, 1993.
58. Gurevitch, M. and D. Gelmont, "Importance of trigger sensitivity to ventilator response delay in advanced chronic obstructive pulmonary disease with respiratory failure", *Crit Care Med*, **17**: 354-359, 1989.
59. Guttman, J., L. Eberhard, B. Fabry, W. Bertschmann, and G. Wolff, "Continuous calculation of intratracheal pressure in tracheally intubated patients", *Anesthesiology*, **79**(3): 503-513, 1993.
60. Harris, N.D., A.J. Suggett, D.C. Barber, and B.H. Brown, "Applied potential tomography: A new technique for monitoring pulmonary function", *Clin Phys Physiol Meas*, **9**, Suppl. A: 79-85, 1988.

61. Heimbach, M. "Data collection errors". In: Webster, J.G. (Ed), *Electrical Impedance Tomography*. Bristol: Adam Hilger, 1990.
62. Hernandez, P., P. Navalesi, F. Maltais, A. Gursahaney, and S.B. Gottfried, "Comparison of static and dynamic measurements of intrinsic PEEP in anesthetized cats", *J Appl Physiol*, **76(6)**: 2437-2442, 1994.
63. Hines, W.W. and D.C. Montgomery, *Probability and statistics in Engineering and management science*. 3rd edition, Toronto: John Wiley & Sons, 1990.
64. Hofmann, R. "Numerische Mathematik". In: Grosche, G., V. Ziegler, and D. Ziegler (Eds), *Bronstein-Semendjajew Taschenbuch der Mathematik*. 22th edition, Frankfurt/Main: Verlag Harri Deutsch, 1985.
65. Hua, P., J.G. Webster, and W.J. Tompkins, "Effect of measurement method on noise handling and image quality of EIT imaging", *Proc Ann Conf IEEE Eng Med Biol Soc*, **9**: 1429-1430, 1987.
66. Hua, P., J.G. Webster, and W.J. Tompkins, "A regularised electrical impedance tomography reconstruction algorithm", *Clin Phys Physiol Meas*, **9**: Suppl A:137-41, 1988.
67. Hua, P. and E.J. Woo, "Reconstruction algorithms". In: Webster, J.G. (Ed), *Electrical Impedance Tomography*. Bristol: Adam Hilger, 1990.
68. Hua, P., E.J. Woo, J.G. Webster, and W.J. Tompkins, "Using compound electrodes in electrical impedance tomography", *IEEE Trans Biomed Eng*, **40(1)**: 29-34, 1993.
69. Hubmayr, R.D. "Setting the ventilator". In: Tobin, M.J. (Ed), *Principles and practice of mechanical ventilation*. New York: McGraw-Hill, 1994.
70. Hunter, I.W. and R.E. Kearney, "Two-sided linear filter identification", *Med & Biol Eng & Comput*, **21**: 203-209, 1983.
71. Hyatt, R.E. "Expiratory flow limitation. [Review]", *J Appl Physiol*, **55(1, Pt 1)**: 1-7, 1983.

72. Ider, Y.Z., N.G. Gencer, E. Atalar, and H. Tosun, "Electrical Impedance Tomography of translationally uniform cylindrical objects with general cross-sectional boundary", *IEEE Trans Med Imaging*, **9(1)**: 49-59, 1990.
73. Isaacson, D. "Distinguishability of Conductivities by Electric Current Computed Tomography", *IEEE Trans Med Imaging*, **5(2)**: 91-95, 1986.
74. Jossinet, J. "A hardware design for imaging the electrical impedance of the breast", *Clin Phys Physiol Meas*, **9, Suppl A**: 25-8, 1988.
75. Jossinet, J. and C. Trillaud, "Imaging the complex impedance in electrical impedance tomography", *Clin Phys Physiol Meas*, **13, Suppl A**: 47-50, 1992.
76. Jossinet, J., C. Trillaud, F. Risacher, and E. McAdams, T, "High frequency electrical impedance tomograph using distributed parallel input channels", *Med Prog Technol*, : 167-172, 1994.
77. Jubran, A., W.B. Van de Graaff, and M.J. Tobin, "Variability of patient-ventilator interaction with pressure support ventilation in patients with chronic obstructive pulmonary disease", *American Journal of Respiratory & Critical Care Medicine*, **152(1)**: 129-136, 1995.
78. Kim, Y., J.G. Webster, and W.J. Tompkins, "Electrical impedance imaging of the thorax", *J Microwave Power*, **18(3)**: 245-257, 1983.
79. Kim, Y. and H.W. Woo, "A prototype system and reconstruction algorithms for electrical impedance technique in medical body imaging", *Clin Phys Physiol Meas*, **8: Suppl A**:63-70, 1987.
80. Kimura, T., J. Takezawa, K. Nishiwaki, and Y. Shimada, "Determination of the optimal pressure support level evaluated by measuring transdiaphragmatic pressure", *Chest*, **100**: 112-117, 1991.

81. Koukourlis, C.S., G.A. Kyriacou, and J.N. Sahalos, "A 32-electrode data collection system for electrical impedance tomography", *IEEE Trans Biomed Eng*, **42(6)**: 632-636, 1995.
82. Lambert, R.K. and T.A. Wilson, "A model for the elastic properties of the lung and their effect on expiratory flow", *J Appl Physiol*, **34**: 34-48, 1973.
83. Lambert, R.K., T.A. Wilson, R.E. Hyatt, and J.R. Rodarte, "A computational model for expiratory flow", *J Appl Physiol*, **52(1)**: 44-56, 1982.
84. Lauzon, A.-M. and J.H.T. Bates, "Estimation of time-varying respiratory mechanical parameters by recursive least squares", *J Appl Physiol*, **71(3)**: 1159-1165, 1991.
85. Lessard, M.R., F. Lofaso, and L. Brochard, "Expiratory muscle activity increases intrinsic positive end-expiratory pressure independently of dynamic hyperinflation in mechanically ventilated patients", *Am J Respir Crit Care Med*, **151(2:Pt 1)**: Pt 1):562-9, 1995.
86. Linton, D.M., P.D. Potgieter, S. Davis, A.T.J. Fourie, J.X. Brunner, and T.P. Laubscher, "Automatic weaning from mechanical ventilation using an adaptive lung ventilation controller", *Chest*, **106**: 1843-1850, 1994.
87. MacIntyre, N.R. "Respiratory function during pressure support ventilation", *Chest*, **89**: 677-683, 1986.
88. Maltais, F., H. Reissmann, P. Navalesi, P. Hernandez, A. Gursahaney, V.M. Ranieri, M. Sovilj, and S.B. Gottfried, "Comparison of static and dynamic measurements of intrinsic PEEP in mechanically ventilated patients", *Am J Respir Crit Care Med*, **150(5, Pt 1)**: 1318-1324, 1994.

89. Mangnall, Y.F., A.J. Baxter, R. Avill, N.C. Bird, B.H. Brown, D.C. Barber, A.D. Seagar, A.G. Johnson, and N.W. Read, "Applied potential tomography: a new non-invasive technique for assessing gastric function", *Clin Phys Physiol Meas*, **8**: Suppl A:119-29, 1987.
90. Marini, J.J., J.S. Capps, and B.H. Culver, "The inspiratory work of breathing during assisted mechanical ventilation", *Chest*, **87**(5): 612-618, 1985.
91. McLeod, C.N., C.W. Denyer, F.J. Lidgley, W.R. Lionheart, K.S. Paulson, M.K. Pidcock, and Y. Shi, "High speed in vivo chest imaging with OXBACT III", *Proc Ann Conf IEEE Eng Med Biol Soc*, **18**: paper no. 1139, 1996.
92. McNamara, J.J., R.G. Castile, M.S. Ludwig, G.M. Glass, R.H. Ingram, Jr., and J.J. Fredberg, "Heterogeneous regional behavior during forced expiration before and after histamine inhalation in dogs", *J Appl Physiol*, **76**(1): 356-360, 1994.
93. Mead, J., J.M. Turner, P.T. Macklem, and J.B. Little, "Significance of the relationship between lung recoil and maximum expiratory flow", *J Appl Physiol*, **22**(1): 95-108, 1967.
94. Metherall, P., D.C. Barber, R.H. Smallwood, and B.H. Brown, "Three-dimensional electrical impedance tomography", *Nature*, **380**(6574): 509-512, 1996.
95. Metherall, P., R.H. Smallwood, and D.C. Barber, "Three-dimensional electrical impedance tomography of the human thorax", *Proc Ann Conf IEEE Eng Med Biol Soc*, **18**: paper no. 69, 1996.
96. Murai, T. and Y. Kagawa, "Electrical Impedance Computed Tomography based on a Finite Element Model", *IEEE Trans Biomed Eng*, **32**(3): 177-184, 1985.
97. Nava, S., C. Bruschi, F. Rubini, A. Palo, G. Iotti, and A. Braschi, "Respiratory response and inspiratory effort during pressure support ventilation in COPD patients", *Intensive Care Med*, **21**(11): 871-879, 1995.

98. Newell, J.C., P.M. Edic, X. Ren, J.L. Larson-Wiseman, and M.D. Danyleiko, "Assessment of acute pulmonary edema in dogs by electrical impedance tomography", *IEEE Trans Biomed Eng*, **43(2)**: 133-138, 1996.
99. Ninane, V., J.C. Yernault, and A. de Troyer, "Intrinsic PEEP in patients with chronic obstructive pulmonary disease. Role of expiratory muscles", *Am Rev Respir Dis*, **148(4:Pt 1)**: Pt 1:1037-42, 1993.
100. Noble, T.J., A.H. Morice, P. Milnes, N.D. Harris, A.D. Leathard, S. Smith, and B.H. Brown, "Electrical impedance tomographic spectroscopy in the detection of increased lung water in heart failure", *Proc Ann Conf IEEE Eng Med Biol Soc*, **18**: paper no. 511, 1996.
101. Nour, S., Y. Mangnall, J.A. Dickson, R. Pearse, and A.G. Johnson, "Measurement of gastric emptying in infants with pyloric stenosis using applied potential tomography", *Archives of Disease in Childhood*, **68(4)**: 484-486, 1993.
102. Pardaens, J., K.P. van de Woestijne, and J. Clément, "A physical model of expiration", *J Appl Physiol*, **33**: 479-490, 1972.
103. Pare, P.D., L.A. Brooks, J. Bates, L.M. Lawson, J.M. Nelems, J.L. Wright, and J.C. Hogg, "Exponential analysis of the lung pressure-volume curve as a predictor of pulmonary emphysema", *Am Rev Respir Dis*, **126(1)**: 54-61, 1982.
104. Patel, A. "Data collection methods". In: Webster, J.G. (Ed), *Electrical Impedance Tomography*. Bristol: Adam Hilger, 1990.
105. Pepe, P.E. and J.J. Marini, "Occult positive end expiratory pressure in mechanically ventilated patients with airflow obstruction", *Am Rev Respir Dis*, **126**: 166-170, 1982.
106. Petrof, B.J., E. Calderini, and S.B. Gottfried, "Effect of CPAP on respiratory effort and dyspnea during exercise in severe COPD", *J Appl Physiol*, **69(1)**: 179-188, 1990.

107. Petrof, B.J., M. Legare, P. Goldberg, J. Milic-Emili, and S.B. Gottfried, "Continuous positive airway pressure reduces work of breathing and dyspnea during weaning from mechanical ventilation in severe chronic obstructive pulmonary disease", *Am Rev Respir Dis*, **141(2)**: 281-289, 1990.
108. Pilkington, T., B.M. Eyuboglu, and P. Wolf, "Utilization of esophageal reference electrode to enhance impedance imaging", *Proc Ann Conf IEEE Eng Med Biol Soc*, **11**: 482, 1989.
109. Piperno, G., E.H. Frei, and M. Hoshitzky, "Breast cancer screening by impedance measurements", *Front Med Biol Eng*, **2**: 111-117, 1990.
110. Pride, N.B., S. Permutt, R.L. Riley, and B. Bromberger-Barnea, "Determinants of maximal expiratory flow from the lung", *J Appl Physiol*, **23(5)**: 646-662, 1967.
111. Purvis, W.R., R.C. Tozer, and I.L. Freeston, "Impedance imaging using induced currents", *Proc Ann Conf IEEE Eng Med Biol Soc*, **12**: 114-115, 1990.
112. Record, P., M. X. Rosell, B. Rigaud, and i. Costa, Riu, "Bio-impedance active electrode for in vivo measurement", *Med & Biol Eng & Comput*, **32(6)**: 679-685, 1994.
113. Riddle, W. and M. Younes, "A model for the relation between respiratory neural and mechanical outputs. II. Methods", *J Appl Physiol*, **51(4)**: 979-989, 1981.
114. Rigaud, B., L. Hamzaoui, N. Chauveau, M. Granie, J.P. Scotto Di Rinaldi, and J.P. Morucci, "Tissue characterization by impedance: a multifrequency approach", *Physiol Meas*, **15, Suppl 2a**: A13-A20, 1994.
115. Riu, P.J., J. Rosell, A. Lozano, and R. Pallas-Areny, "A broadband system for multifrequency static imaging in electrical impedance tomography", *Clin Phys Physiol Meas*, **13**: Suppl A:61-5, 1992.

116. Rohrer, F. "Der Strömungswiderstand in den menschlichen Atemwegen und der Einfluss der unregelmässigen Verzweigung des Bronchialsystems auf den Atmungsverlauf in verschiedenen Lungenbezirken", *Pflügers Arch Ges Physiol, Menschen und Tiere*, **162**: 225-299, 1915.
117. Rosell, J., J. Colominas, P. Riu, R. Pallas-Areny, and J.G. Webster, "Skin impedance from 1 Hz to 1 Mhz", *IEEE Trans Biomed Eng*, **35**: 649-651, 1988.
118. Rosell, J., D. Murphy, R. Pallas, and P. Rolfe, "Analysis and assessment of errors in a parallel data acquisition system for electrical impedance tomography", *Clin Phys Physiol Meas*, **9**: Suppl A:93-9, 1988.
119. Rossi, A., S.B. Gottfried, L. Zocchi, B.D. Higgs, S. Lennox, P.M.A. Calverley, P. Begin, A. Grassino, and J. Milic-Emili, "Measurement of static compliance of the total respiratory system in patients with acute respiratory failure during mechanical ventilation", *Am Rev Respir Dis*, **131**: 672-677, 1985.
120. Rossi, A., R. Brandolese, J. Milic-Emili, and S.B. Gottfried, "The role of PEEP in patients with chronic obstructive pulmonary disease during assisted ventilation. [Review]", *Eur Respir J*, **3**(7): 818-822, 1990.
121. Roupie, E., M. Dambrosio, G. Servillo, H. Mentec, S. el Atrous, L. Beydon, C. Brun-Buisson, F. Lemaire, and L. Brochard, "Titration of tidal volume and induced hypercapnia in acute respiratory distress syndrome", *American Journal of Respiratory & Critical Care Medicine*, **152**(1): 121-128, 1995.
122. Roussos, C. and P.T. Macklem, "The respiratory muscles", *New Engl J Med*, **307**: 786-797, 1982.
123. Ruan, W., R. Guardo, A. Adler, and G. Savoie, "Finite element modeling of impedance imaging using induced currents", *Proc Ann Conf IEEE Eng Med Biol Soc*, **16**: 536-537, 1994.

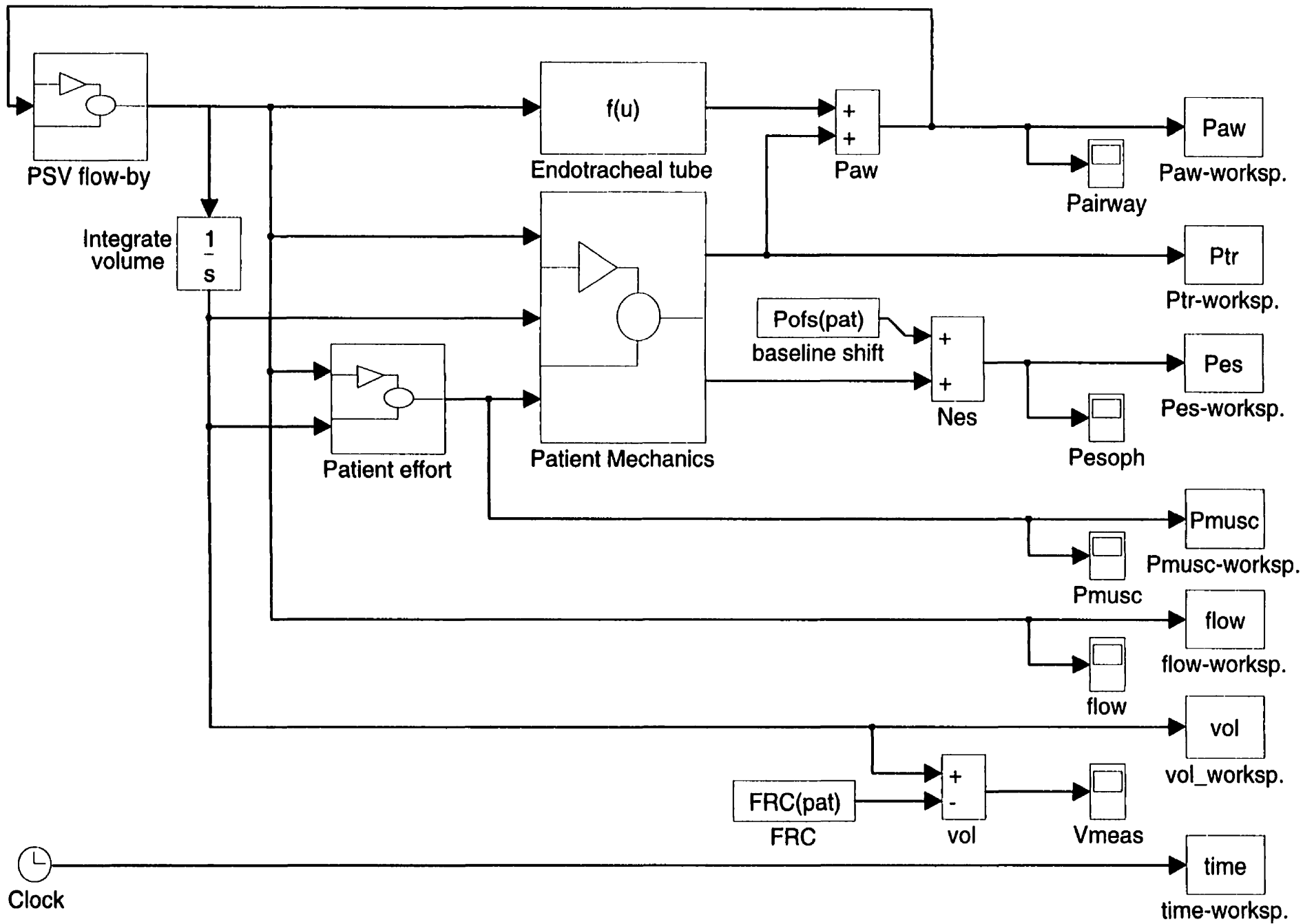
124. Sahalos, J.N., E. Vlachogiannis, C. Koukourlis, G. Kyriacou, and K. Batas, "Electrical impedance measurements for pulmonary disease diagnosis", *Clin Phys Physiol Meas*, **13, Suppl. A**: 171-174, 1992.
125. Salazar, E. and J.H. Knowles, "An analysis of pressure volume characteristics of the lungs", *J Appl Physiol*, **19**: 97-104, 1964.
126. Schwan, H.P. "Electrical properties of tissue and cell suspensions", *Adv Biol Med Phys*, **5**: 147-209, 1957.
127. Shapiro, B.A., R.A. Harrison, R.M. Kacmarek, and R.D. Cane, *Clinical application of respiratory care*. 3rd edition, Chicago: Year book medical publishers, 1985.
128. Sharp, J.T. and R.E. Hyatt, "Mechanical and electrical properties of respiratory muscles". In: Macklem, P.T. and J. Mead (Eds), *Handbook of physiology, Section 3, Volume III*. Bethesda, MD: Am Pysiol Soc, 1986.
129. Shikora, S.A., B.R. Bistran, B.C. Borlase, G.L. Blackburn, M.D. Stone, and P.N. Benotti, "Work of breathing: reliable predictor of weaning and extubation", *Crit Care Med*, **18(2)**: 157-162, 1990.
130. Silvester, P.P. "Construction of triangular finite element universal matrices", *Int J Num Meth Eng*, **12**: 237-244, 1978.
131. Silvester, P.P. and R.L. Ferrari, *Finite Elements for Electrical Engineers*. 2nd edition, Cambridge: Cambridge University Press, 1990.
132. Similowski, T. and J.H.T. Bates, "Two-compartment modelling of respiratory system mechanics at low frequencies: gas redistribution or tissue rheology?", *Eur Respir J*, **4**: 353-358, 1991.
133. Smith, J.C. and S.H. Loring, "Passive mechanical properties of the chest wall". In: Macklem, P.T. and J. Mead (Eds), *Handbook of physiology, Section 3, Volume III*. Bethesda, MD: Am Pysiol Soc, 1986.

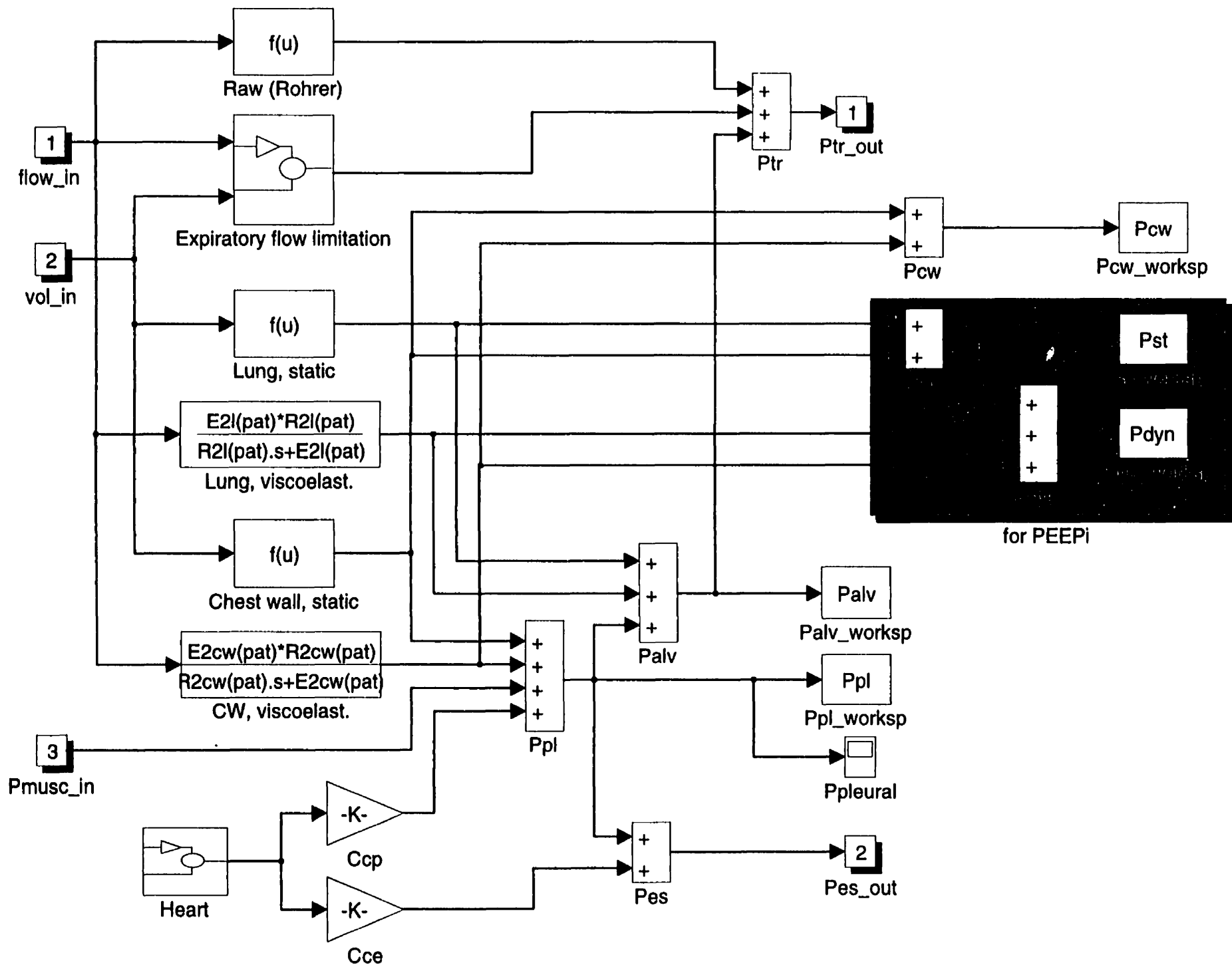
134. Smith, R.W., I. Freeston, L, and B.H. Brown, "Real-time electrical impedance tomography system for clinical use. Design and preliminary results", *IEEE Trans Biomed Eng*, **42(2)**: 133-140, 1995.
135. Smith, T.C. and J.J. Marini, "Impact of PEEP on lung mechanics and work of breathing in severe airflow obstruction", *J Appl Physiol*, **65(4)**: 1488-1499, 1988.
136. Smulders, L.A. and A. van Oosterom, "Application of electrical impedance tomography to the determination of lung volume", *Clin Phys Physiol Meas*, **13**: Suppl A:167-70, 1992.
137. Tai, R., C V and H. Wu, R, "Experimental electrical impedance tomography system", *Proc TENCON*, **2**: 1005-1008, 1993.
138. Taktak, A., P.M. Record, R. Gadd, and P. Rolfe, "Practical factors in neonatal lung imaging using electrical impedance tomography", *Med & Biol Eng & Comput*, **33(2)**: 202-205, 1995.
139. Topulos, G.P., G.J. Nielan, G.M. Glass, and J.J. Fredberg, "Interdependence of regional expiratory flows limits alveolar pressure differences", *J Appl Physiol*, **69(4)**: 1413-1418, 1990.
140. Trillaud, C. and J. Jossinet, "Electrical impedance tomography. An improved design of voltmeter for semi-parallel data acquisition", *Clin Phys Physiol Meas*, **13**: Suppl A:5-10, 1992.
141. von Scheidt, J. "Unendliche Reihen. Funktionenfolgen". In: Grosche, G., V. Ziegler, and D. Ziegler (Eds), *Bronstein-Semendjajew Taschenbuch der Mathematik*. 22th edition, Frankfurt/Main: Verlag Harri Deutsch, 1985.
142. Webster, J.G. "Electrodes". In: Webster, J.G. (Ed), *Electrical Impedance Tomography*. Bristol: Adam Hilger, 1990.

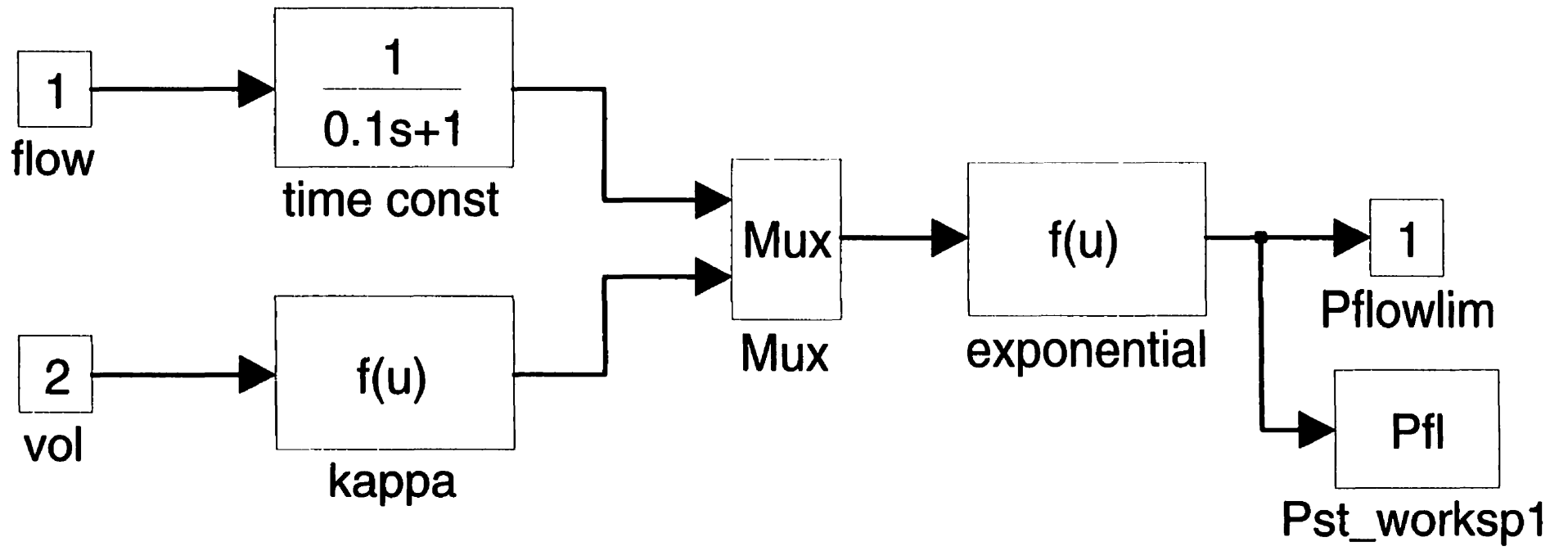
143. Weiss, P.L., I.W. Hunter, and R.E. Kearney, "Reduction of physiological signal contamination using linear filter identification", *Med & Biol Eng & Comput*, **21**: 521-524, 1983.
144. Wellstead, P.E. and S.P. Sanoff, "Extended self-tuning algorithm", *Int J Control*, **34**: 433-455, 1981.
145. West, J.B. *Respiratory physiology*. Baltimore: Williams and Wilkins, 1990.
146. West, J.B. *Pulmonary pathophysiology*. Baltimore: Williams and Wilkins, 1992.
147. Wexler, A., B. Fry, and M.R. Neuman, "Impedance-computed tomography algorithm and system", *Appl Optics*, **24**: 3985-3992, 1985.
148. Whitelaw, W.A., J.P. Derenne, and J. Milic-Emili, "Occlusion pressure as a measure of respiratory centre output in conscious man", *Respir Physiol*, **23**: 181-199, 1975.
149. Wilson, T.A., J.J. Fredberg, J.R. Rodarte, and R.E. Hyatt, "Interdependence of regional expiratory flow", *J Appl Physiol*, **59(6)**: 1924-1928, 1985.
150. Woo, E.J. "Computational complexity". In: Webster, J.G. (Ed), *Electrical impedance tomography*. Bristol: Adam Hilger, 1990.
151. Woo, E.J., P. Hua, J.G. Webster, and W.J. Tompkins, "Measuring lung resistivity using electrical impedance tomography", *IEEE Trans Biomed Eng*, **39(7)**: 756-760, 1992.
152. Woo, E.J., P. Hua, J.G. Webster, and W.J. Tompkins, "A robust image reconstruction algorithm and its parallel implementation in electrical impedance tomography", *IEEE Trans Med Imaging*, **12(2)**: 137-144, 1993.
153. Woo, E.J., P. Hua, J.G. Webster, and W.J. Tompkins, "Finite-element method in electrical impedance tomography", *Med & Biol Eng & Comput*, **32(5)**: 530-536, 1994.

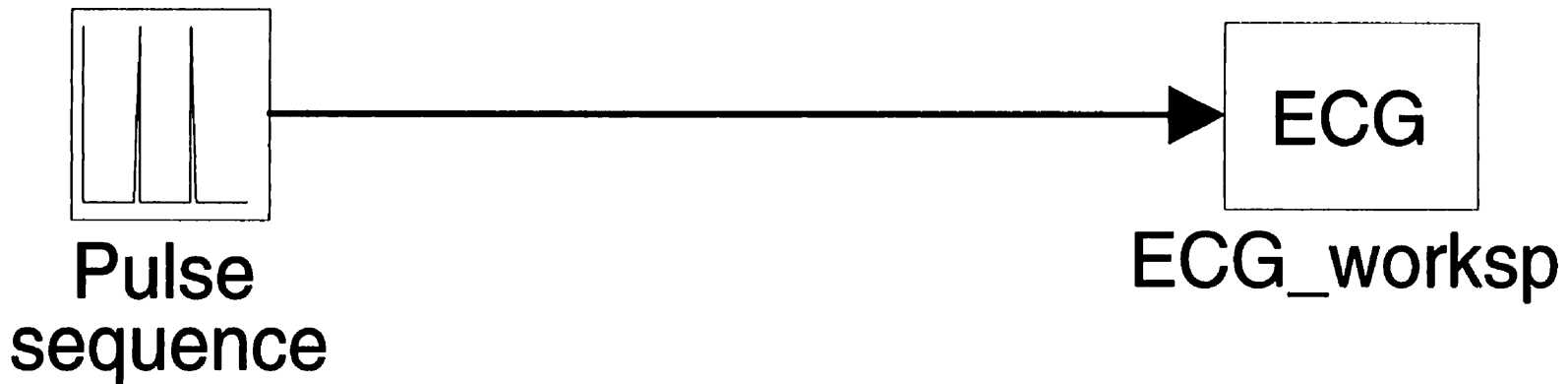
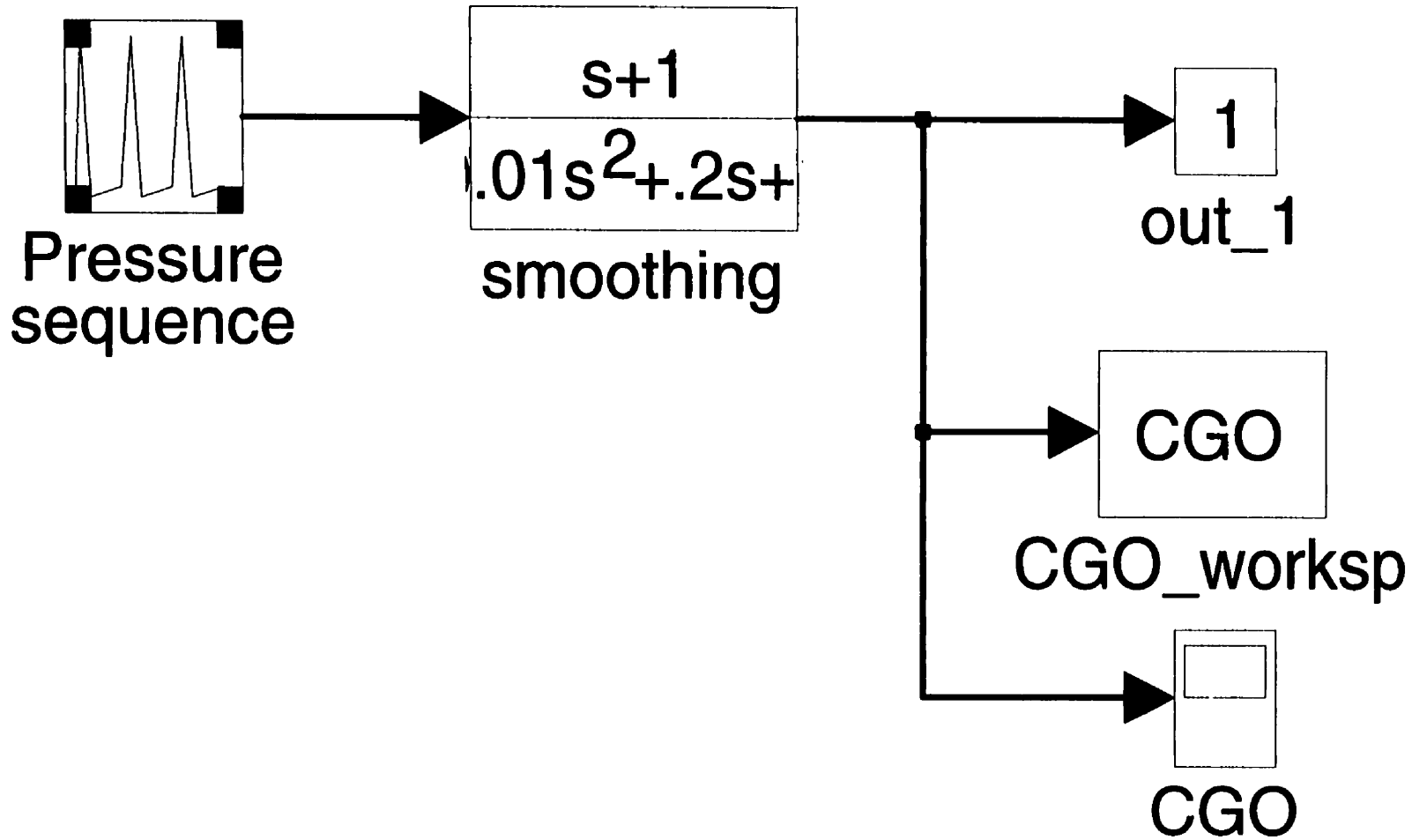
154. Yorkey, T.J., J.G. Webster, and W.J. Tompkins, "Comparing reconstruction algorithms for electrical impedance tomography", *IEEE Trans Biomed Eng*, **34(11)**: 843-852, 1987.
155. Yorkey, T.J., J.G. Webster, and W.J. Tompkins, "An improved perturbation technique for electrical impedance imaging with some criticisms", *IEEE Trans Biomed Eng*, **34(11)**: 898-901, 1987.
156. Younes, M. "Proportional assist ventilation and pressure support ventilation: similarities and differences". In: Marini, J.J. and C. Roussos (Eds), *Ventilatory failure*. Berlin: Springer Verlag, 1991.
157. Younes, M. "Proportional assist ventilation, a new approach to ventilatory support. Theory", *Am Rev Respir Dis*, **145(1)**: 114-120, 1992.
158. Younes, M., A. Puddy, D. Roberts, R.B. Light, A. Quesada, K. Taylor, L. Oppenheimer, and H. Cramp, "Proportional assist ventilation. Results of an initial clinical trial", *Am Rev Respir Dis*, **145(1)**: 121-129, 1992.
159. Younes, M. and W. Riddle, "A model for the relation between respiratory neural and mechanical outputs. I. Theory", *J Appl Physiol*, **51(4)**: 963-978, 1981.
160. Zhu, Q., W.R. Lionheart, F.J. Lidgey, C.N. McLeod, K.S. Paulson, and M.K. Pidcock, "An adaptive current tomography using voltage sources", *IEEE Trans Biomed Eng*, **40(2)**: 163-168, 1993.

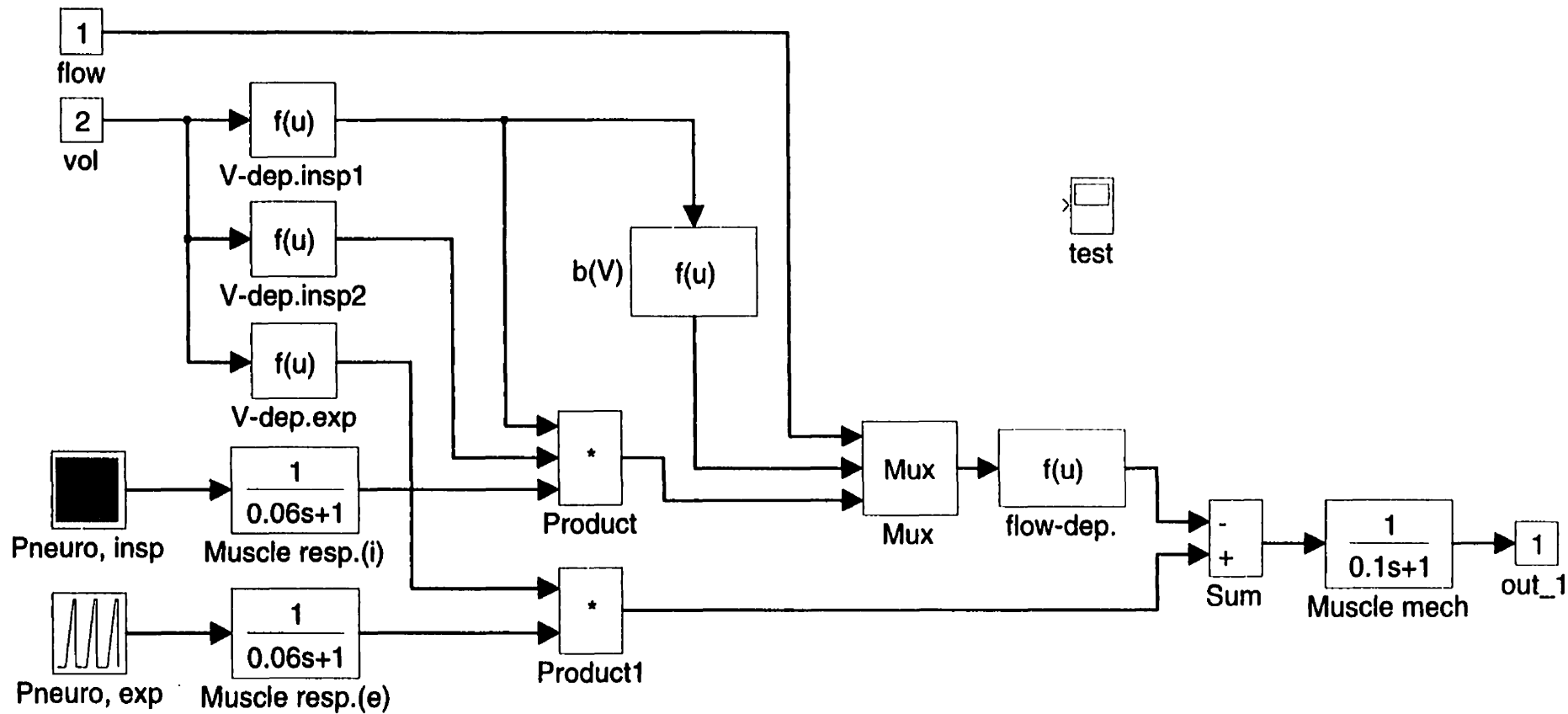
**APPENDIX:
IMPLEMENTATION OF THE MODEL
DESCRIBED IN SECTION 3.1**

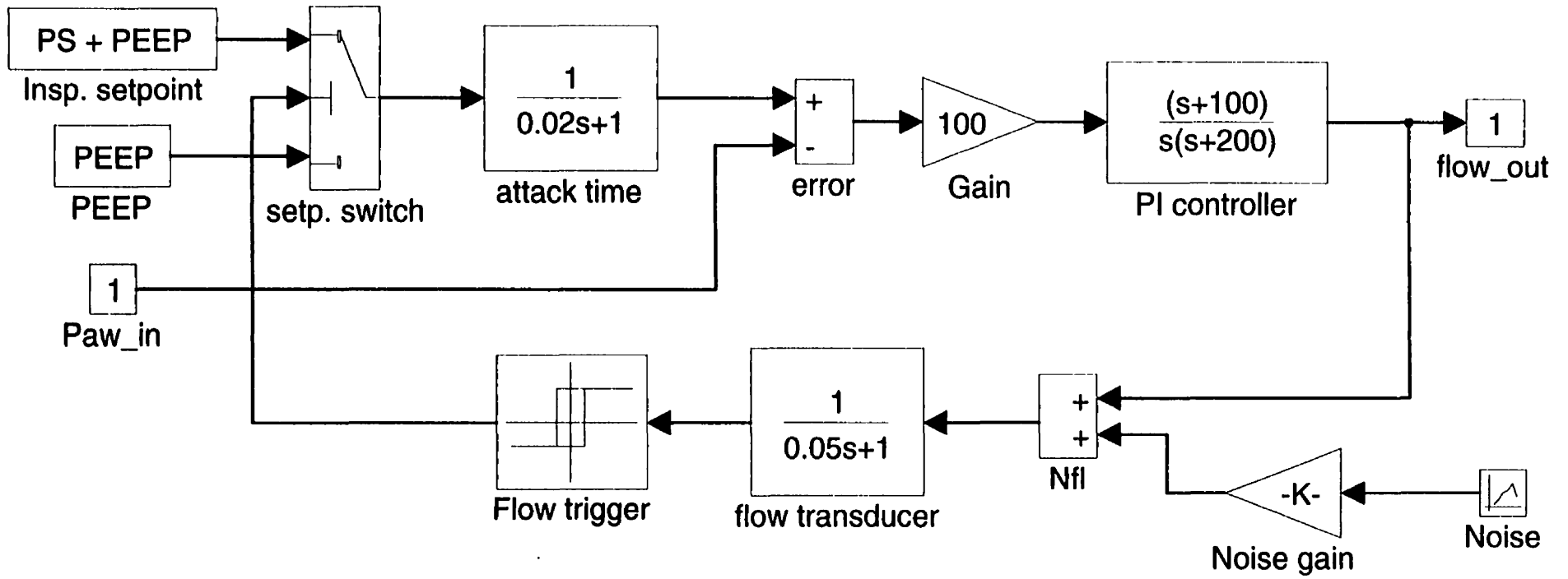












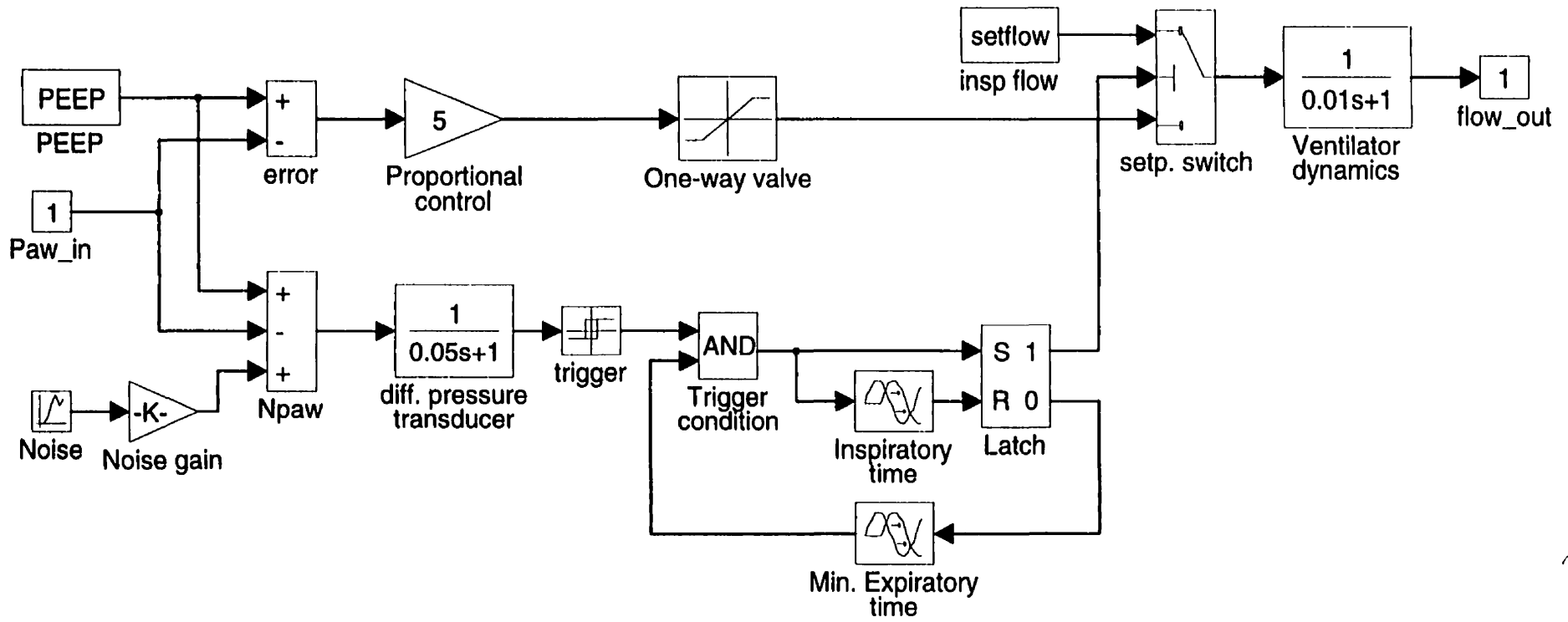
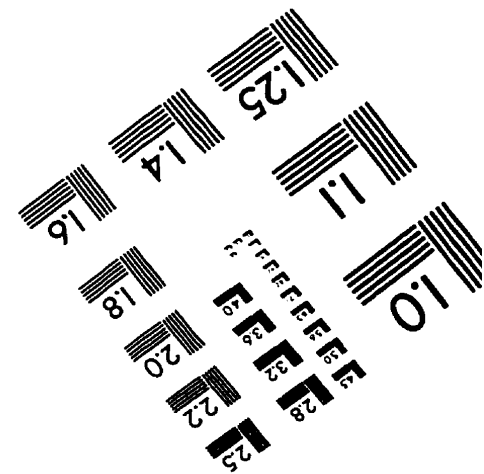
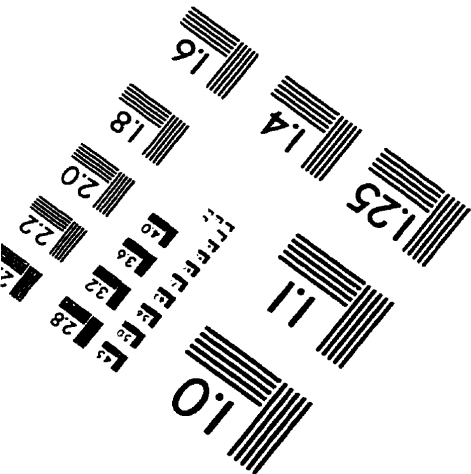
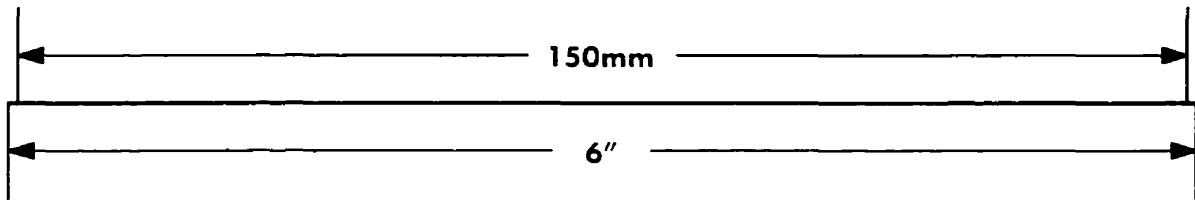
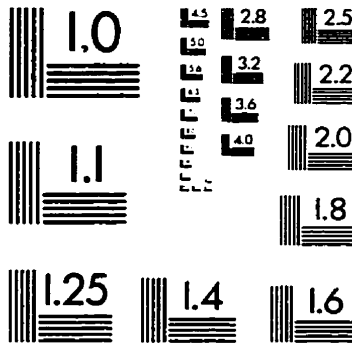
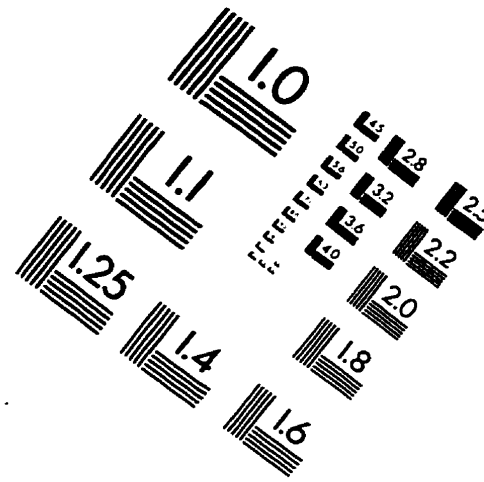
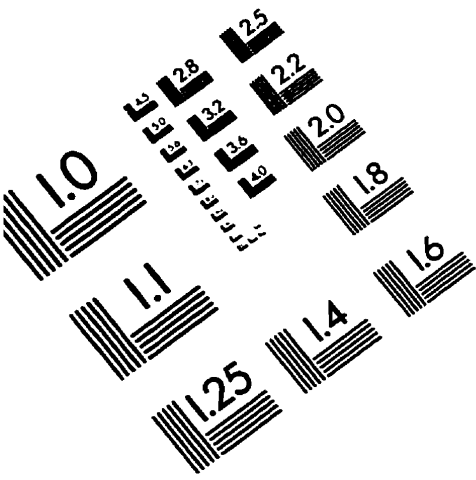


IMAGE EVALUATION TEST TARGET (QA-3)



APPLIED IMAGE . Inc
 1653 East Main Street
 Rochester, NY 14609 USA
 Phone: 716/482-0300
 Fax: 716/288-5989

© 1993, Applied Image, Inc., All Rights Reserved